Proposition et modélisation ab initio de nouveaux matériaux ultra-durs dans le ternaire B C N.

Maurizio Mattesini

N° d'ordre: 2429

THÈSE

PRÉSENTÉE Á

L'UNIVERSITÉ DE BORDEAUX I

ECOLE DOCTORALE DES SCIENCES CHIMIQUES

Par

Maurizio MATTESINI

POUR OBTENIR LE GRADE DE

DOCTEUR

Spécialité: PHYSICO-CHIMIE DE LA MATIÈRE CONDENSÉE

PROPOSITION ET MODÉLISATION *AB INITIO* DE NOUVEAUX MATÉRIAUX ULTRA-DURS DANS LE TERNAIRE BCN

A soutenir le 23 Novembre 2001 après avis de:

M. P. MOHN	*Professeur*	*Rapporteurs*
M. S. CSILLAG	*Professeur*	

Devant la Commission d'examen formée de:

M. J. ETOURNEAU	*Professeur*	*Président*
M. P. MOHN	*Professeur*	*Rapporteurs*
M. S. CSILLAG	*Professeur*	
M. H. DREYSSE	*Professeur*	*Examinateurs*
M. R. AHUJA	*Docteur*	
M. S. F. MATAR	*Directeur de la recherche*	

Abstract

Due to the technological importance behind the possibility to discover novel classes of hard materials an enormous research effort has been directed during the last decades towards the synthesis and characterisation of promising carbon-based compounds such as carbon nitrides and boron carbon nitrides. However, despite many attempts of synthesis and the indisputable progresses made in the field, amorphous samples with unclear crystallographic data have been often obtained in many research laboratories. In particular, several problems arise from the fact that most of the samples are of polymorphic nature, thus leading to a difficult and uncertain spectroscopic characterisation.

A general understanding of the relations between composition and the electronic structure properties has therefore been provided theoretically in this Thesis to get further insight into the characteristics of pure crystalline forms. As one might expect this work has suddenly been turned out into a complicate and challenging task because of the lack of reliable experimental crystal structures to be used as references for the computational inputs. Therefore it became essential to propose hypothetical bi- and three-dimensional model phases to obtain trends on the relative stability, electronic and mechanical properties of carbon- and boron carbon-nitrides. So far as that is concerned, a systematic study of pure crystalline CN_x (where x=0.36 and 1.33) and BC_2N systems has been proposed as an important complement to the experimental knowledge. Thanks to the progress in modern computer technology it has also been possible to compute such an investigation via *ab-initio* (first-principles) methods by testing and probing different solid state calculational approaches. In fact, one of the first objectives of this project has been the search of a valid computational density-functional-based scheme able to reproduce and/or predict the hardness and stability of a wide variety of ultra-hard materials.

Calculations of the cohesive properties and standard enthalpies of formation have been carried out to address the thermodynamic stability of different isoelectronic compositions, namely C_3N_4, $C_{11}N_4$ and BC_2N. The hardness has also been studied by means of the analysis of the calculated elastic and bulk moduli. The investigation of the electronic properties has been achieved with the calculation of the density of states, band structure, electron density maps and crystal orbital overlap population analysis. For some of the studied molecular clusters, the ^{13}C NMR shifts have been evaluated to provide a spectroscopic discrimination between systems with very similar structural characteristics. This is the case of the hexagonal and orthorhombic models of the graphitic-like C_3N_4 form. Finally, the determination of the electron-energy loss near edge structures of C, B and N K ionisation edges has been computed in order to provide reference spectra of pure crystalline materials, likely to allow a discrimination of polymorphic samples.

Results are presented to demonstrate that carbon nitrides are ultra-hard systems with outstanding mechanical properties. In particular, the carbon rich composition, $C_{11}N_4$, has shown larger cohesive energies and it is generally stiffer than the electronic

analogue C_3N_4. However, the possibility to deposit single phase samples should be highly hampered in both stoichiometries by their large positive enthalpies of formation.

The introduction of boron atoms (boron carbon nitrides) has displayed a slight decreasing in the magnitudes of the elastic and bulk moduli, though the calculated values are still higher than that of cubic boron nitride (*i.e.* the second hardest known material). Nevertheless, three-dimensional BC_2N phases have also shown exothermic enthalpies of formation which point to an easier deposition of the "BCN" materials with respect to carbon nitrides. Therefore, by considering the whole set of the investigated model phases, sp^3-bonded boron carbon nitrides result as the best candidates for novel ultra-hard materials which could, in principle, be synthesised with the actual techniques. Very recent experimental results seem to support this general tendency.

Résumé

Compte tenu des enjeux technologiques qui sous-tendent la découverte de nouvelles classes de matériaux ultra-durs, des efforts de recherche considérables ont été destinés durant les deux dernières décades à la synthèse et à la caractérisation de composés légers prometteurs tels que les nitrures et boronitrures de carbone.

Cependant, malgré de nombreuses tentatives de synthèse et les progrès indiscutables réalisés dans ce domaine, seuls des échantillons amorphes (mal caractérisés du point de la cristallographie) ont pu être obtenus dans différents laboratoires de recherche. En particulier, plusieurs problèmes sont soulevés de par la nature polymorphe des échantillons produits, conduisant de ce fait à une caractérisation spectroscopique peu précise.

Par conséquent l'établissement de relations entre composition et propriétés de structure électronique est fourni sur une base théorique dans cette Thèse afin d'approfondir les caractéristiques des formes cristallines des matériaux. Comme on pouvait s'y attendre cette tâche complexe est vite devenue un défi compte tenu du manque de données expérimentales pour les structures cristallines susceptibles de servir de point de départ aux calculs.

Il devint alors essentiel de proposer des phases modèles (hypothétiques) aux échelles bi- et tri-dimensionnelles pour établir des tendances comparatives sur les stabilités, propriétés électroniques et mécaniques des nitrures et boronitrures de carbone. En particulier, les études systématiques des systèmes cristallins binaires CN_x (où x=0,36 et 1,33) d'une part et ternaires BC_2N d'autre part ont été menées et présentées comme une force de proposition vis à vis des expérimentateurs.

Grâce aux énormes progrès de la technologie moderne des ordinateurs, il a été possible de mener ces études au moyen de méthodes *ab initio* (dès le départ) en testant et sondant différentes approches de l'étude du solide. En fait, l'un des premiers objectifs de mon travail de Thèse a été de valider le meilleur schéma calculationnel au sein de la théorie de la fonctionnelle densité, DFT, susceptible de reproduire et/ou de prédire la dureté et la stabilité d'une grande variété de matériaux ultra-durs.

Les calculs des propriétés de cohésion et les enthalpies standard de formation ont été entreprises afin d'expliquer la stabilité thermodynamique des différentes compositions isoélectroniques, nommément C_3N_4, $C_{11}N_4$ et BC_2N. La dureté a été également étudiée au moyen de l'analyse des modules d'élasticité et de compressibilité. L'examen des propriétés de structure électronique a été réalisé par le calcul des densités d'états, de la structure de bandes d'énergie, des cartes de densité électronique et des populations de recouvrement. L'étude des déplacements chimiques par RMN du ^{13}C de clusters moléculaires a permis de fournir un moyen de discrimination entre systèmes ayant des caractéristiques structurales très voisines. C'est notamment le cas des structures hexagonale et orthorhombique de C_3N_4 graphitique. Enfin, les seuils d'ionisation K de C, B et N ont été calculés (spectroscopie électronique par perte d'énergie "EELS") pour les différentes structures cristallines afin de fournir des spectres de référence susceptibles d'aider à la détermination des compositions des

échantillons polymorphes.

Les résultats démontrent que les nitrures de carbone étudiés sont des matériaux ultra-durs ayant des propriétés mécaniques exceptionnelles. En particulier, les phases de la composition riche en carbone, $C_{11}N_4$, montrent des énergies de cohésion supérieures et se présentent comme plus dures que l'analogue iso-électronique C_3N_4. Néanmoins la possibilité de déposer des stoechiométries monophasiques serait pénalisée pour les deux compositions compte tenu de leurs énergies de formation fortement positives.

L'introduction d'atomes de bore (boronitrues de carbone) conduit à une légère diminution des amplitudes des modules d'élasticité et de compressibilité. Mais les valeurs calculées restent supérieures à celles de BN cubique, le second meilleur matériau ultra-dur connu après le diamant. Néanmoins les phases tri-dimensionnelles BC_2N analysées présentent des enthalpies de formation nettement exothermiques, ce qui est en faveur d'une préparation (par dépôt de couches minces par exemple) plus aisée de phases "BCN" par rapport aux nitrures binaires CN_x pour lesquels $\Delta H_f^0 > 0$. Par conséquent en considérant l'ensemble des systèmes modèles, les phases "BCN" à liaisons hybridées essentiellement sp^3 (tri-dimensionnelles) se présentent comme les meilleurs candidats pour de nouveaux matériaux ultra-durs à base d'éléments légers susceptibles d'être synthétisés par les moyens actuels. Ces observations sont appuyées par des résultats expérimentaux récemment obtenus.

Preface

This Thesis illustrates the work that I carried out between 1998 and 2001 at the Institut de Chimie de la Matière Condensée de Bordeaux (ICMCB-CNRS), University of Bordeaux I. The purpose of my research within the European Training and Mobility of Researchers (TMR) Network[1] has been the characterisation of the properties of different carbon- and boron carbon-nitride compounds by attested, highly accurate electronic structure calculations. In particular, the modelling of novel potential hard materials like binary CN_x and ternary $B_xC_yN_z$ have been addressed.

When I started my work in November 1998 there were already several published scientific papers (both theoretical and experimental) dealing with the distinct features of novel compounds, quite often called *super*- or *ultra*-hard materials, that could in principle compete with the hardness of the conventional diamond. However, one of the greatest attractions of this subject that has always appeared important to me is the close link existing between hardness and phase stability on the one hand and the bonding and structure of the material on the other. The connection between these two aspects has been to some degree proved in this Thesis to be one of the essential principles on which the development of the next generation's hard materials should be based.

Although most of the investigations were performed at the solid state level, the study of some molecular clusters has also been successfully integrated for the evaluation of the ^{13}C NMR chemical shifts. The largest part of the calculations have been achieved by using the computational facilities of the intensive centre of calculation "*pôle Modélisation Microscopique et Mésoscopique en Physique, dans l'Environnement et en Chimie*" (M3PEC) of the University of Bordeaux I. The results obtained have been well received in an exchange of information with the other partners of the European commission.

The present manuscript shows an introductory part intended to explain some specific concepts about hard materials and to cover the basic ideas behind the employed theoretical methods. The second part is specifically dedicated to the thorough description of the results obtained during the study of carbon nitride and boron carbon nitride systems.

Bordeaux, September 2001

`Maurizio Mattesini`

[1] *Synthesis, Structure and Properties of New Carbon-Based Hard Materials*, FMRX-CT97-0103.

Nomenclature

Frequently used abbreviations:

APW	Augmented plane wave
ASA	Atomic sphere approximation
ASW	Augmented spherical wave
bcc	Body centered cubic
COOP	Crystal orbital overlap population
CVD	Chemical vapor deposition
DFT	Different density functional theory
DOS	Density of states
EELS	Electron energy loss spectroscopy
$\mathbf{E}_F$	Fermi energy
$\mathbf{E}_g$	Band gap
ELNES	Energy loss near edge structure
fcc	Face centered cubic
FFT	Fast fouries transforms
FP-LAPW	Full-potential linearized augmented plane wave
GGA	Generalized gradient approximation
hcp	Hexagonal close packed
ICOOP	Integrated crystal orbital overlap population
KS orbitals	Kohn-sham orbitals
LAPW	Linearized augmented plane wave
LDA	Local density approximation
LMTO	Linear muffin tin orbital
NMR	Nuclear magnetic resonance
PP	Pseudo-potential
PVD	Physical vapor deposition
R_{mt}	Muffin-tin radius
$\mathbf{sp}^2$, $\mathbf{sp}^3$	Electron orbital hybridization
US-PP	Ultra-soft pseudo-potential
σ, π	Bonding types
xc	Exchange-correlation functional

Published Papers

1. **Relative stabilities, bulk moduli and electronic structure properties of different ultra hard materials investigated within the local spin density functional approximation**, M. Mattesini, S. F. Matar, A. Snis, J. Etourneau, A. Mavromaras, *J. Mater. Chem.*, **9**, 3151 (1999).

2. **Stability and electronic properties investigations of the graphitic C_3N_4 system showing an orthorhombic unit cell**, M. Mattesini, S. F. Matar and J. Etourneau, *J. Mater. Chem.*, **10**, 709-713 (2000).

3. **First-principles characterisation of new ternary heterodiamond BC_2N phases**, M. Mattesini and S. F. Matar, *Comput. Mat. Sci.*, **20/1**, 107-119 (2001).

4. *Ab initio* **search of carbon nitrides, isoelectronic with diamond, likely to lead to new ultra-hard materials**, S. F. Matar and M. Mattesini, *C. R. Acad. Sci. Paris*, **4**, 255 (2001).

5. **Search for ultra-hard materials: theoretical characterisation of novel orthorhombic BC_2N crystals**, M. Mattesini and S. F. Matar, *Int. Jour. of Inorganic Materials*, in press (2001).

6. **DFT investigation of hardness, stability and electron-energy-loss spectra of carbon nitrides in the $C_{11}N_4$ Stoichiometry**, M. Mattesini and S. F. Matar, *Phys. Rev. B*, submitted February (2001).

Contents

Title Page i
Abstract ii
Résumé iv
Preface vi
Nomenclature vii
Published Papers viii
Table of Contents xi
List of Figures xv
List of Tables xix

1 Introduction **1**
1.1 The interest in novel ultra-hard materials 1
1.2 Aims of the Thesis 2
1.3 Outline of the Thesis 3

2 The Hardness and Covalency **5**
2.1 First theoretical proposition of Carbon Nitrides as novel hard materials . 5
2.2 Electron count considerations 6

3 The concept of Hardness **9**
3.1 Introduction 9
3.1.1 Measure of the resistance upon volume change in solids 10
3.1.2 Resistance to reversible deformation upon shape change 11

4 Density Functional Theory **13**
4.1 Introduction 13
4.2 The basic principles of the method 14
4.3 Single particle Kohn-Sham equations 16
4.3.1 The basis sets 19
4.3.2 The Self Consistent Field in DFT 20

5 Planewave Pseudo-Potential methods **21**
5.1 Introduction . . . 21
5.2 Blöch's Theorem and Planewaves . . . 22
5.3 General Approximations . . . 23
5.4 Pseudo-Potentials . . . 23
5.4.1 Norm conserving pseudo-potentials . . . 23
5.4.2 Ultrasoft Pseudo-Potentials (US-PP) . . . 24
5.4.3 Generation of the US-PP . . . 26

6 The Full Potential LAPW method **29**
6.1 Introduction . . . 29
6.2 The LAPW basis . . . 31

7 The ASW method **33**
7.1 About linear methods . . . 33
7.1.1 ASW and LMTO methods . . . 33
7.1.2 The ASA and its implications . . . 34
7.1.3 Solution of the wave function . . . 34
7.2 Further formalism with the ASW method . . . 34
7.2.1 The augmentation process . . . 35
7.2.2 The variational method of Rayleigh-Ritz . . . 38

8 Carbon Nitrides **40**
8.1 Introduction . . . 40
8.2 Study of the C_3N_4 stoichiometry . . . 42
8.2.1 Methods and computational details . . . 42
8.2.2 Structural models for the C_3N_4 stoichiometry . . . 43
8.2.3 Relative stability of variuos C_3N_4 phases . . . 44
8.2.4 Hardness . . . 51
8.2.5 Hexagonal and Orthorhombic *graphitic*-C_3N_4 . . . 55
8.2.6 Calculation of the ^{13}C NMR chemical shifts . . . 66
8.2.7 Conclusions . . . 70
8.3 The isoelectronic $C_{11}N_4$ model system . . . 72
8.3.1 Introduction . . . 72
8.3.2 Methods and computational details . . . 73
8.3.3 The analysed crystalline structures . . . 73
8.3.4 Relative stability and phase transitions . . . 76
8.3.5 Calculations of the elastic and bulk moduli . . . 83
8.3.6 Electronic structure . . . 89
8.3.7 Concluding remarks . . . 93

9 Boron Carbon Nitrides **98**
9.1 Ternary BCN compounds . . . 98
9.2 Setting up novel three-dimensional BC_2N phases . . . 100
9.2.1 Cubic and hexagonal diamond . . . 100
9.2.2 Carbon substitution . . . 101
9.3 Computational details . . . 105
9.4 BC_2N phases and their relative stability . . . 106
9.4.1 Enthalpy of formation . . . 108
9.4.2 Discussion of the results . . . 111
9.5 Theoretical estimation of hardness . . . 114
9.5.1 Mechanical stability . . . 118
9.6 Electronic density of states and band structure . . . 120
9.6.1 The orthorhombic phases (I and II) . . . 120
9.6.2 The trigonal model structure (III-BC_2N) . . . 127
9.7 Theoretical ELNES for BC_2N model systems . . . 127
9.7.1 The layered BC_2N model system . . . 131
9.8 Conclusions . . . 135

10 Summary and Outlook **141**
10.1 Carbon Nitrides . . . 141
10.2 Boron Carbon Nitrides . . . 142
10.3 Prospective studies and "*what's left*" . . . 143

11 Conclusions **144**
11.1 Nitrures de Carbone . . . 144
11.2 Boronitrures de Carbone . . . 145
11.3 Prospectives et "*ce qui reste à faire*" . . . 146

Bibliography **158**

Index **159**

List of Figures

2.1 Schematic ternary composition diagram indicating different "*hard*" stoichiometries. 8

4.1 Schematic representation of various DFT-based methods of calculation. . 17
4.2 Flow-chart for self-consistent density functional calculations. 18

5.1 Illustration diagram of the replacement of the "all-electron" wavefunction and core potential by a pseudo-wavefunction and pseudo-potential. 24

6.1 Adaptation of the basis set by dividing the unit cell into atomic spheres and interstitial regions. 30

7.1 Comparison between the augmented plane (APW) and spherical (ASW) waves. This Figure has been taken from the original work of A. R. Williams, J. Kübler and C. D. Jr. Gelatt [74]. 36

8.1 β-C_3N_4 model system. Carbon and Nitrogen are depicted in grey and white, respectively. This color scheme is kept throughout all the Thesis. . 45
8.2 One layer of the hexagonal *graphitic*-C_3N_4 model. 45
8.3 One layer of the orthorhombic *graphitic*-C_3N_4 phase. 46
8.4 Relative stability between different C_3N_4 phases by using different method of calculations. 46
8.5 Energy dependence of the unit cell volume for *cubic*-C_3N_4 as a function of three different calculational methods. Data point have been fitted with the Birch type EOS. 53
8.6 Figure from R. Riedel [149] showing the scattering of the Vickers hardness for hard materials when compared with bulk and shear moduli. 54
8.7 Electron circulation in the hexagonal *graphitic*-C_3N_4 model. 57
8.8 Electron circulation in the orthorhombic *graphitic*-C_3N_4 model. 57
8.9 The above figure shows the general differences in the ring's geometry for the orthorhombic and hexagonal unit cells. 61

8.10 Total COOP for the hexagonal and the orthorhombic phases (ASW). . . . 63
8.11 Integrated COOP for the hexagonal and the orthorhombic systems (ASW). 63
8.12 Total COOP for the orthorhombic phase (ASW). For clarity each nitrogen-carbon interactions have been shifted along the vertical axis. The labels B and AB define the bonding and the antibonding region, respectively. . . . 64
8.13 Site projected DOS plot for the AAA orthorhombic graphitic phase (ASW). The energy reference along the x-axis is taken with respect to the Fermi level; the y-axis gives the DOS per atom and unit energy. 65
8.14 Site projected DOS for the hexagonal graphitic model system (ASW). . . 66
8.15 Valence electron density map for the orthorhombic *graphitic*-C_3N_4 model system (FP-LAPW). 67
8.16 Total DOS for the orthorhombic phase (FP-LAPW). Notice the absence of energy gap at the top of the VB. 68
8.17 Total DOS for the hexagonal phase (FP-LAPW). 68
8.18 Molecular cluster relative to the hexagonal *graphitic*-C_3N_4. 69
8.19 Molecular cluster relative to the orthorhombic *graphitic*-C_3N_4. 70
8.20 Ball and stick model of the *bl*-C_3N_4 structure. Figure shows the projection of the atoms along the [001] plane. 75
8.21 One layer of the *graphitic*-$C_{11}N_4$ model phase. 75
8.22 Crystal structure of the tetragonal $\alpha - C_{11}N_4$. Projection along the [100] plane exhibiting the "*nitrogen-hole*". 77
8.23 Projection of the orthorhombic $\beta - C_{11}N_4$ crystal structure along the [010] plane. 77
8.24 Free energies (eV/atom) versus atomic volumes (Å^3/atom) for various C_3N_4 and $C_{11}N_4$ phases (US-PP). 80
8.25 Front view of the "*carbon-hole*" in β-$C_{11}N_4$. 81
8.26 The calculated DOS for the *bl*-C_3N_4 phase (FP-LAPW). 90
8.27 The calculated total DOS for the *bl*-C_3N_4 and α-, $\beta - C_{11}N_4$ (FP-LAPW). 92
8.28 Theoretical C K ELNES of diamond and graphite (FP-LAPW). 94
8.29 Theoretical C K ELNES of various phases (FP-LAPW). The spectra for the inequivalent atoms positions have been calculated separately and weighted in the present Figure. 95
8.30 Theoretical N K ELNES of various phases (FP-LAPW). As in Fig. 8.29 inequivalent atoms have been calculated separately and weighted in the present spectra. 96

9.1 Unit cell of cubic diamond. This structure was first determined in 1913 by W. H. and W. L. Bragg [195]. That was also the first time that the structure of an element was determined by the use of X-ray diffraction [196]. 100
9.2 Unit cell of lonsdaleite (hexagonal polymorph of diamond). 101

9.3 Crystal structure of the orthorhombic I-BC_2N. Carbon, nitrogen and boron atoms are depicted in black, white and grey, respectively. 104
9.4 Crystal structure of the orthorhombic II-BC_2N. 105
9.5 Crystal structure of the trigonal III-BC_2N phase. 106
9.6 Cohesive energies (eV/atom) as a function of the atomic volume ($Å^3$/atom) for the starting materials and BC_2N structures. The curves were generated with the US-PP/LDA method. 109
9.7 Crystal structure of the orthorhombic *graphitic*-BC_2N model phase. 110
9.8 Crystal structure of the *h*-BN. 112
9.9 Unit cell of the *c*-BN. 113
9.10 Energy versus pressure for different BC_2N phases (US-PP). 114
9.11 Idealised chemical environment around the B/N site in *c*-BN and various BC_2N phases. Part (a) of the scheme refers to the orthorhombic phases (I and II) while, part (b) concerns the local chemical bonding of the phase III. 115
9.12 Valence electron density map showing the polarisation of the C-C bonds in I-BC_2N. 117
9.13 The calculated partial density of states of I-BC_2N. 121
9.14 Band structure of I-BC_2N along the symmetry lines of the orthorhombic Brillouin zone : X=$(0\frac{1}{2}0)$ → Γ=(000) → Z=$(00\frac{1}{2})$ → U=$(0\frac{1}{2}\frac{1}{2})$ → R=$(\overline{\frac{1}{2}}\frac{1}{2}\frac{1}{2})$ → S=$(\overline{\frac{1}{2}}\frac{1}{2}0)$ → Y=$(\overline{\frac{1}{2}}00)$ → Γ=(000). 122
9.15 The calculated partial density of states of II-BC_2N. 124
9.16 Band structure of II-BC_2N along the symmetry lines of the orthorhombic Brillouin zone : X=$(0\frac{1}{2}0)$ → Γ=(000) → Z=$(00\frac{1}{2})$ → U=$(0\frac{1}{2}\frac{1}{2})$ → R=$(\overline{\frac{1}{2}}\frac{1}{2}\frac{1}{2})$ → S=$(\overline{\frac{1}{2}}\frac{1}{2}0)$ → Y=$(\overline{\frac{1}{2}}00)$ → Γ=(000). 125
9.17 Total DOS for the orthorhombic phases I and II in arbitrary units. 126
9.18 The calculated partial density of states of III-BC_2N. 128
9.19 Band structure of III-BC_2N along the symmetry lines of the hexagonal Brillouin zone : Γ=(000) → M=$(0\frac{1}{2}0)$ → K=$(\overline{\frac{1}{3}}\frac{2}{3}0)$ → Γ=(000) → A=$(00\frac{1}{2})$ → L=$(0\frac{1}{2}\frac{1}{2})$ → H=$(\overline{\frac{1}{3}}\frac{2}{3}\frac{1}{2})$ → A=$(00\frac{1}{2})$. 129
9.20 Theoretical C *K* ELNES of various phases (FP-LAPW). The experimental CVD diamond spectra [204] has been shifted by +1.05 eV along the energy axis in order to align its first σ^* peak with the one of the theoretical curve. 132
9.21 Theoretical N *K* ELNES of various phases (FP-LAPW). The spectra of the high pressure synthesised *c*-BN [205] has been moved by +2.05 eV to match the first theoretical σ^* peak. 133
9.22 Theoretical B *K* ELNES of various phases (FP-LAPW). The high pressure synthesised *c*-BN spectra [205] has been shifted by +3.15 eV in order to align the first σ^* peak with the theoretical curve. 134
9.23 Theoretical C *K* ELNES of *graphitic*-BC_2N in comparison to Graphite. . . 137

9.24 Theoretical N *K* ELNES of *graphitic*-BC_2N in comparison to *h*-BN. 138
9.25 Theoretical B *K* ELNES of *graphitic*-BC_2N in comparison to *h*-BN. 139

10.1 The three-dimensional C_7N_4 model system. Ongoing calculations seem to indicate the same general tendency found for the C_3N_4 and $C_{11}N_4$ compositions. 143

List of Tables

2.1 Hardness of minerals and some synthetic ceramics according to F. Mohs. For synthetic materials micro-hardness values are given in units of Knoop scale. Values are shown as compiled by R. Riedel in Ref. [25]. 7

5.1 Parameters determining the ultra-soft pseudo-potential used in this Thesis. ARC represents the atomic reference configuration and $r_{c,l}$ (where l=s, p, d) the cut-off radii in atomic units. 27

8.1 Total energies and densities for different C_3N_4 phases. Energy values are expressed in eV/C_3N_4 unit and are scaled with respect to the stable *graphitic*-C_3N_4 form. Pseudo-potential calculations refer to the work of D. M. Teter and R. J. Hemley [29]. 47

8.2 Cohesive energies (eV/atom) of different C_3N_4 model systems. Values are confronted with those of the starting materials : diamond/graphite and N_2. For the calculations of the nitrogen dimer it has been used a simple cubic cell (a=10 Å) with atoms displaced along the diagonal direction. It should be noted that an overbinding of more than 1 eV/atom is not unusual in local-density calculations for second-period elemental solids, as for example diamond [136, 137]. 49

8.3 Calculated enthalpy of formation, $\Delta H^o_{f,0}$ (kJ/mol), for different exchange-correlation functionals. The above table shows only values representatives for the layered *graphitic*-$C_{\frac{3}{4}}N$ and the three-dimensional *bl*-$C_{\frac{3}{4}}N$. The complete list of enthalpies is given in Tab. 8.18 of Section 8.3, p. 72. 50

8.4 Equilibrium lattice constants (a_o) for the investigated model systems. The energy *vs.* volume data were fitted with a third order Birch equation. . . . 51

8.5 Bulk modulus, B (GPa) and its pressure derivatives, $B^{'}$ (values in parenthesis) for various C_3N_4 phases and diamond. 52

8.6 Calculated elastic constants (c_{ij} in GPa), atomic densities (ρ in g/cm^3) and isotropic shear moduli (G in GPa) for five different C_3N_4 phases. Values in parenthesis refer to experimental measurements [8]. 55

8.7 Calculated elastic constants (GPa) and bulk moduli (GPa) for diamond as a function of different exchange-correlation methods : Perdew-Wang 91 (PW91) [47], Perdew-Becke (PB) [46], Perdew-Wang 86 (PW86) [57], Langreth-Mehl-Hu (LM) [45]. The subscript "*relaxed*" and "*frozen*" denotes values calculated with or without the relaxation of the atomic positions. 56
8.8 Calculated elastic constants (GPa) and bulk moduli (GPa) for *bl*-C_3N_4 as a function of different exchange-correlation functionals. 56
8.9 Structural parameters for the orthorhombic structure with AAA stacking order. 59
8.10 Bond lengths before and after the optimisation of the orthorhombic structure. 60
8.11 Angles before and after the optimisation of the orthorhombic structure. The notation prime refers to atoms belonging the adiacent unit cell. . . . 60
8.12 FP-LAPW and US-PP cohesive energies (eV/atom) for the orthorhombic and hexagonal lattices. 62
8.13 Calculations of the ^{13}C NMR chemical shift (ppm) for the two graphitic-like phases. For the reference TMS it has been estimated, with the same computational approach, a chemical shift of 184.4 ppm. 71
8.14 Optimised parameters for the *bl*-C_3N_4 and the α-, β-$C_{11}N_4$ phases. The table shows crystal system, space group, atoms·unit cell^{-1} and the atomic positions. Cell constants are expressed in unit of Å and the angles α, β, γ in degrees. 76
8.15 Optimised parameters for the *graphitic*-$C_{11}N_4$ phase. 78
8.16 Cohesive energy, ΔE (eV/atom), for various CN_x phases. Free energy values are scaled with respect to the stable *graphitic*-$C_{11}N_4$ structure. The ratio of the number of chemical bonds per unit cell, $R_{(C-C/C-N)}$, is also shown. 79
8.17 Calculated FP-LAPW cohesive energies of *graphitic*- and α-$C_{11}N_4$. Values are given in eV/atom. 82
8.18 Computed standard molar enthalpy of formation ($\Delta H^o_{f,0}$) for the two CN_x stoichiometries (x=1.33 and 0.36) by using the cohesive energies seen in Tabs. 8.2, 8.12 and 8.17. Values in parenthesis correspond to the use of graphite as a starting material. 82
8.19 Strains and elastic moduli for the orthorhombic phase. 84
8.20 Strains and elastic moduli for the tetragonal phase. 85
8.21 Strains and elastic moduli for a cubic system. By calculating the tetragonal shear constant, $C' = \frac{1}{2}(c_{11} - c_{12})$, and the bulk modulus, $B = \frac{1}{3}(c_{11} + 2c_{12})$, it is possible to extract c_{11} and c_{12}. 86

8.22 Theoretical values of the elastic constants (c_{ij} in GPa), isotropic shear modulus (G in GPa), bulk modulus (B in GPa), its pressure derivative ($B^{'}$), atomic volume (V_o in $Å^3$/atom), cohesive energy (E_o in eV/atom) and atomic densities (ρ in g/cm^3) of *bl*-C_3N_4 and α-, β-$C_{11}N_4$. Values in round brackets refer to the work of A. Y. Liu and R. M. Wentzcovitch [114] whereas those in square brackets concern the bulk modulus calculated by combining the elastic constants. 87

8.23 Table shows the calculated B/G ratio, Young's modulus (GPa) and Poisson's ratio (dimensionless) of *bl*-C_3N_4 and α-, β-$C_{11}N_4$. Diamond has also been listed as a reference material. Values in round brackets concern the properties of CVD diamond as compiled in Ref. [178]. 89

8.24 Positions of peaks I-V in the spectra of Fig. 8.28. All the positions are scaled with respect to the main σ^* peak II. Values are in units of eV. (†) Values as compiled in Ref. [181]. 93

9.1 Crystal structure data for cubic and hexagonal diamond. Cell constants values are expressed in unit of Å. 102

9.2 Substitution of the carbon atoms in the *fcc* diamond. 102

9.3 Optimised parameters for heterodiamond BC_2N structures. Cell constants and bond distances are given in unit of Å. 103

9.4 Substitution of the carbon atoms in the hexagonal diamond. 104

9.5 Structural and cohesive properties of various phases : atomic volume V_o ($Å^3$), bulk modulus B (GPa), pressure derivatives $B^{'}$ and cohesive energy $E_{coh.}$ (eV/atom). The latter values have been obtained by taking the difference between the total energy of the solids and the ground-state energies of the spherical non spin-polarised atoms. No correction for zero-point motion has been made. 107

9.6 Calculated energy difference, ΔE (eV/atom), for various phases relative to the *graphitic*-BC_2N form. 108

9.7 Optimised parameters for the *graphitic*-BC_2N model phase. 111

9.8 Calculated cohesive energies ($E_{coh.}$ in eV/atom) for various BC_2N phases and some of the starting materials as a function of different exchange-correlation functionals. 116

9.9 Calculated standard enthalpy of formation. Values in parenthesis correspond to the formation energy of *graphitic*-BC_2N when graphite is taken as a starting material. 116

9.10 Calculated enthalpy of formation for the reaction : c-$BN_{(c)}$+$2C_{(c)}$→$BC_2N_{(c)}$. Values in parenthesis correspond to the formation enthalpy of the *graphitic*-BC_2N when the layered h-BN and graphite are used as reactants. 116

9.11 Strains and elastic moduli for the trigonal phase. Unlisted δ_{ij} are set equal to zero. 118
9.12 Independent elastic constants, c_{ij}, and isotropic shear moduli for BC_2N, diamond, lonsdaleite and *c*-BN. Values are expressed in units of GPa. . . 119
9.13 The above table shows the calculated B/G ratio, Young's modulus (GPa) and Poisson's ratio of the studied BC_2N phases. Diamond and *c*-BN have also been listed as reference materials. Numbers given within brackets correspond to the use of the experimental B and G values of Tabs. 9.5 and 9.12. †Bulk modulus from the combination of the various elastic constants. ‡Measured elastic modulus from nanoindentations of polycrystalline *c*-BN bulk samples [203]. 120
9.14 Positions of the peaks A-E relative to the spectra shown in Figs. 9.20, 9.21 and 9.22. All the positions are scaled with respect to the main σ^* peak A and refer to the broadened spectra. Values are expressed in units of eV with an estimated error of ± 0.25 eV. 130
9.15 Positions of the peaks A-G relative to the spectra shown in Figs. 9.23, 9.24 and 9.25. All the energies are scaled with respect to the first σ^* peak B and refer to the broadened spectra. The estimated error is ± 0.25 eV. . . 135
9.16 Values of the separation between the first π^* and σ^* peaks (± 0.5 eV) for the *K* edges of *graphitic*-BC_2N. 136

Chapter 1

Introduction

1.1 The interest in novel ultra-hard materials

The possibility to synthesise new materials with hardness[1] similar or even larger than diamond has become of fundamental and technological interest for chemists, physicists and in particular for the whole materials scientists community. It was in the middle of the last century when most of the known ultra-hard materials (*i.e.* diamond and cubic boron nitride) were synthesised and manufactured with high pressure and high temperature processes [1, 2, 3]. The continue research on the field has recently permitted to synthesise or rediscover superhard compounds such as SiO_2-stishovite [4], cubic-Si_3N_4 [5] and cubic-BC_2N [6]. The constant growing interest in this domain is also due to the development (1980's) of new vapor deposition techniques (CVD, PVD and laser ablation), which allow the deposition of hard materials films at low temperature and pressures on different substrates [7, 8, 9, 10, 11].

Diamond exhibits excellent mechanical, chemical and physical properties and nowadays remains the hardest known material. However, it is well known that it cannot be used in cutting tools for steel owing to a certain instability at high temperatures. As a matter of fact, its stability drastically decreases in the presence of oxygen at even moderate temperature ($\sim 873\ K$). It is also not a very suitable abrasive for cutting and polishing ferrous alloys since it tends to react and form iron carbides. Furthermore, its super abrasive performance is somehow limited. For these reasons and because of the need to substitute expensive diamond in many other applications, new hard materials are required. It is mostly the strong industrial demands of wear resistant coatings for cutting and forming tools which has driven the search of novel hard materials. Common hard

[1] **hard·ness** (*härd′nĭs*), n. [AS. heardness.] 1. *The quality or state of being hard, literally or figuratively.* Source: The American Heritage Dictionary of the English Language, Fourth Edition Copyright © 2000 by Houghton Mifflin Company (http://www.dictionary.com/). All rights reserved.

solids are usually classified into compounds with metallic (TiN or WC), ionic (Al_2O_3) or covalent bonding (diamond, Si_3N_4 etc..). Transition metal nitrides and carbides (TiN and TiC) have been largely used as coatings for wear protective applications in the last decades. However, carbon based materials such as artificially grown diamond and hydrogenated carbon compounds have become a valid alternative. These materials possess good protective properties and low friction coefficient, thus open the possibility to use the coatings as solid lubrificants. Another important class of materials is represented by carbon nitrides compounds with general formula CN_x. The growing research interest arose from the theoretical work of A. Y. Liu and M. L. Cohen [12] which predicted for β-C_3N_4 a hardness comparable to that of diamond. Despite the synthesis of pure crystalline and stoichiometric C_3N_4 has been found extremely difficult, some non stoichiometric carbon nitrides have evidenced interesting properties such as high hardness and elasticity, and low friction. These compounds are thus promising candidates for the next generation's wear protective coating. However, the fundamental problem with such materials remains the extreme difficulty found in growing pure crystalline nitrogen-rich samples. Especially with thin film technology various deposition techniques and growth conditions have been tested without great success: non-crystalline and nitrogen-deficient films are always obtained.

The introduction of boron atoms into carbon nitrides leads to the possibility to obtain new hard materials with general formula $B_xC_yN_z$. With such a boron-based compound the low oxidation resistance of diamond might be improved thus removing the problem of using hard materials at high temperatures in air. The recent interest in boron carbon nitrides has been mostly focussed on the BC_2N stoichiometry, which is a phase isoelectronic with the well known C_3N_4. The first evidence of the graphitic BC_2N dates back to the synthesis of Kouvetakis *et al.* [13, 14], where chemical vapor deposition method was used with BCl_3 and CH_3CN as starting materials. Several efforts have been made in order to modify these graphitic BC_2N systems into highly dense three-dimensional phases but unfortunately, despite the use of high-pressure and high-temperature methods, no common results were found in the last decade. Some researchers found problems with a certain limited solubility [15, 16], while others claimed a segregation in a mixture of diamond and cubic boron nitride (c-BN) [17, 18, 19]. Nevertheless, early theoretical calculations [20, 21, 22] have suggested that these compounds should possess an intermediate hardness between diamond and c-BN .

1.2 Aims of the Thesis

It is certain that despite the initial scientific enthusiasm, the synthesis of carbon nitrides and boron carbon nitrides has suddenly turned out in a very difficult task. Many synthesis routes were tested and important human efforts are being made in order to

characterise polymorphic samples. The search of a pure crystalline material and its subsequent spectroscopic characterisation remains nowadays the main topic for all the researchers working on CN_x and $B_xC_yN_z$ compounds.

Given the cost and the complexity of the synthesis/characterisation procedure, computer modelling investigation has here been used to discover new possible crystalline models and to predict their material properties in a faster and cheaper way. The computational methods have already been applied to diamond and cubic boron nitride (*i.e.* the hardest known solids) with great success, provoking a considerable interest in investigating other hypothetical materials. The first goal of my research has been the determination of an efficient computational approach for simulating the relative stability and the hardness of some potential phases that have recently been proposed for the C_3N_4 stoichiometry. In particular, several Density Functional Theory (DFT) methods have been tested, among the various simulation schemes available in our laboratory, in order to inspect their peculiar reliability and usefulness. Subsequently, the most promising first-principles methods have been employed in the rest of the Thesis to calculate the cohesive properties, bulk and elastic moduli of different kinds of carbon nitride and boron carbon nitride model structures. Electronic properties have also been studied by means of density of states and band structure analysis. In addition, the influence of hybridisation on the chemical bonding and stability has been discussed in terms of the site projected densities of states as well as the crystal orbital overlap population. Finally, since the characterisation of carbon nitrides and boron carbon nitrides is mostly restricted by the problem of obtaining pure crystalline samples, the calculation of the theoretical energy loss near edge structure has been shown in order to provide reference spectra.

A large part of this work has also been oriented to the theoretical proposition and characterisation of novel model systems isoelectronic with diamond and cubic boron nitride. I have in my research focused most of the attention on the *crystal engineering* of the C-B-N networks by proposing various binary ($C_{11}N_4$) and ternary (BC_2N) model compounds. Their electronic, mechanical and spectroscopic characterisation given in this Thesis should provide a precious tool for the interpretation of the experimental results.

1.3 Outline of the Thesis

The first Chapters are mostly concerning a general introduction to the domain of ultrahard materials (Chapters 2 and 3) and to the employed computational methods. In particular, Chapter 4 resumes the basic ideas behind the DFT, while Chapters 5, 6 and 7 contain a brief description of the various method of calculations. In Chapter 8 a detailed investigation of the CN_x systems is presented by paying most of the attention to the differences between the C_3N_4 and $C_{11}N_4$ stoichiometries. The study of boron carbon nitrides is given in Chapter 9. The attention is here focused on the BC_2N phases and

in their mechanical and electronic properties. The conclusions are drawn in Chapter 10 where a general discussion is presented for each of the investigated class of compounds.

Chapter 2

The Hardness and Covalency

2.1 First theoretical proposition of Carbon Nitrides as novel hard materials

It was in 1985 that M. L. Cohen [23] proposed an empirical relation between the bulk modulus, B (volumetric compressibility or bulk modulus), and the crystalline solids of elements of the III, IV and V column of the periodic table. In the free-electron gas model, the case of metals, the expression of the B modulus (GPa) scales as the Fermi energy, E_F, and the electron concentration, n,

$$B = \frac{2}{3} n E_F. \tag{2.1}$$

Starting from the model of Phillips-Van Vechten [24] it is possible to extend the expression of B to semiconductors. The bond geometry of covalent bonds is roughly represented with a cylindrical shape with volumes $\sim \pi \left(2a_B\right)^2 d$, where a_B is the Bohr radius and d (Å) the length of the cylinder. Using this approximation we obtain,

$$B = 45.6 E_h \, d^{-1} \tag{2.2}$$

where E_h (eV) represents the homopolar contribution of the optic gap, E_g ($\mathrm{E}_g^2 = E_h^2 + E_{ionic}^2$). Using the scaling of Phillips ($E_h \propto d^{-2.5}$) for the dependence of E_h on d for tetrahedral compounds sharing eight valence electrons per atom pair, we obtain

$$B = 1761 d^{-3.5}, \tag{2.3}$$

where the nearest-neighbor d is again in Å and B in GPa. The introduction of the ionicity parameter, λ, permits to consider the ionic character of the bonding:

$$B = \left(1971 - 220\lambda\right) d^{-3.5}. \tag{2.4}$$

This empirical relation results appropriate for the group-IV ($\lambda = 0$), III-V ($\lambda = 1$) and II-VI ($\lambda = 2$) semiconductors. Furthermore, in order to account for a different coordination number (different from 4 of the tetrahedral site), M. L. Cohen introduced the variables N_c, which represents the mean coordination number. The final version of the equation takes the following form:

$$B = \frac{N_c}{4}\,(1971 - 220\lambda)\,d^{-3.5}. \tag{2.5}$$

The above equation gives an accurate B value for diamond and for semiconductors with a zinc-blende structure. The volumetric compressibility B increases with the lowering of d and λ. The hardest materials are thus those that show lower ionicity and stronger bonds. Diamond responds to these characteristics; indeed it shows N_c=4, λ=0 and d=1.54 Å. The bulk modulus calculated for diamond with the Eq. 2.5 is 435 GPa, which is very close to the experimental one of 443 GPa. In the case of carbon nitrides with formula C_3N_4 the mean coordination number (N_c) is $\frac{24}{7}$ [1] which is lower than that of diamond, 4. Taking into account the small electronegativity difference between carbon and nitrogen, we assume the C-N bond to be slightly ionic with λ=$\frac{1}{2}$. From the values of the covalent radius (r_C=0.77 Å and r_N=0.75 Å) we define a C-N bond length of 1.52 Å. The insertion of these parameters in Eq. 2.5 provides a B value of 430 GPa. Therefore, carbon nitrides with formula C_3N_4 should exhibit a bulk modulus comparable to that of diamond.

This was the first theoretical indication of the possibility to find new promising classes of carbon based hard materials. In particular, the large bulk modulus calculated from the simple empirical relation of M. L. Cohen was sufficient enough to provoke in the middle of the 1980's an outstanding scientific enthusiasm which is, nowadays, still not vanished.

2.2 Electron count considerations

The definition of "*ultra-hard*" materials is usually employed to describe all the compounds that have shown hardness values comparable to that of diamond. Generally speaking, these materials are solids with an hardness in between 8-10 Mohs scale (Tab. 2.2). Since diamond, cubic boron nitride (c-BN) and boron carbides ($B_{13}C_2$-$B_{12}C_3$) are the hardest materials known, it can reasonably be expected that novel ultra-hard solids will be found in the same B-C-N ternary composition diagram (see Fig. 2.1). However, as one might anticipate many combination of C, B and N atoms are, in principle, possible and an huge amount of different stoichiometries and structures can rapidly be imagined for both binary and ternary compounds. Therefore, the proposition of novel hard phases has

[1] Carbon has four valence electrons ($[He]\ 2s^2\ 2p^2$) and can form one covalent bond with four nitrogen atoms, whereas nitrogen possesses five valence electrons ($[He]\ 2s^2\ 2p^3$) and can only have one covalent bond with three atoms of carbon. For this reason N_c=$\frac{(3\cdot4)+(3\cdot4)}{7}$ in the C_3N_4 stoichiometry.

Minerals or Synthetic Materials	Formula	Mohs	Knoop 100 (GPa)
Talcum	$Mg_3\left[(OH)_2/Si_4O_{10}\right]$	1	
Hexagonal Boron Nitride†	$h-BN$		0.15-0.30
Gypsum	$CaSO_4\cdot 2H_2O$	2	
Calcite	$CaCO_3$	3	
Fluorite	CaF_2	4	
Apatite	$Ca_5\left[(F,OH)/(PO_4)\right]$	5	
Feldspar	$K\left[AlSi_3O_8\right]$	6	
Quartz	SiO_2	7	
Topaz	$Al_2\left[F_2/SiO_4\right]$	8	
β-Silicon Nitride†	β-Si_3N_4		17
Corundum§-Titanium Nitride†	Al_2O_3-TiN	9	21
Silicon Carbide†	SiC		26
α-Silicon Nitride†	α-Si_3N_4		26-35
Titanium Crabide†	TiC		28
Boron Carbide†-Titanium Diboride†	B_4C-TiB_2		30
Boron suboxides	B_nO		30-59
Stishovite†	SiO_2		33
Cubic Boron Nitride†	$c-BN$		45
Diamond§	C	10	75-100

[†] Synthetic material. [§] Synthetic material or natural mineral.

Table 2.1: Hardness of minerals and some synthetic ceramics according to F. Mohs. For synthetic materials micro-hardness values are given in units of Knoop scale. Values are shown as compiled by R. Riedel in Ref. [25].

generally been restricted in this Thesis by the adoption of the so-called *electron counting rule*. A systematic investigation of the various stoichiometries becomes thus possible thanks to the limited number of allowed atomic combinations.

If we look, for example, at the building up of the two-dimensional carbon nitride compounds, one could firstly envisage a random replacement of C by N within the layers of graphite. However, this results in an unstable electronic structure configuration. This is due to the additional electrons of the nitrogen atoms which have to be accommodated in energetically unfavourable electronic bands. But if compounds are designed to be isoelectronic to diamond and graphite the stability and the electronic structures are changed. For instance graphitic C_3N_4 has 32 valence electrons per formula unit when the

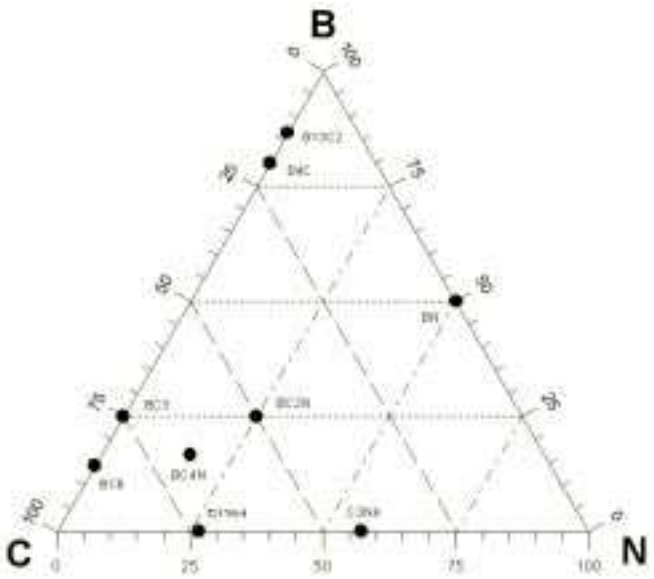

Figure 2.1: Schematic ternary composition diagram indicating different "*hard*" stoichiometries.

2s states are included. Distributing the electrons on eight sites gives four electrons on each site which is isoelectronic with diamond and graphite. The eighth site is a vacancy ($C_3\square_1N_4$) and the lone pairs of three of the nitrogen atoms are pointing toward this hole. From this, graphitic C_3N_4 should have a similar band structure at the Fermi level as graphite, and C_3N_4 with a three-dimensional network is also expected to have a band gap similar to diamond. Consequently a series of different combinations of C, B and N can be investigated for the search of new hard compounds, provided that the following simple condition is respected:

$$p \cdot Z_V\,(B) + m \cdot Z_V\,(C) + l \cdot Z_V\,(N) = 4n \tag{2.6}$$

The values p, m, l and n are integers and $Z_V(B)$, $Z_V(C)$ and $Z_V(N)$ are the atomic valence states (2s and 2p) for boron, carbon and nitrogen, respectively. Examples are represented by the systems C_3N_4, $C_{11}N_4$, BN, B_4C, BC_2N *etc*...

The attention has therefore been restricted only to those compositions that are isoelectronic to carbon, *i.e.*, diamond. This particular choice also derives from the fact that all the substances obeying this rule should likely posses the same attracting properties of the existing hardest materials (*e.g.* cubic boron nitride and diamond).

Chapter 3

The concept of Hardness

3.1 Introduction

From the mechanical point of view we usually define the hardness as the resistance of the material to deformations. This property strongly depends on many parameters like pressure, temperature, porosity, impurities, dislocations and defects. It is usually correlated to various other physical properties (ionicity, melting point, band gap, cohesive energy, etc...) and can thus be studied indirectly. The hardness for a given sample is usually determined by empirical methods such as the scratch test (Mohs scale) or indentation by dropping a weight on the sample. The results are very useful but difficult to interpret and they often dependent on the sample and its state of purity. In the Vickers test the hardness is estimated by measuring the indentation left by a diamond stylus under a fixed load. This test and the scratch test (irreversible methods) are quite often employed experimentally to classify the hardness of the various compounds.

Many theoretical predictions on the hard materials have been made in the last two decades by looking at the magnitude of the bulk modulus, B, [26, 27, 23, 28, 12, 29]. However, in 1977 A. P. Gerk [30] has already suggested that the shear modulus, G, which defines the resistance to reversible deformation upon shape change, might be a better predictor of the hardness. More recently, D. M. Teter [22] showed that for a wide variety of materials the shear modulus is really more correlated to the Vickers hardness than the bulk modulus (further details are given in Section 8.2.4, p. 53). The hardness of crystalline materials thus becomes better defined by taking into account the dislocation theory, *i.e.*, by measuring how readily a large number of dislocations are generated and are able to move throughout the solid in response to the shear stresses.

In the following subsections we show how to describe the hardness of solids with the calculation of the bulk modulus, elastic constants and shear modulus.

3.1.1 Measure of the resistance upon volume change in solids

The bulk modulus measures the resistance to the volume change in solids and provides an estimation of the elastic response of the material to an external hydrostatic pressure. The $B(V)$ value is related to the curvature of $E(V)$,

$$B(V) = -V\frac{\partial P}{\partial V} = V\frac{\partial^2 E}{\partial V^2} \tag{3.1}$$

where V is the volume of the unit cell, $E(V)$ is the energy per unit cell at volume V, and $P(V)$ is the pressure required to keep the unit cell at volume V. Since the calculations can only provide a restricted set of energies $E(V_i)$, the second derivative, $\frac{\partial^2 E}{\partial V^2}$, must be approximated. The least squares fit of the curves E *vs.* V has been performed in this Thesis by using the first three terms of the Birch equation [31]:

$$E(V) = E(V_o) + \frac{9}{8}V_o B\left[\left(\frac{V_o}{V}\right)^{\frac{2}{3}} - 1\right]^2 + \frac{9}{16}B\left(B^{'} - 4\right)V_o\left[\left(\frac{V_o}{V}\right)^{\frac{2}{3}} - 1\right]^3 + \sum_{n=4}^{N}\gamma_n\left[\left(\frac{V_o}{V}\right)^{\frac{2}{3}} - 1\right]^n, \tag{3.2}$$

where E_o, V_o, B and $B^{'}$ are the equilibrium energy, volume, bulk modulus and pressure derivatives of the bulk modulus, respectively. In the above summation the γ_n symbol represents the total contraction terms [32], whilst the maximum order of the fit is symbolised by the N index. The Eq. 3.2 is normally employed by assuming the following trend: the larger the value of B, the harder is the material. The magnitude of B' is generally utilised to describe the variation of the hardness with respect to a given change of the pressure (ΔP).

Different semiempirical relations such as finite stress-strain have been proposed to describe the so-called Equation of State (EOS) (see Ref. [33] and Refs. therein). Scaling experimental compression data for measured isotherms of different sorts of solids the EOS is known. The above Birch type equation of state is a well tested fitting form able to describe the P, V, T data for a wide variety of solids. The main assumption made in its utilisation is that no phase transition occurs during the compression of the material. Despite the existence of different varieties of EOS, the calculations of the bulk modulus have mostly been performed in this Thesis by using the Birch type equation. Since such a fitting form provides good results for systems like diamond and *c*-BN I thought worthwhile to use the same equation for the investigation of new hypothetical phases for which the experimental data are not yet available. Furthermore, by doing this a homogeneous analysis of the results becomes possible with respect to the previously achieved theoretical and experimental results.

3.1.2 Resistance to reversible deformation upon shape change

In the study of mechanical strength the elasticity of solids, *i.e.*, the response of a material to applied forces, must be taken into account. The forces are described by tensors called stresses which determine the direction of the force and the plane to which it is applied. The responses in terms of relative changes in dimensions or shape are called strains and they are also given by tensors. The ratio stress/strain is called elastic modulus. For small stresses the modulus is constant and the material behaves elastically so that it returns to the original condition when the stress is removed. For large stress the sample undergoes a permanent or plastic deformation. When the force acts only in one dimension the stress is called compressional, and when it acts in all directions the stress is hydrostatic. In the shearing stress, forces act to move parallel planes of the solid so that at the microscopic level these stresses cause the gliding of planes of atoms over each other. This is the easiest way for a solid to change its shape and the force needed (hardness) depends very much on the presence of crystal defects. Edge and screw dislocations are the most important defects for gliding motion. An applied shearing stress will cause the dislocations to move throughout the crystal.

According to the finding of A. P. Gerk and D. M. Teter, the hardness of the solids has mostly been investigated in this Thesis by computing the value of the isotropic shear modulus. This magnitude can be expressed as a linear combination of a set of elastic constants, c_{ij}, and is considered nowadays as the best hardness predictor for solids. The c_{ij} constants determine the response of the crystal to external forces and provides information about the bonding characteristics between adjacent atomic planes, anisotropic character of the bonding and structural stability. Each of the elastic constants is a measure of hardness for a particular kind of unit cell deformation.

Calculation of the elastic constants: cubic system as a simple example

The basic problem in calculating elastic constants from *ab initio* methods is not only the demand of accurate calculational schemes for evaluating the total energy of the solid but also the massive and onerous computations implied in the estimation of the entire set of the inequivalent c_{ij}. For instance, when the symmetry of the system is decreased, the number of independent elastic constants expands and a larger number of distortions is necessary to compute the full set of c_{ij} [34]. These constants can be deduced by applying small strains to the equilibrium lattice and then determining the resulting change in the total energy. In particular we calculate the linear combinations of the elastic constants by straining the lattice vectors R according to the rule $\tilde{R} = R \cdot D$. The matrix D represents the symmetric distortion matrix which contains the strain components and $\tilde{R}$ is the matrix that contains the components of the distorted lattice vectors. In order to conserve the elastic limit of the crystal, only small lattice distortions must be applied

(*e.g.* strains within ±1.5 %).

In cubic materials there are only three inequivalent elastic constants: c_{11}, c_{12} and c_{44}. These values can be estimated by calculating the total energy of the system as a function of the shears described below [35]. For c_{11} and c_{12} the following shear, D_1, is considered,

$$D_1 = \begin{pmatrix} 1+\delta & 0 & 0 \\ 0 & 1+\delta & 0 \\ 0 & 0 & \frac{1}{(1+\delta)^2} \end{pmatrix} \tag{3.3}$$

where the z axis is modified and the x and y axes are kept the same in a volume conserving way. The variation of the strain energy density ($U = Energy/Volume$) as a function of the shear δ is described with the following equation,

$$U = 6C'\delta^2 + O(\delta^3) \tag{3.4}$$

with $C' = \frac{1}{2}(c_{11} - c_{12})$. From the calculation of C' and the bulk modulus, $B = \frac{1}{3}(c_{11} + 2c_{12})$, one can evaluate the first two elastic constants. With the same procedure, but considering the following shear,

$$D_2 = \begin{pmatrix} 1 & \delta & 0 \\ \delta & 1 & 0 \\ 0 & 0 & \frac{1}{(1-\delta^2)} \end{pmatrix} \tag{3.5}$$

the c_{44} constant can be calculated from the equation,

$$U = 2c_{44}\delta^2 + O(\delta^4). \tag{3.6}$$

Isotropic shear modulus The isotropic shear modulus, G_{Iso}, was firstly expressed by A. Reuss as long ago as in 1929 [36]. In the Voigt's approximation the equation takes the following form:

$$G_{Iso} = \frac{1}{15}\left[(c_{11} + c_{22} + c_{33}) - (c_{23} + c_{31} + c_{12}) + 3(c_{44} + c_{55} + c_{66})\right] \tag{3.7}$$

For the special case of a cubic symmetry the above relation translates into the form of

$$G_c = \frac{1}{15}\left(3c_{11} - 3c_{12} + 9c_{44}\right). \tag{3.8}$$

Therefore, after having accomplished the calculation of the whole set of single crystal elastic constants, it is possible to estimate (for all the materials) the elastic shear moduli for a polycrystalline[1] solid by simply applying the above relation (Eq. 3.7). According to the finding of A. P. Gerk [30] and D. M. Teter [22], the larger is the value of the calculated G, the harder should be the material.

[1] In general, a single crystal is more difficult to prepare than a polycrystalline material. As a matter of fact, most of the available experimental elastic moduli refer to polycrystalline samples.

Chapter 4

Density Functional Theory

4.1 Introduction

Condensed matter physics and materials science are basically related to the understanding and exploiting the properties of systems of interacting electrons and atomic nuclei. In principle, all the properties of materials can be addressed given suitable computational tools for solving this quantum mechanics problem. In fact, through the knowledge of the electronic properties it is possible to obtain information on structural, mechanical, electrical, vibrational, thermal and optic properties. However, the electrons and nuclei that compose materials constitute a strongly interacting many body system and unfortunately this makes the direct solution of the Schrödinger's equation an impractical proposition. As stated by Dirac in the far 1929 [37], progress depends mostly on the elaboration of sufficiently accurate and approximate techniques.

The development of density functional theory and the demonstration of the tractability and accuracy of the Local Density Approximation (LDA) represents an important milestone in condensed matter physics. The DFT of Hohenberg and Kohn [38] was adopted by the LDA which was firstly developed and applied by Slater [39] and his coworkers [40]. First principles quantum mechanical calculations based on the LDA have become one of the most frequently used theoretical tools in materials science. Nonetheless, the great contribution of the local density approximation calculations remained limited until the late 1970's when several works have demonstrated the accuracy of the approach in determining properties of solids [41, 42, 43, 44]. Even though it has been a great deal to state why the LDA should or should not be adequate for calculating properties of materials, there is however no doubt that the most convincing arguments have been derived from the direct comparison of calculations with experiments. In particular, despite its simplicity the local density approximation has been very successful in describing materials properties during the last decades. However, it is worth to note that there

are also situations where the above approach do not lead to sufficiently accurate results. This can be the case when the differences in the total energy, which are usually relevant in calculating structural properties and binding, are to be estimated very accurately. As a matter of fact, small inaccuracies may have here a dramatic effects. In general, LDA suffer from more or less well-known failures and therefore there have during the last decade been several attempts to go beyond this local approximation by including effects depending on the variation of the electron density.

Nowadays, improved theoretical schemes and the rapid growth in computing facilities have caused many types of systems and properties to be studies successfully with density functional methods. In the next following Sections we briefly resume the fundamental concepts which are at the base of this important and fascinating theory.

4.2 The basic principles of the method

The theorem of Hohenberg and Kohn is at the base of the DFT and states that the total energy, E, of a non-spin-polarised system of interacting electrons in an external potential is given exactly as a functional of the ground state electronic density, ρ.

$$E = E[\rho] \tag{4.1}$$

They further showed that the true ground state density is the density that minimises $E[\rho]$ and that the other ground state properties are also functionals of the ground state density. The extension to spin-polarised systems is also possible where E and the other ground state properties become functionals of both the up and down spin densities.

$$E = E[\rho_{\uparrow}, \rho_{\downarrow}] \tag{4.2}$$

The Hohnenberg-Kohn theorem provides no guidance to the form of $E[\rho]$, thus the utility of DFT depends on the discovery of sufficiently accurate approximations. In order to do this, the unknown functional $E[\rho]$ is rewritten as the Hartree total energy plus another smaller unknown functional called exchange-correlation (xc) functional, $E_{xc}[\rho]$.

$$E[\rho] = T_s[\rho] + E_{ei}[\rho] + E_H[\rho] + E_{ii}[\rho] + E_{xc}[\rho] \tag{4.3}$$

In Eq. 4.3 $T_s[\rho]$ represents the single particle kinetic energy while $E_{ei}[\rho]$ denotes the Coulomb interaction energy between the electrons and the nuclei. The term $E_{ii}[\rho]$ arises from the interaction of the nuclei with each other and $E_H[\rho]$ is the Hartree component of the electron-electron energy.

$$E_H[\rho] = \frac{e^2}{2} \int d^3\mathbf{r} d^3\mathbf{r}' \frac{\rho(\mathbf{r})\,\rho(\mathbf{r}')}{|\,\mathbf{r}-\mathbf{r}'\,|} \tag{4.4}$$

In the LDA, $\mathrm{E}_{xc}[\rho]$ is written as

$$E_{xc}[\rho] = \int d^3\mathbf{r}\rho(\mathbf{r})\,\varepsilon_{xc}(\rho(\mathbf{r})) \tag{4.5}$$

where $\varepsilon_{xc}(\rho)$ is approximated by a local function of the density, which usually reproduces the known energy of the uniform electron gas. Refinement of the LDA are the so-called generalised gradient approximation (GGA) and the weighted approximation (WDA). An expression similar to Eq. 4.5 is used in the GGA where the $\varepsilon_{xc}(\rho)$ is replaced by a local function of the density and the magnitude of its gradient, $\varepsilon_{xc}(\rho, |\nabla\rho|)$. From the incorporation of the additional information contained in the local gradient a better description of the system is expected [45, 46, 47]. Several different parameterisations of the GGA functional have been proposed [47] and tested on a wide variety of materials. The GGA improve significantly the ground state properties of light atoms, molecules and solids and generally tends to produce larger equilibrium lattice parameters and band gaps with respect to the LDA.

A more sophisticated approach is the WDA that incorporates true non-local information through Coulomb integrals of the density with model exchange correlation holes [48, 49, 50]. It ameliorates greatly the energies of atoms and for the diamond structures of Si and Ge yields bulk properties that are much improved as well. Nonetheless, the WDA is more demanding computationally than the LDA or GGA, and accordingly few WDA studies have been reported for solids.

Following the Kohn and Sham indications [51], the electron density can be written as a sum of single particle densities. Given the functional E_{xc} the ground state energy and density can be obtained by the self-consistent solution of a set of single particle Schrödinger-like equations, known as the Kohn-Sham equations with a density dependent potential,

$$(T + V_{ei}(\mathbf{r}) + V_H(\mathbf{r}) + V_{xc}(\mathbf{r}))\,\varphi_i(\mathbf{r}) = \epsilon_i\varphi_i(\mathbf{r}) \tag{4.6}$$

where the density is given by a Fermi sum over the occupied orbitals.

$$\rho(\mathbf{r}) = \sum_{occ} \varphi_i^*(\mathbf{r})\,\varphi_i(\mathbf{r}) \tag{4.7}$$

The φ_i are single particle orbitals, ϵ_i are the corresponding eigenvalues, T is the kinetic energy operator, V_{ei} is the Coulomb potential due to the nuclei, V_H is the Hartree potential and V_{xc} is the exchange correlation potential. V_H and V_{xc} depend on ρ as follows:

$$V_H(\mathbf{r}) = e^2 \int d^3(\mathbf{r}')\,\frac{\rho(\mathbf{r})}{|\mathbf{r}-\mathbf{r}'|} \tag{4.8}$$

and

$$V_{xc}(\mathbf{r}) = \frac{\delta E_{xc}[\rho]}{\delta \rho(\mathbf{r})} \tag{4.9}$$

In this framework, a calculation requires the self-consistent solution of equations 4.6 and 4.7. This means that a certain density has to be found such that it yields an effective potential that, inserted into the Schrödinger-like equations, yields orbitals that can reproduce it. For this reason, instead of facing-up with the problem of solving a many-body Schrödinger equation, using DFT we can now have the easier problem of determining the self-consistent solution to a series of single particle equations. In solids, a further simplification that facilitates DFT calculations is provided by the Blöch's theorem, where the charge density and the single particle KS Hamiltonian have the periodicity of the lattice. Thus KS orbitals with different Blöch momenta are coupled only indirectly through the density dependent potential. Therefore, in DFT based calculations, the single particle KS equations may be solved separately on a grid of sampling points in the symmetry irreducible wedge of the Brillouin zone and the resulting orbitals used to construct the charge density (this is not the case, for example, in Hartree-Fock methods).

As already mentioned the great advantage of the density functional approach is that the resulting single-particle equations are computationally simpler to solve then the equivalent Hartree-Fock equations. This makes possible to consider systems that are more complex (*i.e.* larger size or complicate structure) then those treated by the Hartree-Fock derived methods.

4.3 Single particle Kohn-Sham equations

Depending on the representations that are used for density, potential and KS orbitals, different DFT based electronic structure methods can be classified. Many different choices are made in order to minimise the computational and human costs of calculations, while maintaining sufficient accuracy. A brief summary of the many possibilities to solve the Schrödinger's equation is given in Fig. 4.1. In this Thesis calculations have been mostly concerned with two particular approaches namely, planewave Pseudo-Potential (PP) and the Linearized Augmented Plane-Wave (LAPW). Other simpler and faster methods, such as Augmented Spherical Wave (ASW) and the Linear Muffin Tin Orbital (LMTO), have also been employed in the study of carbon based hard materials. However, these computational approaches are usually reliable only when applied to crystalline materials with high symmetry and large compactness.

The explicit use of a basis can be avoided in constructing the KS orbitals by numerically solving the differential equations on grids. However, it is important to note that nearly all approaches that have been proposed for solids, including the PP and the

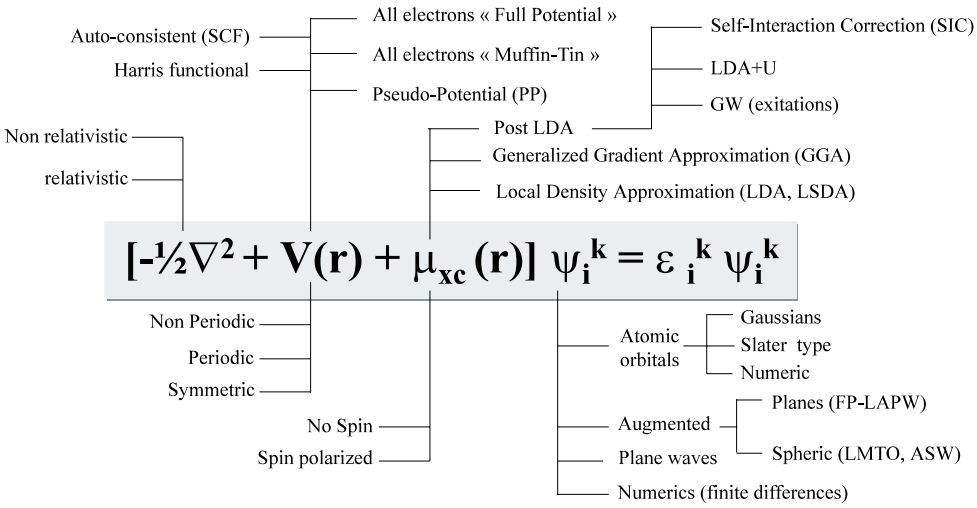

Figure 4.1: Schematic representation of various DFT-based methods of calculation.

LAPW methods, do rely on a basis set expansion for the KS orbitals. Because of this, the discussion is here confined to methods that do use a basis in which the KS orbitals are:

$$\varphi_i(\mathbf{r}) = \sum C_{i\alpha}\phi_\alpha(\mathbf{r}) \tag{4.10}$$

where the $\phi_\alpha(\mathbf{r})$ are the basis functions and the $C_{i\alpha}$ are the expansion coefficients. Given a choice of basis, the coefficients are the only variables in the problem, since the density depends only on the KS orbitals. Since the total energy in DFT is variational, the solution of the self-consistent KS equations permits to determine the $C_{i\alpha}$ for the occupied orbitals that minimise the total energy. In order to eliminate the unknown functional $T_s[\rho]$ the total energy can be rewritten using the single particle eigenvalues:

$$E[\rho] = E_{ii}[\rho] + \sum_{occ}\epsilon_i + E_{xc}[\rho] - \int d^3\mathbf{r}\,\rho(\mathbf{r})\left(V_{xc}(\mathbf{r}) + \frac{1}{2}V_H(\mathbf{r})\right) \tag{4.11}$$

where the sum is over the occupied orbitals and ρ, V_H and V_{xc} are given by Eqs. 4.7, 4.8 and 4.9, respectively.

Density functional calculations require the optimisation of the $C_{i\alpha}$ and the determination of the charge density (Fig. 4.2). This procedure is usually performed separately and hierarchically. Using standard matrix techniques it is possible to repeatedly determine the $C_{i\alpha}$ that solve the single Eq. 4.6 for a fixed charge density. Hence, given the

basis, the Hamiltonian and the overlap matrices, H and S, can be constructed and the following matrix eigenvalue equation,

$$(\mathbf{H} - \epsilon_i \mathbf{S})\, \mathbf{C}_i = 0 \tag{4.12}$$

is solved at each **k**-point in the irreducible wedge of the Brillouin zone. The optimised

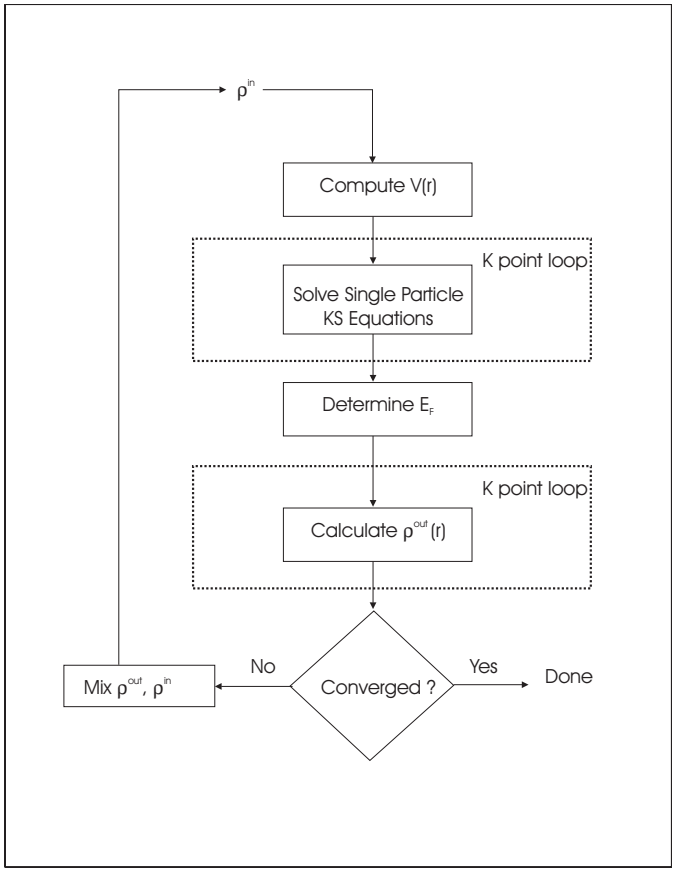

Figure 4.2: Flow-chart for self-consistent density functional calculations.

$C_{i\alpha}$ will yield the exact self-consistent solution only if the true occupied KS orbitals can be expressed as a linear combination of the basis functions. In the case where they cannot be expressed exactly in term of the basis, an approximate optimal solution (*i.e* the one that gives the lowest possible total energy for the basis) will be found. Therefore, the quality of a basis set can be measured by comparing how much the total energy evaluated with the orbitals of Eq. 4.10 differs from the true KS energy.

4.3.1 The basis sets

With the general term *efficiency* we usually refer to the number of basis functions needed to achieve a given level of convergence, whereas with the *bias* we describe whether or not a basis could favour certain regions of space over the others like, for example, being more flexible near the nuclei than the interstitial regions. By looking at the difficulty in estimating the matrix elements, the *simplicity* of the basis is also defined. The basis *completeness* indicates whether the basis can be improved by increasing the number of the functions. Planewave sets are known to be inefficient in the above sense for a large part of solids. However, this is not necessary a defect since it only reflects the fact that they are unbiased. Moreover, planewaves form a simple and complete basis. Accuracy can be reached by increasing the number of planewaves in the basis and the convergence of a calculation can be monitored by changing the planewave cut-off. Furthermore, due to the simplicity of this basis the implementation of the planewave codes is relatively easy and the matrix elements of many operators can be rapidly estimated. Many operators can be made diagonal since the planewaves expanded wavefunctions can be transformed efficiently from reciprocal space, *i.e.* coefficients of the planewave expansion, to real space using Fast Fouries Transforms (FFT). In particular, it is important to note that the kinetic energy and momentum operators are diagonal in reciprocal space and the operation of the local potentials is diagonal in real space. Looking at the equation 4.10 it is evident that the most efficient basis set consists of the KS orbitals themselves and an exact calculation is thus achieved using a basis set size equal to the number of occupied orbitals. However, despite this possibility the KS orbitals are, in general, unknown at the beginning of the calculation.

Atomic and Muffin-tin orbitals are also common basis sets used in electronic structure calculations. Despite the fact that the crystal potentials are often different from atomic potentials (even close to the nuclei), a linear combination of atomic orbitals (LCAO) methods have been used successfully for large systems. With this method, problems often arise when attempts are made in order to add large numbers of basis functions to get highly converged calculations. Atomic orbitals centred at a single site are already complete, thus the LCAO's which have as well orbitals centred at each site are over-complete. Owing to this problem the overlap matrix, S, in Eq. 4.12 becomes ill-conditioned for large basis sets. Muffin-tin orbitals derived basis sets are based on the solutions of the radial Schrödinger's equation and usually a better approximation to the crystal potential is provided in the vicinity of the site with respect to that used in constructing LCAOs. This basis set has been discussed in more details in the Section 6.2.

4.3.2 The Self Consistent Field in DFT

As shown by the theorem of Hohenberg-Kohn the total energy is variational and this means that the true ground state density is that which minimises the energy. When the LDA approximation is introduced to the $E_{xc}[\rho]$ the true variational principle does not exists anymore and there is no guarantee that the energy obtained by minimising the energy functional will be higher than the exact ground state energy. Consequently, the true ground state charge density will in general not minimise the approximate energy functional. However, calculations can be done by knowing that minimising a good approximation to the energy functional, a good energy and density should be obtained. The procedure is thus exact only for the true energy functional.

Since we do not know the form of the single particle kinetic energy, $T_s[\rho]$, in Eq. 4.3, the minimisation proceeds through the KS equations, where the variation is with respect to the orbitals, or in a basis set expansion to the coefficients $C_{i\alpha}$. With a fixed basis these are the only parameters that can be varied. The problem is to find the coefficients that minimise the energy functional (Eq. 4.11) paying attention on keeping the orbitals orthonormal to each other. The direct minimisation of the total energy with respect to the $C_{i\alpha}$ was proposed by Bendt and Zunger in 1982 [52] and is the core of the Car-Parrinello (CP) method [53]. In spite of the computational advantages, this approach has not yet become popular for methods that use non-planewave basis sets. This is due to the complexity of the optimisation problem where typically hundreds or thousands of parameters are present even for small problems. Therefore, it is because of this complications that historically the standard self-consistency cycle shown in Fig. 4.2 has been used to refine iteratively the density by alternately solving the Eqs. 4.6 and 4.7. For a given charge density the Eq. 4.12 is diagonalised (ensuring the orthonormal orbitals) and an output charge density is constructed from the eigenvectors using Eq. 4.7. This charge density is then mixed with the input to yield a refined input for the next iteration. The simplest mixing scheme is represented by the straight mixing:

$$\rho_{in}^{i+1} = (1-\alpha)\,\rho_{in}^{i} + \alpha\rho_{out}^{i} \tag{4.13}$$

The superscript refers to the iteration number and α is the mixing parameter. In order to avoid the decreasing of the radius of convergence with the increasing, for example, of the unit cell volume a more sophisticated mixing procedure which takes into account the information from previous iterations is used. The convergence is normally accelerated by using the Broyden's method [54].

Chapter 5

Planewave Pseudo-Potential methods

5.1 Introduction

The pseudo-potential (PP) approach employs a quantum mechanical description of the electronic interactions as specified by the density functional theory. This approach consists basically of a pseudo-potential and planewaves coupled with a Fourier transform technique. The above method appears extremely accurate and reasonably fast for material modelling and especially it has shown good ability in predicting ground state structures of ultra-hard materials [55]. In particular, two different approaches, the local density approximation [56] and the generalized gradient approximation [57], have been widely tested.

A general characteristic, common to all the PP methods, is that once the description of the electronic interactions has been achieved, the forces acting on atoms can be easily calculated, thus giving the possibility to determine the minimum energy position for atoms belonging the unit cell. Using this process, all the phases proposed in the next following Chapters have been obtained by relaxing the initial crystalline structures with the planewave pseudo-potential approach. Such a procedure is at the moment considered the state-of-the-art in the modelling of the carbon based materials.

In our investigations we used the Vienna *ab-initio* simulation package (VASP) [58] for the determination of the optimised geometries, relative stability and elastic constants of various carbon nitride and boron carbon nitride configurations. The calculations have mostly been performed within the local density approximation to the DFT [59] using the Ceperly-Alder [56] exchange correlation functional as parameterised by Perdew and Zunger [60] and the pseudo-potential method described by Vanderbilt [61]. Our studies were executed by using an energy cut-off of 434.8 eV for the planewave basis

set and converged with respect to the **k**-point integration. The tetrahedron method with Blöchl corrections [62] was normally applied for both geometry relaxation and total energy calculations. Brillouin-zone integrals were approximated using the special **k**-point sampling of Monkhorst and Pack [63].

5.2 Blöch's Theorem and Planewaves

The ions in a perfect crystal are arranged, at 0 °K, in a regular periodic way. Therefore the external potential felt by the electrons will also be periodic; the period being the same as the length of the unit cell, ℓ. That is, the external potential on an electron at $\mathbf{r}$ can be expressed as $V(\mathbf{r}) = V(\mathbf{r} + \ell)$. This is the requirement needed for the use of Blöch's theorem. By using this theorem it is possible to express, see Eq. 5.1, the single particle wavefunction, ϕ_k, of the infinite crystal in terms of wavefunctions at reciprocal space vectors of a Bravais lattice.

$$\phi_k(\mathbf{r} + \mathbf{R_L}) = e^{i\mathbf{k}\mathbf{R_L}} \phi_k(\mathbf{r}) \tag{5.1}$$

In the above equation, $\mathbf{k}$ represents the crystal momentum and $\mathbf{R_L}$ the direct lattice vector. The first term is the wave-like part, whereas the second one is the cell periodic part of the wavefunction. The last term can be expressed by expanding it into a finite number of planewaves whose wave vectors are reciprocal lattice vectors of the crystal. Hence, the Blöch's theorem gives the boundary condition for the single particle wavefunctions. The following equation represents the general solution that satisfies these boundary conditions, where $\mathbf{G}$ are the reciprocal lattice vectors.

$$\phi_k(\mathbf{r}) = e^{i\mathbf{k}\mathbf{r}} \sum_{\mathbf{G}} C_{\mathbf{G}}(\mathbf{k}) e^{i\mathbf{G}\mathbf{r}} = e^{i\mathbf{k}\mathbf{r}} w(\mathbf{k}, \mathbf{r}) \tag{5.2}$$

By the use of Blöch's theorem, the problem of the infinite number of electrons has now been mapped onto the problem of expressing the wavefunction in terms of an infinite number of reciprocal space vectors within the first Brillouin zone of the periodic cell, $\mathbf{k}$. This problem is dealt with the sampling the Brillouin zone at special sets of **k**-points. The electronic wavefunctions at each **k**-point are now expressed in terms of a discrete planewave basis set. In principle, this Fourier series is infinite. However, the coefficients for the planewaves, $\mathrm{C}_{\mathbf{G}}(\mathbf{k})$, each have a certain kinetic energy $\left(\hbar^2/2m\right) \mid \mathbf{k} + \mathbf{G} \mid^2$. The planewaves with a smaller kinetic energy typically have a more important role than those with a very high kinetic energy. Therefore, the introduction of a planewave energy cut-off reduces the basis set to a finite size. This kinetic energy cut-off will lead to an error in the total energy of the system but in principle it is possible to make this error arbitrarily small by increasing the size of the basis set by allowing a larger energy cut-off. The cut-off that is used in practice depends on the system under investigation.

5.3 General Approximations

In most of the systems, the core electrons are strongly bound and do not respond to the more rapid motions of the valence electrons: they are essentially fixed. This is the so-called "*frozen core approximation*". The pseudo-potential method is based on the following approximations:

(1) We replace the strong core potential by a pseudo-potential, whose ground state wavefunction, ϕ^{PS}, reproduces the all electron wavefunction outside a selected core radius (see Fig. 5.1). By doing this we can now eliminate the core states and the orthogonalization in the valence wavefunctions.

(2) The resulting pseudo-wavefunctions ϕ^{PS} are usually smooth for many elements and can be thus easily described using low **G** planewaves. The planewaves become thus a simple and efficient basis for the pseudo-wavefunctions.

(3) We need to generate the pseudo-potential, and this is normally the more complex part of the method. This construction is usually more expensive then the calculation itself.

5.4 Pseudo-Potentials

5.4.1 Norm conserving pseudo-potentials

A valid pseudo-potential should be *soft*, *transferable* and the pseudo-charge density should accurately reproduce the valence charge density as much as possible. With the term *soft* it is meant that the expansion of the valence pseudo-wavefunctions should be allowed by using few planewaves. Thus, the pseudo-potential should be as soft as possible. The *transferability* is related to how much a pseudo-potential, generated for a given atomic configuration, can reproduce others accurately. This is a quite important property for solid state calculations, where the crystal and atomic potentials are different. These conflicting goals can be solved by using the concept of norm conservation [64, 65]. In this way the pseudo-wavefunctions are made to be equal to the true valence wavefunctions outside a certain core radius, r_c. For $r < r_c$ the pseudo-wavefunctions differ from the true wavefunctions but the norm is forced to be the same, as shown in the following equation:

$$\int_0^{r_c} dr\, r^2 \phi^{PS*}(r)\, \phi^{PS}(r) = \int_0^{r_c} dr\, r^2 \phi^{*}(r)\, \phi(r) \tag{5.3}$$

In the above equation the wavefunctions refer to the atomic reference state, thus a spherical symmetry is imposed. The wavefunction and eigenvalue are different for different

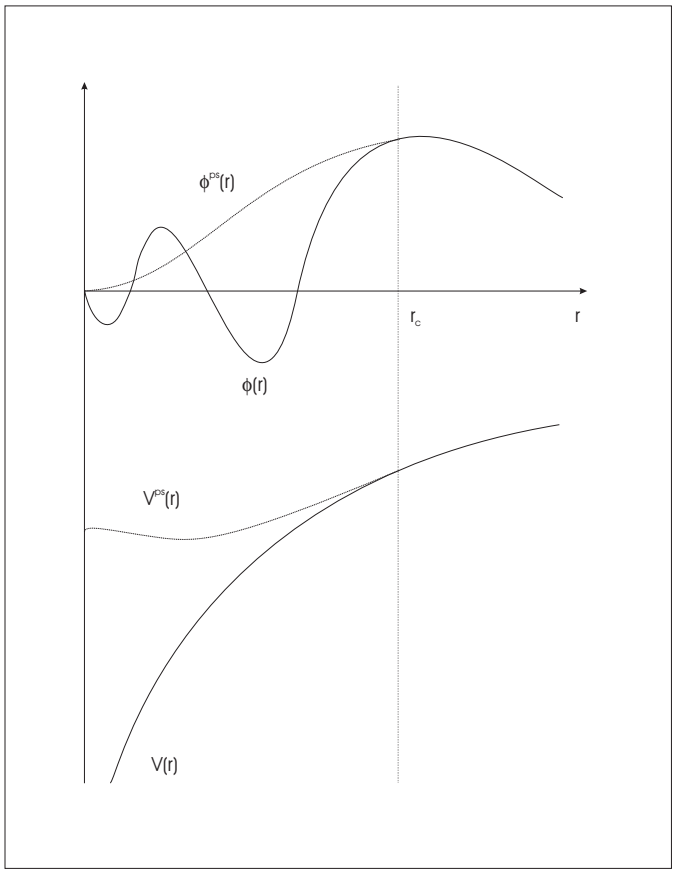

Figure 5.1: Illustration diagram of the replacement of the "all-electron" wavefunction and core potential by a pseudo-wavefunction and pseudo-potential.

angular momenta, l, and this means that the pseudo-potential should also be l dependent. These kind of pseudo-potentials are called "*semi-local*" since a different $\mathrm{V}^{PS}(r)$ is generated for each l values.

5.4.2 Ultrasoft Pseudo-Potentials (US-PP)

In 1990 Vanderbilt [61] introduced a new approach where the pseudo-wavefunctions are forced to be equal to the all electron wavefunctions outside the r_c, as in the concept of norm conservation, but inside they are allowed to be as soft as possible. In order to fulfill this last point, the norm conservation constraint was removed. Therefore, large values of r_c can be used in this scheme and consequently the planewave cut-off needed in

calculations can be greatly reduced. However, the following drawbacks have to be taken into account:

(1) The pseudo-wavefunctions are not normalised, since they are equal to the all-electron wavefunctions in the interstitial part (they have the same norm), but do not have the same norm inside r_c. This introduces a non-diagonal overlap in the secular equation.

(2) The pseudo-charge density is not calculated by solving $\sum \phi^* \phi$ as in norm conserving method. An augmentation term has to be added in the core region.

(3) By removing the norm conservation the resulting pseudo-potentials became less transferable.

However, the pseudo-potentials proposed by Vanderbilt were introduced for use in large scale calculations, for which the cost of generating pseudo-potentials is nearly negligible with respect to the cost of the calculations.

The total energy in the Vanderbilt's scheme is expressed as following:

$$E = \sum_{occ} \langle \phi_j | \, T + V^{NL} \, | \phi_j \rangle + \int d^3\mathbf{r} \, V^L(\mathbf{r}) \, \rho(\mathbf{r}) + \frac{1}{2} \int d^3\mathbf{r} \, d^3\mathbf{r}' \, \frac{\rho(\mathbf{r}) \; \rho(\mathbf{r}')}{|\mathbf{r} - \mathbf{r}'|} + E_{xc}[\rho] + E_{ii} \tag{5.4}$$

The T term is the kinetic energy operator, V^L is the local component of the pseudo-potential and the ϕ_j are the pseudo-wavefunctions. For the V^{NL} the following non local form is used

$$V^{NL} = \sum_{mn} D^0_{nm} \, |\beta_n\rangle \, \langle \beta_m| \, , \tag{5.5}$$

where the pseudo-potential is characterised by the β_m functions, the coefficients D^0_{nm} and the local component $V^L(\mathbf{r})$. For simplicity, in the above formula only one atom has been considered. β_m are expressed in an angular representation by spherical harmonics times radial functions, which vanish outside r_c.

The pseudo-charge density ρ is given by the square of the pseudo-wavefunctions and the augmentation inside the spheres.

$$\rho(\mathbf{r}) = \sum_{occ} \left[\phi_j^*(\mathbf{r}) \, \phi_j(\mathbf{r}) + \sum_{mn} Q_{mn}(\mathbf{r}) \, \langle \phi_j | \beta_n \rangle \, \langle \beta_m | \phi_j \rangle \right] \tag{5.6}$$

In the above Eq. 5.6 the term $Q_{mn}(\mathbf{r})$ indicates the local functions determined during the generation of the pseudo-potential.

Using the variational principle to Eqs. 5.4, 5.5 and 5.6, the secular determinant is

$$H\left|\phi_j\right\rangle \;=\; \varepsilon_j S\left|\phi_j\right\rangle \tag{5.7}$$

with

$$H = T + V_{xc}(\mathbf{r}) + V_H(\mathbf{r}) + V^L(\mathbf{r}) + \sum_{mn} D_{nm}\left|\beta_n\right\rangle\left\langle\beta_m\right| \tag{5.8}$$

and

$$S = 1 + \sum_{mn} q_{nm}\left|\beta_n\right\rangle\left\langle\beta_m\right| \tag{5.9}$$

where 1 indicates the identity operator and

$$q_{nm} = \int_{\alpha} d^3\mathbf{r}\; Q_{nm}(\mathbf{r}) \tag{5.10}$$

with the integral over the sphere defined by r_c. The D_{nm} are the $\mathrm{D}^{(0)}_{nm}$ with a screening term.

$$D_{nm} = D^{(0)}_{nm} + \int_{\alpha} V(\mathbf{r})\;\; Q_{nm}(\mathbf{r}) \tag{5.11}$$

where V denotes the local potential given by the local pseudo-potential plus the exchange correlation and Hartree potentials.

5.4.3 Generation of the US-PP

The generation of the ultra-soft pseudo-potentials starts with all-electron atomic calculations in a certain reference configuration. A set of reference energies, E_{lj}, is selected through the range over which band states will be calculated. The regular solution of the radial Schrödinger equation ($\phi_{lmj}(\mathbf{r}) = u_{lj}(\mathbf{r})\,Y_{lm}(\mathbf{r})$) is then solved within r_c at each E_{lj}. A smooth pseudo-wavefunction, $\phi^{PS}_{lmj}(\mathbf{r}) = u_{lj}(\mathbf{r})\,Y_{lm}(\mathbf{r})$, is generated for each lmj set providing that it matches to ϕ_{lmj} at r_c. In the same way a smooth local potential, V^L, that matches the all-electron potential outside r_c is determined. The following orbitals are then constructed:

$$\left|\chi_{lmj}\right\rangle \;=\; \left[E_{lj} - T - V^L(\mathbf{r})\right]\left|\Phi_{lmj}\right\rangle \tag{5.12}$$

If ϕ^{PS} and V^L are equal to ϕ and all-electron potential respectively outside r_c and ϕ satisfies the Schrödinger's equation at E_{ij}, χ assumes the zero value outside r_c. We can now write down the $Q_{nm}(\mathbf{r})$ term knowing that it must account for the difference between the true charge density and $\phi^{*PS}\phi^{PS}$.

$$Q_{nm}(\mathbf{r}) = \phi_n^*(\mathbf{r})\,\phi_m(\mathbf{r}) - \Phi_n^*(\mathbf{r})\,\Phi_m(\mathbf{r}) \tag{5.13}$$

The n and m indices run over the lmj set. Usually a smoothing is applied to Q_{nm} in order to facilitate the representations of the charge density. The moments of the original Q_{nm} are preserved. In a similar way the $|\beta_n\rangle$ are constructed

$$|\beta_n\rangle = \sum_m \left(\mathbf{B}^{-1}\right)_{mn} |\chi_m\rangle\,, \tag{5.14}$$

with $\mathbf{B}_{nm} = \langle\phi_n|\chi_m\rangle$. The rest of the components of the pseudo-potential, V^L and D_{nm} are determined by using the following identity,

$$\left[T + V + \sum_{nm} D_{nm}\,|\beta_n\rangle\,\langle\beta_m|\right]|\Phi_n\rangle = E_n\left[1 + \sum_{nm} q_{nm}\,|\beta_n\rangle\,\langle\beta_m|\right]|\Phi_n\rangle \tag{5.15}$$

with

$$D_{nm} = B_{nm} + E_m q_{nm} \tag{5.16}$$

The $D_{nm}^{(0)}$ are determined using Eq. 5.11 and the Hartree and exchange correlation contributions are subtracted from V to obtain V^L.

	B	C	N
ARC	$2s^2 2p^1$	$2s^2 2p^2$	$2s^2 2p^3$
$r_{c,s}$	1.8	1.6	1.8
$r_{c,p}$	1.8	1.8	1.8
$r_{c,d}$	1.8	1.8	1.8

Table 5.1: Parameters determining the ultra-soft pseudo-potential used in this Thesis. ARC represents the atomic reference configuration and $r_{c,l}$ (where l=s, p, d) the cut-off radii in atomic units.

During the self-consistent iterations, the contribution of the augmenting charge inside the sphere changes with the wavefunctions and contributes to the potential used in the Kohn-Sham equations. We can thus consider the pseudo-potential as evolving during the calculation. This effect allows the use of very *soft* pseudo-potentials (large values of r_c) in

the Vanderbilt scheme without affecting the accuracy of the calculation. Extensive tests of the accuracy, transferability and convergence properties of ultra-soft pseudo-potential for C, B and N were performed in Refs. [66, 67]. In this Thesis, the parameters used for the optimal pseudo-potential are given in Table 5.1.

Chapter 6

The Full Potential LAPW method

6.1 Introduction

In this Thesis, investigation of the electronic properties (density of states, band structure, electron density maps and EELS spectra) were carried out with the density functional theory Full-Potential Linearized Augmented PlaneWave (FP-LAPW) program package WIEN97 [68]. The LAPW method is a very accurate calculational scheme for the electronic structure investigation in crystals. It is characterised by the use of a basis set which is especially adapted to the problem. This method is basically derived from the augmented planewave (APW) approach of Slater [69, 70] where the space is divided into regions and different basis expansions are used in the various domains (Fig. 6.1). In particular, radial solutions of Schrödinger's equation are employed inside non overlapping atom centred spheres and planewaves in the remaining interstitial zone. The introduction of such a basis set is due to the fact that close to the nucleus the potential and wavefunctions are very similar to those in an atom, while between the atoms are smoother.

$$\varphi(\mathbf{r}) = \begin{cases} \frac{1}{\Omega^{1/2}} \sum_G C_G \, e^{i(\mathbf{G}+\mathbf{k})\mathbf{r}} & \mathbf{r} \in \mathit{Interstitial} \\ \sum_{\ell m} A_{\ell m} u_\ell(r) \, Y_{\ell m}(\mathbf{r}) & \mathbf{r} \in \mathit{Sphere} \end{cases} \tag{6.1}$$

In the above relations φ is the wavefunction, Ω the cell volume and u_ℓ the regular solution of Eq. 6.2. C_G and $A_{\ell m}$ are expansion coefficients, E_ℓ is a parameter (set equal to the band energy) and V the spherical component of the potential in the sphere.

$$\left[-\frac{d^2}{dr^2} + \frac{\ell(\ell+1)}{r^2} + V(r) - E_\ell \right] r u_\ell(r) = 0 \tag{6.2}$$

The use of these functions has been motivated by Slater by noting that planewaves are

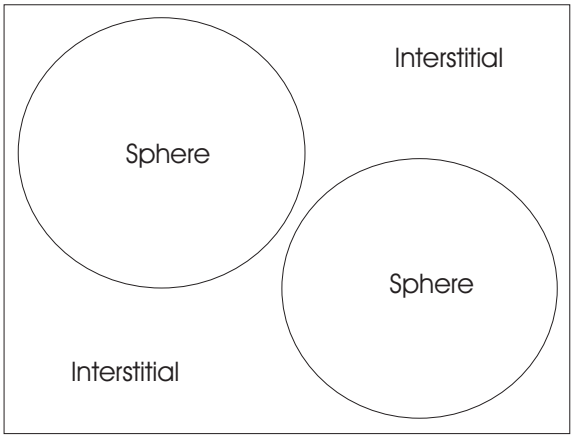

Figure 6.1: Adaptation of the basis set by dividing the unit cell into atomic spheres and interstitial regions.

the solutions of the Schrödinger's equation in a constant potential and radial functions are solutions in a spherical potential. This approximation to the potential is called "*muffin-tin*" (MT) and results very good for close packed materials like fcc and hcp.

Since the continuity on the spheres boundaries needs to be guaranteed on the dual representation defined in Eq. 6.1, constraint must be imposed. In the APW method this is done by defining the $A_{\ell m}$ in terms of C_G in the spherical harmonic expansion of the planewaves.

$$A_{\ell m} = \frac{4\pi i^{\ell}}{\Omega^{1/2} u_{\ell}(R)} \sum_{G} C_G \, j_{\ell}(\mid \mathbf{k}+\mathbf{g} \mid R) \, Y^{*}_{\ell m}(\mathbf{k}+\mathbf{G}) \tag{6.3}$$

The coefficient of each ℓm is matched at the sphere boundary and the origin is taken at the centre of the sphere (R is the sphere radius). The $A_{\ell m}$ are determined by the planewave coefficients (C_G) and the energy parameters E_{ℓ}, which are the variational coefficients in APW method. The functions labelled **G** are the augmented planewaves (APWs) and consist of single planewaves in the interstitial zone which are matched to the radial functions in the spheres.

A more flexible and accurate band structure calculational scheme is the LAPW method where the basis functions and their derivatives are made continuous by matching to a radial function at fixed E_{ℓ} plus its derivative with respect to E_{ℓ}.

6.2 The LAPW basis

The basis functions inside the spheres are linear combinations of a radial functions $u_\ell(r)\,Y_{\ell m}(r)$ and their energy derivatives[1]. The u_ℓ are defined as in the APW method (Eq. 6.2) and the energy derivative, $\dot{u}_\ell(r)\,Y_{\ell m}(r)$, satisfies the following:

$$\left[-\frac{d^2}{dr^2}+\frac{\ell(\ell+1)}{r^2}+V(r)-E_\ell\right] r\dot{u}_\ell(r)=ru_\ell(r) \tag{6.4}$$

These functions are matched to the values and derivatives of the planewaves on the sphere boundaries. Such augmented planewaves are the LAPW basis (LAPWs),

$$\varphi(\mathbf{r})=\begin{cases}\frac{1}{\Omega^{1/2}}\sum_G C_G\, e^{i(\mathbf{G}+\mathbf{k})\mathbf{r}} & \mathbf{r}\in Interstitial\\ \sum_{\ell m}\left[A_{\ell m}u_\ell(r)+B_{\ell m}\dot{u}_\ell(r)\right]Y_{\ell m}(\mathbf{r}) & \mathbf{r}\in Sphere\end{cases} \tag{6.5}$$

where the $B_{\ell m}$ are coefficients for the energy derivative analogous to the $A_{\ell m}$. The LAPWs are planewaves in the interstitial zone of the unit cell which match the numerical radial functions inside the spheres with the requirement that the basis functions and their derivatives are continuous at the boundary. In this method no *shape approximations* are made and consequently such a procedure is often called "full-potential LAPW" (FP-LAPW). The much older muffin-tin approximation corresponds to retain only the L=0 and M=0 component in Eq. 6.5. A spherical average inside the spheres and the volume average in the interstitial region is thus taken.

Inside atomic sphere a linear combination of radial functions times spherical harmonics, $Y_{\ell m}(\mathbf{r})$, is used. The linear combination of $u_\ell(r)$ and $\dot{u}_\ell(r)$ constitute the so-called "*linearization*" of the radial function. $u_\ell(r)$ and $\dot{u}_\ell(r)$ are obtained by numerical integration of the radial Schrödinger equation on a radial mesh inside the sphere.

The LAPWs have more variational freedom inside the spheres than APWs. This greater flexibility is due to the presence of two radial functions instead of one; non-spherical potentials inside spheres can be now treated with no difficulty. There is however, a price to be paid for the additional flexibility of the LAPWs: the basis functions must have continuous derivatives and consequently higher planewave cut-offs are required to achieve a given level of convergence. Further, the asymptote problem[2] found in the APW method is now overcome by the presence of the non-zero $\dot{u}_{\ell m}(R)$ value. The solution of

[1] $u_\ell(r)\,Y_{\ell m}(r)$ and $\dot{u}_\ell(r)\,Y_{\ell m}(r)$ are the augmenting functions.

[2] $u_{\ell m}(R)$ appears in the denominator of expression (6.3) and if zero leads to a decoupling between planewaves and radial functions. In the vicinity of the asymptote the secular determinant is strongly varying.

the KS equations are expanded in this combined basis according to the linear variation method:

$$\psi_k = \sum_n c_n \varphi_{k_n} \tag{6.6}$$

and the coefficients c_n are determined bu the Rayleigh-Ritz variational principle. In the WIEN97 package the total energy is calculated according to the Weinert scheme [71]. The convergence of the basis set is controlled by the cut-off parameter $R_{mt}K_{max}$ (determining the matrix-size of the system), which usually assumes values in between 6 and 9. The R_{mt} represents the smallest of all atomic sphere radii in the unit cell and ${K_{max}}^3$ is the magnitude of the largest K vector (planewave cut-off).

[3] K^2_{max} represents the planewave cut-off parameter in Ry used in pseudo-potential calculation.

Chapter 7

The ASW method

7.1 About linear methods

Among the prime methods for the computation of the band structure the augmented planewave [72] in 1965 and KKR (Korringa Kohn Rostoker) [73] in 1954 were known at the time of their derivation to be highly time consuming. A solution to this contextual difficulty was brought by the so-called linear methods whose impact became increasingly dominant within the community of physicists. Therefore, the analysis of more realistic and complex systems was made possible with the existing computational means. The augmented spherical wave, the linear muffin tin orbital and the linearized augmented planewave are among such linearized methods. This implies that the energy dependence of the wave function is lifted by expressing it with a product of energy dependent coefficients $a(\mathbf{k})$, on which the variational procedure is conducted, and energy independent radial functions $\chi(\mathbf{r})$.

7.1.1 ASW and LMTO methods

The ASW method was originally derived in 1979 by Williams *et al.* [74, 75]. This computational approach shows very close similarities with the LMTO method introduced earlier by Andersen [76], though the formalism is somehow different. The muffin-tin approximation is employed in both cases and refers to non overlapping atomic spheres which well describe compact close packed solids such as the *fcc*, *bcc* and *hcp* structures of metals and alloys. It is obvious that the remaining interstitial region is in these special cases very small. Nevertheless, properties have to be computed explicitly beside the intra-atomic region. This is actually done through planewaves as in the FP-LAPW method [68] which despite its high precision remains very time consuming even with the actual computers. The incontestable general advantages arising with the use of ASW or LMTO methods are found in their simple interpretation and on the possibility to perform very

fast calculations. In particular, these methods are excellent for a first general description of the electronic properties of solids. However, in spite of these great advantages, a certain limited precision characterise these methods and often their use is circumscribed to the description of compact systems (empty spheres are needed to describe less compact structures).

7.1.2 The ASA and its implications

To a good approximation the interstitial region can be neglected if the MT spheres are enlarged so that their volume becomes identical to the unit cell volume. The MT spheres become then Wigner-Seitz spheres [77]. This approximation is called the Atomic Sphere Approximation, ASA, and is used by both methods. The LMTO approach becomes, for example, the LMTO-ASA method in order to differentiate from the full potential method, FP-LMTO, derived later by Savrasov *et al.* [78]. The unit cell is thus divided into atomic spheres in a way that their total volume equals the volume of the cell.

$$\sum_i \Omega_i := \sum_i \frac{4}{3}\pi S_i^3 \stackrel{!}{=} \Omega_c \tag{7.1}$$

where S_i is the radius of the sphere i and $\Omega_{i,c}$ the volume of the unit cell. Another assumption is embedded within the ASA: the potential and the electron density are spherically averaged. This can be a drawback when electric field gradients or electron density plots are to be produced.

7.1.3 Solution of the wave function

Both ASW and LMTO-ASA methods use *envelop* functions cantered on the atomic sites. These are subjected to the Laplacien which is almost the same for both methods:

$$(\Delta + \epsilon_0)\chi_L(\mathbf{r}) = 0 \tag{7.2}$$

where L refers to the n and l quantum numbers and ϵ_0 is an energy parameter put to zero in LMTO and to a small (fixed) negative value ($\epsilon_0 \sim$ -0.015 Ry) in ASW. It determines the degree of localisation of the envelop wave function given by spherical Hankel functions $h_l^+(\kappa r)$, $\kappa = \sqrt{\epsilon}_0$.

7.2 Further formalism with the ASW method

The ASW method provides an approximate solution to the single-particle Schrödinger equation:

$$[-\nabla^2 + V(\vec{r}) - \epsilon]\Psi(\vec{r}, \epsilon) = 0 \tag{7.3}$$

The electronic structure problem is solved within the DFT approach via a repetitive solution of the above equation (self-consistent procedure). The wavefunctions $\Psi(\vec{r},\epsilon)$ is determined by developing an expansion in energy-dependent, $C_n(\epsilon)$, and energy-independent, $X_n(\vec{r})$ coefficients:

$$\Psi(\vec{r},\epsilon) = \sum_n C_n(\epsilon) X_n(\vec{r}) \tag{7.4}$$

With the above expansion of $\Psi(\vec{r},\epsilon)$ in energy-independent base functions, the solution of the Schrödinger equation (Eq. 7.3) reduces to a matrix eigenvalue problem for which efficient numerical procedure can be applied.

Another important feature of this approach involves the basis set $X_n(\vec{r})$. In particular the intra- and inter- atomic part of the calculation can be decoupled and the orthogonalization and core-state readjustment can be done without the inclusion of the core states in the basis set used to expand the states of the interatomic interaction. The removing of the core states from the interatomic basis set permits to increase the efficiency of the calculational scheme. The augmented spherical wave (ASW's) are the selected energy-independent single-particle basis set. In the intra-atomic portion of a polyatomic system, the strong potential causes $\Psi(\vec{r},\epsilon)$ to vary rapidly, whereas in the inter-atomic region a slowly varying (weak potential) wavefunction is found. From this picture the inter-atomic region can be thus expanded in planewaves (APW method), however treating all portion of the interstitial volume equally is a "*luxury for which the price is relatively inefficiency*". A less flexible (and less accurate) LCAO-like treatment of the inter-atomic region is made by assuming the solutions of the Schrödinger's equation to be a linear combination of atomic-orbital "tails" extending out of each of the intra-atomic region.

$$\Psi(\vec{r},\epsilon) = \sum_{L\nu} C_{L\nu}(\epsilon) H_L(\vec{r} - \vec{R_\nu}) \tag{7.5}$$

where $\vec{R}_\nu$ are nuclear position and $C_{L\nu}(\epsilon)$ are the energy-dependent expansion coefficients. The atomic-like functions $H_L(\vec{r})$ are spherical waves as follow,

$$H_L(\vec{r}) \equiv i^l k^{l+1} Y_L(\hat{r}) h_l^+(kr) \qquad L = l, m \tag{7.6}$$

with $Y_L(\hat{r})$ representing the spherical harmonics and $h_l^+(x)$ the outgoing spherical Hankel function.

7.2.1 The augmentation process

Each of the intra-atomic region is described by a very strong potential. The effective potential can be thus approximated with a spherical symmetry and the basis functions constructed by solving the radial Schrödinger's equation. A comparison between the APW's and ASW's is shown in Fig. 7.1. The two bases are very similar, even though

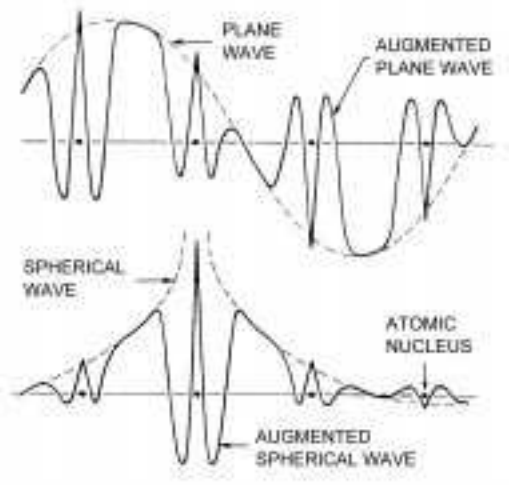

Figure 7.1: Comparison between the augmented plane (APW) and spherical (ASW) waves. This Figure has been taken from the original work of A. R. Williams, J. Kübler and C. D. Jr. Gelatt [74].

a single ASW can be identified with a particular atom, like an atomic orbital. The spherical wave $H_L(\vec{r})$ is continued into the intra-atomic region due to the particular linear combination of the Schrödinger's equation which joins smoothly to $H_L(\vec{r})$ at the interface of the intra- inter- atomic region. Therefore, for all r_ν less than the sphere radius S_ν it is possible to replace $H_L(\vec{r}_\nu)$ with its augmented counterpart $\tilde{H}_L(\vec{r}_\nu)$, where

$$\tilde{H}_L(\vec{r}_\nu) = i^l Y_L(\hat{r}_\nu)\tilde{h}_l(r_\nu), \tag{7.7}$$

and $\tilde{H}(\vec{r}_\nu)$ is the solution of the intra-atomic Schrödinger equation,

$$[-\nabla^2 + V(\vec{r}_\nu + \vec{R}_\nu) - \epsilon_{ln}^{(H)}] = 0. \tag{7.8}$$

The aforementioned equation can be rewritten as

$$\left(-\frac{1}{r_\nu}\frac{\partial^2}{\partial r_\nu^2}r_\nu + \frac{l(l+1)}{r_\nu^2} + V(\vec{r}_\nu + \vec{R}_\nu) - \epsilon_{l\nu}^{(H)}\right)\tilde{h}_l(r_\nu) = 0, \tag{7.9}$$

and $V(\vec{r}_\nu + \vec{R}_\nu)$ is assumed to depend only on r_ν for $r_\nu < S_\nu$. The continuity and differentiability through the spherical surface $r_\nu = S_\nu$ is guaranteed by the possibility of choosing the $\tilde{h}_l(r_\nu)$ and $\epsilon_{l\nu}^{(H)}$,

$$\left(\frac{\partial}{\partial r_\nu}\right)^n [\tilde{h}_l(r_\nu) - k^{l+1}h_l^+(kr_\nu)]_{\mathbf{r}_\nu=\mathbf{S}_\nu} = 0, \qquad n = 0, 1. \tag{7.10}$$

Since the effective potential vary strongly on the intra-atomic region, the augmentation of the function $H(\vec{r}_\nu)$ must be operated not only inside the sphere centred at R_ν but in all other intra-atomic regions, $R_{\nu'}$, where $\nu' \neq \nu$. Such an augmentation is computed by expanding with the Bessel functions, $J_L(\vec{r}')$, centred at the $R_{\nu'}$ site

$$H_L(\vec{r}_\nu) = \sum_{L'} J'_L(\vec{r}'_\nu) B_{L'L}(\vec{R}_{\nu'} - \vec{R}_\nu), \tag{7.11}$$

where

$$J_L(\vec{r}) = i^l k^{-l} Y_L(\hat{r}) j_l(kr) \tag{7.12}$$

and $j_l(kr)$ is the spherical Bessel function. $B_{L'L}(\vec{R})$ are the structure constants developed in the KKR method [73]:

$$B_{LL'}(\vec{R}) = 4\pi \sum_{L''} I_{LL'L''} k^{l+l'-l''} H_{L''}(\vec{R}) \tag{7.13}$$

and

$$I_{LL'L''} \equiv \int d\hat{r} Y_L(\hat{r}) Y_{L'}(\hat{r}) Y_{L''}(\hat{r}). \tag{7.14}$$

are the Gaunt's coefficients. The augmentation of the $H_L(\vec{r} - \nu)$ on the neighbours of $R_{\nu'}(|\vec{r} - \vec{R}_{\nu'}| \leq S_{\nu'})$ reduces to the augmentation of the $j_l(kr_{\nu'})$,

$$\tilde{H}_L(\vec{r} - \vec{R}_\nu) = \sum_{L'} \tilde{J}'_L(\vec{r} - \vec{R}'_\nu) B_{L'L}(\vec{R}_{\nu'} - \vec{R}_\nu), \tag{7.15}$$

where

$$\tilde{J}_L(\vec{r}'_\nu) \equiv i^l Y_L(\hat{r}'_\nu) \tilde{j}_l(r'_\nu) \tag{7.16}$$

and $\tilde{j}_l(r'_\nu)$ is the solution of the radial Schrödinger equation relative to the sphere centered at R'_ν,

$$\left(-\frac{1}{r'_\nu} \frac{\partial^2}{\partial r'^2_{\nu'}} r'_\nu + \frac{l(l+1)}{r'^2_\nu} + V(\vec{r}'_\nu + \vec{R}'_\nu) - \epsilon^{(J)}_{l\nu'} \right) \times \tilde{j}_l(r'_\nu) = 0, \tag{7.17}$$

that joins smoothly the spherical Bessel function at $r'_\nu = S'_\nu$.

$$\left(\frac{\partial}{\partial r'_\nu} \right)^n [\tilde{j}_l(r'_\nu) - k^l j_l(kr'_\nu)]_{\mathbf{r}'_\nu = \mathbf{S}'_\nu} = 0, \qquad n = 0, 1 \tag{7.18}$$

Proceeding in the same way, as in the augmentation of $h_l^+(kr)$, the above continuity condition specifies the normalisation of $\tilde{j}_l(k\nu')$ and the energy $\epsilon^{(J)}_{l\nu'}$. The augmented spherical waves $\tilde{H}_L(\vec{r} - \vec{R})$ are now defined in all the regions and are continuous, energy independent and continuously differentiable. With such a basis set functions, it becomes possible to expand the solutions of the Schrödinger's equation.

$$\Psi(\vec{r}, \epsilon) = \sum_{L,\nu} C_{L,\nu}(\epsilon) \tilde{H}_L(\vec{R}_\nu) \tag{7.19}$$

7.2.2 The variational method of Rayleigh-Ritz

Starting from $\mathcal{H}\Psi = E\Psi$ the eigenenergy ϵ and expansion coefficients $C_L\nu(\epsilon)$ (Eq. 7.19) may be evaluated with the Rayleigh-Ritz variational method. The secular matrix from the Rayleigh-Ritz procedure looks as follow:

$$\sum_{L',\nu'} (\langle \nu\tilde{L}|\mathcal{H}|\tilde{L}'\nu'\rangle - \epsilon\langle \nu\tilde{L}|\tilde{L}'\nu'\rangle)C_{L'\nu'}(\epsilon) = 0 \tag{7.20}$$

where $\mathcal{H} \equiv -\nabla^2 + V(\vec{r})$ and $\langle \cdots | \cdots \rangle$ is the integral extending over the whole space:

$$\langle \nu\tilde{L}|\tilde{L}'\nu'\rangle \equiv \int d^3r \tilde{H}^*_L(\vec{r} - \vec{R}_\nu)\tilde{H}_{L'}(\vec{r} - \vec{R}_{\nu'}) \tag{7.21}$$

The approximation of the intra-atomic regions with atomic spheres (ASA) gives:

$$\langle \nu\tilde{L}|\mathcal{H}|\tilde{L}'\nu'\rangle = \sum_{\nu''} \langle \nu\tilde{L}|\mathcal{H}|\tilde{L}'\nu'\rangle_{\nu''} \tag{7.22}$$

In order to improve the convergence of the numerical calculation[1] the above equation is modified as follow:

$$\langle \nu\tilde{L}|\mathcal{H}|\tilde{L}'\nu'\rangle = \langle \nu L|\mathcal{H}_0|L'\nu'\rangle + \sum_{\nu''} (\langle \nu\tilde{L}|\mathcal{H}|\tilde{L}'\nu'\rangle_{\nu''} - \langle \nu L|\mathcal{H}_0|L'\nu'\rangle_{\nu''}) \tag{7.23}$$

where $\mathcal{H}_0 \equiv -\nabla^2$ denotes the free-particle Hamiltonian. The final thing that has to be noted is that in all the integrals of the matrix elements the ASW is an eigenfunction of the Hamiltonian. The integrals over the atomic spheres (Eq. 7.23) are of three types, one-center, two-center or three-center depending on the number of the two ASW's centered in the sphere. Four different contributions are found:

- The first expression on the right side of the Eq. 7.23 and the second member within the parenthesis are relatively easy to solve since the term is an eigenvalue of $\mathcal{H}_0$.

  $$\langle \nu L|\mathcal{H}_0|L'\nu'\rangle = k^2\langle \nu L|L'\nu'\rangle \tag{7.24}$$

  The representation of the matrix elements requires an integral over all space involving unaugmented spherical waves, which can be solved analytically.

- The one-center contributions are those in which both ASW's are centred in the sphere ($\nu = \nu' = \nu''$). Only augmented Hankel functions are considered:

  $$\langle \nu\tilde{L}|\mathcal{H}|\tilde{L}'\nu'\rangle_\nu = \epsilon^{(\mathcal{H})}_{l\nu}\langle \tilde{H}_L|\tilde{H}_L\rangle_\nu \delta_{LL'} \tag{7.25}$$

[1] The effective potential has been taken to be zero in the interstitial region so that the matrix element can be written as in Eq. 7.23. For details see Ref. [74].

- The two-centres integrations ($\nu = \nu'' \neq \nu'$ or $\nu \neq \nu'' = \nu'$), require the expansion of one of the two ASW's. Therefore, both augmented Hankel and Bessel functions are taken:

$$\langle \nu'' \tilde{L} | \mathcal{H} | \tilde{L}' \nu' \rangle_{\nu''} = \epsilon^{(J)}_{l\nu''} \langle \tilde{H}_L | \tilde{J}_L \rangle_{\nu''} B_{LL'}(\vec{R}_{\nu''} - \vec{R}_{\nu'}) \tag{7.26}$$

  and

$$\langle \nu \tilde{L} | \mathcal{H} | \tilde{L}' \nu'' \rangle_{\nu''} = \epsilon^{(H)}_{l'\nu''} \langle \tilde{J}_{L'} | \tilde{H}_{L'} \rangle_{\nu''} B^{\dagger}_{LL'}(\vec{R}_{\nu} - \vec{R}_{\nu''}) \tag{7.27}$$

  where

$$B^{\dagger}_{LL'}(\vec{R}_{\nu} - \vec{R}_{\nu'}) \equiv B^{*}_{LL'}(\vec{R}_{\nu} - \vec{R}_{\nu'}). \tag{7.28}$$

- Finally in the three-center contributions ($\nu \neq \nu' \neq \nu''$), only the augmented Bessel functions are used. In this case neither of the two ASW's involved in the matrix element are centred in the intra-atomic region over which the integration is performed.

$$\langle \nu \tilde{L} | \mathcal{H} | \tilde{L}' \nu' \rangle_{\nu''} = \sum_{L''} B^{\dagger}_{LL''}(\vec{R}_{\nu} - \vec{R}_{\nu''}) \epsilon^{(J)}_{l''\nu''} \times \langle \tilde{J}_{L''} | \tilde{J}_{L''} \rangle_{\nu''} B_{L''L'}(\vec{R}_{\nu''} - \vec{R}_{\nu'}) \tag{7.29}$$

The above individual integrals can be combined to complete the secular matrix. Integrals involving augmented functions need only one-dimensional numerical integration and those containing unaugmented spherical Bessel functions can be found in the work of Morse and Feshbach [79].

Chapter 8

Carbon Nitrides

8.1 Introduction

Networks made of covalently bonded carbon nitride are expected to show remarkable physical properties such as high hardness, wide band gap and high thermal conductivity. They can be used as a protective coating on hard discs and recorder heads and are being tested for several other tribological applications. Other utilisation areas can be found, for example, in flat-panel display industry. The possibility to synthesise nanotubes- [80] and nanofibers-like [81, 82, 83] CN_x structures in a solid film may open the possibility of using such films for field emission electron source [84, 85, 86, 87]. Carbon nitrides have also been tested for the development of ossointegrated joint arthroplastie. The major problem with these implants is the wear debris generation which might provokes serious tissue reactions. Amorphous CN_x samples have been recently identified as an interesting coating for human implants [88]. Because of these great expectations they have rapidly become the focus of an enormous attention and nowadays they are widely investigated both experimentally and theoretically as potential candidates for new ultra-hard materials [89]. The starting interest on carbon nitrides dates back to the Liu et Cohen's theoretical work of 1989 [12] where the properties of the β-C_3N_4 phase were proposed to be similar or even superior to those of diamond. From this finding many researchers were positively stimulated to find an adequate way to synthesise pure crystalline C_3N_4 materials. The first attempt to make carbon nitride films refers to J. J. Cuomo *et al.* in 1979 [90], who grew paracyanogen-like thin films with N/C ratios equal to one. Much more recently, a wide variety of techniques such as ion implantation [91], rf sputtering of carbon targets in a nitrogen atmosphere [92], plasma deposition of various hydrocarbons [93], nitrogen ion implantation with simultaneous carbon vapour deposition [94], dc magnetron sputtering of a graphite target in a nitrogen ambient [95], shock wave compression of carbon nitride precursor [96], plasma-enhanced chemical vapour deposition

[97], ion-assisted dynamic mixing [98] and laser ablation of a carbon target in a stream of atomic nitrogen [99], have been investigated. From these attempts we know that many compositions of carbon nitrides exist and more than a few are stable to at least 800 °C. Beside this, the experimental evidence also seems to point out to the possible existence of different phases with a very similar stability: mixed-phase deposits are quite often obtained. As a matter of fact, despite many efforts, the synthesis of carbon nitride films with stoichiometry C_3N_4 (57.14 % of nitrogen concentration) is still restricted to the production of amorphous samples with unclear crystallographic data. It is because of the above problem that in the first part of this Chapter (Section 8.2, p. 42) it has been shown a cross-checking on the relative stability and hardness of different hypothetical C_3N_4 phases by using various DFT solid state calculational methods. This was also the first occasion to probe and test our codes in treating the electronic properties of a novel class of carbon-based hard materials.

Another crucial problem found during the synthesis of carbon nitrides is that of nitrogen concentration. From the deposition of CN_x films, with $0 \leq x \leq 0.35$, by reactive magnetron sputtering[1] in Ar/N_2 discharges we know, for example, that the maximum nitrogen concentration obtainable in the film is strongly dependent on the formation of stable molecules, like N_2 and C_2N_2, that can with high probability desorb and leave the growth surface at even low substrate temperatures [100, 101, 102]. Moreover, the possible transition at ~ 200 °C from a "*graphitic-like*" $\rightarrow$ "*fulleren-like*" phase, recently presented by N. Hellgren *et al.* [100], could be imagined to take place from a nitrogen-poor CN_x graphitic form. In fact, this transition is observed when the nitrogen concentration increases from 5 to 15 % and the fulleren-like structure is found to be stable when the nitrogen amount is between 10 and 25 %. These concentrations are much closer to the $C_{11}N_4$ stoichiometry than the well-known C_3N_4. Furthermore, the carbon-nitrogen ratio in CN_x films ($0.2 \leq x \leq 0.35$) observed by H. Sjöstrom *et al.* [103] for buckled turbostatic microstructures formed at high temperatures is again close to the composition of the $C_{11}N_4$. Such carbon-nitrogen systems have been found to be both hard and elastic from nanoindentation experiments [103, 100].

Therefore, from the above evidences it becomes of primarily importance to understand, at least theoretically, whether or not the $C_{11}N_4$ stoichiometry could be in competition or even favoured over the formation of the C_3N_4. It is also interesting to check what would be the changing in the mechanical and electronic properties if a pure crystalline carbon nitride sample would be synthesised in the $C_{11}N_4$ composition. This has been investigated in the second part of the present Chapter (Section 8.3, p. 72). In particular, it has been stressed the importance of the use of theoretical methods and models to obtain further characterisation and trends in the bonding configurations of the CN_x

[1] This technique implies the evaporation of carbon (carbon atoms) and the interaction with a plasma made of ionised nitrogen atoms. Permanent magnets behind the sputtering target are used to confine most of the electrons in the region of the target surface.

structures. The attention is mostly focalised on the study of the stability and the hardness of two different stoichiometries: C_3N_4 and $C_{11}N_4$. It should also be noted that the analysed systems are isoelectronic to each other and to diamond, although the nitrogen concentration on the latter phase (26.67 %) is much lower than in the former one (57.14 %). In other words, the investigation is here restricted only to those compounds that are electronically analogue[2] to carbon [104, 105, 106]. This particular choice derives from the fact that all the substances satisfying this rule should likely show the same interesting properties of the hardest known materials (*e.g.* cubic boron nitride and diamond).

8.2 Study of the C_3N_4 stoichiometry

By using an empirical formula (see Eq. 2.5 in p. 6) which relates the bulk modulus of tetrahedrally coordinated systems to the length and ionicity of their bonds, it was predicted as early as in 1985 that a material made of carbon and nitrogen should exhibit a bulk modulus higher than diamond [23]. This possibility was addressed to the short length and the high covalency of the C-N bond. As a consequence carbon nitrides have been proposed as candidates for new ultra-hard materials. However, despite this great expectation the synthesis of C_3N_4 is nowadays still restricted to the production of small amounts of samples, which are not sufficient enough for a correct structural characterisation. This restriction is possibly due to the technological difficulties to produce materials with large amounts of nitrogen that is required to chemically interact with carbon [100]. Experimentalists have observed carbon nitride materials in amorphous or disordered phases [107, 108, 109] as well as crystalline aggregates dispersed in an amorphous matrix [110, 111]. Theoretical investigations on the subject have also been made to explain the stability and mechanical properties of the synthesised samples and to predict the properties of some of the new hypothetical forms [22, 29, 112, 113, 114, 115, 116, 117, 118]. Recently, first principles calculations, within the local density approximation, on the cubic form of C_3N_4 have shown a bulk modulus exceeding that of diamond [29, 117, 119]. Such an important finding has in part confirmed the original intuition of M. L. Cohen about the possibility for a three-dimensional CN_x compound to be ultra-hard. A complete theoretical description of the hardness and the stability of various hypothetical C_3N_4 phases is reported in the following Sections.

8.2.1 Methods and computational details

The main goal of this work is to employ a fast and reasonably accurate calculational scheme in order to describe the electronic structure properties of carbon nitrides. For this purpose the output of the usually very accurate full potential approach has been

[2] The same four averaged number of valence electrons per atom is kept.

compared with those from methods based on the spherical shape approximation of the crystal potential. The entire set of results have also been correlated with the early PP calculations. In this Section the attention is finalised on the simple C_3N_4 stoichiometry and as a starting point the relative energy stabilities and hardness of five hypothetical C_3N_4 model phases, namely graphitic-like, α, β, cubic and pseudo-cubic, have been checked. Three different DFT based methods within the LDA have been tested: *Augmented Spherical Wave* [74, 120], *Linear Muffin-tin Orbitals* [76, 121] and *Full-potential Linearized Augmented Plane-Wave* [68]. For the exchange and correlation effects the parameterisation scheme of Van Barth, Hedin [122] and Janak [123] was used in the ASW and LMTO methods, while in the FP-LAPW the Perdew and Wang 92 [47] functional was assumed.

For the C_3N_4 system total energies were evaluated within the LMTO and ASW calculations using the tetrahedron method for the **k**-space integration and a uniform 12×12×12 mesh according to the Monkhorst-Pack [63] scheme (energy converging with **k**-points, $\Delta E < 1$ mRy). In both methods the atomic sphere approximation is used, in which each atom is represented by a sphere. Inside the spheres the potential and charge density are assumed to be spherically symmetric. Then the sum of all sphere volumes is made to equal the volume of the unit cell. Within the ASA one usually has to introduce pseudo-atoms (with atomic number Z=0) or empty spheres in order to ensure a continuous electronic density in open structures. In the present calculations we paid particular attention to an optimal choice of the atomic radii as well as the number and position of empty spheres used to meet the ASA criteria. For the diamond and *c*-BN a 12×12×12 mesh was found to ensure the desired convergence.

The full potential total energy calculations of the C_3N_4 phases were performed using the same plane wave cut-off (87 plane waves/atom) and **k**-point number (300 total **k**-points), as they were optimised for the α-C_3N_4 structure, a phase with the largest number of atoms per unit cell (*i.e.* 28). For carbon and nitrogen atom types the same muffin-tin radius (R_{mt}=1.33 Å) was used and maintained fixed for all the investigated structures. By using different basis set cut-offs it has also been found that at the equilibrium volume approximately 87 plane-wave per atom were sufficient enough to predict the bulk modulus of carbon nitride without any significant change when increasing the number of basis functions used. For the *c*-BN system the FP-LAPW calculations were performed by employing the same parameter as Park, Terakura and Hamada [124].

8.2.2 Structural models for the C_3N_4 stoichiometry

The crystal geometries of the C_3N_4 phases were taken from the theoretical work of D. M. Teter *et al.* [29], in which the equilibrium structures were determined with a pseudopotential plane wave approach [55]. The hexagonal beta phase (β-C_3N_4) contains 14 atoms/unit cell (P3 space group) and consists of fourfold co-ordinated carbon and three

fold co-ordinated nitrogen atoms (Fig. 8.1)[3]. This phase is a network of three-, four- and six-fold rings of tetrahedra. The alpha phase (α-C_3N_4) has hexagonal symmetry and contains 28-atoms/unit cell (P31c space group). It can be viewed as a sequence of A and B layers in an ABAB stacking in which A is the β-C_3N_4 unit cell and B the mirror image of A. The cubic structure (*cubic*-C_3N_4) is based on the high-pressure willemite-II structure of Zn_2SiO_4, where C substitutes Zn and Si and N substitutes O. This phase contains 28-atoms/unit cell and belongs to the space group $I\overline{4}3m$. The pseudo-cubic structure, usually called defect-zinc blende structure (*bl*-C_3N_4), exhibits $P\overline{4}2m$ symmetry and contains 7-atoms/unit cell. The graphitic form of C_3N_4 (*graphitic*-C_3N_4) is represented by a planar structure with an ABA [29] stacking mode (Fig. 8.2). The hexagonal unit cell contains 14 atoms and the symmetry is $P\overline{6}m2$. Each C atom is three-fold coordinated, as is one of the four N atoms per cell. The other three N atoms are two-fold coordinated (resonant bonds). This phase has been taken as a reference for the graphite-based structure in making comparison between the relative stabilities of different carbon nitride phases. For the graphitic-like phase four other forms are predicted in the earlier works. The first one (AAA stacking mode [115]) has 7 atoms·unit cell^{-1} and a space group $P\overline{6}m2$. The second phase (ABC stacking mode [114]) which belongs to the R3m space group, shows 7 atoms in the unit cell and consists of graphite-like sheets with ABC rhombohedral stacking order. The other two phases were recently suggested by I. Alves *et al.* [125, 126]. These authors claim to have succeeded in the preparation of a carbon nitride powder with C_3N_4 composition by using high pressure synthesis methods. From the analysis of the X-ray diffraction patterns a crystal structure (P2mm space group) with an orthorhombic unit cell has been presented (Fig. 8.3). Both types of AAA and ABA stacking modes have been suggested. For these model phases a very different vacancy ordering has been displayed inside each of the graphitic planes with respect to the hexagonal system introduced by D. M. Teter and R. J. Hemley ($P\overline{6}m2$).

8.2.3 Relative stability of variuos C_3N_4 phases

For the investigated systems the full potential method predicts the same energy trend as found by D. M. Teter *et al.* [22] in their pseudo-potential plane-wave calculations (see Fig. 8.4 and Tab. 8.1). While the graphitic-like phase with ABA stacking sequence is the most stable from, the α system lies only marginally higher in energy by 0.036 eV. The energy of the β phase has been found to be 0.615 eV above that of the α structure. Even though the calculated energy difference between graphitic and the α phases is of the same order of magnitude as that calculated with PP method, *i.e.* 0.041 eV, the energy difference between α and β has been estimated to be 0.615 eV instead of 0.266

[3] In Fig. 8.1 we show the structure of the β-C_3N_4 phase as representative for a three-dimensional CN_x system. For the other structures, the reader should refer to the original work of D. M. Teter and R. J. Hemley in Ref. [29].

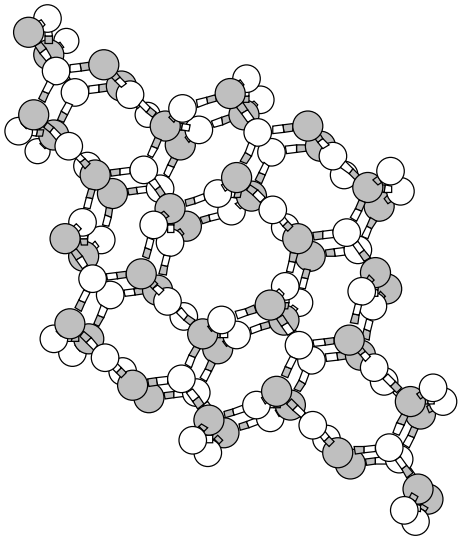

Figure 8.1: β-C_3N_4 model system. Carbon and Nitrogen are depicted in grey and white, respectively. This color scheme is kept throughout all the Thesis.

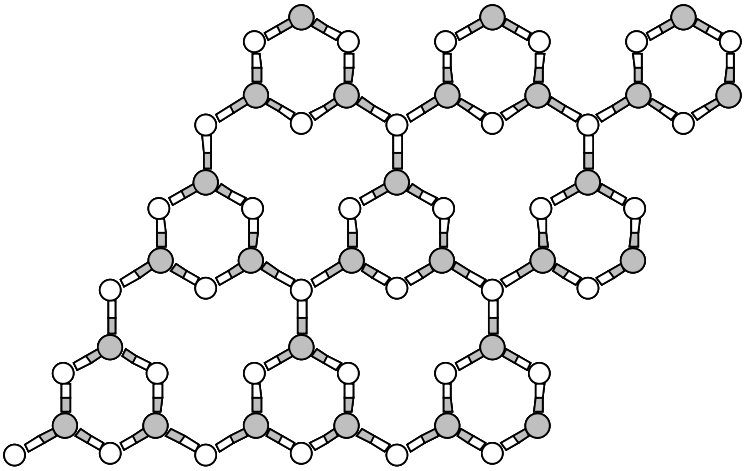

Figure 8.2: One layer of the hexagonal *graphitic*-C_3N_4 model.

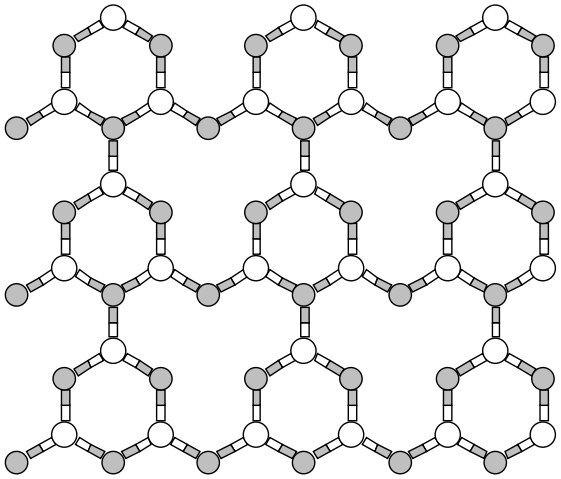

Figure 8.3: One layer of the orthorhombic *graphitic*-C_3N_4 phase.

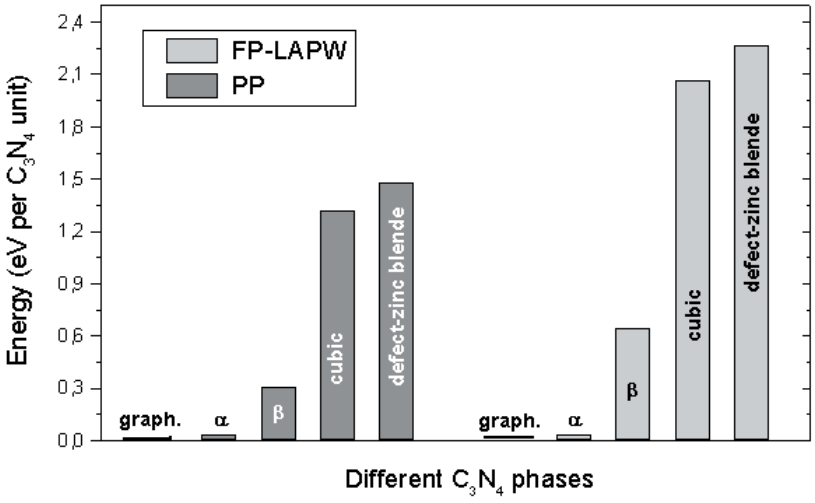

Figure 8.4: Relative stability between different C_3N_4 phases by using different method of calculations.

	graphitic-	*α-*	*β-*	*cubic-*	*bl-*
FP-LAPW	0	0.036	0.651	2.065	2.238
PP	0	0.041	0.307	1.322	1.485
ρ (g/cm^3)	2.33	3.77	3.57	3.89	3.86

Table 8.1: Total energies and densities for different C_3N_4 phases. Energy values are expressed in eV/C_3N_4 unit and are scaled with respect to the stable *graphitic*-C_3N_4 form. Pseudo-potential calculations refer to the work of D. M. Teter and R. J. Hemley [29].

eV. Finally, the cubic and pseudo-cubic structure (simple cubic and defect-zinc blende phases) are estimated to have the highest total energies. The simple cubic phase lies at 1.414 eV above the β phase, while the defect-zinc blende lies at 1.587 eV higher. The energy difference found for $\beta \leftrightarrow$ cubic is 1.414 eV instead of 1.015 eV as calculated with the pseudo-potential approach. In the same way the $\beta \leftrightarrow$ pseudo-cubic energy difference is estimated to be 1.587 eV in place of 1.178 eV. The use of Y. Liu et R. M. Wentzcovitch geometries [114] for β-C_3N_4 and *bl*-C_3N_4 gives rise to only small differences in the values of the total energies, confirming thus the PP energy trend. In particular, the β phase now lies slightly higher in energy (+0.0215 eV) and the pseudo-cubic slightly lower (-0.038 eV) with respect to the previous calculation (D. M. Teter's geometries).

By contrast, the LMTO and ASW methods predict lower energies for cubic structures and a higher one for the graphite-like phase. The obtained energy trend follows exactly the atomic densities, indicating that in less compact structures (*i.e.* graphite-like phases) the ASA approximation is no longer acceptable. As a matter of fact, the layered phase is the least dense (ρ= 2.33 g/cm^3) and it lies at high energy, while the cubic phase is the most dense (ρ= 3.89 g/cm^3) and consequently is predicted to have the lowest energy. Hence, the relative stability trends observed with LMTO and ASW are not comparable with those deduced from FP-LAPW and PP. This is due to the difficulty of getting reliable results from the use of empty spheres in describing phases with very different atomic packing. In fact, in the graphitic phase a large amount of empty space must be filled in the unit cell whereas the reverse situation is true for the cubic structures where the ASA worked best. However, even if it is not possible to make a strict comparison between the calculated relative stabilities, it is important to note that all the tested DFT methods are in agreement in predicting equilibrium volumes, bulk moduli and their pressure derivatives [117]. Details are given in Section 8.2.4 for the whole set of analysed C_3N_4 phases.

Thermodynamic stability of the C_3N_4 stoichiometry

When considering the possibility to synthesise carbon nitrides, one has to account for their thermodynamic stability with respect to the starting materials. The formation reaction of a C_3N_4 compound is given below.

$$3C_{(c)} + 2N_{2(g)} \rightarrow C_3N_{4(c)} \tag{8.1}$$

For simplicity it has been considered here the reaction between diamond, which is slightly less stable than graphite[4] (ΔG_f=2.9 kJ/mol), and nitrogen to form carbon nitrides. An important thing that has to be noted in Eq. 8.1 is that both diamond and molecular nitrogen possess strong bonds (C-C $\sim$ 350 kJ/mol and N-N $\sim$ 956 kJ/mol) while the reaction product (C_3N_4) contains only weaker C-N bonds (260-320 kJ/mol)[5]. It is thus quite evident that carbon nitrides are likely to be thermodynamically unstable under atmospheric pressure. Nonetheless, if a synthetic process can produce C_3N_4 a rather large activation energy would be needed to break the C-N bonds. Carbon nitrides could be thus result metastable at ambient conditions.

In order to get a quantitative insight into the stability of carbon nitrides with respect to decomposition to the elements, accurate values of their cohesive energies, $E_{coh.}$[6], are needed. Then, by knowing the experimental or theoretical values for the energy required to dissociate the nitrogen molecule and the cohesive energy of diamond, the enthalpy change for the reaction 8.1 can be evaluated. It is well known that the DFT-LDA approach normally tends to overestimate the cohesive energies for structures made of elements of the second row of the periodic table such as carbon and nitrogen [127, 128]. The cohesive energy of diamond is in fact significantly overestimated by $\sim$ 150 kJ/mol (see Tab. 8.2 and Ref. [67]) with respect to the experimental value [129]. Nonetheless, the general tendency of the LDA to overestimate the strength of C-C bond can be reduced by using the generalized gradient corrections [47], though the prediction of some of the structural properties, such as the interlayer distance in graphite, are sometimes worse than in LDA [67]. The computed cohesive energies (with the accurate FP-LAPW method) are shown in Tab. 8.2 as a function of different exchange-correlation potentials: LDA [130], Perdew-Burke-Ernzerhof (PBE) [131] and Perdew-Wang 91 (PW91) [47]. Calculations suggest that in spite of the general improving of the results obtained with GGA functionals, the availability of very accurate cohesive energies can only be overcome with the use of Quantum Monte Carlo (QMC) method. However, at the moment QMC energy values have not yet been published for carbon nitrides.

[4] Graphite is the most stable form of carbon, so that formally we should have taken it as reactant instead of diamond.

[5] Bonds between elements from the second row of the periodic table in which one of the atoms contain lone pairs are usually weaker.

[6] Energy required to break apart a structure into isolated atoms.

				The investigated C_3N_4 phases				
$E_{coh.}$	N_2	graphite	diamond	*graphitic-*	*α-*	*β-*	*cubic-*	*bl-*
LDA	-11.35	-8.93	-8.93	-6.89	-6.88	-6.80	-6.60	-6.57
	-11.34*		-8.87†					
PBE	-10.28	-7.99	-7.85	-6.04	-6.03	-5.93	-5.73	-5.68
			-7.72†					
PW91	-10.27	-7.98	-7.84	-6.03	-6.02	-5.92	-5.72	-5.68
			-7.72†					
exp.	-9.91§	-7.37‡	-7.37‡					

Values as compiled in Ref. (§)=[132], (‡)=[133], (∗)=[134] and (†)=[135].

Table 8.2: Cohesive energies (eV/atom) of different C_3N_4 model systems. Values are confronted with those of the starting materials: diamond/graphite and N_2. For the calculations of the nitrogen dimer it has been used a simple cubic cell (a=10 Å) with atoms displaced along the diagonal direction. It should be noted that an overbinding of more than 1 eV/atom is not unusual in local-density calculations for second-period elemental solids, as for example diamond [136, 137].

An elegant way to get out from the problem of having precise cohesive energies was given in 1997 by J. V. Badding [138]. He proposed a simple chemical approach to the thermodynamic stability of C_3N_4 starting from the use of bond enthalpies derived from molecular system. Covalently bonded systems such as diamond and carbon nitrides can be though as "*giant molecules*", so that simple bond enthalpy techniques can be used to estimate their stability. If we imagine, for example, to remove one carbon atom from the diamond structure, which is characterised by carbon tetrahedral bonds, four C-C connections will be broken. Such process will leave four carbon atoms with one dangling bond, which is equivalent to the removal of a second carbon. The whole cost of removing two C atoms amounts to the breakage of four C-C single bonds, which have in a molecular system a bond energy of about 350 kJ/mol. The cohesive energy of diamond can be thus estimated to be 350×2=700 kJ/mol, which is in good agreement with the experimental value of 711 kJ/mol [133]. In this approach it has been assumed that the contributions of the chemical bonds to the cohesive energy are additives. This hypothesis has been examined in details for solid state structures by D. A. Johnson [139]. For three-dimensional (sp^3 network) carbon nitrides the removal of one nitrogen atom has as a consequence the breakage of three C-N bonds. This will leave three carbon atoms each with one dangling bond, which is equivalent to the removal of $\frac{3}{4}$ of a carbon. Hence, the breaking of three bonds amounts to removal of a fragment with $C_{3/4}N$ stoichiometry. Using the tabulated bond energies for C-N (286-305 kJ/mol [139, 140]), the cohesive

energy for carbon nitrides should be in the range 858-915 kJ/mol of $C_{3/4}N$ fragment (or 490-522 kJ per mole of atoms, *i.e* 490=$\frac{4}{7}\times$858). The enthalpy for the formation reaction, ΔH^o_f, as in Eq. 8.2 can be thus calculated by knowing the experimental values of the energy required to dissociate a nitrogen molecule (956 kJ/mol [132]) and the cohesive energy of diamond (711 kJ/mol).

$$\frac{3}{4}C_{(c)} + \frac{1}{2}N_{2(g)} \rightarrow C_{\frac{3}{4}}N_{(c)} \tag{8.2}$$

$$\Delta H^o_f = \frac{3}{4}(711\ kJ/mol) + \frac{1}{2}(956\ kJ/mol) - E_{coh.}(C_{\frac{3}{4}}N) \tag{8.3}$$

The ΔH^o_f ranges from 96 to 153 kJ/mol of $C_{\frac{3}{4}}N$ (or 384-612 kJ/mol of C_3N_4), depending on the choice of C-N bond enthalpy. Using the cohesive energies as calculated in Tab. 8.2[7] we obtain the standard molar enthalpy change of formation at 0 K ($\Delta H^o_{f,0}$) listed in Tab. 8.3. Values were converted in kJ/mol (1 eV= 10^{-19} J) and the cohesive energy per $C_{\frac{3}{4}}N$ fragment, $E_{coh.}(C_{\frac{3}{4}}N)$, was obtained using the relation $E_{coh.}(C_{\frac{3}{4}}N) = \frac{7}{4} \times E_{coh.}(C_3N_4)$, where the term $E_{coh.}(C_3N_4)$ represents the computed energy per mole of atoms of Tab. 8.2. The estimated $\Delta H^o_{f,0}$ for the Eq. 8.3 are all positive and their

functional	$\Delta H^o_{f,0}$ (*graphitic*-$C_{\frac{3}{4}}N$)	$\Delta H^o_{f,0}$ (*bl*-$C_{\frac{3}{4}}N$)
LDA	30.3	84.4
PBE	44.1	104.9
PW91	44.6	103.7

Table 8.3: Calculated enthalpy of formation, $\Delta H^o_{f,0}$ (kJ/mol), for different exchange-correlation functionals. The above table shows only values representatives for the layered *graphitic*-$C_{\frac{3}{4}}N$ and the three-dimensional *bl*-$C_{\frac{3}{4}}N$. The complete list of enthalpies is given in Tab. 8.18 of Section 8.3, p. 72.

magnitudes agree quite well with the enthalpies of formation obtained with the Badding's method. This is especially true for the hard and three-dimensional phases, such as *bl*-C_3N_4, for which the above chemical approach has been hypothesised. However, since the GGA functionals (PBE and PW91) have shown a better description of the cohesive energies of the end members it is thus likely that the $\Delta H^o_{f,0}$ for the formation of *graphitic*-C_3N_4 and *bl*-C_3N_4 lays at about 177 and 417 kJ/mol, respectively. This large and positive

[7] These values have been obtained by taking the difference between the total energy of the solids and the ground-state energies of the non spin-polarised atoms. No correction for zero-point motion has been made. All the cohesive energies listed in this Thesis have been computed with the aforementioned procedure.

enthalpy of formation will be thus the most predominant contribution to the free energy of formation. However, this instability should not be very large to preclude the synthesis of CN_x compounds. As matter of fact, metastable carbon-based molecules with large and positive (endothermic) enthalpies of formation such as acetylene (226 kJ/mol) are known [139]. Using the shifts in the free energy described from the integration of the equations of state (Eq. 8.4),

$$\Delta G_p = \int_0^p V\,dp \tag{8.4}$$

J. V. Badding [138] determined the pressures to form thermodynamically stable C_3N_4 compounds to be of the order of 50-150 GPa. Despite these very large values, such pressures are nowadays attainable with current technologies. Carbon nitrides could be thus synthesised in high pressure and high temperatures conditions.

8.2.4 Hardness

Isotropic compression

The main purpose is here the investigation of the hardness of carbon nitrides with different DFT methods by evaluating the compressibility of the system. The resistance upon the volume change have also been investigated for diamond and cubic boron nitride in order to allow a cross-checking between the theoretical and experimental results. Calculations were performed by using the three previously mentioned DFT-based methods to evaluate the total energy as a function of different unit cell volumes. That is, the total energy has been computed after the application of an isotropic compression to the unit cell (by means of keeping constant the c/a ratio). The data sets $E(V_i)$ were then fitted with a third order Birch equation (Eq. 3.2 of Chapter 3, p. 9) to determine the equilibrium volumes, bulk moduli and pressure derivatives. As shown in Tab. 8.4, all the

Lattice constants (a_{eq}/c_{eq})	α-	β-	*cubic-*	*bl-*
LMTO	12.274/8.936	12.100/4.538	10.302	6.562
ASW	12.225/8.904	12.117/4.545	10.368	6.492
FP-LAPW	12.211/8.894	12.102/4.539	10.201	6.484
PP	12.220/8.900	12.114/4.543	10.199	6.469

Table 8.4: Equilibrium lattice constants (a_o) for the investigated model systems. The energy *vs.* volume data were fitted with a third order Birch equation.

DFT methods employed for the prediction of the equilibrium lattice constants and hence

Bulk modulus	α-	β-	*cubic*-	*bl*-	diamond
LMTO	438 (3.6)	455 (3.9)	468 (4.0)	441 (4.0)	453 (3.7)
ASW	414 (3.6)	431 (3.6)	452 (4.0)	427 (3.9)	440 (3.8)
FP-LAPW	431 (3.3)	460 (3.3)	518 (4.7)	445 (3.6)	466 (3.6)
PP	425 (3.1)	451 (3.3)	496 (3.4)	448 (3.4)	464 (3.7)

Table 8.5: Bulk modulus, B (GPa) and its pressure derivatives, $B^{'}$ (values in parenthesis) for various C_3N_4 phases and diamond.

volumes, give values that are in good agreements with the early pseudo-potential calculations [29]. The FP-LAPW method usually tends to estimate shorter a and c lengths, though they are often very similar to those computed with the pseudo-potential approach. The calculated compressibility of various carbon nitrides with composition C_3N_4 is listed in Tab. 8.5. Due to the short lengths found within the FP-LAPW method, the predicted bulk modulus is usually higher than what is expected. This is particularly true for the *cubic*-C_3N_4 phase for which a very large B (518 GPa) has been obtained (see Fig. 8.5). This value is even larger than that calculated for diamond. Employing a basis set of the same size, FP-LAPW calculations yield for diamond a bulk modulus of 466 GPa ($B^{'}$=3.60 and a_{eq}=6.679 a_o) to be compared with an experimental value of 442 GPa. While the predicted bulk moduli of the other hypothetical materials (α-C_3N_4, β-C_3N_4, and *bl*-C_3N_4) approach that of diamond ($\sim$ 430-460 GPa), the *cubic*-C_3N_4 clearly exceeds it. The cubic phase is estimated to be harder than diamond also from ASW (diamond: B=440 GPa; *cubic*-C_3N_4: B=452 GPa) and LMTO (diamond: B=453 GPa; *cubic*-C_3N_4: B=468 GPa) calculations. It is worth to note that all the DFT methods predict the cubic phase to be hardest carbon nitride, with a bulk modulus larger than diamond, while the alpha structure is computed to have the lowest B (highest compressibility for a three-dimensional C-N network)[8]. For the c-BN system the bulk moduli are of the same order of magnitude (B_{LMTO}=352 GPa, B_{ASW}=345 GPa and $B_{FP-LAPW}$=356 GPa) and close to the values given in the early theoretical works [142, 124, 143, 144]. However, it should be mentioned that all the three methods compute bulk moduli that are at about 100 GPa below the experimental value (456 GPa [145, 146]). Since the reverse tendency (B generally overestimated with respect to the experimental bulk modulus) is found for diamond, it is only possible to conclude that the hardness of the hypothetical *cubic*-C_3N_4 should be at least, if properly synthesised, of the same order of magnitude as that of diamond. The calculated pressure derivatives of the bulk modulus ($B^{'}$) for the C_3N_4 systems lies

[8]The layered *graphitic*-C_3N_4 is in absolute the phase with the highest compressibility with a bulk modulus ranging between 198-253 GPa (cfr. Ref. [141]). This is due to the graphitic-like form which is generally soft upon compression in the direction perpendicular to the sheets.

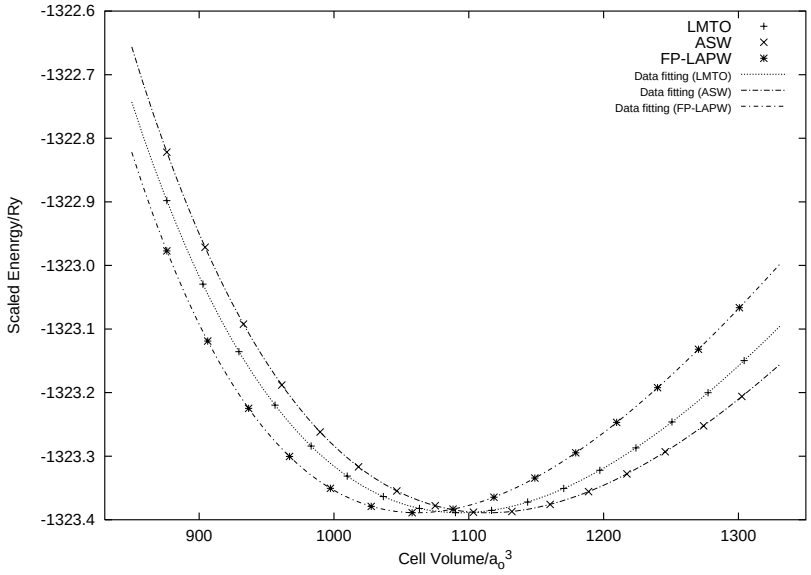

Figure 8.5: Energy dependence of the unit cell volume for *cubic*-C_3N_4 as a function of three different calculational methods. Data point have been fitted with the Birch type EOS.

between 3 and 4 as shown in Tab. 8.5. The FP-LAPW calculation usually gives a better agreement with the PP results except in the case of the cubic phase for which a larger value has been extrapolated.

Resistance to reversible deformation upon shape change

Since materials deform plastically only when subjected to shear stress, it becomes important to apply external strains to the crystal to estimate its resistance against deformation. The strength of an ideal crystalline material is proportional to its elastic shear modulus [147, 148], while for a real solid, the strength is determined by lattice defects (dislocations and or point defects) and it is usually smaller than an ideal system. However, the shear stress needed for dislocation motion (Peierls stress) and thus for plastic deformation is also proportional to the elastic shear modulus of the deformed material. It was in 1998 when Teter argued that in many hardness tests one measures plastic deformation which is directly connected to the deformation of a shear character [22]. In particular he compared the Vickers hardness data to the bulk and shear moduli from many hard solids and found that the shear modulus of polycrystalline materials is a better hardness predictor than the bulk modulus (Fig. 8.6). Experimental bulk moduli can be obtained from the

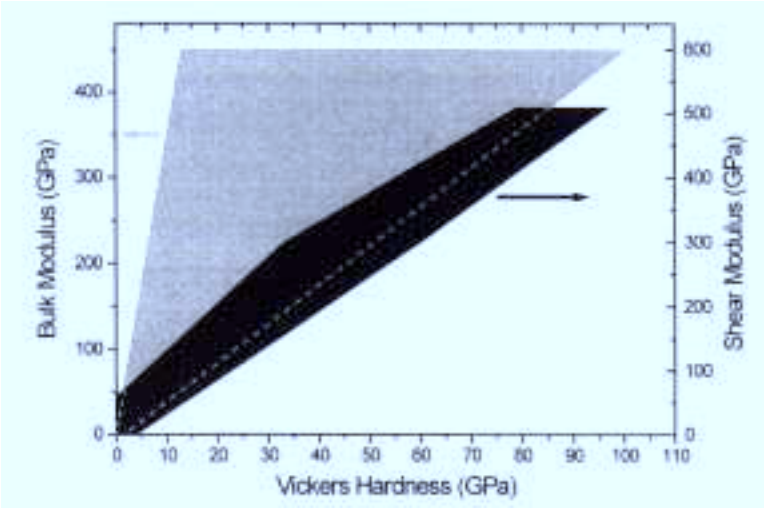

Figure 8.6: Figure from R. Riedel [149] showing the scattering of the Vickers hardness for hard materials when compared with bulk and shear moduli.

measurements of the volumes as a function of the pressure [113], while the single crystal elastic moduli can be estimated with Brillouin spectroscopy, inelastic neutron scattering, ultrasonic techniques or Schaefer-Bergmann method [150]. Once we know the complete set of the single crystal moduli, it is possible to derive the values of B and G of a polycrystalline material [151]. As shown in Tab. 8.6 the calculated elastic moduli give the possibility to express the hardness in form of isotropic shear modulus. As one may notice the hardness trend has been completely changed with respect to the one described in Tab. 8.5. The highest G value has been computed for the *bl*-C_3N_4 whereas the other model systems show an isotropic shear moduli in between 300 and 326 GPa. The two-dimensional phase (*graphitic*-C_3N_4) exhibits the lowest hardness with a shear modulus of 188 GPa. The major difference between the calculated bulk and shear moduli resides mostly in the fact that while, the B values are generally approaching or even exceeding that of diamond, the calculated G are at least 120 GPa lower. Therefore, it is very likely that diamond will remain the hardest known material with high elastic constants and the largest shear modulus [29], though various hypothetical C_3N_4 phases have shown very interesting properties. As a matter of fact, the value of G for the *bl*-C_3N_4 has been calculated to be quite close to that of *c*-BN (409 $\pm$6 GPa [22]), which is the second hardest known material.

The dependence of the elastic constants on the various different exchange-correlation choices is shown in Tabs. 8.7 and 8.8 for the US-PP method. As expected the LDA

	α- [152]	*β*- [114]	*cubic*- [29]	*bl*- [114]	*graphitic*- [114]	diamond [153]
c_{11}	576	834	863	840	870	1117 (1080)
c_{33}	700	1120	-	-	57	-
c_{44}	279	305	348	452	14	604 (557)
c_{12}	-31	279	313	213	148	137 (137)
c_{13}	-17	138	-	-	-3	-
c_{14}	-	-	-	-	-	-
c_{15}	-20	-	-	-	-	-
c_{66}	304		-	-	-	-
c_{46}	20	-	-	-	-	-
G	300	326	319	397	188	559 (523, 535 [22])
ρ	3.77	3.57	3.89	3.79	2.56	3.52

Table 8.6: Calculated elastic constants (c_{ij} in GPa), atomic densities (ρ in g/cm^3) and isotropic shear moduli (G in GPa) for five different C_3N_4 phases. Values in parenthesis refer to experimental measurements [8].

predicts larger bulk moduli compared to the tested GGA functionals. In particular, the best agreement with the experimental diamond bulk modulus has been obtained by using the PW91 and PB methods. However, in the case of diamond the set of c_{ij} calculated within the local density approximation agree reasonably well with the experimental elastic constants and in particular with values obtained from PW91 and PB calculations. It is also important to note that the LDA provides a very good description of the c_{12} modulus compared to the others tested GGA functionals. This confirm the general tendency of LDA to work well for stiffer materials. The estimated isotropic shear moduli result very similar to each other with G values confined within a difference of 16 GPa. For diamond, the ion relaxation does not bring any significant improving to the description of the elastic constants (cfr. values of the LDA_{frozen} and $\mathrm{LDA}_{relaxed}$ in Tab. 8.7). On the other hands, in the case of the hard *bl*-C_3N_4 the relaxation of the internal degrees of freedom results crucial for both bulk and elastic moduli. Generally, the relaxation of the internal atomic positions becomes necessary for those cases where the applied strain induces a significant reduction of the symmetry or when the atomic positions are not completely fixed by the space group symmetry.

8.2.5 Hexagonal and Orthorhombic *graphitic*-C_3N_4

The graphitic C_3N_4 structure has been considered as one of the possible forms for the carbon nitrides [115, 29, 154]. It is certain that such a model system is not likely to

diamond	exp.	LDA_{frozen}	$LDA_{relaxed}$	PW91	PB	PW86	LM
B	443	463.7	463.1	449.6	444.9	429.6	463.1
c_{11}	1080	1116.6	1111.3	1112.8	1110.2	1106.5	1158.9
c_{12}	137	137.2	138.9	118.0	112.2	91.1	115.2
c_{44}	557	604.3	603.5	606.0	604.7	612.9	611.0
G	523	559	557	563	562	571	575

Table 8.7: Calculated elastic constants (GPa) and bulk moduli (GPa) for diamond as a function of different exchange-correlation methods: Perdew-Wang 91 (PW91) [47], Perdew-Becke (PB) [46], Perdew-Wang 86 (PW86) [57], Langreth-Mehl-Hu (LM) [45]. The subscript "*relaxed*" and "*frozen*" denotes values calculated with or without the relaxation of the atomic positions.

bl-C_3N_4	LDA_{frozen}	$LDA_{relaxed}$	Ref.[114]	PW91	PB	PW86	LM
B	445.4	425.9	425	400.1	396.2	376.6	423.7
c_{11}	902.3	842.9	840	869.9	866.8	856.9	880.1
c_{12}	217.0	217.4	213	165.2	160.8	136.4	195.5
c_{44}	518.3	454.6	452	514.7	514.3	518.8	519.4
G	448	398	397	450	450	455	449

Table 8.8: Calculated elastic constants (GPa) and bulk moduli (GPa) for *bl*-C_3N_4 as a function of different exchange-correlation functionals.

show low compressibility due to the presence of weak inter-layer bonding. Nonetheless, its major interests arise from the possibility to represent a low energy model structure. In order to obtain the graphitic form of C_3N_4 two carbon atoms must be replaced with a single nitrogen in graphite with a consequent creation of a carbon vacancy. In the first model introduced by D. M. Teter and R. J. Hemley the vacancies are ordered in such a way that a hexagonal unit cell is found (Fig. 8.7). For this system different stacking ordering types were proposed leading to hexagonal [115, 29] or rhombohedral lattices [114, 115]. All these phases are based on the same order of the vacancies. However, very recently, I. Alves *et al.* [125] have introduced a new order of the carbon vacancies which leads to an orthorhombic unit cell (Fig. 8.8). This phase has been proposed after having analysed the X-ray data relative to samples obtained from the polycondensation of Melamine (Eq. 8.5) at 3 GPa and 800 °C.

$$C_3N_6H_6 \rightarrow C_3N_4 + 2NH_3 \tag{8.5}$$

For such a model system a different bonding conjugation is expected due to the par-

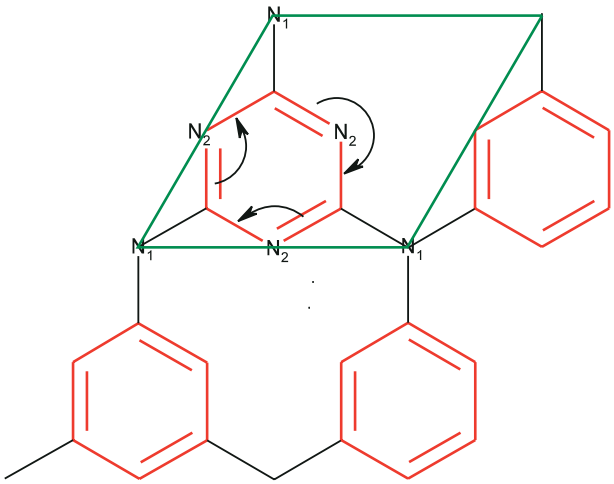

Figure 8.7: Electron circulation in the hexagonal *graphitic*-C_3N_4 model.

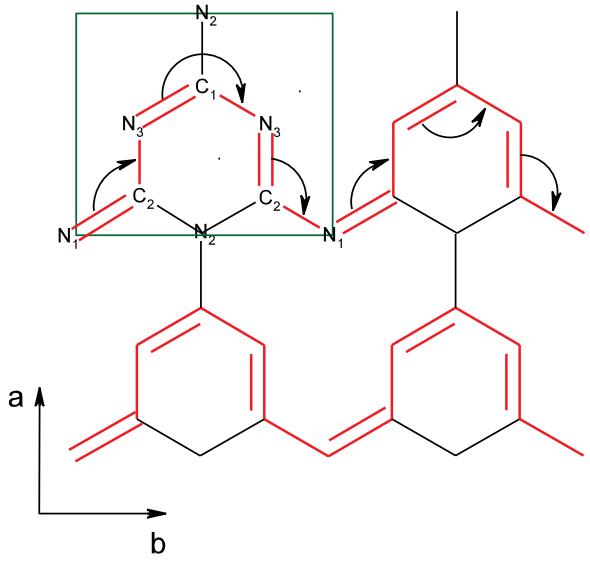

Figure 8.8: Electron circulation in the orthorhombic *graphitic*-C_3N_4 model.

ticipation of the nitrogen N_1 to the π-delocalisation along the b-axis (see Fig. 8.8). In particular, the double coordination of the N_1 atom allows the connection between the double bonds resonance located in the adjacent C_3N_3 rings, offering thus the possibility to show an electron delocalisation along the graphitic layer. On the contrary, the hexagonal phase shows a three coordinated N_1 atom which hinders the expansion of the electron delocalisation along the graphitic plane. In short, the hexagonal lattice possess a localised electronic resonance confined in each of the C_3N_3 rings while, the orthorhombic phase guarantee an extended electron delocalisation along the b-axis.

The purpose of this Section is to examine the stability and the electronic properties of the orthorhombic lattice with respect to the hexagonal one. The study is here finalised to the search of new stable layered model systems for carbon nitrides. In particular, the possibility of looking at the orthorhombic phase as a novel model for the C_3N_4 stoichiometry, has been accurately considered and theoretically justified in the following subsections. By using the pseudo-potential and the FP-LAPW LDA methods, the differences in the stability and in the electronic properties have been highlighted between the two lattices. For simplicity, the AAA stacking mode has been used for both lattice types. Further, the ASW method has been considered to describe the hybridisation influence on the chemical bonding inside the graphitic layer: the Crystal Orbital Overlap Population (COOP) analysis is presented.

Computational details

The calculations were carried out in the same framework of the DFT with the VASP plane wave pseudo-potential package [58]. The interactions between the ions and the electrons are described by using ultra-soft Vanderbilt pseudo-potential [61]. The parameterisation scheme used for the LDA is the Ceperley-Alder exchange-correlation potential [56]. A complete ions and volume relaxation was performed for the orthorhombic phase by using the conjugate-gradient algorithm [155] and an energy cut-off of 25.57 Ry for the plane wave basis set. The Methfessel-Paxton smearing scheme [156] was used for geometry relaxation while the tetrahedron method with Blöchl corrections [62] was implied for the total energy calculations. All the energies were converged with a **k**-point sampling using a 10×10×10 Monkhorst-Pack grid [63]. Accurates total energy calculations and electron density maps were also performed on the optimised structures by using the FP-LAPW method (WIEN97 package [68]). The number of plane waves per atom used was 172 and a total of 100 **k**-points were implied, with a 4×4×4 sampling. For carbon and nitrogen atom types the same muffin-tin radius was used (R_{mt}=1.33 Å).

A qualitative stabilisation feature was also assessed using the chemical bonding criteria. The COOP were evaluated for the two graphitic-like C_3N_4 systems by using the ASW-LDA method [120, 74]. Calculations were performed by applying the tetrahedron method for the **k**-space integration and 217 irreducible **k**-points generated from a uni-

form 12×12×12 mesh according to the Monkhorst-Pack scheme. It has to be noted that the energy convergence criterion of $\Delta E=10^{-8}$ Ry is in the ASW more precise than in FP-LAPW ($\Delta E=10^{-5}$ Ry) because of the faster method in use.

Geometry optimisation

The geometry of the orthorhombic phase was taken from the original work of I. Alves and for the sake of simplicity the AAA stacking order was considered. This phase consists of 7 atoms per unit cell and belongs to the P2mm space group. The optimised geometry of the hexagonal phase was taken from the early works [115, 29] and an AAA stacking of the layers was assumed. In both unit cells, each C atom is three-fold coordinated as is one of the four N atoms per cell, while the other three N atoms are two-fold coordinated. As it can be seen from Figs. 8.7 and 8.8, a different vacancy ordering inside the graphitic planes is found for the orthorhombic system with respect to the hexagonal one.

Starting from the geometry given by [125], the orthorhombic structure was optimised by using the US-PP method. Tab. 8.9 shows the structural parameters relative to the orthorhombic phase before and after the full geometry optimisation. The most striking

	Starting geometry	Optimised structure (US-PP)
Space group	P2mm	P2mm
Parameters (Å)	a=4.1, b=4.7, c=3.2	a=4.1197, b=4.7105, c=3.1233
Atomic positions	N_1 (1a) (0.000 0.000 0.000)	N_1 (-0.021 0.000 0.000)
	N_2 (1c) (0.000 0.500 0.000)	N_2 (0.009 0.500 0.000)
	N_3 (2e) (0.500 0.250 0.000)	N_3 (0.505 0.258 0.000)
	C_1 (1c) (0.333 0.500 0.000)	C_1 (0.351 0.500 0.000)
	C_2 (2e) (0.833 0.750 0.000)	C_2 (0.824 0.757 0.000)

Table 8.9: Structural parameters for the orthorhombic structure with AAA stacking order.

modification found in the relaxed structure is the changing of the geometry relative to the C_3N_3 heterocycle. These rings are now no more symmetric as they were before the structural relaxation. A shortening in the interlayer distance from 3.20 Å to 3.12 Å is also found in the optimised system. A brief summary of the most important geometry changing in the orthorhombic phase is shown in Tabs. 8.10 and 8.11. The atomic labeling scheme is given in Fig. 8.8. It is important to note that the optimisation of the hexagonal phase under the same conditions still leads to a symmetric geometry of the C_3N_3 rings. The schematic differences between the two optimised structures are drawn in Fig. 8.9.

	Starting geometry	Optimised structure (US-PP)
Bond lengths (Å)	d(N_1-C_2)=1.359	d(N_1-C_2)=1.311
	d(C_2-N_2)=1.359	d(C_2-N_2)=1.431
	d(C_2-N_3)=1.365	d(C_2-N_3)=1.316
	d(C_1-N_3)=1.359	d(C_1-N_3)=1.305
	d(N_2-C_1)=1.365	d(N_2-C_1)=1.409

Table 8.10: Bond lengths before and after the optimisation of the orthorhombic structure.

	Starting geometry	Optimised structure (US-PP)
Angles (°)	N_1-C_2-N_3=120.23	N_1-C_2-N_3=122.23
	N_1-C_2-N_2=119.54	N_1-C_2-N_2=118.65
	N_3-C_2-N_2=120.23	N_3-C_2-N_2=119.12
	C_2-N_3-C_1=120.23	C_2-N_3-C_1=122.18
	N_3-C_1-N_3=119.54	C_2-N_3-C_1=121.80
	C_2-N_2-C_2=119.54	C_2-N_2-C_2=115.62
	C_2-N_1-C_2'=119.54	C_2-N_1-C_2'=121.69
	C_2-N_2-C_1'=120.23	C_2-N_2-C_1'=122.19

Table 8.11: Angles before and after the optimisation of the orthorhombic structure. The notation prime refers to atoms belonging the adiacent unit cell.

Relative stability between the two graphitic forms

The FP-LAPW and US-PP methods agree quite well with each other in predicting a comparable stability between the orthorhombic and the hexagonal models. Tab. 8.12 list all the calculated cohesive energies for the two structures. Although the energy reference is not the same for the two methods (core states are not included in the pseudo-potential method), the energy difference between the two forms show values of similar order of magnitude, in favour of the orthorhombic variety. The very small difference in stability let us confirm the possibility of looking at the orthorhombic phase as a reasonable model for describing the *graphitic*-C_3N_4.

The stabilisation features can be further assessed using chemical bonding criteria based on the crystal orbital overlap populations [157] which consist of the expectation values from operators of the non-diagonal elements of the overlap population matrix,

$$c_{ni}^{*}(\mathbf{k})\, S_{ij} c_{nj}(\mathbf{k}) \quad = \quad c_{ni}^{*}(\mathbf{k}) \left\langle \chi_{\mathbf{k}i}(\mathbf{r}) \left| \chi_{\mathbf{k}j}(\mathbf{r}) \right\rangle c_{nj}(\mathbf{k}) \right. \tag{8.6}$$

where S_{ij} represents an element of the overlap matrix of the basis functions and the

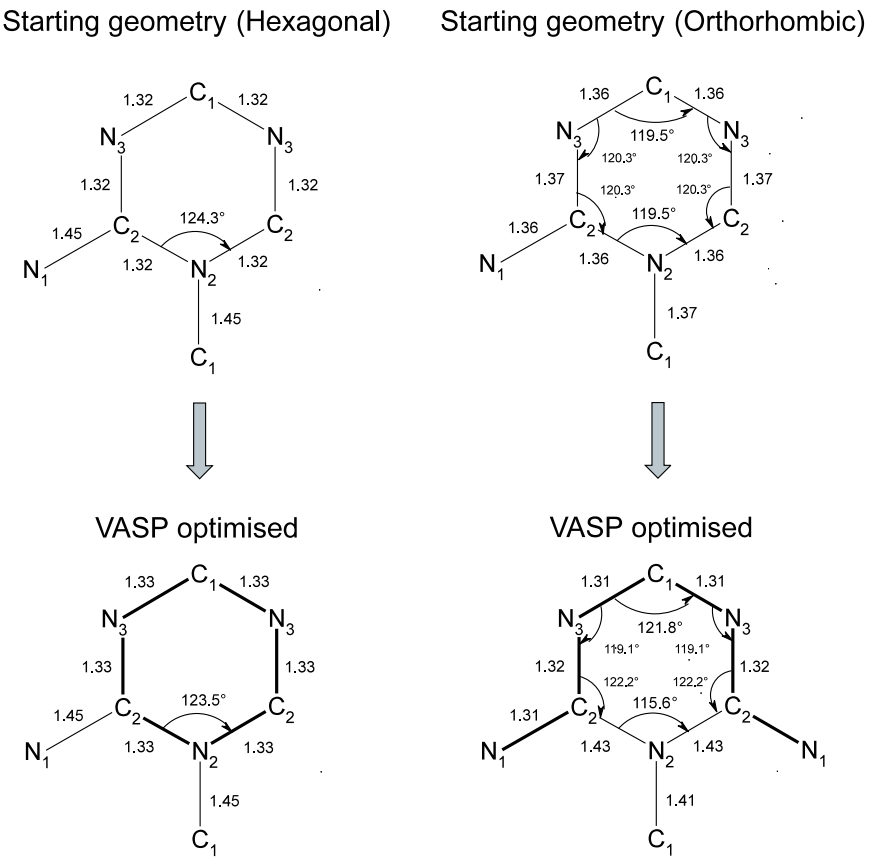

Figure 8.9: The above figure shows the general differences in the ring's geometry for the orthorhombic and hexagonal unit cells.

$c_{nj}(\mathbf{k})$ are the expansion coefficients entering the wave function of the n^{th} band (Eq. 8.7).

$$\psi_{\mathbf{k}}(\mathbf{r}) = \sum_i c_i(\mathbf{k})\,\chi_{\mathbf{k}i}(\mathbf{r}) \tag{8.7}$$

Partial COOP coefficients $C_{ij}(E)$ are then obtained by integrating the expression (8.6) over the Brillion zone:

$$C_{ij}(E) = C_{ji}(E) = \frac{1}{\Omega_{BZ}} \sum_n \int_{\Omega_{BZ}} d^3\mathbf{k} Re\left(c^*_{ni}(\mathbf{k})\, S_{ij} c^*_{nj}(\mathbf{k})\right) \delta\left(E - \varepsilon_{n\mathbf{k}}\right) \tag{8.8}$$

	FP-LAPW method			
Structure	LDA	PBE	PW91	US-PP/LDA
Hexagonal	-6.88990	-6.04012	-6.03002	-9.26143
Orthorhombic	-6.89044	-6.04070	-6.03059	-9.26174
$\|\Delta E\|$	$5.4 \cdot 10^{-4}$	$5.8 \cdot 10^{-4}$	$5.7 \cdot 10^{-4}$	$3.1 \cdot 10^{-4}$

Table 8.12: FP-LAPW and US-PP cohesive energies (eV/atom) for the orthorhombic and hexagonal lattices.

(Dirac function delta serving as a counter of states) which is often loosely designated as the overlap-population-weighted-DOS. Starting from Eq. (8.8), the total COOP are then evaluated as the sum over all non-diagonal elements,

$$C(E) = \sum_{ij, i \neq j} C_{ji}(E). \tag{8.9}$$

The above calculational procedure has been specifically implemented in the ASW method by Dr. V. Eyert of the University of Augsburg to enable for precise chemical bonding determinations from self consistent calculations. For a detailed description and for significant examples the reader is referred to the following papers [120, 74, 118]. The COOP curves are positive when they describe bonding states and negative (negative terms in Eq. (8.8)) when they describe anti-bonding states; non-bonding states should exhibit very low intensity-COOP. In order to get more insight into the chemical stability, in the following Section, it has also been proposed the calculation of the integrated COOP (ICOOP) which is defined as follow,

$$\overline{C}(E') = \int_{-\infty}^{E'} dEC(E). \tag{8.10}$$

The total and integrated COOPs for the hexagonal and the orthorhombic phases are shown in Fig. 8.10 and Fig. 8.11, respectively. The two phases nearly show the same trend in the total COOP; in the lower energy region of the valence band the two curves are mainly of bonding character, while at energies closer to the Fermi level the antibonding states of the *p*-orbitals start to dominate. The antibonding counterparts are found in the conduction band centred at 2 and 7 eV while a bonding behaviour appears at higher energy. Due to the larger electron delocalisation present in the orthorhombic lattice the smearing out of the curve is somehow found with respect to the COOP of the hexagonal system. The projection of the total COOP onto the corresponding contributions arising from the different atoms (Fig. 8.12) clearly shows that in the lower region of the valence

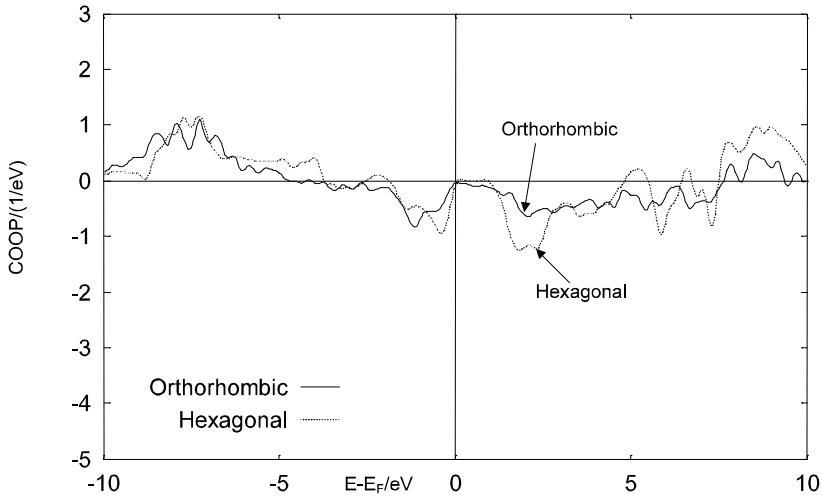

Figure 8.10: Total COOP for the hexagonal and the orthorhombic phases (ASW).

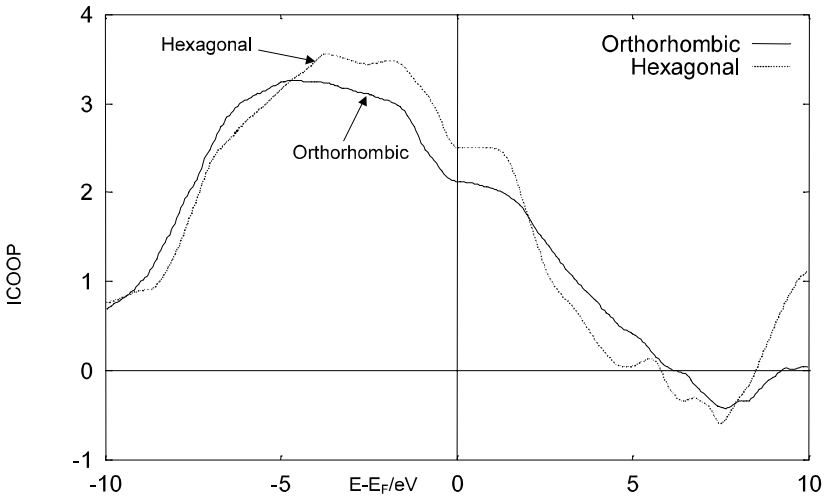

Figure 8.11: Integrated COOP for the hexagonal and the orthorhombic systems (ASW).

band (VB) the interaction N_3-C_1 determines the positive contribution to the COOP even if all the other carbon-nitrogen interactions are showing a bonding character. At

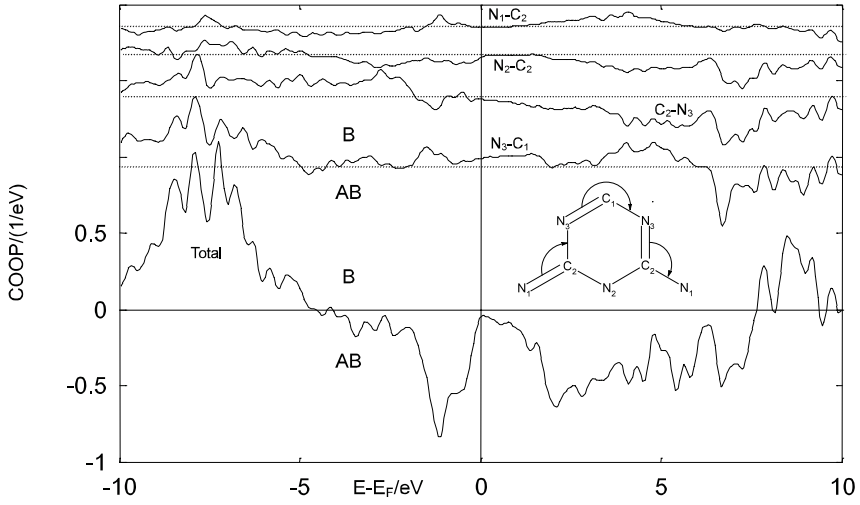

Figure 8.12: Total COOP for the orthorhombic phase (ASW). For clarity each nitrogen-carbon interactions have been shifted along the vertical axis. The labels B and AB define the bonding and the antibonding region, respectively.

energy close the E_F the main bonding character is found for the interactions N_3-C_1 and N_1-C_2 while N_2-C_2 and C_2-N_3 show a negative COOP. The description of the bonding within the layer seems to favour a sort of "*snake-like*" delocalisation in as far as the N_3-C_1 and the C_2-N_3 globally display a positive interaction throughout the valence region. However, this shows the difficulty of carrying out this analysis to the point of making it resemble to the picture expected by a chemist in his view of the resonant bonds. Such restriction is mainly due to the fact that COOP analysis does not use directional orbitals view since all contributions from p_x, p_y and p_z are included. As shown in Fig. 8.10 the orthorhombic phase is predicted to be slightly more stable than the hexagonal system. This can be addressed to the lower intensity of the anti-bonding states close to the Fermi level. By contrast, the integrated COOP of Fig. 8.11 has shown a sensible advantage for the hexagonal model (cfr. bonding-states in the region between -5 and 0 eV). Therefore, even though the investigation of the COOP represents an important step in predicting the relative stability of different phases, it has here been shown that the discrimination of the two phases cannot only be assessed qualitatively. Nonetheless, it is relevant to stress that accurate full potential calculations performed on the same systems have also shown very small energy differences in favour of the orthorhombic phase (Tab. 8.12).

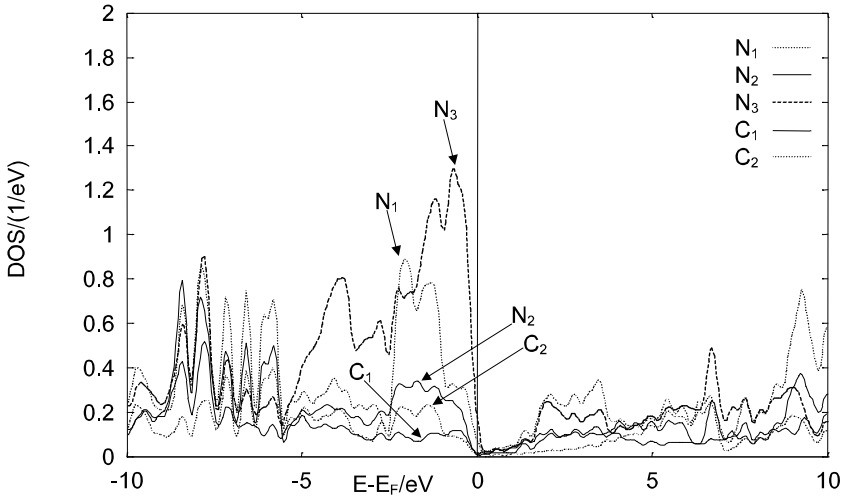

Figure 8.13: Site projected DOS plot for the AAA orthorhombic graphitic phase (ASW). The energy reference along the x-axis is taken with respect to the Fermi level; the y-axis gives the DOS per atom and unit energy.

In any case, it can be concluded that the orthorhombic system result stable enough to be considered as one of the most reasonable models for the description of the layered *graphitic*-C_3N_4.

Electronic properties

The DOS plot calculated with the ASW method for the orthorhombic phase (Fig. 8.13) clearly shows that a semi-metallic behaviour is present in this new graphitic C_3N_4 form. The electronic levels are now crossing the Fermi energy and a more significant contribution of the electronic states from the N_1 atom is found at the E_F (compare with N_1 peak in Fig. 8.14). In contrast to the band gap of 0.938 eV calculated for the hexagonal form, a semi metallic-like behaviour is thus found in the orthorhombic phase. Moreover, the nitrogen DOS in the orthorhombic structure is broadened with respect to the DOS of the hexagonal one (Fig. 8.14). This behaviour can be addressed to the strong role played by the N_1 atom in mediating in between neighbouring heterocycle rings. With the help of the FP-LAPW method the change in the electronic properties can also be visualised by looking at the electron density maps. The orthorhombic system shows a clear delocalisation of the charge density along the direction of the b-axis with a sort of snake-like shape (Fig. 8.15). Using the same method of calculation, the total density of states shows, for the orthorhombic phase (Fig. 8.16), an increasing metallic behaviour.

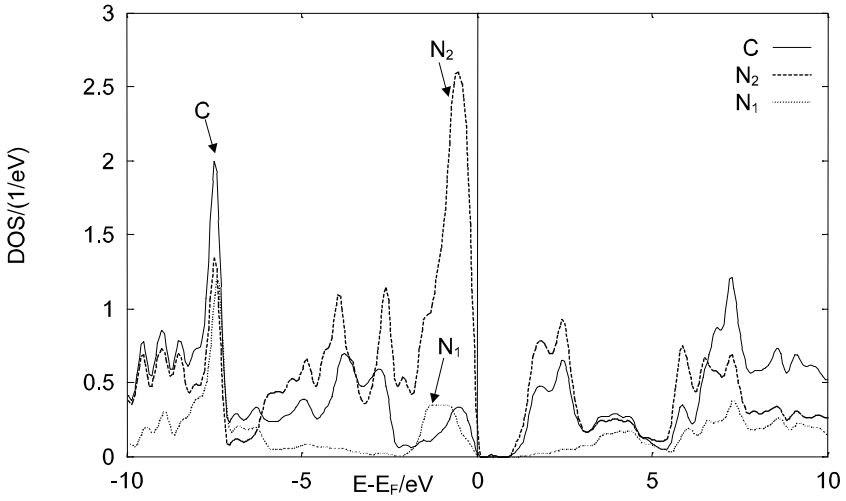

Figure 8.14: Site projected DOS for the hexagonal graphitic model system (ASW).

In particular, the electronic states of the nitrogen and the carbon atoms are crossing the E_F as already stressed in the total DOS calculated with the ASW approach. For the hexagonal system the calculated electronic density map shows a confined electronic circulation inside the C_3N_3 rings [118]. A band gap of 1.48 eV is found in the total DOS analysis (Fig. 8.17). The two methods of calculation confirm the previous hypothesis of I. Alves *et al.* about a drastic modification on the electronic properties.

8.2.6 Calculation of the ^{13}C NMR chemical shifts

As already discussed, a recent interpretation of the X-ray diffraction pattern made on the graphitic-like sample prepared via bulk chemistry [125, 126] has suggested the existence of a possible orthorhombic system. However, the investigation of the crystal structure is not yet concluded and further efforts are needed to state clearly whether the unit cell could be hexagonal or orthorhombic. Therefore, it becomes of fundamental interest the possibility to provide theoretical spectroscopic properties able to discriminate between the two different forms. The synthesis of carbon-13 enriched samples is actually under investigation in different laboratories to provide insight on the ^{13}C NMR shielding. Nevertheless, due to the high cost needed to prepare carbon enriched samples and to the difficulty to obtain pure crystalline materials, the related ^{13}C chemical shifts are nowadays still unknown.

In this subsection the theoretical calculation of the magnetic shielding tensor, Eq.

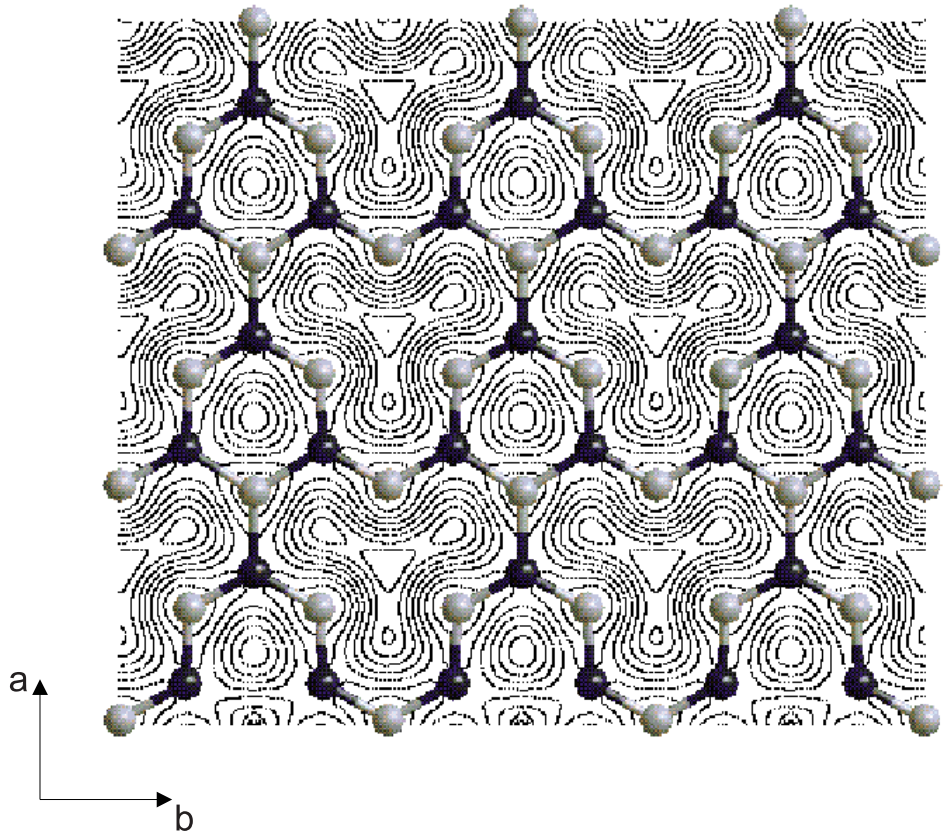

Figure 8.15: Valence electron density map for the orthorhombic *graphitic*-C_3N_4 model system (FP-LAPW).

8.11, has been computed for both the hexagonal and the orthorhombic phases.

$$\sigma_{uv}(N) = (\partial^2 E/\partial_{B_u}\partial_{\mu_{Nv}})_{B=0,\mu=0} \tag{8.11}$$

Since the chemical shift depends on the electron density about a given nucleus (*i.e* shielding), it is thus expected that the different electronic circulation present in the two model phases could give rise to a sensible variation on the respective NMR signals.

Method and computational details

In this theoretical approach it has been employed the GAUSSIAN98 molecular calculation package [158] with an implemented Gauge Independent Atomic Orbital (GIAO) method

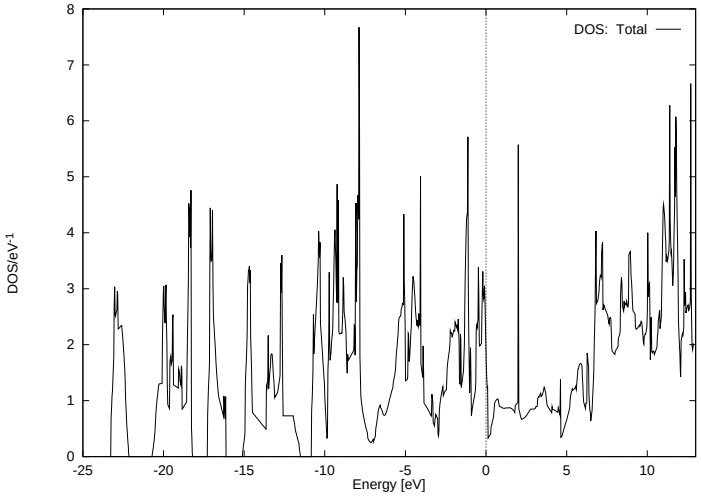

Figure 8.16: Total DOS for the orthorhombic phase (FP-LAPW). Notice the absence of energy gap at the top of the VB.

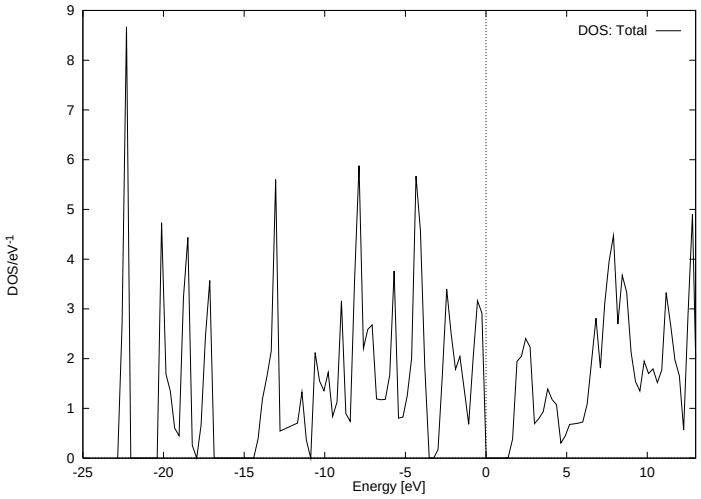

Figure 8.17: Total DOS for the hexagonal phase (FP-LAPW).

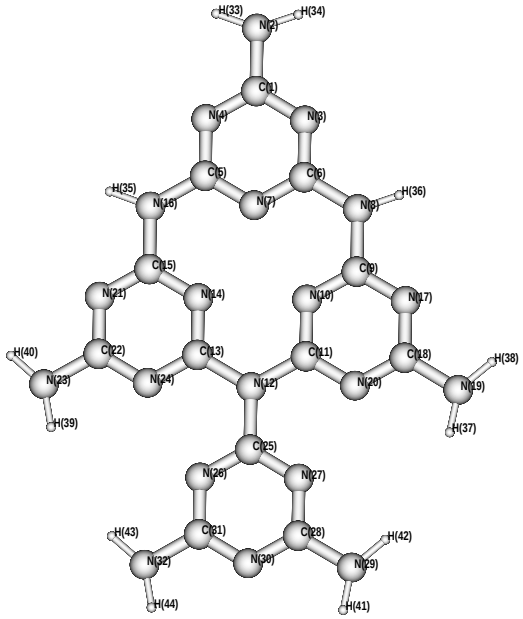

Figure 8.18: Molecular cluster relative to the hexagonal *graphitic*-C_3N_4.

[159] for the *ab initio* self-consistent-field calculation of the nuclear magnetic resonance chemical shifts. In particular, the 6-311G* basis set has been used with the Perdew-Wang (PW91) [160] functional [9]. The molecular input was created for each of the investigated phases by using a well defined *graphitic*-C_3N_4 cluster. The optimised solid state geometry (US-PP method) has been cut into 2×2×0 cells and the edges have been closed with hydrogens to guarantee the electron neutrality. The obtained clusters are shown in Figs. 8.18 and 8.19 for the hexagonal and the orthorhombic system, respectively. Hydrogens have been relaxed and the amount of the residual forces present on the atoms have also been checked.

Comment of the results

The calculated isotropic shieldings are provided in Tab. 8.13 with respect to the standard tetramethyl silane (TMS). The carbon chemical shift relative to the hexagonal phase has been estimated by taking the mean values between atoms belonging the symmetric C_3N_3 ring (*i.e.* C(11), C(13) and C(25)) while in the orthorhombic phase we have averaged the

[9] Calculations were performed in collaboration with Prof. H. Ågren and Dr. B. Schimmelpfennig at the Department of Theoretical Chemistry, Royal Institute of Technology, Stockholm (Sweden).

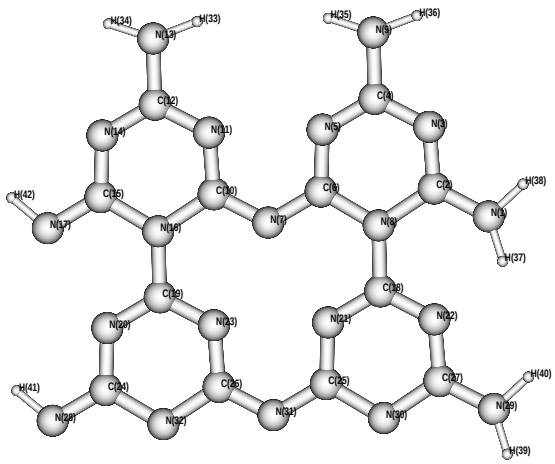

Figure 8.19: Molecular cluster relative to the orthorhombic *graphitic*-C_3N_4.

^{13}C shifts of atoms along the two snake-like paths (C(06), C(10), C(18) and C(19). The chemical shifts related to carbons which have hydrogens in the second nearest neighbour positions (the edges of the cluster) have been neglected (*e.g.* C(4), C(12), C(25), C(26), C(24), C(27), C(2) and C(15)). That is, it has only been accounted for an averaged ^{13}C chemical shift by weighting only the cluster's atoms which have a carbon-nitrogen environment similar to the original periodic structure. As shown in Tab. 8.13 a difference of about 15 ppm has been found in the chemical shifts of the carbon atoms constituting the symmetric rings with respect to those belonging the snake-like electron density path[10]. Therefore, calculations suggest that the discrimination between the two phases should be, *a priori*, feasible by measuring the ^{13}C NMR chemical shift in graphitic-like samples.

8.2.7 Conclusions

Using three different first-principles techniques, it has been examined a series of hypothetical C_3N_4 phases to determine their stability and hardness. With the use of FP-LAPW method the relative energy trend has been computed to be in good agreement with the former PP calculations. The *graphitic*- and α-C_3N_4 phases are predicted to have the lowest total energies and the highest compressibilities, while the two cubic phases are energetically less stable but with larger bulk moduli. On the contrary, the ASA based

[10] This result is in very good agreement with the latest measurements of the ^{13}C NMR shifts for a polymorphic graphitic-like C_3N_4 samples (private communication from Dr. M. Ménétrier).

	Isotropic shielding (^{13}C)	
Atomic labelling	hexagonal	orthorhombic
C(11)	169.3	-
C(13)	169.3	-
C(25)	168.7	-
Mean value	*169.1*	-
C(06)	-	154.0
C(10)	-	154.1
C(18)	-	154.4
C(19)	-	154.2
Mean value	-	*154.2*

Table 8.13: Calculations of the ^{13}C NMR chemical shift (ppm) for the two graphitic-like phases. For the reference TMS it has been estimated, with the same computational approach, a chemical shift of 184.4 ppm.

LMTO and ASW methods cannot reproduce a reasonable energy trend due to the difficulty of describing phases with different atomic densities. The ASA approximation fits quite well for the cubic structures but it does not for less compact systems such as that of the graphitic-like. However, even though it is not possible to compare the relative stabilities, LMTO and ASW techniques reproduce the lattice constants and the bulk moduli in close accordance with the FP-LAPW and PP methods. As a matter of fact, all the three methods predict the highest B for the *cubic*-C_3N_4 and the lowest one for the α-C_3N_4. This demonstrates that all the employed DFT codes are suitable for simulating the bulk modulus of carbon nitrides. However, according to the finding of D. M. Teter a different hardness trend has been calculated by using the magnitude of the isotropic shear modulus as an indicator. The three-dimensional *bl*-C_3N_4 phase now shows the highest G value, whereas the α-C_3N_4 has the lowest one. Following this more accurate approach, all the investigated C_3N_4 crystals behave as hard and elastic materials, though their mechanical properties are always predicted to be subordinated to those of diamond.

The enthalpy for the formation reaction, $\Delta H^o_{f,0}$, has been calculated for the layered C_3N_4 phase (the most stable form for carbon nitrides with C_3N_4 stoichiometry) to be of the order of 177 kJ/mol. This result indicates that a thermodynamically stable graphitic-like C_3N_4 system could in principle be synthesised by using high temperature and high pressure reaction. Moreover, since an important activation energy should be required to break the C-N bonds, it is reasonable to believe that a substance with C_3N_4 composition could be isolated in a metastable form even at ambient conditions.

The optimisation of the orthorhombic phase with the US-PP method has led to

an asymmetric equilibrium structure for the "C_3N_3" rings of the *graphitic*-C_3N_4. A shortening of the carbon-nitrogen bonds has been found along the snake-like path owing to the π-delocalisation along the b-axis. The calculated FP-LAPW electron density map has also confirmed the possibility for the orthorhombic phase to extend its electron delocalisation to the adjacent C_3N_3 rings. This behaviour is mainly due to the changing of the coordination number for the N_1 atom which goes from three in the hexagonal lattice to two in the orthorhombic phase. The DOS analysis performed with the FP-LAPW and ASW methods has shown an increased semi-metallic behaviour for the orthorhombic system: the electronic states are crossing the E_F and the band gap disappears. Moreover, the FP-LAPW and US-PP methods agree quite well each other in predicting a small energy difference between the hexagonal and the orthorhombic phases. Both lattice systems seem to be a reasonable proposal for the *graphitic*-C_3N_4 model, though a clear changing in the electronic properties has been found for the orthorhombic structure. Finally, from molecular calculations the ^{13}C NMR shifts have been evaluated for both model systems. A high-field shifting of about 15 ppm was calculated for the orthorhombic phase. Such an increased shielding is attributed to the very different electron density flows present in the two graphitic-like forms. These phases could be thus likely discriminated via NMR analysis at the experimental level.

However, despite the outcome of this work we still need to meet furthermore the experimental findings as to the low concentrations of nitrogen found in the carbon nitride films. These observations have led to the proposal of carbon nitrides with $C_{11}N_4$ composition. Its thorough study within the same framework is shown in the next Section.

8.3 The isoelectronic $C_{11}N_4$ model system

8.3.1 Introduction

The characterisation of carbon nitride films with stoichiometry C_3N_4 is heavily restricted by the problem of getting pure crystalline samples with the right C/N ratio. However, thin films with lower nitrogen concentration (5-25 %) have been found relatively easier to deposit, for example, with reactive magnetron sputtering. It is also in this range of nitrogen content that the recently discovered *graphitic-like* $\rightarrow$ *fulleren-like* transition has been suggested to take place. Therefore, in order to add more information to the above experimental evidence, it is important to use theoretical tools to characterise carbon nitride model structures with an higher ratio of C/N, such as that of $C_{11}N_4$. It becomes thus relevant to investigate the role played by the nitrogen concentration in determining the stability, hardness and electronic properties of the CN_x compounds. For the sake of simplicity it has here been compared the C_3N_4 and $C_{11}N_4$ systems, which are isoelectronic to each other. For this purpose two $C_{11}N_4$ phases, namely α and β, have been presented and investigated with density functional theory methods within the local

density approximation. These phases contain less than ~ 30 % of nitrogen than the well known C_3N_4 stoichiometry and are formally derived from the so-called pseudo-cubic form of C_3N_4 (*i.e.* *bl*-C_3N_4). Cohesive properties, bulk and elastic moduli have been calculated and a full detailed analysis of the DOS and Energy Loss Near Edge Structure (ELNES) is presented. Calculations suggest that the lowering of the nitrogen concentration does not prevent the finding of ultra-hard materials and indeed brings a significant increase in the cohesive energy and hardness of carbon nitrides.

8.3.2 Methods and computational details

Calculations of the optimised geometries, relative stability and elastic constants were performed *ab initio* within the local density approximation to the density functional theory using the Ceperly-Alder [56] exchange correlation functional as parameterised by Perdew and Zunger [60] and the US-PP method [61, 58]. The calculations were computed by using an energy cut-off of 434.8 eV for the planewave basis set and converged with respect to the **k**-point integration. The tetrahedron method with Blöchl corrections [62] was applied for both geometry relaxation and total energy calculations. Brillouin-zone integrals were approximated using the special **k**-point sampling of Monkhorst and Pack [63]. The investigation of the density of states and of the Electron Energy Loss Spectroscopy (EELS) spectra were carried out with the density functional theory FP-LAPW program [68]. The local spin density approximation according to Perdew and Wang was employed [47]. The planewave cut-off was adjusted so that approximately 145 planewaves per atom were used for the phases with $C_{11}N_4$ stoichiometry. The differences in total energies were converged to below 0.001 eV with respect to **k**-points integration. For carbon and nitrogen atom types the same muffin-tin radius (R_{mt}=1.35 Å) was used and maintained fixed for all the investigated structures. Only for the graphitic $C_{11}N_4$ model a relatively smaller R_{mt} value of 1.24 Å was employed. For diamond, graphite and the other isoelectronic C_3N_4 phases the amount of **k**-points and cut-off parameter were in accordance with our previous calculations (cfr. Section 8.2 and Ref. [117]).

8.3.3 The analysed crystalline structures

In order to investigate the different properties of the C_3N_4 and $C_{11}N_4$ stoichiometries it has here been presented a cross-checking between two different forms of carbon nitrides: the stable two-dimensional graphitic phase and the hard three-dimensional pseudo-cubic system. First of all, the graphitic form has been chosen because representative for a stable layered CN_x network whereas the pseudo-cubic form stands for an hard three-dimensional system. Secondly, since many sp^3-bonded C_3N_4 phases have been proposed in the early works [29, 115, 114], as a starting point of our investigation we thought worthwhile to focus the attention only on certain phases for which the generation of the

analogous $C_{11}N_4$ stoichiometry can be easily figured out, for example, by simply doubling the length of one of the unit cell vectors. The pseudo-cubic system results as a perfect example of a three-dimensional C_3N_4 phase from which the corresponding $C_{11}N_4$ can be readily generated without any drastic increase of the number of inequivalent atoms per unit cell. Further details are given separately in the following subsections for each of the analysed CN_x forms.

The graphitic and pseudo-cubic C_3N_4

The graphitic-like structure (*graphitic*-C_3N_4) has been theoretically predicted to be the most stable C_3N_4 phase [29, 117, 118, 115, 114]. For simplicity, the same intra-layer geometry as in the hexagonal structure (ABA stacking) introduced by Teter *et al.* [29] has been assumed in our graphitic-like model. Inside the layer each of the C atoms is three-fold coordinated as is one of the four N atoms per cell, while the other three nitrogens show a two-fold coordination (see Fig. 8.2). The whole system was fully relaxed with the pseudo-potential method assuming an AAA packing sequence between the sheets. Such relaxation was required in order to adapt the intra-layer geometry to the new stacking order. Despite the fact that the AAA packing is not the most energetically stable form, it has been explicitly chosen to stack the layers directly on top of each other to enable an easier comparison of the results with the analogue graphitic-like $C_{11}N_4$ form. As a matter of fact, a graphitic-like $C_{11}N_4$ system with a stacking sequence ABA or ABC would have led to a larger number of inequivalent atoms per unit cell, yielding thus to an enormous increasing of the calculational time. Beside this, since the total energy interaction found in between the layers is weak (as in the case of graphite) it has been finally decided to compare the two graphitic-like stoichiometries by assuming a common AAA packing of the sheets.

The pseudo-cubic structure (*bl*-C_3N_4) shown in Fig. 8.20 is usually called "*defect zinc-blende*" and exhibits a $P\bar{4}3m$ symmetry and contains 7 atoms per unit cell [29, 114]. This phase has been previously predicted by A. Y. Liu *et al.* [114] by substituting carbon and nitrogen in the pseudo-cubic α-$CdIn_2Se_4$ [161]. Since the *bl*-C_3N_4 originally optimised by A. Y. Liu in Ref. [114] has shown some residual forces in our pseudo-potential code, it has been decided to fully relax again the system for better results. The new optimised geometry is now shown in Table 8.14.

The *graphitic*-, α- and β-$C_{11}N_4$ phases

The *graphitic*-$C_{11}N_4$ depicted in Fig. 8.21 has been theoretically introduced in our Institute by A. Snis *et al.* in 1999 [162, 163]. This phase is isoelectronic with diamond and C_3N_4 [117] and has been suggested as a possible hard material [104]. The configuration with layers in a stacking sequence AAA has been fully geometry optimised with

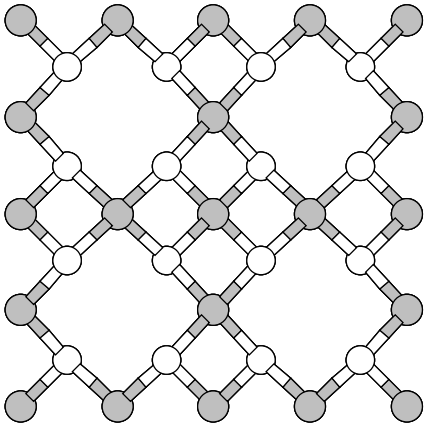

Figure 8.20: Ball and stick model of the *bl*-C_3N_4 structure. Figure shows the projection of the atoms along the [001] plane.

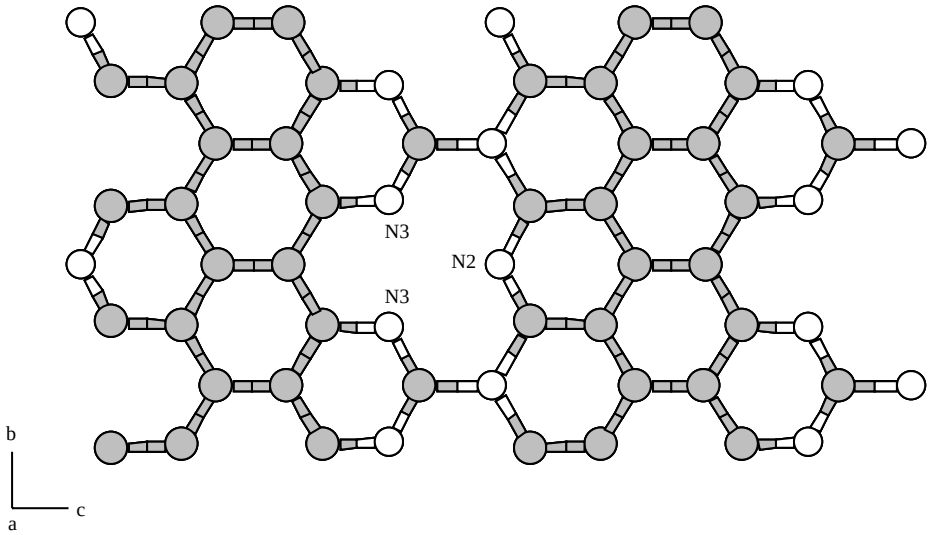

Figure 8.21: One layer of the *graphitic*-$C_{11}N_4$ model phase.

bl-C_3N_4	β-$C_{11}N_4$	α-$C_{11}N_4$
Cubic	Orthorhombic	Tetragonal
P$\overline{4}$3m (215)	P222 (16)	P$\overline{4}$2m (111)
7	15	15
C_1(0.5000, 0.5000, 0.0000)	C_1(0.5000, 0.5000, 0.2559)	C_1(0.0000, 0.5000, 0.2575)
N_1(0.2553, 0.2553, 0.2553)	C_2(0.0000, 0.5000, 0.5000)	C_2(0.0000, 0.0000, 0.0000)
	C_3(0.0000, 0.0000, 0.2793)	C_3(0.5000, 0.5000, 0.0000)
	C_4(0.2315, 0.2368, 0.1392)	C_4(0.2552, 0.2552, 0.1281)
	C_5(0.0000, 0.5000, 0.0000)	C_5(0.0000, 0.0000, 0.5000)
	C_6(0.0000, 0.0000, 0.0000)	N_1(0.2355, 0.2355, 0.6254)
	N_1(0.7568, 0.2680, 0.3803)	
a=b=c=3.4087	a=3.4454	a=b=3.4944
	b=3.5540	
	c=7.2394	c=6.9004
90, 90, 90	90, 90, 90	90, 90, 90

Table 8.14: Optimised parameters for the *bl*-C_3N_4 and the α-, β-$C_{11}N_4$ phases. The table shows crystal system, space group, atoms·unit cell^{-1} and the atomic positions. Cell constants are expressed in unit of Å and the angles α, β, γ in degrees.

the same *ab initio* pseudo-potential planewave program [58]. The resulting geometry is listed in Tab. 8.15. It is certain that such a model system is not likely to show low compressibility due to the presence of weak inter-layer bonding. Nonetheless, its major interests arise from the possibility to represent a low energy carbon rich model structure. The pseudo-cubic $C_{11}N_4$ configuration has been obtained from the analogue pseudo-cubic C_3N_4 phase by simply doubling the unit cell along the *a*-lattice vector. In order to reach the right stoichiometry one carbon has been added in the middle of the second cell, while the four nitrogen atoms, constituting the "*nitrogen-hole*", have been substituted with four carbons [164]. This phase is here called α-$C_{11}N_4$ (Fig. 8.22). Following the same procedure but performing a slightly different atomic substitution, another phase called β-$C_{11}N_4$ can be obtained (Fig. 8.23). The relaxation of the three-dimensional phases gives the final optimised geometries as shown in Table 8.14.

8.3.4 Relative stability and phase transitions

There is no doubt that one of the most important effects in determining the stability of carbon nitrides is the role played by the non-bonded N-N repulsions. These unfavorable electrostatic interactions have already been demonstrated to be relevant in accounting for the stability of some of the C_3N_4 phases [165, 138]. In fact, an interesting attempt to

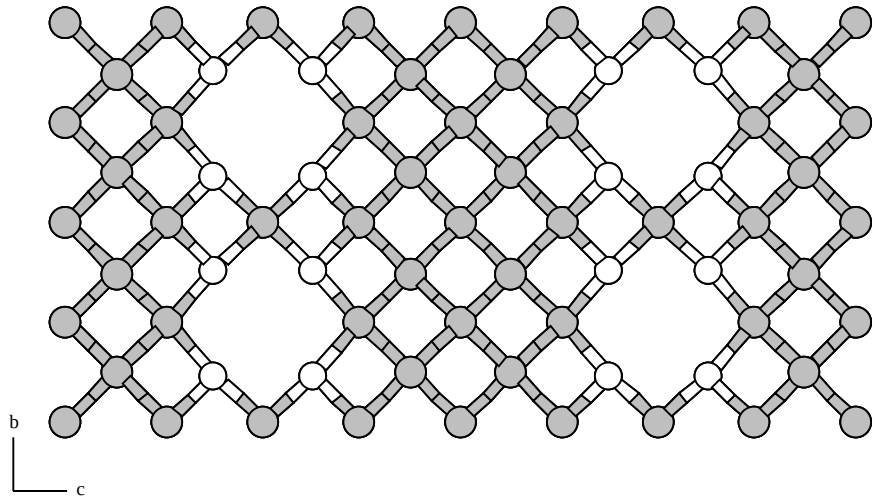

Figure 8.22: Crystal structure of the tetragonal $\alpha - C_{11}N_4$. Projection along the [100] plane exhibiting the "*nitrogen-hole*".

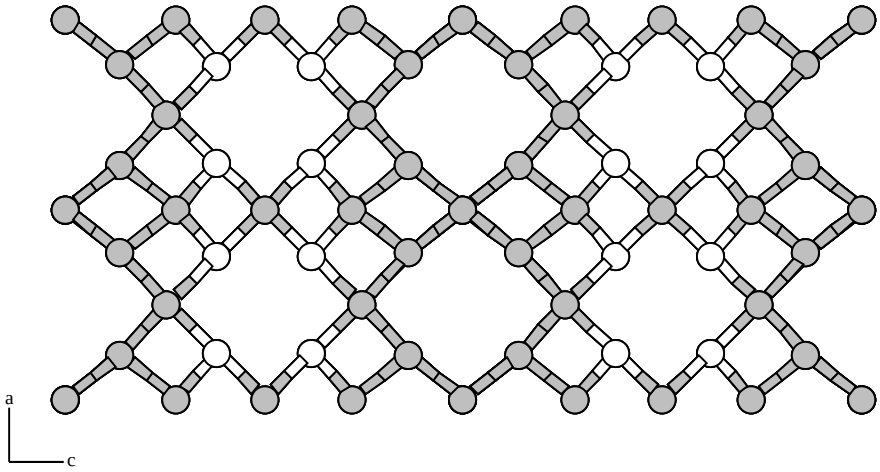

Figure 8.23: Projection of the orthorhombic $\beta - C_{11}N_4$ crystal structure along the [010] plane.

Property	*graphitic*-$C_{11}N_4$
Crystal System	Orthorhombic
Space Group	Pmm2 (25)
Atoms/unit cell	15
Atom type	Coordinates (x, y, z)
C_1	(0.5000, 0.5000, 0.4425)
C_2	(0.5000, 0.2600, 0.2050)
C_3	(0.5000, 0.2490, 0.1875)
C_4	(0.5000, 0.5000, 0.2735)
C_5	(0.5000, 0.2450, 0.5265)
C_6	(0.5000, 0.0000, 0.4375)
C_7	(0.5000, 0.0000, 0.7575)
C_8	(0.5000, 0.0000, 0.2715)
N_1	(0.5000, 0.0000, 0.9305)
N_2	(0.5000, 0.5000, 0.9495)
N_3	(0.5000, 0.2360, 0.6835)
Cell constants (Å)	a=3.4125; b=4.9214; c=8.5198
α, β, γ (°)	90, 90, 90

Table 8.15: Optimised parameters for the *graphitic*-$C_{11}N_4$ phase.

remove such interactions was made in 1995 by T. Hughbanks and Y. Tian [165], who proposed the substitution of one N atom with one C to attenuate the critical N-N lone pair repulsion in the β-C_3N_4 system. However, such a procedure imposes in most of the cases the use of new carbon-rich models (*e.g.* C_4N_3) for which the departure from the isoelectronic systems becomes inevitable. In order to overcome this problem, and keep working on isoelectronic models, it has here been studied the $C_{11}N_4$ system within which the electrostatic contributions are kept similar to the analogue C_3N_4 models. One may notice that, a much more difficult and interesting task would have been the use of isoelectronic model systems where the smothering of the N-N interactions is provided, for example, by avoiding lone pairs pointing directly one to each other. Unfortunately, despite many efforts it has not been possible to provide such a model $C_{11}N_4$ phase. Nonetheless, focusing the attention only on the changing of the C/N ratio, it has been found that the interactions between sp^2-hybridised nitrogens (*e.g.* atoms N_3 and N_2 of the 12-centers carbon-nitrogen rings of Fig. 8.21) is not the only effect involved in accounting for the stability of carbon nitrides. The larger cohesive energy revealed in the $C_{11}N_4$ stoichiometry is here assigned to the presence of an increased number of carbon-carbon connections (see the ratio $R_{(C-C/C-N)}$ in Table 8.16), which have large bonding energies. According

Structure	ΔE_{US-PP}	$\Delta E_{FP-LAPW}$	$R_{(C-C/C-N)}$
graphitic-$C_{11}N_4$	-9.6967	-7.9214	26/12
α-$C_{11}N_4$	+0.034	+0.028	16/12
graphitic-C_3N_4	+0.435	+1.030	0/14
bl-C_3N_4	+0.581	+1.176	0/12
β-$C_{11}N_4$	+0.993	+1.588	16/12

Table 8.16: Cohesive energy, ΔE (eV/atom), for various CN_x phases. Free energy values are scaled with respect to the stable *graphitic*-$C_{11}N_4$ structure. The ratio of the number of chemical bonds per unit cell, $R_{(C-C/C-N)}$, is also shown.

to the bond counting rule [166, 167, 20, 153], the most stable structure maximises the number of highly energetic bonds. It is well known that bonds between elements from the 2^{nd} row of the periodic table in which one or both elements possess lone pairs are weaker than bonds in which neither of the constituents show lone pairs. As a matter of fact, the C-N bonds (260-320 kJ/mol) are not as strong as C-C bonds ($\sim$ 350 kJ/mol) [168, 169]. Therefore, it is mostly due to the presence of a large number of chains and/or rings, made of highly energetic C-C bonds, that the $C_{11}N_4$ stoichiometry results energetically favoured over the C_3N_4 one. As shown in Fig. 8.24 and Table 8.16 this stoichiometry is predicted, from both US-PP and FP-LAPW methods, to have a cohesive energy larger than that of C_3N_4. Its graphitic form is energetically well below, 0.435 eV/atom with US-PP, the corresponding *graphitic*-C_3N_4 as is the three-dimensional α phase (0.401 eV/atom). In particular, the layered $C_{11}N_4$ form results energetically more stable than the corresponding C_3N_4 model because of the presence of an extended graphitic-like matrix around the carbon-nitrogen ring in the direction of the *c*-axis (Fig. 8.21). The introduced carbon system with thirteen C-C bonds per layer is here responsible of an evident lowering of the energy of the system. Such a model phase results also as the most stable $C_{11}N_4$ form not only because of the highest fraction of C-C/C-N bonds but also because of the possibility to delocalise the nitrogen's lone pair (atoms N_2 and N_3) into the graphitic-like matrix. Similarly, the same delocalisation effect is present in the *graphitic*-C_3N_4, where lone pairs can be dispersed into the π-electron circulation of the C_3N_3 rings. It is because of this peculiar characteristic that layered phases represent, in both stoichiometries, the low energy structure models [170]. In three-dimensional phases the above possibility is limited by the presence of a uniform framework with sp^3 bonds. However, the introduced diamond-like matrix with sixteen strong C-C bonds per unit cell (Tab. 8.16) limits in the α phase (Fig. 8.22) the propagation of the neighbouring carbon-nitrogen holes to the *b*-axis. Compared to the *bl*-C_3N_4 analogue (Fig. 8.20), where each

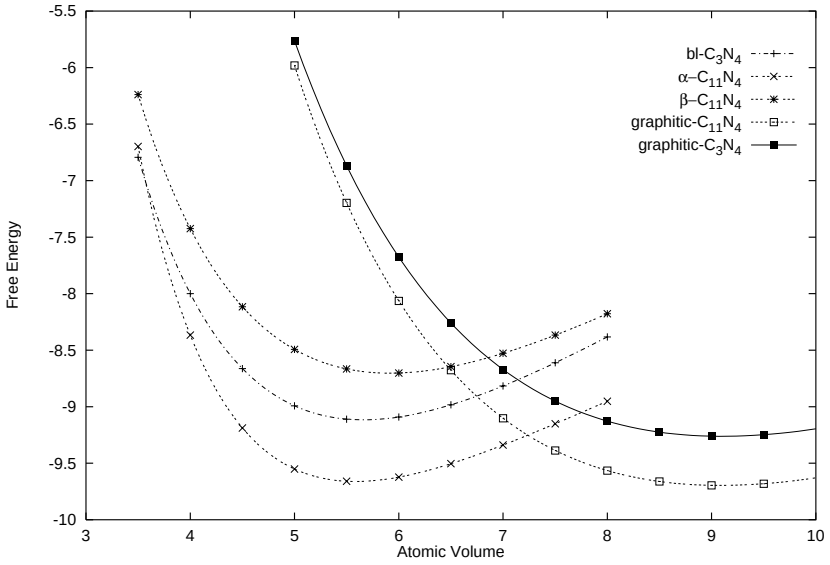

Figure 8.24: Free energies (eV/atom) versus atomic volumes (Å^3/atom) for various C_3N_4 and $C_{11}N_4$ phases (US-PP).

of the carbon-nitrogen rings is surrounded by four others (network of pure C-N bonds), it has here been reached a mixed C-C/C-N system using the same averaged number of valence electrons. It is thus on the possibility to fit and weight the carbon-nitrogen ring into a more stable three-dimensional carbon network that the α-$C_{11}N_4$ results energetically favourable over the *bl*-C_3N_4. However, in spite of this general finding a very low stability has been predicted for the β phase, where the presence of a "*carbon-hole*" (Fig. 8.25) drastically destabilises the three-dimensional $C_{11}N_4$ arrangement. More precisely, the poor stability can be here attributed to the presence of carbon atoms (*i.e.* C_4, C_5 and C_6) with dangling bonds in the carbon cavity. Owing to these considerations, in the following sections, we will mostly focus our attention on the α model.

Only a modest pressure is needed to overcome the energy barrier separating the *graphitic*- and the α-$C_{11}N_4$ phases and to induce a transition between them. Estimation of this pressure from the slope at the common energy/volume intersection gives a hydrostatic transition pressure necessary for the transfer less than $\sim$ 2 GPa (1.7 GPa). Again from the slope at the common energy intersection it has been calculated that a pressure of about 82 GPa is needed to go from the *graphitic*- to the β-$C_{11}N_4$ phase.

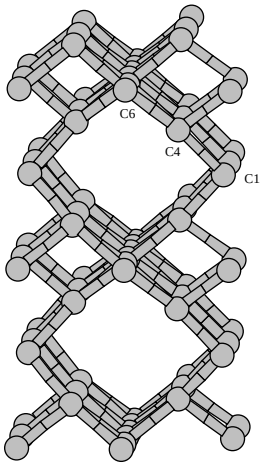

Figure 8.25: Front view of the "*carbon-hole*" in β-$C_{11}N_4$.

Some thermodynamic considerations

To get further insight into the different stabilities of the CN_x stoichiometries a theoretical estimation of the standard molar enthalpy change of formation at 0 K is here presented. The $\Delta H^o_{f,0}$ computed for the formation reaction given in Eq. 8.12 has been estimated with the FP-LAPW to be positive and sensibly larger than that of the of C_3N_4 (cfr. Eq. 8.1 in Sec. 8.2.3, p. 48).

$$11C_{(c)} + 2N_{2(g)} \rightarrow C_{11}N_{4(c)} \tag{8.12}$$

By using the calculated cohesive energies of Tab. 8.17 to estimate the formation enthalpies shown in Tab. 8.18 it may be predicted that a layered form of $C_{11}N_4$ could be, "*in the best case*", only in competition with the formation of a three-dimensional C_3N_4 phase (*e.g.* β-C_3N_4). In particular, for the two graphitic-like forms the difference in the magnitudes of $\Delta H^o_{f,0}$ has been computed to be between 77 and 83 kJ/mol in favour of the *graphitic*-C_3N_4, depending on the applied functional. When considering the synthesis of carbon nitrides with an extended sp^3-bonded network (the two α phases), the same trend in the enthalpy of formation has been highlighted. Calculations show again an enthalpy difference between 69 and 96 kJ/mol in favour of the C_3N_4. A straightforward explanation can be found in the energy balance proposed in Eq. 8.12. From the equation of the formation reaction it appears quite obvious that the energy required for the breaking of the strong C-C bonds can be hardly compensated with the cohesive energy calculated for the $C_{11}N_4$ stoichiometry ($\sim$ 1.0 eV/atom larger than that of C_3N_4 with

LDA). Therefore, from a pure thermodynamic point of view the C_3N_4 composition should be generally favoured over the synthesis of the isoelectronic $C_{11}N_4$.

functional	*graphitic*-$C_{11}N_4$	α-$C_{11}N_4$
LDA	-7.92	-7.89
PBE	-6.95	-6.91
PW91	-6.94	-6.90

Table 8.17: Calculated FP-LAPW cohesive energies of *graphitic*- and α-$C_{11}N_4$. Values are given in eV/atom.

	Standard enthalpy of formation in kJ/mol		
CN_x phase	LDA	PBE	PW91
graphitic-C_3N_4 (hex.)	121.65 (121.65)	176.51 (217.04)	178.50 (219.03)
graphitic-C_3N_4 (orth.)	121.29 (121.29)	176.12 (216.64)	178.13 (218.65)
α-C_3N_4	128	183	185
β-C_3N_4	184	253	255
graphitic-$C_{11}N_4$	197 (197)	257 (407)	259 (405)
α-$C_{11}N_4$	240	302	317
cubic-C_3N_4	321	389	391
bl-C_3N_4	336	419	415

Table 8.18: Computed standard molar enthalpy of formation ($\Delta H^o_{f,0}$) for the two CN_x stoichiometries (x=1.33 and 0.36) by using the cohesive energies seen in Tabs. 8.2, 8.12 and 8.17. Values in parenthesis correspond to the use of graphite as a starting material.

At first sight, this result seems to be in contrast with the experience accumulated in depositing carbon based compounds with magnetron sputtering, which is one of the most dominating processes for depositing hard materials. However, it is important to specify that this conclusion has been drawn by comparing results coming from a limited number of model systems, which have been assumed to be representative for the layered and the three-dimensional forms. Therefore, it cannot be excluded that a further spanning of the space of the crystal structures might lead to discover other stable phases with a very different trend in the enthalpy of formation. Further, the experimental results are mostly relevant to amorphous samples with a graphitic-/fulleren-like form for which the analogy with the presented crystalline models is somehow arbitrary. Finally, a full kinetic study should be introduced for a complete understanding of the problem. It is crucial to note that the synthesis of carbon nitrides is usually performed at high temperatures where

kinetic factors can play an important and predominating role. The stability of *graphitic*-$C_{11}N_4$, for example, cannot only be inferred by accounting for its thermodynamic but also needs a deep kinetic investigation to understand its real phase stability. As a matter of fact, $C_{11}N_4$ compounds could result thermodynamically unstable but at the same time kinetically more favourable than C_3N_4.

8.3.5 Calculations of the elastic and bulk moduli

In what follows we elucidate how it has been deduced the complete set of elastic constants for the presented crystalline materials. The elastic constants determine the response of the crystal to an externally applied strain (stiffness) and provide information about the bonding characteristics between adjacent atomic planes, anisotropic character of the bonding and structural stability. The main problem in estimating elastic constants from first-principles is not only the requirement of accurate methods for evaluating the total energy but also the heavy computations involved in their calculation. In particular, if the symmetry of the system is reduced, the number of independent moduli increases and hence a larger number of distortions is required to calculate the full set of elastic constants [34]. For an orthorhombic material (like β-$C_{11}N_4$) there are nine independent elastic constants referred to as c_{11}, c_{22}, c_{33}, c_{44}, c_{55}, c_{66}, c_{12}, c_{13} and c_{23} [171]. They can be deduced by applying small strains to the equilibrium lattice and determine the resulting change in the total energy. The entire set of the elastic constants were determined by straining the lattice vectors according to the rule,

$$\tilde{R} = R(1 + \delta) \tag{8.13}$$

where $\tilde{R}$ and R are, respectively, the matrix that contains the components of the distorted and undistorted lattice vectors, 1 is the unity matrix and δ the symmetric distortion matrix.

$$\delta = \begin{pmatrix} \delta_{11} & \delta_{12} & \delta_{13} \\ \delta_{21} & \delta_{22} & \delta_{23} \\ \delta_{31} & \delta_{32} & \delta_{33} \end{pmatrix} \tag{8.14}$$

The internal energy of a distorted crystal $E(V, \delta)$ can be Taylor expanded in powers of the components of δ with respect to the initial internal energy of the static crystal $E(V_o, 0)$ in the following way:

$$E(V, \delta) = E(V_o, 0) + V_o \sum_{k=2}^{n} \sum_{i_1 \ldots i_k} \frac{1}{k!} c_{i_1 \ldots i_k} \delta_{i_1} \ldots \delta_{i_k} \tag{8.15}$$

V and V_o denote the volume of the strained and unstrained crystal, respectively and $c_{i_1 \ldots i_k}$ the kth-order elastic constants of the unstrained crystal in the Voigt notation. In Eq. 8.15, the distortion components are defined according to $\delta_k = \delta_{ij}$ for k = 1, 2, 3

Strain	Parameters (unlisted δ_{ij}=0)	$2\Delta E/\left(V_o\delta^2\right)$
1	$\delta_{11}=\delta$	c_{11}
2	$\delta_{22}=\delta$	c_{22}
3	$\delta_{33}=\delta$	c_{33}
4	$\delta_{11}=\delta_{22}=\delta_{33}=\frac{1}{(1-\delta^2)^{1/3}}-1;\ \delta_{23}=\delta_{32}=\frac{\delta}{(1-\delta^2)^{1/3}}-1$	$4c_{44}$
5	$\delta_{11}=\delta_{22}=\delta_{33}=\frac{1}{(1-\delta^2)^{1/3}}-1;\ \delta_{13}=\delta_{31}=\frac{\delta}{(1-\delta^2)^{1/3}}-1$	$4c_{55}$
6	$\delta_{11}=\delta_{22}=\delta_{33}=\frac{1}{(1-\delta^2)^{1/3}}-1;\ \delta_{12}=\delta_{21}=\frac{\delta}{(1-\delta^2)^{1/3}}-1$	$4c_{66}$
7	$\delta_{11}=\frac{1+\delta}{(1-\delta^2)^{1/3}}-1;\ \delta_{22}=\frac{1-\delta}{(1-\delta^2)^{1/3}}-1;\ \delta_{33}=\frac{1}{(1-\delta^2)^{1/3}}-1$	$(c_{11}+c_{22}-2c_{12})$
8	$\delta_{11}=\frac{1+\delta}{(1-\delta^2)^{1/3}}-1;\ \delta_{22}=\frac{1}{(1-\delta^2)^{1/3}}-1;\ \delta_{33}=\frac{1-\delta}{(1-\delta^2)^{1/3}}-1$	$(c_{11}+c_{33}-2c_{13})$
9	$\delta_{11}=\frac{1}{(1-\delta^2)^{1/3}}-1;\ \delta_{22}=\frac{1+\delta}{(1+\delta^2)^{1/3}}-1;\ \delta_{33}=\frac{1-\delta}{(1-\delta^2)^{1/3}}-1$	$(c_{22}+c_{33}-2c_{23})$

Table 8.19: Strains and elastic moduli for the orthorhombic phase.

and $\delta_k = 2\delta_{ij}$ for k = 4, 5 and 6. The quantity $E(V,\delta)$ has been computed by using the first-principles theory for different strains of the system. The Taylor expansion limited to the second-order is here employed for the fitting of the numerical data. The elastic constants, V_o and $E_o = E(V_o, 0)$ are the fitting parameters.

In particular, the independent elastic constants for an orthorhombic material have been found by considering nine different matrices δ to which correspond nine different expressions of the total energy (see Table 8.19). The components of the distortion matrix (Eq. 8.14) which do not appear in the table are set equal to zero. For each of the applied strains, the total energy of the system has been computed for seven different small distortions ($\delta = \pm 0.02n, n = 0-3$). Relaxation of the internal degrees of freedom has also been carried out for the entire set of deformations. Finally, the elastic constants have been found by fitting the energies against the distortion parameter. A similar procedure has been utilised to deduce the six distinct, non-vanishing elastic constants (c_{11}, c_{12}, c_{13}, c_{33}, c_{44} and c_{66}) [172] for a tetragonal solid (α-$C_{11}N_4$) and the three independent moduli (c_{11}, c_{12} and c_{44}) [173] for a cubic crystal system (bl-C_3N_4). The complete list of the applied strains is shown in Table 8.20 and 8.21 for the tetragonal and the cubic systems, respectively.

After having completed the calculation of the whole set of elastic constants it is possible to estimate, for each of the investigated structures, the shear moduli by simply applying the following linear relations. According to the finding of A. P. Gerk and D. M. Teter, it has been assumed that the larger is the value of G, the harder is the material. The general formula of the isotropic shear modulus, G_{Iso}, was initially expressed as

Strain	Parameters (unlisted δ_{ij}=0)	$\Delta E/V_o$
1	$\delta_{11} = \delta_{22} = \delta$	$(c_{11} + c_{12})\,\delta^2$
2	$\delta_{11} = \delta_{22} = \delta;\ \delta_{33} = \frac{1}{(1+\delta^2)^2} - 1$	$(c_{11} + c_{12} + 2c_{33} - 4c_{13})\,\delta^2$
3	$\delta_{33} = \delta$	$\frac{1}{2}c_{33}\delta^2$
4	$\delta_{11} = \left[\frac{(1+\delta)}{(1-\delta)}\right]^{\frac{1}{2}} - 1;\ \delta_{22} = \frac{-\delta_{11}}{(1+\delta_{11})}$	$(c_{11} - c_{12})\,\delta^2$
5	$\delta_{31} = \delta_{32} = \delta_{13} = \delta_{23} = \frac{1}{2}\delta;\ \delta_{33} = \delta^2/4$	$c_{44}\delta^2$
6	$\delta_{12} = \delta_{21} = \frac{1}{2}\delta;\ \delta_{11} = \delta_{22} = \left(1 + \frac{\delta^2}{4}\right)^{\frac{1}{2}} - 1$	$\frac{1}{2}c_{66}\delta^2$

Table 8.20: Strains and elastic moduli for the tetragonal phase.

follows by A. Reuss in 1929 [36]:

$$G_{Iso} = \frac{1}{15}\left[(c_{11} + c_{22} + c_{33}) - (c_{23} + c_{31} + c_{12}) + 3(c_{44} + c_{55} + c_{66})\right] \tag{8.16}$$

Taking into account the proper symmetry relations, this modulus modifies as in the following for an orthorhombic, tetragonal and cubic system, respectively:

$$G_o = \frac{1}{15}(c_{11} + c_{22} + c_{33} - c_{12} - c_{13} - c_{23}) + \frac{1}{5}(c_{44} + c_{55} + c_{66}) \tag{8.17}$$

$$G_t = \frac{1}{15}(2c_{11} + c_{33} - c_{12} - 2c_{13} + 6c_{44} + 3c_{66}) \tag{8.18}$$

$$G_c = \frac{1}{15}(3c_{11} - 3c_{12} + 9c_{44}). \tag{8.19}$$

Furthermore, for the calculation of the bulk modulus an isotropic strain has been applied to the crystal cell. Then, the Birch type equation of state [31] has been used to adjust the variation of the energy versus volume. This equation represents a well known and tested fitting form able to describe P, V, T data for a wide class of solids. The main assumption made is that no phase transition occurs during compression of the material.

Analysis of the results and discussion

In this subsection we comment the results achieved with the US-PP method (Table 8.22) by straining the crystals in a volume and shape changing way. The calculated bulk modulus for the α-$C_{11}N_4$ has been found to be 460.6 GPa. This value is larger than the estimated moduli for the *bl*-C_3N_4 (425.9 GPa), cubic boron nitride (396.6 GPa) and close to those of cubic (463.7 GPa) and hexagonal (456.0 GPa) diamond [153]. On the contrary,

Strain	Parameters (unlisted δ_{ij}=0)	Energy
1	$\delta_{11} = \delta_{22} = \delta$; $\delta_{33} = \frac{1}{(1+\delta^2)} - 1$	ΔE=$6V_oC'\delta^2$
2	$\delta_{12} = \delta_{21} = \delta$; $\delta_{33} = \frac{\delta^2}{1-\delta^2}$	ΔE=$2V_oc_{44}\delta^2$

Table 8.21: Strains and elastic moduli for a cubic system. By calculating the tetragonal shear constant, $C' = \frac{1}{2}(c_{11} - c_{12})$, and the bulk modulus, $B = \frac{1}{3}(c_{11} + 2c_{12})$, it is possible to extract c_{11} and c_{12}.

for the β phase a much lower B (367.2 GPa) has been calculated. However, its magnitude approaches that of cubic boron nitride. As already discussed, the difference in the bulk moduli between α and β can be roughly related to the lower stability of β. Adjusting the variation of the energy versus the unit cell volume for the layered C_3N_4 and $C_{11}N_4$ phases we found the following B numbers: 209.5 GPa and 226.0 GPa. These moduli are quite close to each other indicating that the hardness of layered carbon nitrides remains mostly invariant with respect to a significant lowering of the nitrogen concentration.

The systematic investigation of the lattice stability was originally done by M. Born and K. Huang [174, 175], who showed that by expanding the internal crystal energy in a power of series in the strain and by imposing the convexity of the energy, it is possible to obtain stability criteria in terms of a set of conditions on the elastic constants. The requirement of mechanical stability in a cubic crystal leads, for example, to the following restrictions on the three elastic constants [176]

$$(c_{11} - c_{12}) > 0,\ c_{11} > 0,\ c_{44} > 0,\ (c_{11} + 2c_{12}) > 0. \tag{8.20}$$

For a tetragonal crystal, which has six independent elastic constants, these conditions are as follows [176]

$$\begin{aligned}(c_{11} - c_{12}) > 0,\ (c_{11} + c_{33} - 2c_{13}) > 0,\\ c_{11} > 0,\ c_{33} > 0,\ c_{44} > 0,\ c_{66} > 0,\\ (2c_{11} + c_{33} + 2c_{12} + 4c_{13}) > 0.\end{aligned} \tag{8.21}$$

Finally, for orthorhombic crystals with nine elastic constants, the mechanical stability leads to the following restrictions [176]

$$\begin{aligned}(c_{11} + c_{22} - 2c_{12}) > 0,\ (c_{11} + c_{33} - 2c_{13}) > 0, (c_{22} + c_{33} - 2c_{23}) > 0,\\ c_{11} > 0,\ c_{22} > 0,\ c_{33} > 0,\ c_{44} > 0, c_{55} > 0, c_{66} > 0,\\ (c_{11} + c_{22} + c_{33} + 2c_{12} + 2c_{13} + 2c_{23}) > 0.\end{aligned} \tag{8.22}$$

The complete set of zero-pressure elastic constants are shown in Table 8.22 together with the related isotropic shear moduli. The first thing to note is that the whole sets of c_{ij}

Property	*bl*-C_3N_4	α-$C_{11}N_4$	β-$C_{11}N_4$
c_{11}	842.9 (840)	959.4	728.5
c_{12}	217.4 (213)	151.7	206.9
c_{13}	-	261.0	205.6
c_{22}	-	-	727.2
c_{23}	-	-	209.1
c_{33}	-	889.0	616.2
c_{44}	454.6 (452)	617.8	252.8
c_{55}	-	-	348.0
c_{66}	-	589.0	235.5
G	397.9 (397)	507.2	263.9
B	425.9 (425) [425.9]	460.6 [461.7]	367.2 [368.3]
$B^{'}$	3.80	5.27	3.61
V_o	5.66	5.58	5.91
E_o	-9.1162	-9.6610	-8.7033
ρ	3.86	3.71	3.52

Table 8.22: Theoretical values of the elastic constants (c_{ij} in GPa), isotropic shear modulus (G in GPa), bulk modulus (B in GPa), its pressure derivative ($B^{'}$), atomic volume (V_o in Å^3/atom), cohesive energy (E_o in eV/atom) and atomic densities (ρ in g/cm^3) of *bl*-C_3N_4 and α-, β-$C_{11}N_4$. Values in round brackets refer to the work of A. Y. Liu and R. M. Wentzcovitch [114] whereas those in square brackets concern the bulk modulus calculated by combining the elastic constants.

satisfy all the above conditions, indicating a certain mechanical stability for the α and β phases. Therefore, even though they are not the most energetically favored structures for the $C_{11}N_4$ stoichiometry, they could be at least metastable materials. The calculated shear moduli validate the same hardness trend as found with the estimated bulk moduli. The isotropic G value for the α phase is at about 110 GPa higher than that of *bl*-C_3N_4, indicating a clear hardening of the $C_{11}N_4$ stoichiometry over the C_3N_4 analogue. As expected, for the β phase the calculated modulus has been found well below the value of the α structure, confirming thus the destabilising effect of the carbon-holes with dangling bonds.

It is certain that the introduction of arbitrary deformations of the unit cell followed by the calculation of the total energy, which is many orders of magnitude larger than elastic energy, tends to decrease the accuracy of the calculated moduli. Nonetheless, the extrapolated isotropic shear moduli for diamond and cubic boron nitride have recently been shown to be in good agreements with the experimental results [153]. Consequently,

the large and positive c_{ij} values found for the three-dimensional α-$C_{11}N_4$ model system can be taken as a reference in accounting for its large hardness. It is also worth to note that by augmenting the number of sp^3 carbon tetrahedra, the hardness of the material gets closer to that of diamond (G_{exp}=535 GPa and B_{exp}=443 GPa [29]; G_{cal}=558.5 GPa and B_{cal}=463.7 GPa [153]). As a matter of fact, the resistance to deformation is improved in the α phase by the presence of a large number of sp^3 carbons which have difficult access to higher electronic states, namely *d*-states. From this picture, the process of rehybridisation, which takes place after deformation of the solid, results not favored leading thus to less compliant bonds. It is because of this characteristic that diamond will probably remain the hardest known material with high elastic constants values and a large shear modulus [29, 177].

Poisson's ratio and Young's modulus For all the investigated crystal structures, the bulk modulus of a polycrystalline material has also been estimated in the Voigt's approximation from the following equation:

$$B = \frac{1}{9}\left(c_{11} + c_{22} + c_{33}\right) + \frac{2}{9}\left(c_{12} + c_{13} + c_{23}\right) \tag{8.23}$$

The calculated values are given in the square brackets of Tab. 8.22. The bulk moduli computed from the elastic constants and from the fit to a Birch equation are almost the same, giving thus a consistent prediction of the compressibility of the analysed phases. Because of the special significance of the Young's modulus[11] and Poisson's ratio for the technological and engineering applications, these quantities have also been calculated by combining together the bulk and shear moduli. In particular, the elastic properties of materials may be mainly characterised by the Poisson's ratio, which gives a measure of the stability of a crystal against shear. The Young's modulus, E, and Poisson's ratio, ν are given by

$$E = \frac{9BG}{3B + G} \tag{8.24}$$

$$\nu = \frac{3B - 2G}{2(3B + G)} \tag{8.25}$$

The calculated Poisson's ratios and Young's moduli are shown in Tab. 8.23. The smaller value of the Poisson's ratio for the α-$C_{11}N_4$ indicates that this phase is relatively stable against strain. The estimated Young's moduli support the same hardness trend as already predicted with the use of B and G.

[11] The Young's modulus, E, (also known as the elastic modulus) is defined as the ratio between stress and strain and indicates the stiffness of the material.

	bl-C_3N_4	α-$C_{11}N_4$	β-$C_{11}N_4$	diamond
B/G	1.07	0.91	1.40	0.83 (0.83)
E	910	1114	639	1196 (1140)
ν	0.144	0.098	0.211	0.070 (0.069)

Table 8.23: Table shows the calculated B/G ratio, Young's modulus (GPa) and Poisson's ratio (dimensionless) of *bl*-C_3N_4 and α-, β-$C_{11}N_4$. Diamond has also been listed as a reference material. Values in round brackets concern the properties of CVD diamond as compiled in Ref. [178].

Brittleness and ductility In order to predict the brittle and ductile behaviour of materials, S. F. Pugh [179] introduced in 1954 the quotient of bulk modulus to shear modulus of polycrystalline phases (B/G) by considering the shear modulus G representing the resistance to plastic deformation and the bulk modulus B the resistance to fracture. Therefore, with such an assumption a high (low) B/G value becomes associated with the ductility (brittleness) of a certain solid. The critical number which separates ductile and brittle materials has been fixed at about 1.75.

The calculated B/G ratio for the phase α-$C_{11}N_4$ is 0.91 (see Tab. 8.23) whereas for the analogue *bl*-C_3N_4 1.07. These results suggest that both CN_x stoichiometries provide rather brittle materials, though their values are still slightly higher than that of diamond (B/G=0.83).

8.3.6 Electronic structure

Density of states of *bl*-C_3N_4

The calculated electronic density of states (DOS) of *bl*-C_3N_4 at the equilibrium structure is shown in Fig. 8.26. A band gap, E_g, of 2.86 eV has been computed with the use of LDA approximation. From the partial components of the DOS, it has been found that the lower part of the valence band consists mainly of 2s orbitals from nitrogen and carbon atoms, whereas the middle portion (-15 eV $\leq$ E $\leq$ -5 eV) is dominated by the mixing of the C and N 2p orbitals. The very sharp VB edge indicates the presence of highly localised N states with 2p character. These states can be attributed to the non-bonding electrons belonging the so-called "*nitrogen-hole*". Finally, the portion of the conduction band in between 5 and 15 eV is mostly dominated by the states of carbon and nitrogen 2p.

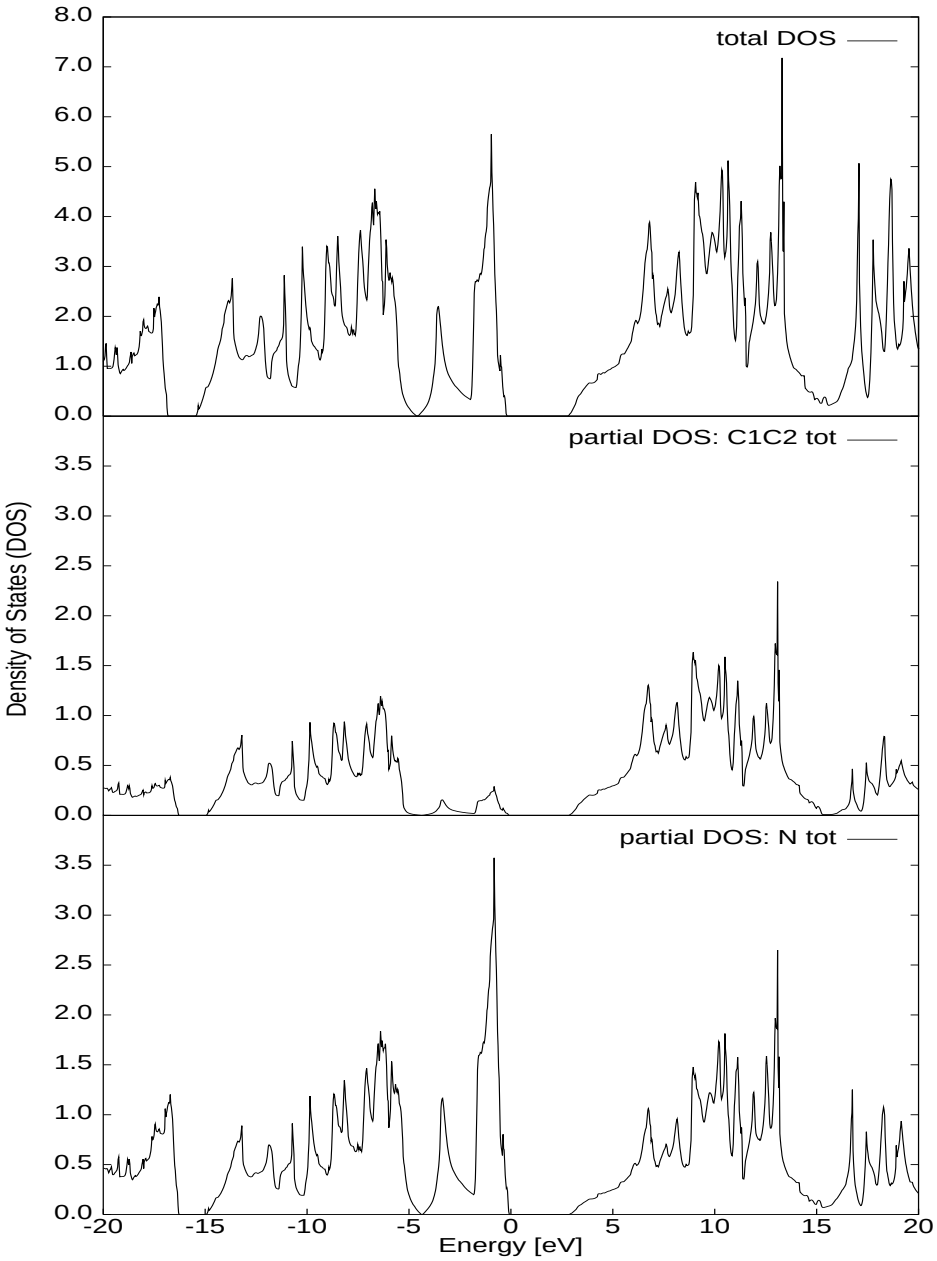

Figure 8.26: The calculated DOS for the *bl*-C_3N_4 phase (FP-LAPW).

Density of states of α- and β-$\mathbf{C_{11}N_4}$

The total DOS for the α and the β phases are illustrated in Fig. 8.27. The first structure shows a band gap of 2.40 eV whereas in the latter no E_g has been found (cfr. the two density of states in Fig. 8.27). The total DOS relative to α displays nearly the same 2p states mixing as in the isoelectronic *bl*-C_3N_4. The peak located at the top of the VB still consists of nitrogen states with 2p character. Both the VB and CB are sharper and indicative of a larger electron density. As already mentioned, the β phase does not show any band gap. This is mainly due to the presence of carbon states located just above the Fermi energy. Their existence is assigned to the highly distorted tetrahedral geometries of the atoms constituting the "*carbon-hole*". More precisely, the most prominent contributions have been found (partial DOS not shown here) from the 2p orbitals of the atoms C_6 and C_5, which are composing the carbon cavity.

Calculation of Energy Loss Near Edge Structure

For light elements like carbon, boron and nitrogen, electron energy loss spectroscopy is a useful technique because of its ability to differentiate the types of bonding in a polymorphic material. The characteristic fine structure in the first few eV beyond the beginning of the core loss ionisation edges supplies the so-called coordination fingerprints, which can be used to distinguish different phases in complex systems. Since in our case of theoretically predicted CN_x phases such reference spectra do not exist, it becomes worth having a theoretical approach to simulate the ELNES. The calculations of the energy loss near edge structures have been performed with the WIEN97 code according to the formalism of M. Nelhiebel *et al.* [180]. In this part of the Chapter, we present spectra due to the carbon and nitrogen *K*-shell excitation (n=1, l=0) of various CN_x compounds. Parameter settings have been used to simulate polycrystalline samples by averaging over all possible incident-beam directions (integral over 4π). Nonetheless, the neglected anisotropy effects which are mostly important for layered structures should only change the intensity of the peaks but not their positions. The energy of the incident electrons was fixed to 200 KeV and the energy loss of the first edge to 285 and 400 eV for carbon and nitrogen, respectively.

In order to probe our calculational method, diamond and graphite have also been investigated. Their relative C *K* ELNES spectra are depicted in Fig. 8.28 and the positions of the most prominent peaks (labelled I to IV) are listed in Tab. 8.24. Peak I in the C *K* edge of graphite corresponds to the electronic transitions 1s $\rightarrow \pi^*$. This feature usually identifies sp^2-hybridised materials and consequently it does not appear in the diamond spectra. The peaks II-V are related to 1s $\rightarrow \sigma^*$ transitions. A reasonable correspondence between our calculations and the experimental results has been found in Tab. 8.24. Moreover, the computed relative peak positions match better with the

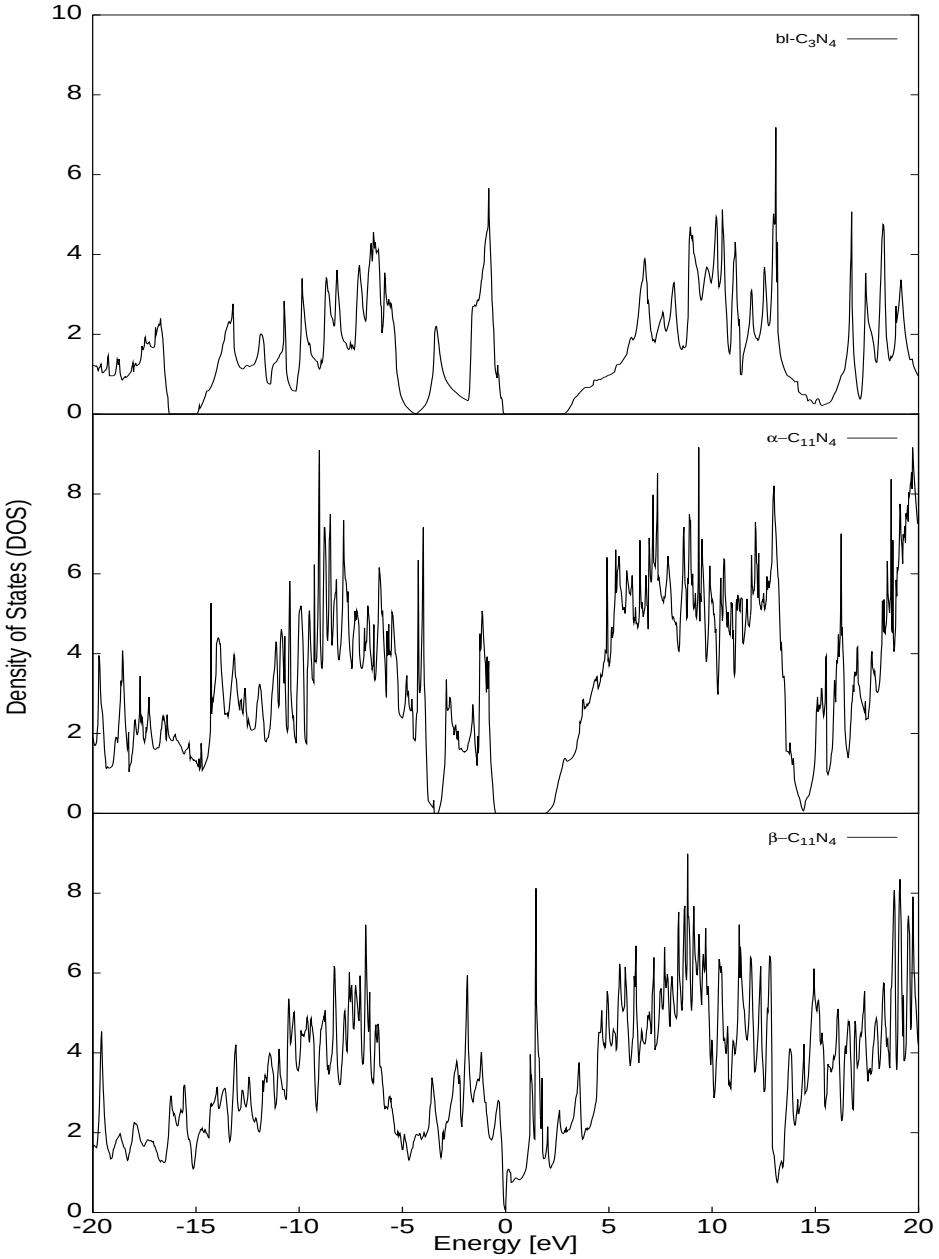

Figure 8.27: The calculated total DOS for the *bl*-C_3N_4 and α-, $\beta - C_{11}N_4$ (FP-LAPW).

Phase	Edge		I	II	III	IV	V
Diamond	C *K*	Thesis	-	0	5.3	12.9	-
		MS approach†	-	0	4.4	12.0	-
		exp.†	-	0	5.5	12.9	-
Graphite	C *K*	Thesis	-6.4	0	4.6	10.0	14.3
		MS approach†	-4.9	0	2.5	6.6	10.3
		exp.†	-6.8	0	4.4	11.2	14.7

Table 8.24: Positions of peaks I-V in the spectra of Fig. 8.28. All the positions are scaled with respect to the main σ^* peak II. Values are in units of eV. (†) Values as compiled in Ref. [181].

experimental finding than the Multiple Scattering (MS) approach [181].

The calculated plain and broadened spectra for different CN_x materials are shown in Fig. 8.29 and 8.30 for the C and N *K* edges, respectively. The spectra for graphitic-like C_3N_4 and $C_{11}N_4$ reveal mainly graphitic features (Fig. 8.29), whereas the three-dimensional *bl*-C_3N_4 and α-$C_{11}N_4$ exhibit a closer similitude to the diamond spectra. However, despite this general similarity the shape and the number of σ^* peaks relative to the $C_{11}N_4$ edges differ quite evidently from those calculated for the C_3N_4 stoichiometry. Especially in the region between 5 and 15 eV (in both edges) a different characteristic fingerprint can be assigned to each of the studied systems, opening thus the possibility of identifying these model phases in thin-film samples via EELS technique. The particular sharp π^* peak found at the beginning of the N edge of the *graphitic*-$C_{11}N_4$ (plain line of Fig. 8.30) indicates the presence of a pronounced sp^2 bonding character. The main contributions to this feature are due to the N_2 and N_3 atoms constituting the 12-centers carbon-nitrogen rings.

8.3.7 Concluding remarks

The present investigation reports the study of the stability and hardness of two model carbon nitride stoichiometries isoelectronic with diamond: C_xN_4, where x=3 and 11. In the first part of this Section it has been carried out the theoretical determination of the equilibrium structural parameters and cohesive energies of novel $C_{11}N_4$ phases. Calculations have shown that the introduction of an extended carbon system, which can be of graphitic-like or diamond-like type, can represent an important way to increment the phase stability of carbon nitrides. Both layered and three-dimensional $C_{11}N_4$ materials have been predicted to have a cohesive energy larger than the corresponding isoelectronic C_3N_4. This result has been achieved using two different computational methods within the DFT: US-PP and FP-LAPW. However, in spite of the increased cohesive energy the

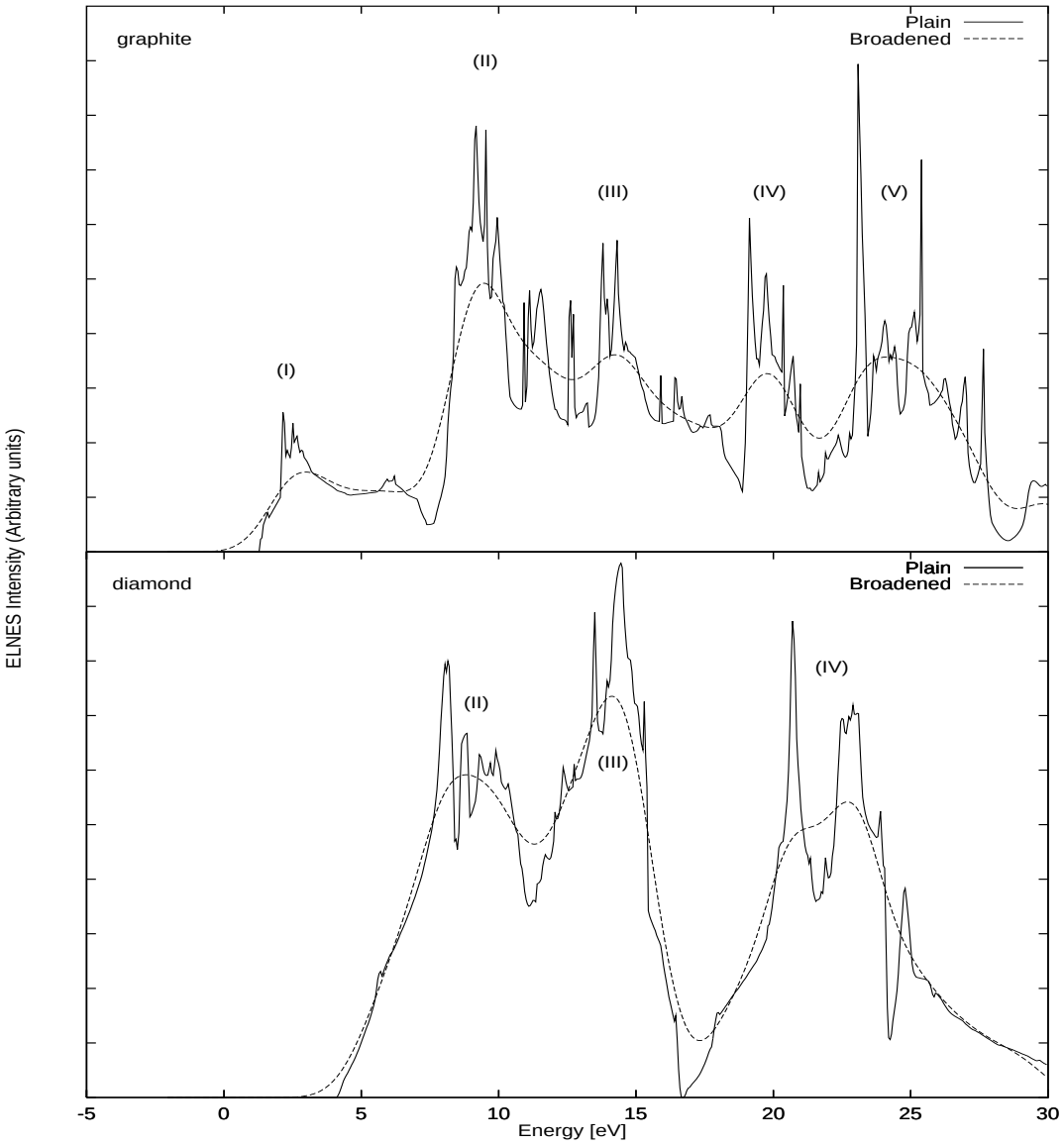

Figure 8.28: Theoretical C K ELNES of diamond and graphite (FP-LAPW).

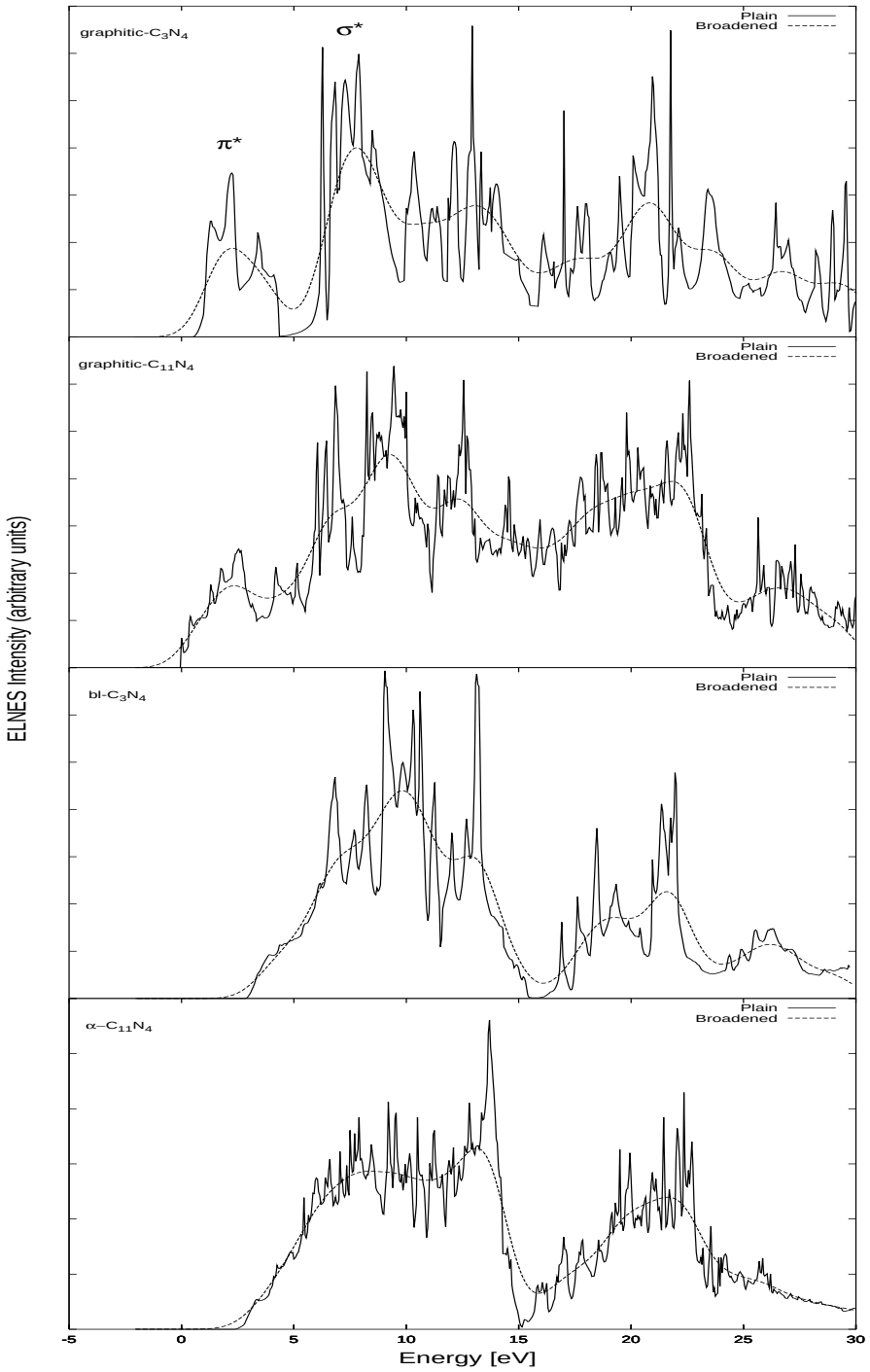

Figure 8.29: Theoretical C K ELNES of various phases (FP-LAPW). The spectra for the inequivalent atoms positions have been calculated separately and weighted in the present Figure.

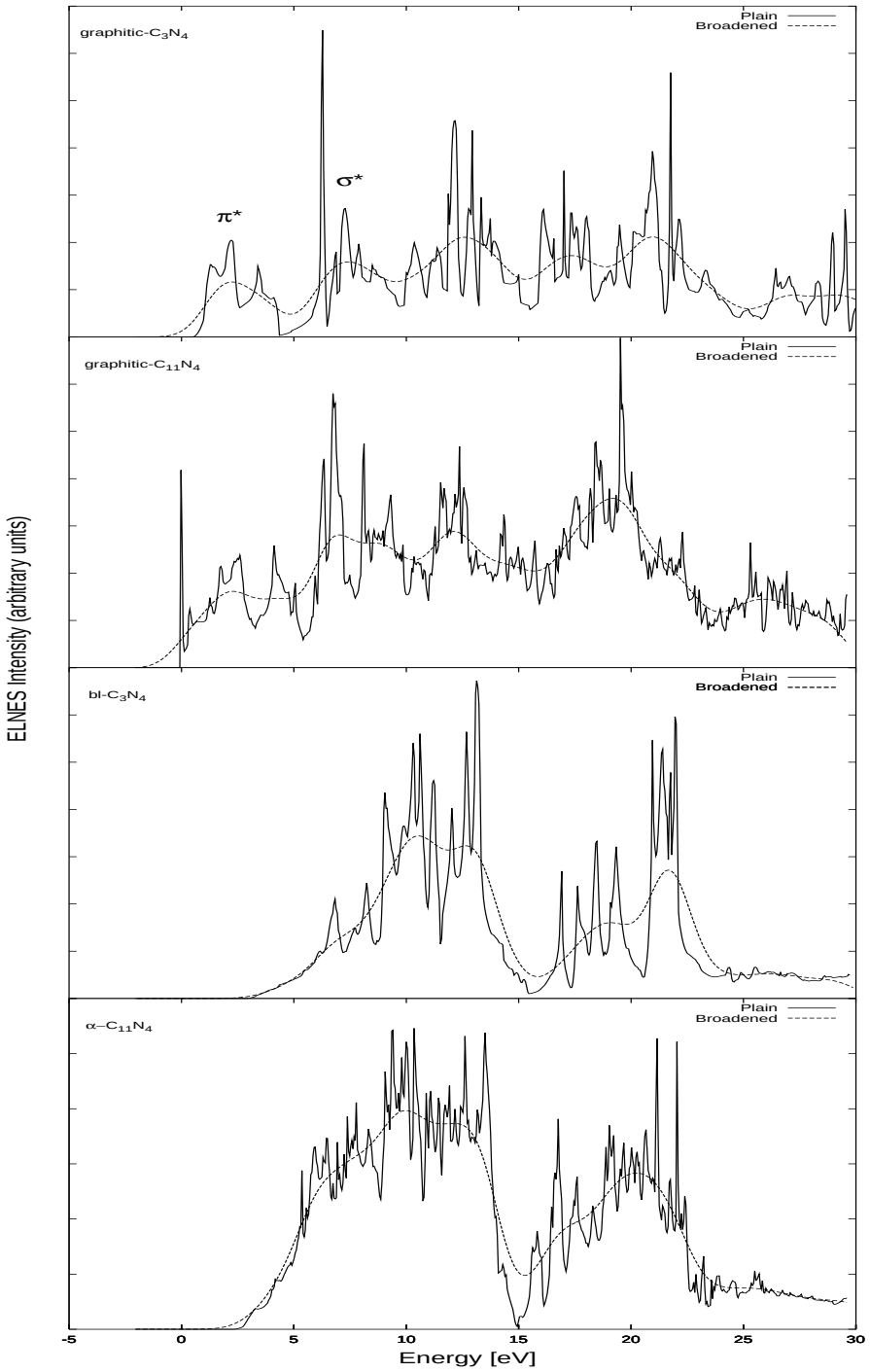

Figure 8.30: Theoretical N K ELNES of various phases (FP-LAPW). As in Fig. 8.29 inequivalent atoms have been calculated separately and weighted in the present spectra.

standard enthalpy of formation has been calculated for all the investigated $C_{11}N_4$ phases to be positive and generally larger than those of the analogues C_3N_4 forms. Therefore, from a simple thermodynamic approach the synthesis of crystalline carbon nitrides with higher carbon content should be less feasible than the well-known C_3N_4 stoichiometry. However, if a sample with $C_{11}N_4$ composition could be realised by means of some type of synthetic process, a considerable activation energy would be required to break the large number of strong C-C and C-N bonds, thus making this substance thermodynamically metastable at ambient conditions. Furthermore, even though the calculated enthalpy difference between the stable graphitic-like forms of C_3N_4 and $C_{11}N_4$ seems to be large enough (75-80 kJ/mol) to favour the synthesis of one stoichiometry over the other, amorphous samples will be probably often obtained upon trying to deposit any of the CN_x compositions. This general conclusion has been drawn by looking at the small energy separations found in between the $\Delta H^o_{f,0}$'s calculated for the whole set of CN_x phases. It is thus expected that a mixture of different phases such as graphitic-like and other three-dimensional networks will be always obtained simultaneously. Therefore, different $C_{11}N_4$ and C_3N_4 forms with a very close energy stability could exist and their discrimination would be thus nearly impossible at the experimental level. The possibility to have few stable structures which could be in dynamical equilibrium at room-temperature has also been hypothesised in 2000 by É. Sandré [182] for CN_x (x=0.33) systems. So far as that is concerned, it would be worthwhile to investigate different fulleren-like phases to check if any larger increase in the stability could be found. Unfortunately, due to the high cost of computational time needed for such an investigation we reserve this study for a possible future project.

A large part of this Section has also been directed to the calculation of the independent, non-zero elastic constants from first-principles. The analysis of the complete set of elastic moduli for the α phase shows that the $C_{11}N_4$ stoichiometry can lead to the formation of very stiff materials. More generally, the increasing of the carbon concentration induces to a significant improvement of the hardness of carbon nitrides, provided that the same isoelectronic structure is kept in the model system. Furthermore, the density of states have been analysed in order to gain insight into the chemical bonding of phases with different stoichiometries. A band gap of 2.4 eV has been calculated for the three-dimensional α structure. Finally, the characteristic ELNES coordination fingerprints have been reported for various CN_x forms. The proposed spectra may be used as a precious tool for the characterisation and the identification of novel carbon nitrides phases in polymorphic samples.

Chapter 9

Boron Carbon Nitrides

9.1 Ternary BCN compounds

The interest in the boron carbon nitrides with general composition $B_xC_yN_z$ arose from the difficulty to obtain new materials for abrasives, heat sinks and protective coating applications. Ternary systems with a diamond-like structure in which some of the carbon atoms are replaced with nitrogen and boron are expected to show the same interesting properties found in diamond and cubic boron nitride, such as hardness, wide band gap and high melting points. As a consequence their potential applications could be found in several mechanical and electronic devices [183, 17, 184]. Moreover the low oxidation resistance of diamond, which is one of the most important drawbacks for its applications, might be improved in the boron-based hard materials. As a matter of fact diamond can only be used at around 600 °C in air, while cubic boron nitride avoids the oxidation up to 1100 °C [145, 185]. The first evidence of a graphitic-like BCN compound with BC_2N stoichiometry dates back to the synthesis of Kouvetakis *et al.* [13, 14], where chemical vapor deposition method was used with BCl_3 and CH_3CN as starting materials. These layered structures have been largely investigated both experimentally [13, 14] and theoretically [166, 186, 187, 188, 189, 190]. Further investigations concerning highly dense three-dimensional phases were carried out by Tateyama and Tsuneyuki [20] who have shown the possibility to obtain ordered BC_2N structures directly through compression of the layered BC_2N form. An elegant study of the electronic properties along the C_2-BN pseudo-binary junction has also been presented by W. R. L. Lambrecht and B. Segall [191, 192]. Early theoretical calculations of the bulk [20] and shear [21, 22] moduli have suggested that these compounds should possess an intermediate hardness between diamond and cubic boron nitride. At the experimental level several efforts have been made in order to modify the graphitic BC_2N systems into hard three-dimensional phases [183, 17, 184, 193, 194, 18, 19]. Despite the use of high-pressure and high-temperature

methods no common results were found in the last decade. Some researchers had problems with a certain limited solubility [15, 16], while others claimed an evident segregation in a mixture of diamond and *c*-BN [17, 18, 19]. However, very recently a promising work of L. Solozhenko *et al.* [6] has been published on the same subject. These authors have shown results that seem to point out to a successful synthesis of a cubic BC_2N phase with a lattice parameter of 3.642(2) Å at ambient conditions. Even though the interpretation of the diffraction patterns has led the authors to the conclusion of a space group between F*d*-3*m* and F-43*m*, the atomic structure has not yet been properly defined. Therefore, it is important to use three-dimensional BC_2N models to provide insight on the uncertain experimental results. That is, to help the interpretation of the experimental finding via a detailed study of the chemical bonding implied in highly dense boron carbon nitrides.

In this Chapter the investigation has been focalised on the determination of the stability and the hardness of novel hypothetical BC_2N structures obtained from the relaxation of the substituted diamond. What is required is to find a system, like diamond, where the sp^3 bonds form strong and uniform three-dimensional frameworks. To discover the existence of new ultra-hard phases the substitution of some of the carbon atoms with boron and nitrogen has been performed in two different diamond forms: cubic and hexagonal. The number of substituted carbon was fixed in order to get isoelectronic heterodiamond BC_2N phases. After the carbon replacement a full geometry relaxation was performed with a first-principle pseudo-potential method to find the fundamental electronic ground state. The obtained hypothetical compounds are expected to be more thermally and chemically (*i.e.* versus oxidation) stable than diamond and harder than cubic boron nitride. This possibility makes them the most interesting class of materials capable to supersede the expensive diamond in various applications.

The Chapter has been organised as follows: first of all we elucidate the building strategy adopted to create novel three-dimensional BC_2N models. Secondly, the relative stability between different phases is qualitatively discussed from a chemical bonding point of view and the mechanical properties are studied via bulk and elastic moduli. In particular, the hardness of the solid was analysed by measuring the resistance of the material upon both volumetric (B) and shape (G) changes. The major difference is in the fact that B requires variations in bond distances only, while G depends mainly on the changes in bond angles. Density of states, band structures and electron-energy-loss-spectroscopy spectra are also presented.

9.2 Setting up novel three-dimensional BC_2N phases

9.2.1 Cubic and hexagonal diamond

Cubic diamond and lonsdaleite[1] (sometimes called *"hexagonal diamond"*) are both crystalline forms of pure carbon (Tab. 9.1), where all the atoms are tetrahedrally bonded (sp^3-type). Their unit cell structure is shown in Fig. 9.1 and Fig. 9.2 for diamond and lonsdaleite, respectively. These two structures are related to each other as the spha-

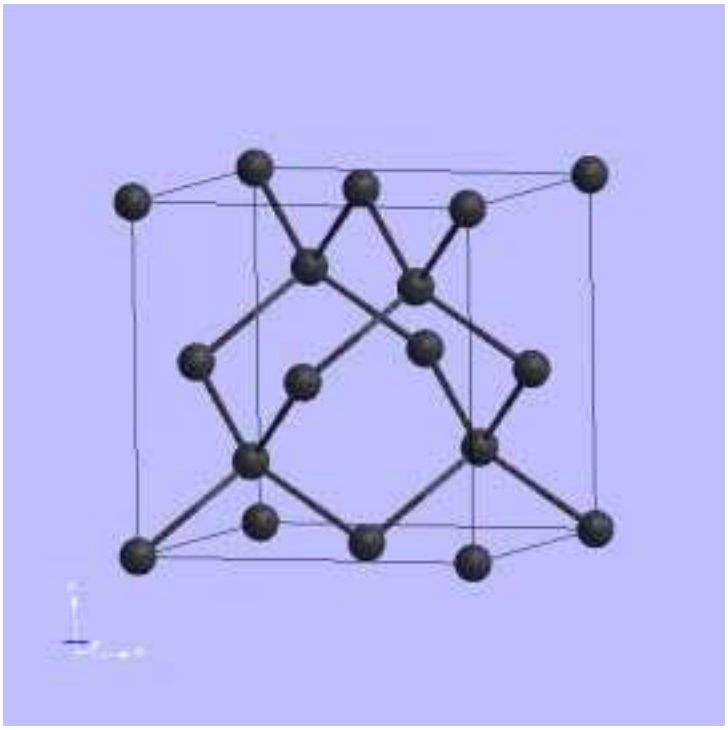

Figure 9.1: Unit cell of cubic diamond. This structure was first determined in 1913 by W. H. and W. L. Bragg [195]. That was also the first time that the structure of an element was determined by the use of X-ray diffraction [196].

lerite with the wurzite. The {111} planes on the diamond structure and {001} planes in lonsdaleite are identical; they are made of puckered hexagonal rings with a chair-form.

[1] It is a rare hexagonal polymorph of diamond, believed to have formed when meteoric graphite falls to earth. When this happened, great heat and stress transformed the graphite into diamond, but it retained graphite's hexagonal crystal lattice. Lonsdaleite is currently found only in the famous Barringer Crater (also known as meteor crater) in Arizona.

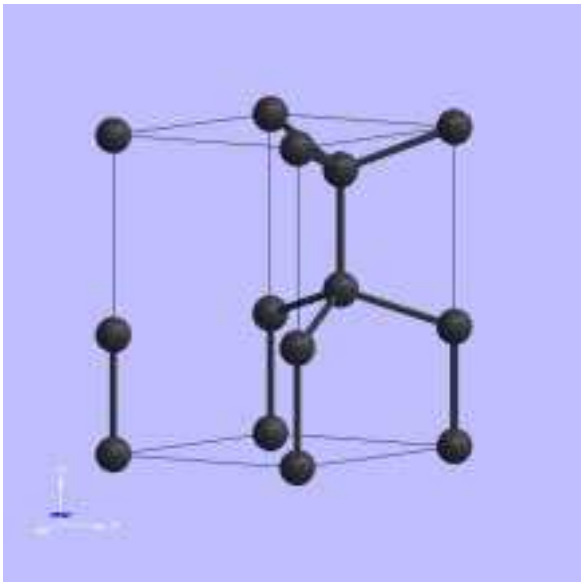

Figure 9.2: Unit cell of lonsdaleite (hexagonal polymorph of diamond).

The difference between these two structures is in the stacking of these planes. Diamond shows a staggered configuration of the C-C second-neighbour bonds with a chair-form configuration of the puckered hexagonal rings, while lonsdaleite shows an eclipsed configuration with a boat-form (see Ref. [8] for a detailed discussion). The slightly higher energy of these eclipsed lonsdaleite carbons causes its structure to be slightly less stable than that of diamond.

The basic idea behind the theoretical work presented in this Chapter starts from the fact that an introduction of the B and N atoms in the above diamond structures should, *in principle*, lead to the formation of new systems with large hardness and an increased oxidation resistance. It is because of this great expectation, that a major portion of the work has been directed to the understanding of the properties related to the BC_2N model phases. The following subsections show the criteria applied in replacing the carbon atoms in both cubic and hexagonal diamond phases.

9.2.2 Carbon substitution

Starting from the cubic form of diamond we have replaced four of the eight carbon positions with two nitrogen and two boron atoms. Two different ways of replacing the carbon atoms are shown in Tab. 9.2. Successively, the lattice vectors and atom positions were fully optimised with the US-PP/LDA method to obtain the BC_2N ground state.

Property	Diamond	Lonsdaleite
Crystal system	cubic	hexagonal
Space group	Fd3m (227)	$P6_3/mmc$ (194)
Atoms per unit cell	8	4
Positions of atoms	(0, 0, 0), $(\frac{1}{2}, \frac{1}{2}, 0)$ $(0, \frac{1}{2}, \frac{1}{2}), (\frac{1}{2}, 0, \frac{1}{2})$ $(\frac{1}{4}, \frac{1}{4}, \frac{1}{4}), (\frac{3}{4}, \frac{3}{4}, \frac{1}{4})$ $(\frac{1}{4}, \frac{3}{4}, \frac{3}{4}), (\frac{3}{4}, \frac{1}{4}, \frac{3}{4})$	$(0, 0, 0), (0, 0, \frac{3}{8})$ $(\frac{1}{3}, \frac{2}{3}, \frac{1}{2}), (\frac{1}{3}, \frac{2}{3}, \frac{7}{8})$
Cell constants	a=3.57	a=2.52; c=4.12

Table 9.1: Crystal structure data for cubic and hexagonal diamond. Cell constants values are expressed in unit of Å.

Atom positions	Diamond	I-BC_2N	II-BC_2N
(0, 0, 0)	C	C	B
$(\frac{1}{2}, \frac{1}{2}, 0)$	C	C	B
$(0, \frac{1}{2}, \frac{1}{2})$	C	N	C
$(\frac{1}{2}, 0, \frac{1}{2})$	C	N	C
$(\frac{1}{4}, \frac{1}{4}, \frac{1}{4})$	C	B	C
$(\frac{3}{4}, \frac{3}{4}, \frac{1}{4})$	C	C	C
$(\frac{1}{4}, \frac{3}{4}, \frac{3}{4})$	C	C	N
$(\frac{3}{4}, \frac{1}{4}, \frac{3}{4})$	C	B	N

Table 9.2: Substitution of the carbon atoms in the *fcc* diamond.

We have explicitly chosen to start from a primitive diamond system with eight atomic positions per unit cell so that no symmetry conditions are imposed and all the atoms in the cell are free to optimise independently. In the above substitution process we have applied the consideration made in 1997 by Tateyama *et al.* [20]. He discovered that the bond counting rule, *i.e.* maximum number of C-C and B-N bonds, found in the layered structures is also valid for heterodiamond BC_2N. In particular, it has been predicted that the most stable BC_2N structures have no B-B or N-N bonds and maximise the number of C-C and B-N connections with C-B disfavoured. It has also been proposed that the phase with alternate -C-C- and -B-N- chains or rings is the most stable one. Following these suggestions it has been found that the carbon atom positions as substituted in Tab. 9.2 are the best choice to avoid the formation of low energetic bonds. A dense three-dimensional orthorhombic phase is proposed by substituting four carbon atoms with two

Property	I-BC_2N	II-BC_2N	III-BC_2N
System	orthorhombic	orthorhombic	trigonal
Space group	P2221 (17)	Pmm2 (25)	P3m1 (156)
Atoms/cell	8	4	4
x,y,z	$N(0.258, 0.000, 0.000)$	$N(0.500, 0.500, 0.380)$	$N(0.000, 0.000, 0.571)$
	$B(0.000, 0.748, 0.250)$	$B(0.500, 0.000, 0.124)$	$B(0.333, 0.667, 0.441)$
	$C_1(0.742, 0.500, 0.000)$	$C_1(0.000, 0.500, 0.631)$	$C_1(0.000, 0.000, 0.934)$
	$C_2(0.500, 0.255, 0.250)$	$C_2(0.000, 0.000, 0.866)$	$C_2(0.333, 0.667, 0.054)$
Cell const.	a=3.5536	a=2.5280	a=b=2.4955
	b=3.5986	b=2.5024	
	c=3.5528	c=3.5871	c=4.1923
α, β, γ	90, 90, 90	90, 90, 90	90, 90, 120
d_{N-C}	1.539	1.552	1.522
d_{N-B}	1.565	1.549	1.540
d_{B-C}	1.558	1.569	1.625
d_{C-C}	1.519	1.509	1.525

Table 9.3: Optimised parameters for heterodiamond BC_2N structures. Cell constants and bond distances are given in unit of Å.

nitrogen at the positions (0, $\frac{1}{2}$, $\frac{1}{2}$) and ($\frac{1}{2}$, 0, $\frac{1}{2}$) and two boron at ($\frac{1}{4}$, $\frac{1}{4}$, $\frac{1}{4}$) and ($\frac{3}{4}$, $\frac{1}{4}$, $\frac{3}{4}$). The optimisation of the lattice parameters and the ions relaxation were performed iteratively until the minimum on the total energy was met (see Tab. 9.3). This system is here called I-BC_2N and consists of an orthorhombic crystal where carbon, nitrogen and boron atoms are tetrahedrally coordinated (Fig. 9.3). The crystal motif is made of C_4NB, C_3N_2B, C_3B_2N and $C_2B_2N_2$ rings with a chair form configuration. Following the same procedure another orthorhombic phase called II-BC_2N (see Fig. 9.4 and Tab. 9.3) was found starting from the cubic diamond. This structure is obtained by replacing the carbon atoms in positions (0, 0, 0) and ($\frac{1}{2}$, $\frac{1}{2}$, 0) with boron and in ($\frac{1}{4}$, $\frac{3}{4}$, $\frac{3}{4}$) and ($\frac{3}{4}$, $\frac{1}{4}$, $\frac{3}{4}$) with nitrogen. The phase II-BC_2N is characterised by the same hexagonal rings with a chair form configuration as in I-BC_2N but a different atom type disposition is used to build-up the rings. However, in both phases each electron rich nitrogen is bonded with two electron poor boron atoms and two carbons in order to reach the fourth co-ordination. In the same way the boron atoms are connected with two nitrogens and two carbons. The structure is then completed with carbon atoms tetra-coordinated with two nitrogen (or two borons) and two carbon atoms each.

To individuate new ternary B-C-N phases, the same above procedure has been applied to the lonsdaleite, where two of the four carbon positions have been substituted with one

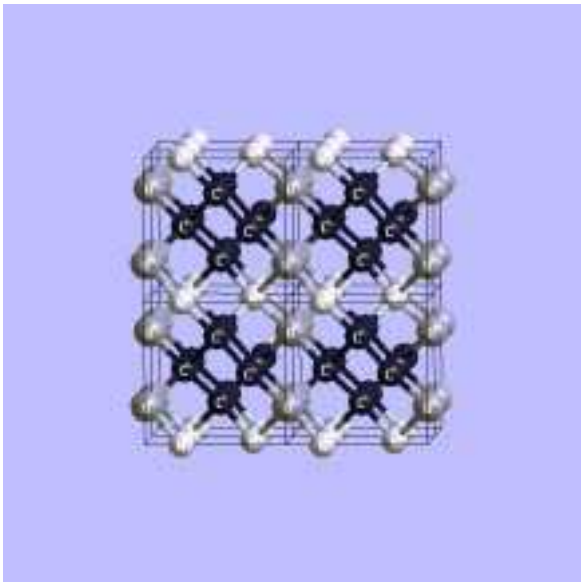

Figure 9.3: Crystal structure of the orthorhombic I-BC_2N. Carbon, nitrogen and boron atoms are depicted in black, white and grey, respectively.

boron and one nitrogen (Tab. 9.4). In particular, a trigonal structure called III-BC_2N (Fig. 9.5) has been found when two carbon atoms in the positions (0, 0, $\frac{3}{8}$) and ($\frac{1}{3}$, $\frac{2}{3}$, $\frac{1}{2}$) were replaced with nitrogen and boron, respectively. Subsequent geometry optimisation (Tab. 9.3) brings the phase in an energy minimum state where the boron atoms are four co-ordinated with three nitrogens and one carbon. Nitrogen atoms show a fourth co-ordination with three borons and one carbon while the carbon atoms are tetrahedrally bonded to one boron and three other carbons. This phase is built-up with C_6 and B_3N_3 rings connected with each other via C-B and C-N bonds. According to the bond counting rule, this phase contains C-C and B-N bonds and no B-B or N-N bonds are present.

Atom Positions	Lonsdaleite	III-BC_2N
(0, 0, 0)	C	C
(0, 0, $\frac{3}{8}$)	C	N
($\frac{1}{3}$, $\frac{2}{3}$, $\frac{1}{2}$)	C	B
($\frac{1}{3}$, $\frac{2}{3}$, $\frac{7}{8}$)	C	C

Table 9.4: Substitution of the carbon atoms in the hexagonal diamond.

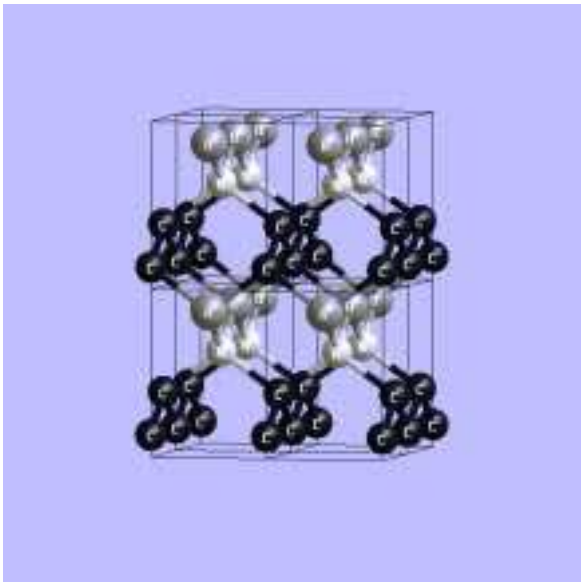

Figure 9.4: Crystal structure of the orthorhombic II-BC_2N.

9.3 Computational details

Calculations of the ground state geometries were carried out in the framework of density functional theory in its local density approximation to the electron exchange and correlation within the VASP package. The interactions between the ions and the electrons are described by using ultra-soft Vanderbilt pseudo-potential and the electron-electron interaction is treated within the LDA by the Ceperley-Alder exchange-correlation potential. In our computational scheme the conjugate-gradient algorithm was used to relax the atom positions of the BC_2N systems into their ground states. The structural parameters were considered to be fully relaxed when forces on the atoms were less than 0.02 eV/Å and all stress components were less than 0.003 eV/Å^3. The calculations were performed by using an energy cut-off of 434.8 eV for the plane wave basis set. The tetrahedron method with Blöchl corrections was applied for both geometry relaxation and total energy calculations. Brillouin-zone integrals were approximated using the special **k**-point sampling of Monkhorst and Pack. Density of states, band structures and energy loss near edge structure spectra were performed on the optimised US-PP structures by using the accurate full-potential linearized augmented plane wave method (WIEN97 package). For the exchange-correlation potential the LDA approximation has been used as parameterised by Perdew and Wang [130]. The maximum spherical harmonic l value of partial waves inside the atomic spheres was set equal to 10. A local s-orbital was added

Figure 9.5: Crystal structure of the trigonal III-BC_2N phase.

to the LAPWs in order to avoid the presence of unphysical states (*e.g.* ghost bands) and to improve the flexibility of the basis set. FP-LAPW calculations were completed for the I-BC_2N at approximately 106 plane waves per atom (pws/atom) and 91 inequivalent **k**-points with a 7×7×7 k-mesh in the BZ, whilst for the II-BC_2N 119 pws/atom and 150 inequivalent **k**-points (8×8×6) were sufficient enough to achieve the desired accuracy. Finally, 101 pws/atom and 95 inequivalent **k**-points (9×9×5) were employed to describe the trigonal III-BC_2N phase. For all the investigated model systems, the difference in total energies were converged to below 0.002 eV with respect to **k**-point integration and kinetic energy cut-off. For carbon, nitrogen and boron the same muffin-tin radius of 1.40 Å was kept in all the analysed structures.

9.4 BC_2N phases and their relative stability

From the performed calculations both methods, FP-LAPW and US-PP, predict for the III-BC_2N to be the most stable structure (Tab. 9.5). With the use of the US-PP method this phase is estimated to be around 0.24 eV/atom more stable than I and II and close to the energy of the layered BC_2N. Calculations computed with the FP-LAPW tend to emphasise the energy differences between the various BC_2N structures. Nevertheless, the energy trend agrees quite well with the US-PP estimations (see Tab. 9.6). According to

Structure	V_o	$E_{coh.}$	B	B′
cubic diamond	5.488	-10.15800	463.68	3.68
(exp.)[8]	(5.673)		(443)	(3.67)
hexagonal diamond	5.508	-10.12760	456.03	3.68
(exp.)[196]	(5.61-5.67)			
c-BN	5.705	-9.74120	396.60	3.61
(exp.)[197]	(5.930)		(369-382)	(4.0-4.5)
h-BN	8.853	-9.69480	248.76	3.94
(exp.)[198]	(9.042)			
graphitic-BC_2N	8.403	-9.69482	276.99	3.43
I-BC_2N	5.679	-9.51096	459.41	2.11
II-BC_2N	5.673	-9.51404	408.95	3.54
III-BC_2N	5.653	-9.75195	420.13	3.40

Table 9.5: Structural and cohesive properties of various phases: atomic volume V_o ($Å^3$), bulk modulus B (GPa), pressure derivatives B′ and cohesive energy $E_{coh.}$ (eV/atom). The latter values have been obtained by taking the difference between the total energy of the solids and the ground-state energies of the spherical non spin-polarised atoms. No correction for zero-point motion has been made.

the bond counting rule, phase III contains a large number of C-C and B-N bonds and no B-B or N-N connections are present. The larger stability found for this phase can be addressed to the presence of C_6 and B_3N_3 rings connected to each other by C-B and C-N bonds. As already predicted by Tateyama *et al.* [20], phases made up of alternate -C-C- and -B-N- rings show a significant increasing of the stability. As a matter of fact the lowering in the cohesive energy found for the phase I-BC_2N can be attributed to the fact that the pure -C-C- and -B-N- chains are repetitively broken by the presence of B and C atoms (refer to the *zig-zag* ion chains going from left to right of Fig. 9.3). The US-PP energy curves of the phases I, II and III are shown in Fig. 9.6 together with some of the starting materials. All the presented systems have previously been optimised with the same method of calculation. For simplicity, the *graphitic*-BC_2N phase has been taken from the semi-conducting model (II) for a BC_2N monolayer proposed by Liu, Wentzcovitch and Cohen [166]. Assuming the graphite-like stacking AB of these sheets (Fig. 9.7), an orthorhombic crystal with an Ama2 (40) space group has been found after having performed the full geometry relaxation. The optimised structural parameters have been used to represent the *graphitic*-BC_2N model phase (Tab. 9.7). The *h*-BN refers to the layered hexagonal BN structure (graphite-like form) with four atoms in the unit cell

BC_2N structure	ΔE_{US-PP}	$\Delta E_{FP-LAPW}$
graphitic	0.0	0.0
I	+0.184	+0.202
II	+0.181	+0.197
III	-0.057	-0.073

Table 9.6: Calculated energy difference, ΔE (eV/atom), for various phases relative to the *graphitic*-BC_2N form.

[198][2]. This system exhibits an $AA^{'}AA^{'}$... stacking sequence with boron atoms in layer A placed directly below the nitrogen atoms in layer A' (see Fig. 9.8). The diamond-like form of BN (*c*-BN) has a zinc blende structure with space group $F\overline{4}3m$ (Fig. 9.9). This cubic form shows two atoms·cell^{-1} and a lattice constant of 3.615 Å [2][3].

From the energy-volume curves it is clear that the phases I- and II-BC_2N could only be metastable forms of the heterodiamond BC_2N system while the III-BC_2N is in principle expected to be in competition with the formation of the graphitic-like model. Since the energy curves of both I- and II-BC_2N lay at about 0.65 and 0.23 eV/atom (cfr. Tab. 9.5 and Fig. 9.6), respectively above the curves of diamond and *c*-BN, a segregation in a mixture of the starting materials is expected during a hypothetical attempt of preparation. Starting from the *graphitic*-BC_2N a transition pressure of ~ 65 GPa has been predicted in order to obtain the formation of the phases I- and II-BC_2N (Fig. 9.10). On the contrary the energy curve minimum relative to the III-BC_2N appears very close to that of the cubic and hexagonal BN. This phase is also slightly more stable (0.057 eV/atom) than the layered BC_2N form. Therefore, in all probability it could be synthesised over the phases I and II, and a competition with the formation of the *graphitic*-BC_2N is also very probable to happen.

9.4.1 Enthalpy of formation

From the values of the cohesive energies it is possible to estimate the standard enthalpy for the formation reaction of a three-dimensional BC_2N phase as in Eq. 9.1. The energies have been computed with the accurate FP-LAPW method as a function of different exchange-correlation functionals (values are listed in Tabs. 9.8 and 8.2).

$$2C_{(c)} + B_{(c)} + \frac{1}{2}N_{2(g)} \rightarrow BC_2N_{(c)} \tag{9.1}$$

[2]Space group: $P\overline{6}m2$ (187). Optimised cell parameters: a=b=2.481 Å, c=6.643 Å, α=β=90° and γ=120°. Equilibrium atom positions: $B_1(0,0,\frac{1}{2})$, $B_2(\frac{1}{3},\frac{2}{3},0)$, $N_1(0,0,0)$, $N_2(\frac{1}{3},\frac{2}{3},\frac{1}{2})$

[3]Atomic positions: B(0,0,0) and $N(\frac{1}{4},\frac{1}{4},\frac{1}{4})$. Optimised lattice constant: a=3.570 Å

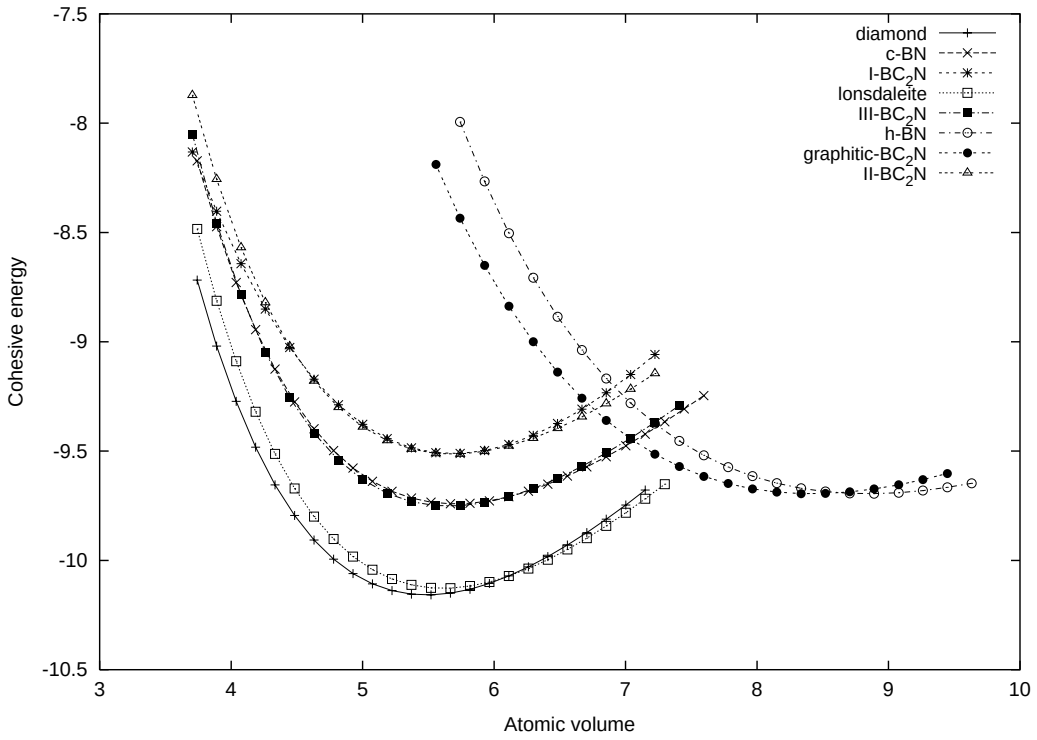

Figure 9.6: Cohesive energies (eV/atom) as a function of the atomic volume (Å^3/atom) for the starting materials and BC_2N structures. The curves were generated with the US-PP/LDA method.

For the calculation of the ΔH_f^o it has been assumed that diamond[4] and molecular nitrogen are the most stable forms (at 25 °C and 1 atm) of carbon and nitrogen, respectively. For Boron, the phase α_{12}-boron (α_{12}-B) has been used as reference material. In spite of the many different allotropes of solid boron [196], we consider here only the simplest form, the α-rhombohedral phase (metastable at ambient conditions), which shows one 12-atom icosahedron per primitive cell [5]. The calculated standard molar enthalpy change of formation at 0 K ($\Delta H_{f,0}^o$) ranges for the phase III between -208 (LDA) and -136/-129 kJ/mol (PBE/PW91) depending on the employed exchange-correlation functional

[4]As stated in Sec. 8.2.3 calculations show small differences in the cohesive energies of diamond and graphite. Therefore, using diamond as a starting material instead of graphite brings only a slight changing in the magnitude of the resulting enthalpy of formation.

[5]Details on the structural data for α_{12}-B are given in Ref. [196]. The crystal is rhombohedral with a=5.057 Å , α=58.06° and the boron atoms located at ±(xxz),±(xzx) and ±(zxx). For the six B(1) atoms, x=0.0104 and z=-0.3427 while for the six B(2) atoms, x=0.2206 and z=-0.3677.

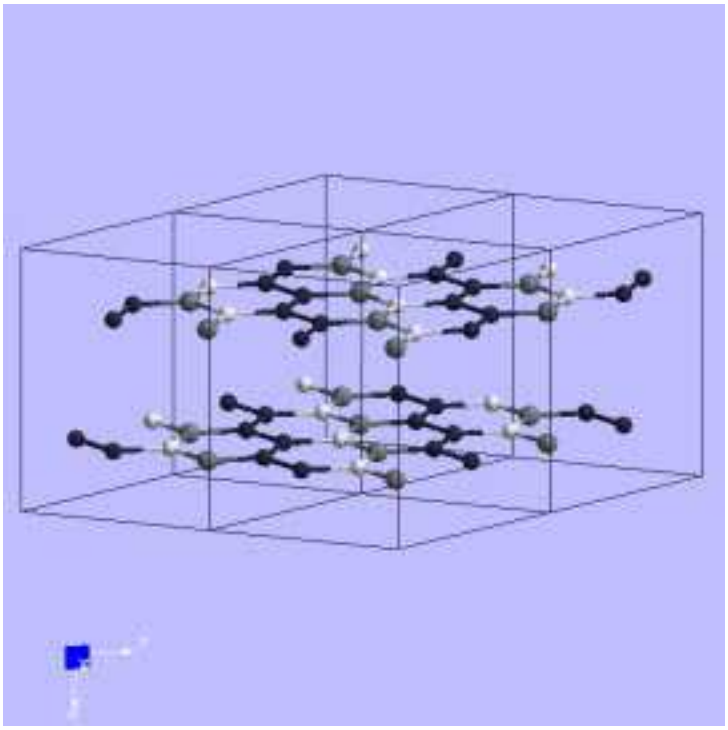

Figure 9.7: Crystal structure of the orthorhombic *graphitic*-BC_2N model phase.

(see Tab. 9.9). Using the cohesive energies of graphite and *graphitic*-BC_2N, calculation suggest an enthalpy of formation of the order of -180, -82 and -83 kJ/mol for LDA, PBE and PW91, respectively. The quality of these estimations has been verified when trying to reproduce the heat of formation of cubic boron nitride (Eq. 9.2).

$$B_{(c)} + \frac{1}{2}N_{2(g)} \rightarrow BN_{(c)} \tag{9.2}$$

Using the GGA approach it has been computed a $\Delta H^o_{f,0}$ of -240.3 (PBE) and -242.7 kJ/mol (PW91), which compares reasonably well with the experimental data: $\Delta H^o_{f,298}$=-254.4 [199] and -266.9±2.2 kJ/mol [200]. On the other hand, the LDA calculation gives an enthalpy of formation sensibly larger than the experimental value with a magnitude of -315.0 kJ/mol.

Therefore, after having probed the employed calculational scheme on *c*-BN, it is possible to conclude that results from PBE and PW91 should be accurates enough to indicate the phase III of BC_2N as an exceedingly stable substance with a formation reaction largely favoured (exothermic) with respect to those of the C_3N_4 and $C_{11}N_4$ (cfr. with Sec. 8.2.3

Property	*graphitic*-BC_2N
Crystal system	Orthorhombic
Space group	Ama2 (40)
Atoms/unit cell	16
Atom type	Coordinates (x, y, z)
C_1	(0.2500, 0.8333, 0.9378)
C_2	(0.2500, 0.2500, 0.6875)
C_3	(0.2500, 0.2500, 0.1875)
C_4	(0.2500, 0.3335, 0.9380)
B_1	(0.2500, 0.0000, 0.9375)
B_2	(0.2500, 0.0000, 0.4375)
N_1	(0.2500, 0.0833, 0.6878)
N_2	(0.2500, 0.0835, 0.1880)
Cell constants (Å)	a=6.819; b=8.591; c=4.860
α, β, γ (°)	90, 90, 90

Table 9.7: Optimised parameters for the *graphitic*-BC_2N model phase.

in p. 48 and Sec. 8.3.4 in p. 81). The synthesis and characterisation of novel hard BC_2N materials seems to be thus more promising and feasible than CN_x samples. As a matter of fact, the recently announced preparation of a stable and crystalline *cubic*-BC_2N phase [6] could be interpreted in terms of the above thermodynamic outcome.

Moreover, the estimation of the enthalpy for the formation reaction of a sp^3-bonded BC_2N phase as in Eq. 9.3 suggests that a hypothetical synthesis route to form BC_2N from *c*-BN and diamond would require the overcoming of a positive enthalpy of formation of about 108 kJ/mol for the phase III within the local density approximation (Tab. 9.10).

$$c - BN_{(c)} + 2C_{(c)} \rightarrow BC_2N_{(c)} \tag{9.3}$$

Looking at the magnitudes of the computed $\Delta H_{f,0}$'s and neglecting all the kinetic considerations, which might however play an important rule in the synthesis of BCN materials, the phase III of BC_2N will be probably results metastable with respect to a segregation into the end members (*i.e.* *c*-BN and diamond).

9.4.2 Discussion of the results

One might expect that compounds between BN and C would have a stability lower than diamond but at least close to that of *c*-BN. This is reasonably true when substitution leads to systems within which B-N bonds are maximised and favoured over the B-C and

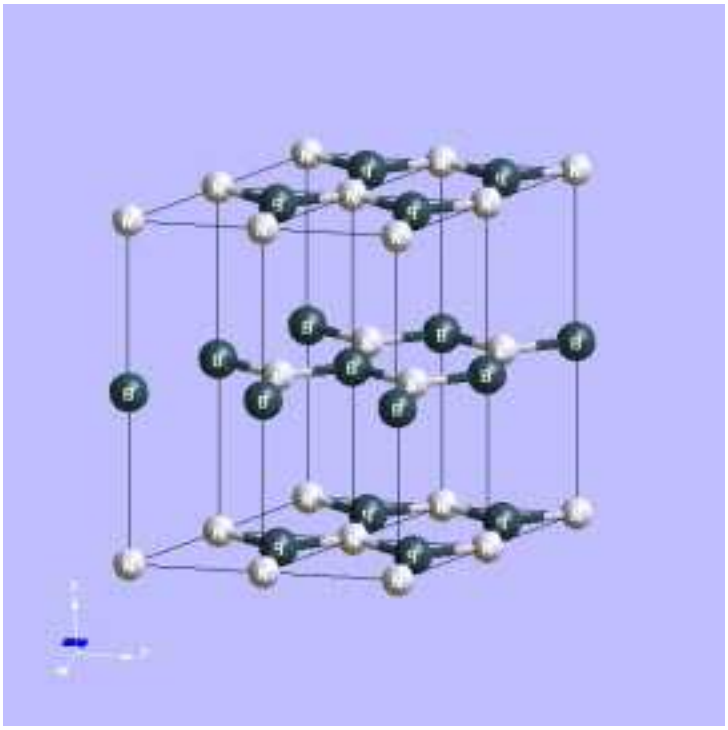

Figure 9.8: Crystal structure of the *h*-BN.

N-C connections. The presented orthorhombic BC_2N crystals show N atoms coordinated with two B and two C, whilst the B atoms are surrounded by two N and two C as shown in Fig. 9.11. Such a kind of configuration brings two N-C bonds around each N and two B-C bonds around each B. Compared to the *c*-BN phase we have here replaced four strong B-N connections with four weaker bonds (*i.e.* 2 N-C and 2 B-C)[6]. Even though robust C-C interactions are introduced in the system, they are not sufficient enough to compensate the loss of two B-N bonds at each N and B sites. Moreover, the C-C interactions, which usually have large bond energies (values are close to that of B-N from experimental standard formation enthalpy [202]), are weakened with respect to those found in diamond (pure covalent system) because of the presence of polarised $\text{-}\overset{\delta^+}{C}\text{-}\overset{\delta^-}{C}\text{-}$ bonds. The covalent character is thus reduced due to the presence of electron rich (N) and electron poor (B) neighbouring atoms. This effect is clearly shown in Fig. 9.12.

[6]There are six different possible types of chemical bonds in BC_2N and their bond energies can be estimated from experimental standard formation enthalpy [202]. The estimated bond energies of C-C, B-C, N-C, B-N, B-B and N-N are 3.71, 2.59, 2.83, 4.00, 2.32 and 2.11 eV, respectively.

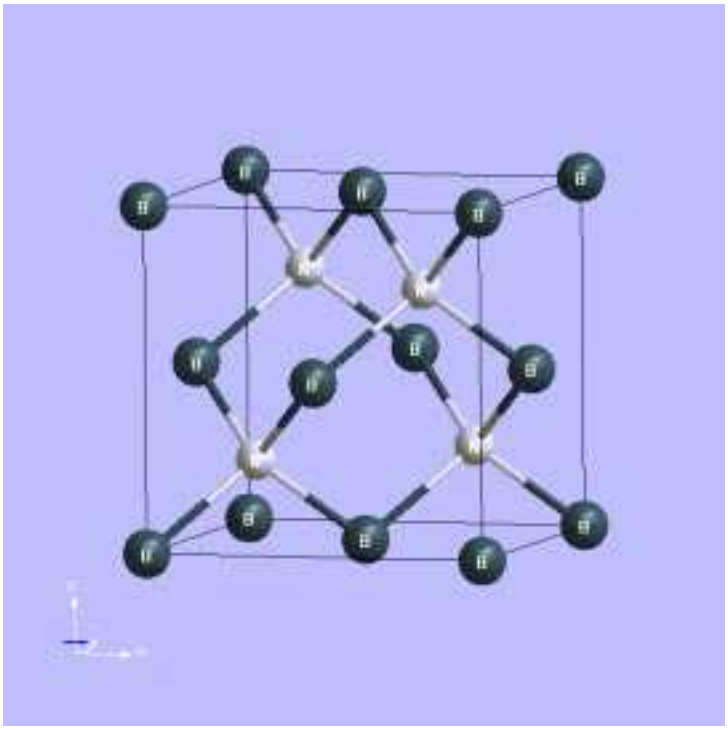

Figure 9.9: Unit cell of the *c*-BN.

The overall outcome accounts for the decreasing of the stability of the two orthorhombic phases with respect to the *c*-BN system. As a matter of fact, the calculated US-PP/LDA cohesive energies relative to the two BC_2N systems are smaller than that of *c*-BN and diamond. The same energy trend has also been obtained with the FP-LAPW/LDA calculational scheme. Another important thing that has to be noted is the fact that the presented orthorhombic phases have shown a very similar energy stability. This is not surprising since the bonding configuration around the B and N sites is equivalent in both cases. Such tendency clearly reflects the above picture where the local chemical connections are assumed to play the most important role in accounting for the relative stability of sp^3-bonded boron carbon nitrides.

Nonetheless, it is worthwhile to stress that when performing carbon substitution in the hexagonal diamond it becomes possible to design BC_2N materials, such as the trigonal III-BC_2N model system, with only one C atom at each B and N sites. As one might expect the phase stability can be here increased leading to a cohesive energy approaching that of *c*-BN. These phases represent the highest level of stability reachable with a three-

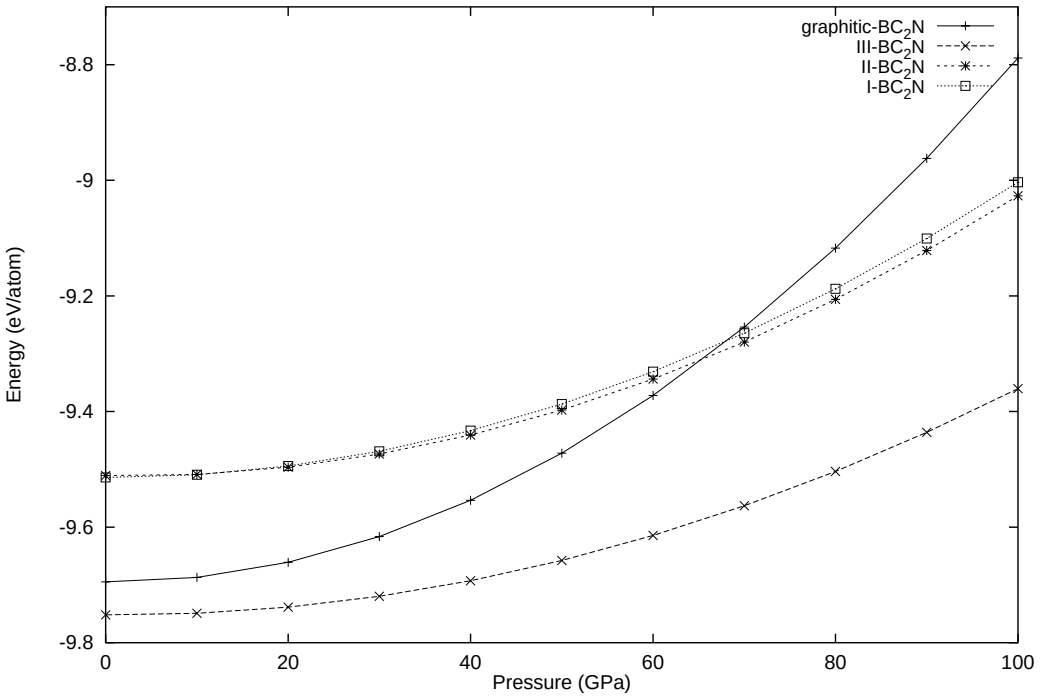

Figure 9.10: Energy versus pressure for different BC_2N phases (US-PP).

dimensional model in the BC_2N stoichiometry. This upper limit lies very close to the cohesive energy of *c*-BN but it cannot approach that of diamond due to the restriction imposed by the bonding counting rule.

9.5 Theoretical estimation of hardness

Prima facie, we briefly describe the procedure used to calculate the complete set of elastic constants for the investigated phases. In the orthorhombic BC_2N models (I and II) there are nine-independent elastic constants, namely c_{11}, c_{22}, c_{33}, c_{44}, c_{55}, c_{66}, c_{12}, c_{13} and c_{23} [171]. The values of c_{11}, c_{22}, c_{33}, c_{44}, c_{55} and c_{66} can be directly deduced from the fitting of the energy *vs.* strain, while c_{12}, c_{13} and c_{23} are found by scaling the fitting parameter with the already calculated c_{11}, c_{22} and c_{33} (see Chapter 8, Sec. 8.3.5, p. 83). For the trigonal phase (III-BC_2N), the six-independent elastic constants, c_{11}, c_{12}, c_{13}, c_{14}, c_{33} and c_{44} [34] can be evaluated by applying the strains listed in Tab. 9.11 to the equilibrium lattice and determine the resulting change in the total energy. For both orthorhombic and

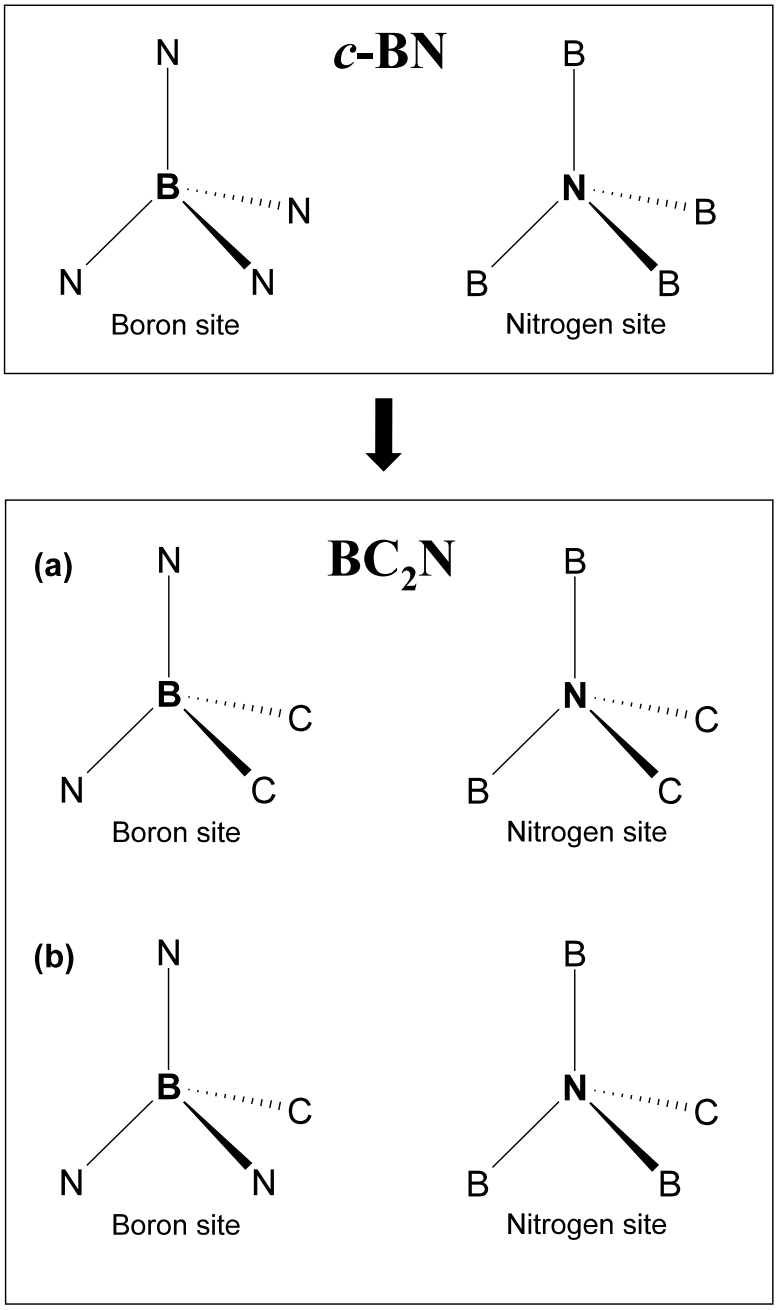

Figure 9.11: Idealised chemical environment around the B/N site in c-BN and various BC_2N phases. Part (a) of the scheme refers to the orthorhombic phases (I and II) while, part (b) concerns the local chemical bonding of the phase III.

$E_{coh.}$	α_{12}-B	*c*-BN	*h*-BN	I	II	III	*graphitic*
LDA	-7.20, -7.40 [137]	-8.07	-7.99	-7.94	-7.95	-8.22	-8.15
PBE	-6.43	-7.03	-6.93	-6.87	-6.88	-7.17	-7.10
PW91	-6.45	-7.05	-6.93	-6.88	-6.90	-7.15	-7.10
exp.	-5.90 [201]	-6.60 [67]	-	-	-	-	-

Table 9.8: Calculated cohesive energies ($E_{coh.}$ in eV/atom) for various BC_2N phases and some of the starting materials as a function of different exchange-correlation functionals.

	$\Delta H^o_{f,0}$ (kJ/mol)			
method	I	II	III	*graphitic*
LDA	-99	-103	-208	-180 (-180)
PBE	-20	-24	-136	-109 (-82)
PW91	-25	-32	-129	-110 (-83)

Table 9.9: Calculated standard enthalpy of formation. Values in parenthesis correspond to the formation energy of *graphitic*-BC_2N when graphite is taken as a starting material.

trigonal symmetries, small strains have been applied ($\delta = \pm 0.02n, n = 0-3$) to avoid the influence of higher order terms on the calculated elastic constants. The isotropic shear modulus is then calculated for the orthorhombic phases by using the relation 8.17 as written in Chapter 8, Sec. 8.3.5, p. 83. For the trigonal BC_2N, the value of the isotropic G can be estimated from Eq. 3.7 (Chapter 3, Sec. 3.1.2, p. 12), knowing that $c_{11} = c_{22}$, $c_{23} = c_{13}$, $c_{44} = c_{55}$ and $c_{66} = \frac{1}{2}(c_{11} - c_{12})$. The isotropic trigonal shear modulus can be

	$\Delta H_{f,0}$ (kJ/mol)			
method	I	II	III	*graphitic*
LDA	214	212	108	137 (120)
PBE	220	216	104	131 (138)
PW91	218	210	114	133 (137)

Table 9.10: Calculated enthalpy of formation for the reaction: $c\text{-}BN_{(c)} + 2C_{(c)} \rightarrow BC_2N_{(c)}$. Values in parenthesis correspond to the formation enthalpy of the *graphitic*-BC_2N when the layered *h*-BN and graphite are used as reactants.

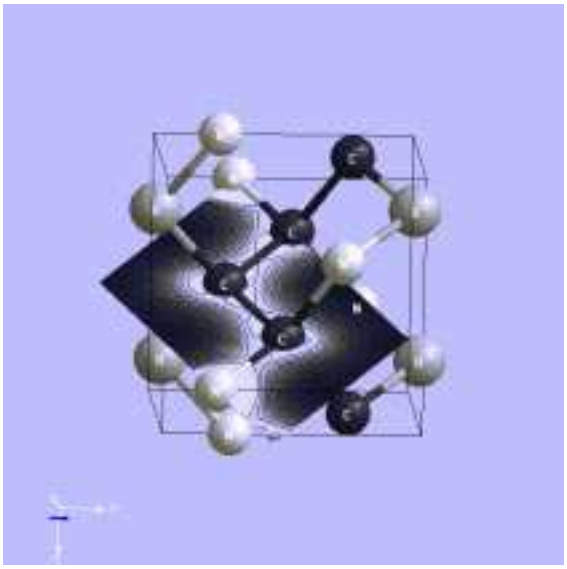

Figure 9.12: Valence electron density map showing the polarisation of the C-C bonds in I-BC_2N.

finally expressed as in the following:

$$G_{trig.} = \frac{1}{15}(\frac{7}{2}c_{11} - \frac{5}{2}c_{12} + c_{33} - 2c_{13} + 6c_{44}) \tag{9.4}$$

The complete set of elastic constants are shown in Tab. 9.12 together with the related G values. The calculated isotropic shear moduli for the proposed BC_2N phases are in between the values of diamond and *c*-BN. We estimate for the phases I, II and III values of 482.0 GPa, 461.9 GPa and 471.5 GPa respectively, while for diamond and *c*-BN 558.5 GPa and 425.9 GPa. By this it is implied that, in the substituted diamond a clear hardening of the system is found with respect to the cubic boron nitride. The calculated bulk moduli confirm the same trend, where the magnitudes of B are found in between those of the reference materials (Tab. 9.5). The only difference to be noted is that the bulk modulus estimates the hardness of the BC_2N crystals to be much closer to that of diamond than does the shear modulus. This general behaviour can be assigned to the different intrinsic characteristics that are distinguishing one modulus from the other. However, when considering the computational scheme used for the calculation of the c_{ij} constants, it is important to observe that errors can be easily accumulated in the evaluation of the total energies and in the fitting of the various energy curves. The introduction of arbitrary deformations of the unit cell followed by the calculation of the

Strain	Parameters	$\Delta E/V_o$
1	$\delta_{11} = \delta_{22} = -\frac{1}{2}\delta_{33} = \delta$	$[\frac{1}{4}(c_{11} + c_{12}) - c_{13} + \frac{1}{2}c_{33}]\delta^2$
2	$\delta_{11} = \delta_{22} = \delta_{33} = \delta$	$(c_{11} + c_{12} + 2c_{13} - \frac{1}{2}c_{33})\delta^2$
3	$2\delta_{23} = \delta$	$\frac{1}{2}c_{44}\delta^2$
4	$2\delta_{12} = \delta$	$\frac{1}{2}(c_{11} - c_{12})\delta^2$
5	$2\delta_{12} = 2\delta_{13} = \delta$	$[c_{14} + \frac{1}{2}c_{44} + \frac{1}{4}(c_{11} - c_{12})]\delta^2$
6	$\delta_{33} = \delta$	$\frac{1}{2}c_{33}\delta^2$

Table 9.11: Strains and elastic moduli for the trigonal phase. Unlisted δ_{ij} are set equal to zero.

total energy, which is many orders of magnitude larger than elastic energy, could also decrease the accuracy of the computed elastic moduli. However, despite the possibility to pile up a large amount of errors, the extrapolated isotropic shear moduli result for diamond and *c*-BN in good agreement with the experimental values ($G^{exp.}_{diam.}$=535 GPa [22], $G^{cal.}_{diam.}$=558.5 GPa and $G^{exp.}_{c-BN} = 409 \pm 6$ GPa [22], $G^{cal.}_{c-BN}$=425.9 GPa), proving thus the quality of this calculational procedure. Therefore, the larger difference in the shear moduli found in between the BC_2N phases and diamond can be considered as an index of an accentuated sensibility of G in describing the mechanical hardness of the materials.

Nonetheless, by using the estimated bulk and shear moduli the ratio B/G has been computed for the phase I to be of the order of 0.92, while for both phases II and III a value of 0.90 has been found (Tab. 9.13). Since these numbers are very similar to the one calculated for the α-$C_{11}N_4$ system (cfr. with data in Section 8.3.5, p. 89), the two classes of materials should nearly display the same degree of brittleness. The computed Poisson's ratios are also very close to the value of α-$C_{11}N_4$. The only difference has been found in the calculated Young's moduli, for which the BC_2N phases have shown E values that are in between *bl*-C_3N_4 and α-$C_{11}N_4$.

9.5.1 Mechanical stability

A necessary condition for a crystal to be mechanically stable is that the elastic constant matrix, C, be positive definite (*i.e.* Born's criterion). For a trigonal symmetry the c_{ij} matrix is represented in Eq. 9.5 and is positive definite if the determinants of the matrices

c_{ij}	I-BC_2N	II-BC_2N	III-BC_2N	diamond	lonsdaleite	*c*-BN
c_{11}	916.0	1003.0	925.3	1116.6 (1080)†	1448.0	824.6 (820)‡
c_{22}	1064.2	1106.1	-	-	-	-
c_{33}	939.0	938.1	942.8	-	1517.8	-
c_{44}	460.3	528.6	647.5	604.3 (557)†	-	495.8 (480)‡
c_{55}	524.0	496.5	-	-	486.8	-
c_{66}	627.5	384.9	-	-	-	-
c_{12}	120.2	27.1	320.3	137.2 (137)†	-84.7	182.6 (190)‡
c_{13}	199.6	153.4	95.6	-	1030.7	-
c_{14}	-	-	25	-	-	-
c_{23}	205.3	168.5	-	-	-	-
G	482.0	461.9	471.5	558.5 (535)§	510.5	425.9 (409$\pm$6)§

Values as compiled in Ref. ($\dagger$)=[8], ($\ddagger$)=[197] and ($\S$)=[22].

Table 9.12: Independent elastic constants, c_{ij}, and isotropic shear moduli for BC_2N, diamond, lonsdaleite and *c*-BN. Values are expressed in units of GPa.

of successive orders are all positive.

$$C = \begin{pmatrix} c_{11} & c_{12} & c_{13} & c_{14} & 0 & 0 \\ c_{12} & c_{11} & c_{13} & -c_{14} & 0 & 0 \\ c_{13} & c_{13} & c_{33} & 0 & 0 & 0 \\ c_{14} & -c_{14} & 0 & c_{44} & 0 & 0 \\ 0 & 0 & 0 & 0 & c_{44} & c_{14} \\ 0 & 0 & 0 & 0 & c_{14} & c_{66} \end{pmatrix} \tag{9.5}$$

These restrictions translates into the following conditions:

$$c_{11} - \mid c_{12} \mid > 0,\ (c_{11} + c_{12})\, c_{33} - 2c_{13}^2 > 0,\ (c_{11} - c_{12})\, c_{44} - 2c_{14}^2 > 0. \tag{9.6}$$

The calculated elastic constants for the phase III-BC_2N comply with the above relations indicating the presence of a certain mechanical stability for the trigonal model system. In the same way the c_{ij} constants calculated for the two orthorhombic models respect the Born stability criteria for an orthorhombic symmetry (Eq. 8.22 in Chapter 8, Sec. 8.3.5, p. 85). Therefore, even though they are not the most energetically favoured forms for the BC_2N stoichiometry, they could be at least metastable materials. At the moment it is important to highlight the fact that from an energetic point of view the phase III appears as the most likely candidate for an heterodiamond BC_2N system (see Sec. 9.4.2), though both shear and bulk moduli have shown a marked hardening for the model phase I. However, all the proposed three-dimensional BC_2N structures could

	I-BC_2N	II-BC_2N	III-BC_2N	*c*-BN	diamond
B[†]	441.0	416.1	424.0	396.6	463.7
B/G	0.92	0.90	0.90	0.93 (0.90-0.93)	0.83
E	1060	1011	1032	941 (850±150)[‡]	1196
ν	0.099	0.095	0.094	0.105 (0.095-0.105)	0.070

Table 9.13: The above table shows the calculated B/G ratio, Young's modulus (GPa) and Poisson's ratio of the studied BC_2N phases. Diamond and *c*-BN have also been listed as reference materials. Numbers given within brackets correspond to the use of the experimental B and G values of Tabs. 9.5 and 9.12. [†]Bulk modulus from the combination of the various elastic constants. [‡]Measured elastic modulus from nanoindentations of polycrystalline *c*-BN bulk samples [203].

likely behave, if properly synthesised, as hard materials capable to substitute diamond and *c*-BN in different mechanical applications. Compared to diamond, they should also show an increased resistance towards oxidation at high temperatures due to the presence of boron and nitrogen atoms.

9.6 Electronic density of states and band structure

9.6.1 The orthorhombic phases (I and II)

The density of states of the phase I-BC_2N (Fig. 9.13) shows a valence band mainly dominated by the states of the atoms N, C_1 and C_2. From the partial components of the DOS (not shown) it is found that the 2s orbitals of N dominate the bottom of the VB. At energies between -10 and -5 eV the N 2p dominate the DOS, while the VB edge consists principally of 2p orbitals of the C_1 atom. The bottom of the CB, just above the Fermi level, is principally determined by the states of N and C_2 (2p character) with some admixture of B states. The higher portion of the CB consists mostly of 2p orbitals of C_1 with some mixing of the B and N states. From the band structure analysis (Fig. 9.14) a direct LDA band gap of 2.04 eV has been found at the Γ point. For the II-BC_2N, the contribution of each atom to the total DOS is shown in Fig. 9.15. The VB DOS can be viewed as mainly composed of 2p orbitals from N and C_2 with some mixing of B and C_1 states, whilst the bottom of the CB is mostly derived from an admixture of the 2p orbitals of N and C_1. From the calculated band structure (Fig. 9.16) we obtain a direct E_g of 1.87 eV at Γ (at which the larger band dispersion is observed) and an indirect gap of 1.69 eV with the top of the valence band being at the point Γ and the bottom of the conduction band at S. It is worth to be noted that the calculated E_g, which results from

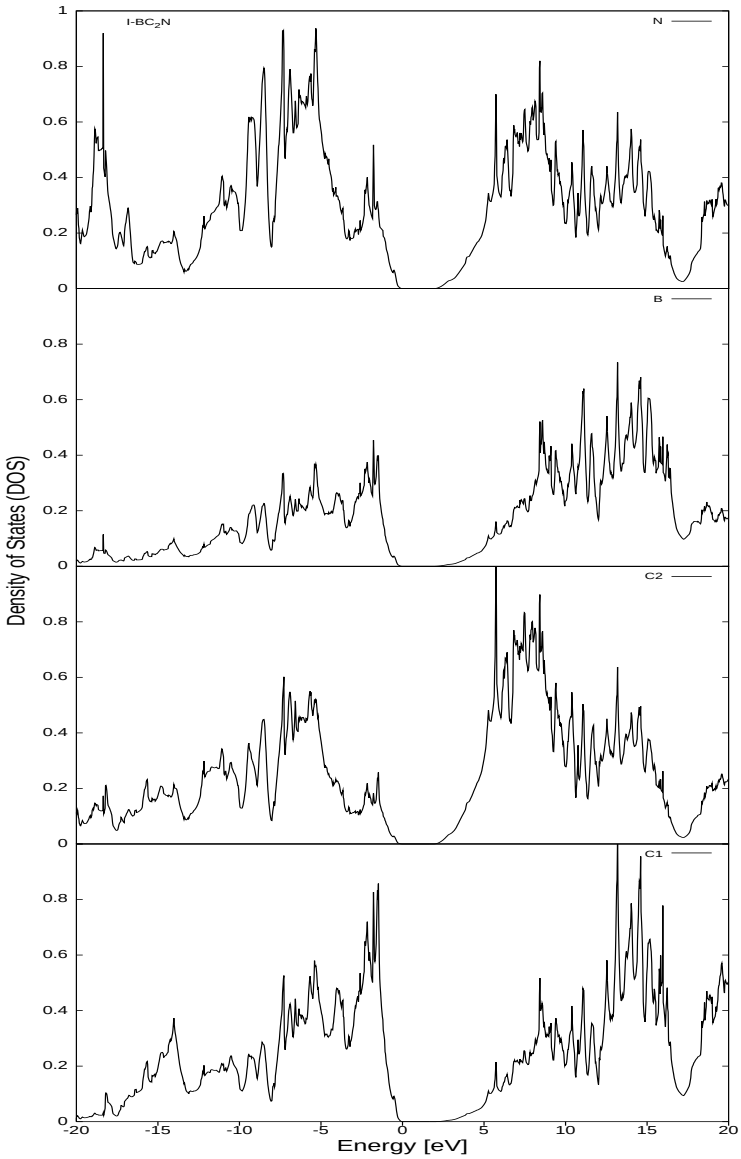

Figure 9.13: The calculated partial density of states of I-BC_2N.

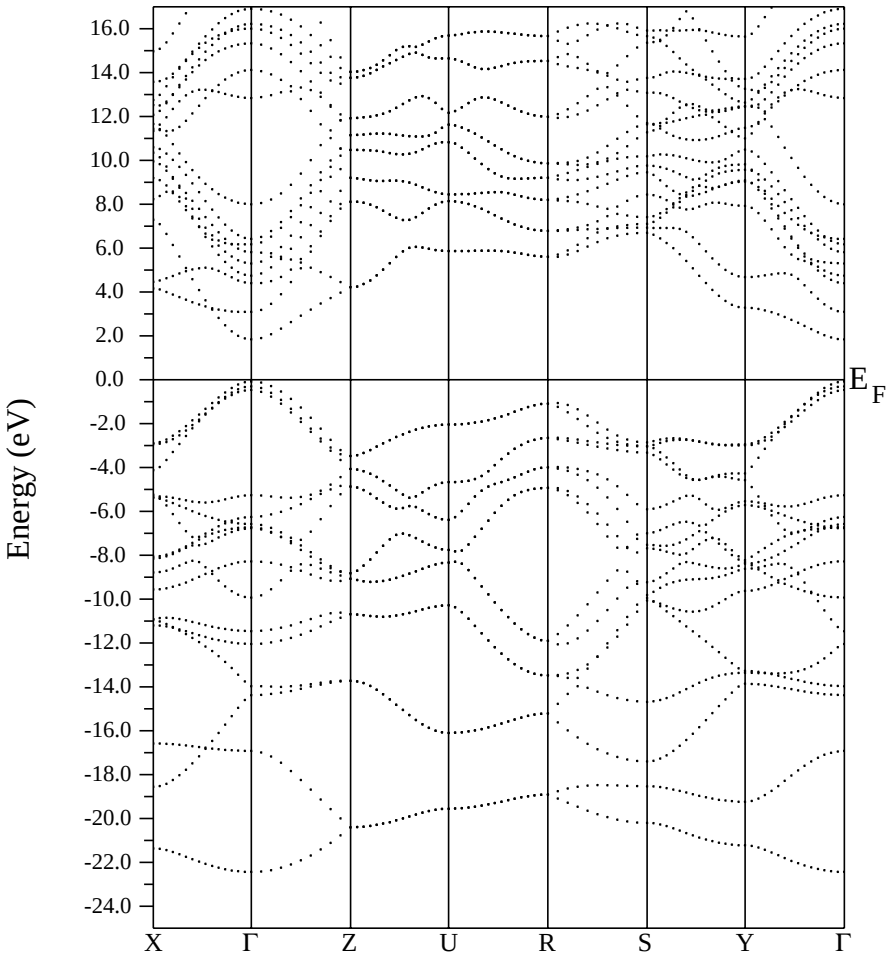

Figure 9.14: Band structure of I-BC_2N along the symmetry lines of the orthorhombic Brillouin zone: X=$(0\frac{1}{2}0)$ → Γ=(000) → Z=$(00\frac{1}{2})$ → U=$(0\frac{1}{2}\frac{1}{2})$ → R=$(\overline{\frac{1}{2}}\frac{1}{2}\frac{1}{2})$ → S=$(\overline{\frac{1}{2}}\frac{1}{2}0)$ → Y=$(\overline{\frac{1}{2}}00)$ → Γ=(000).

the interaction of the conduction electron waves with the ion cores of the crystal, are probably underestimated due to the use of the LDA approximation. The total density of states for the phases I- and II-BC_2N at the equilibrium geometries are shown in Fig. 9.17. In particular, the calculated DOS for the two orthorhombic phases are confronted with those of the cubic boron nitride and diamond. Looking at the total density of states it appears evident, from the changing in the shape of the VB, the presence of a different covalent character in the investigated BC_2N phases. Diamond presents a continuous valence band, pointing thus to the existence of a strong covalent mixing between the carbon states. On the other hand, *c*-BN shows in the bottom of the VB a band gap of $\sim$ 4 eV stating the presence of a ionic bonding condition. In between these two limits lies the BC_2N system where the VB results largely indented but with no band gaps. Such an intermediate situation is due to the various bonding types established between elements of group-III, -IV and -V: C-C (ΔZ=0), C-N (ΔZ=+1), B-C (ΔZ=-1) and B-N (ΔZ=0).

Our previous calculations, obtained by the same computational method, yielded a band gap of diamond and *c*-BN of 4.11 eV and 4.36 eV [7], respectively. As can be clearly seen the E_g values found for the two BC_2N structures are nearly half of those calculated for diamond and *c*-BN. If we roughly consider the C_2(BN) phase as made of diamond doped with 50 % of BN one might expect a band gap larger than that of diamond, that is $E_g > 4.11$ eV. On the contrary a sort of "*band gap bowing*" has been found according to W. R. L. Lambrecht [191, 192] upon alloying *c*-BN into diamond or vice versa. This effect can be here assigned to the shift of the carbon states (atoms C_1 and C_2) to higher energy in the VB and to an analogue lowering of the states in the CB. As a matter of fact the VB and CB edges are determined by the carbon atoms in both the two BC_2N systems. The shifting of the energies of the carbon states and the consequent reduction of the band gap can be correlated to a certain weakening (*i.e.* polarization effect) of the carbon bonds in mixed diamond-*c*-BN crystals. The two heterodiamond phases are predicted to have a band gap which is at the boundary between the semiconductors and the insulators. Nevertheless, in the phase I the size of the energy gap should be wide enough to avoid large thermal conductivity at room temperature. By considering the fraction of electrons excited across the gap roughly of order $e^{-E_g/2K_bT}$ and the value of K_bT at room temperature $\approx$ 0.025 eV we can assume that essentially a small part of electrons are excited across the gap ($e^{-40.8} \approx 1.9 \cdot 10^{-18}$). Wide band gap materials such as diamond, gallium nitride, silicon carbide, aluminum nitride, and cubic boron nitride are of great interest as they have potential for applications in the electronics, energy, aerospace and defense industries.

[7] cfr. with the experimental values of $E_g^{diam.}$=5.5 eV and E_g^{c-BN}=6.4 eV.

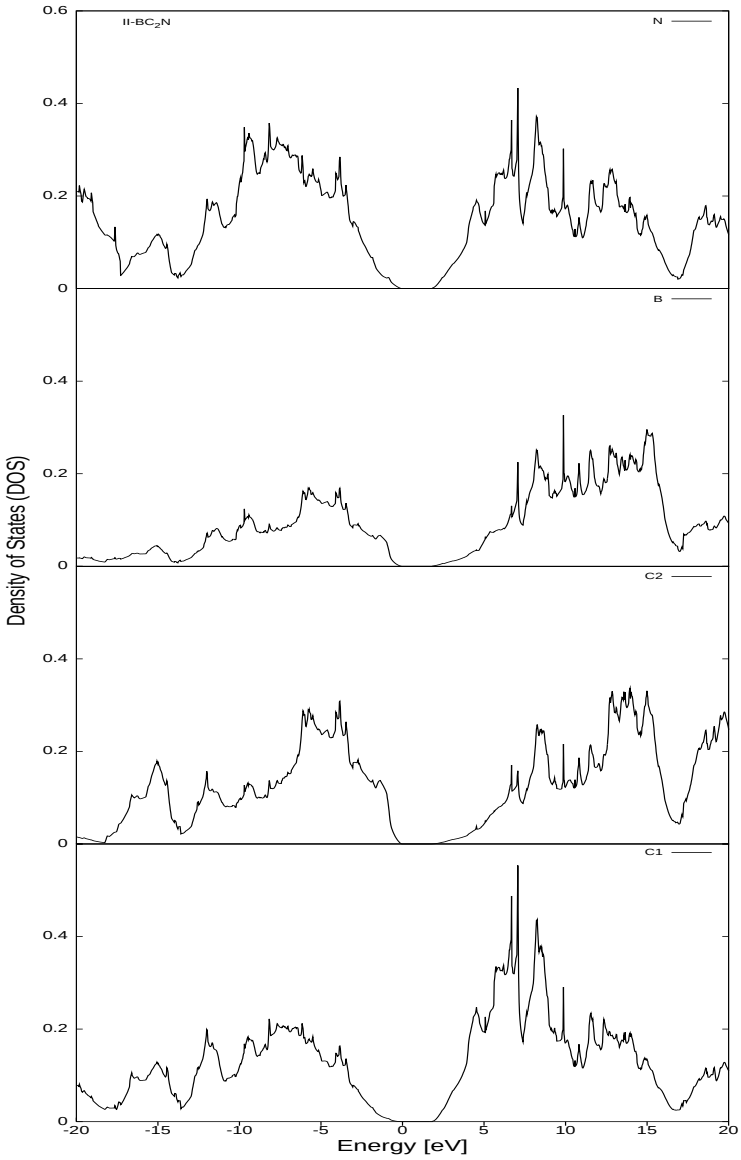

Figure 9.15: The calculated partial density of states of II-BC_2N.

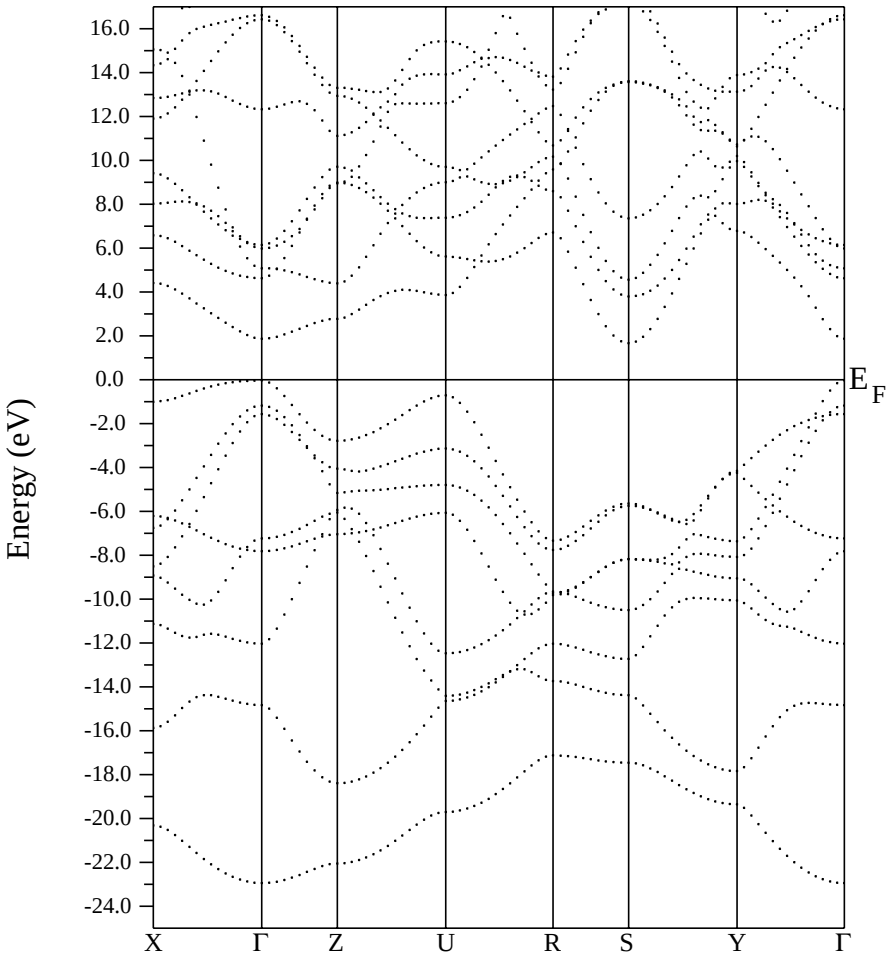

Figure 9.16: Band structure of II-BC_2N along the symmetry lines of the orthorhombic Brillouin zone: X=$(0\frac{1}{2}0)$ → Γ=(000) → Z=$(00\frac{1}{2})$ → U=$(0\frac{1}{2}\frac{1}{2})$ → R=$(\overline{\frac{1}{2}}\frac{1}{2}\frac{1}{2})$ → S=$(\overline{\frac{1}{2}}\frac{1}{2}0)$ → Y=$(\overline{\frac{1}{2}}00)$ → Γ=(000).

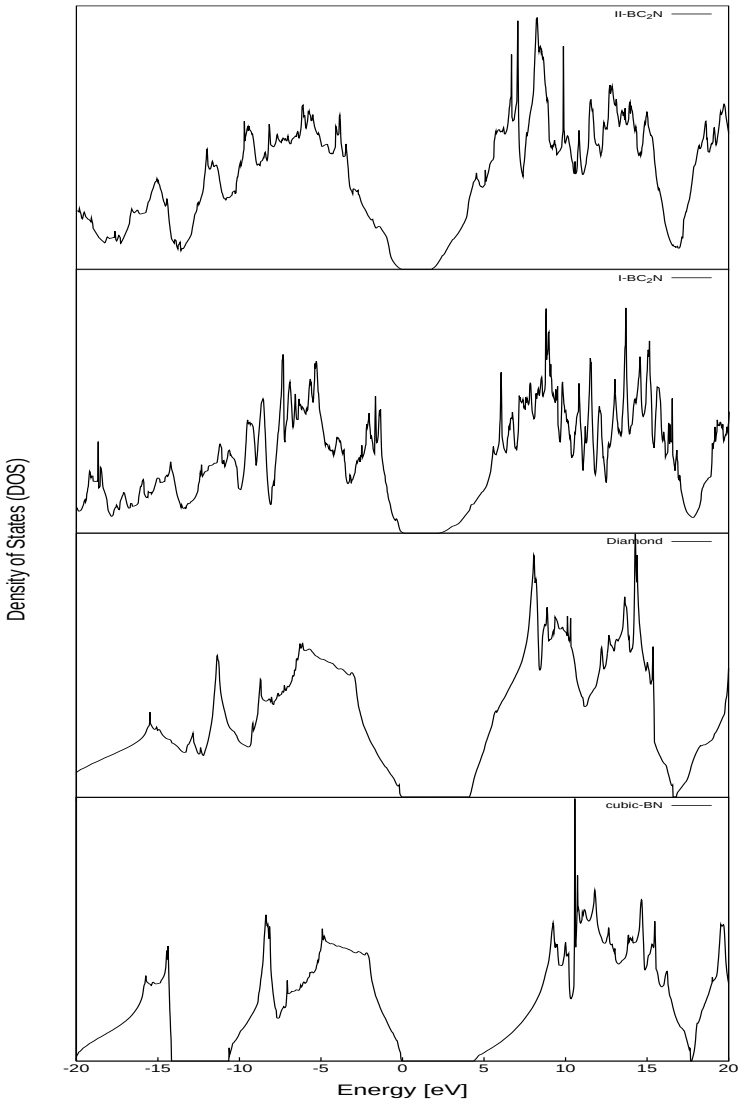

Figure 9.17: Total DOS for the orthorhombic phases I and II in arbitrary units.

9.6.2 The trigonal model structure (III-BC_2N)

In this phase the small peak located at the bottom of the VB is mainly derived from N 2s orbitals while at higher energy the N 2p states start to dominate the DOS (Fig. 9.18). The VB edge is slightly less sharp than the one found in the orthorhombic phases and is principally derived from the 2p orbitals of C_2 with a contribution of the N states with 2p character. The mixing of the B 2p orbitals with the other carbon and nitrogen states is basically present only at the top of the VB. The lower region of the CB consists mainly of N and C_1 2p orbitals, while in the upper region the N and C_2 2p states dominate the DOS. The two carbon atoms C_1 and C_2 are strongly contributing to the edges of the valence and conduction bands as in the previously described orthorhombic models. However, in phase III the smearing out of both VB and CB edges is somehow indicative of a certain lowering of the electron and hole effective masses. An indirect LDA energy band gap of 1.79 eV in magnitude was calculated with the top of the valence band being at the point Γ and the bottom of the conduction band at the point of symmetry K (Fig. 9.19).

9.7 Theoretical ELNES for BC_2N model systems

Electron energy loss spectroscopy is a technique widely used for the characterisation of boron carbon nitride samples because of its great ability to differentiate the types of bonding in a polymorphic material. As already mentioned in Section 8.3.6, the characteristic fine structure at the beginning of the core loss ionisation edges can provide important information for light elements. The possibility to obtain peculiar fingerprints for C, N and B atoms opens to the opportunity to distinguish different BC_2N phases in complex systems. Since the characterisation of dense BC_2N materials with a three-dimensional network is heavily restricted by the problem of getting pure crystalline samples, a theoretical approach to simulate ELNES becomes important for providing reference spectra.

In this Section we present the calculation of the energy loss near edge structures by using the formalism of M. Nelhiebel *et al.* [180] implemented within the FP-LAPW code. The spectra of carbon, nitrogen and boron K-shell excitation (n=1, l=0) are presented for the proposed BC_2N forms: I, II and III. Samples were simulated by averaging over all possible incident-beam directions since the attention is here primarily concentrated on the peak positions. Anisotropy effects which usually change the intensity of the peaks but do not shift their positions, are thus neglected. The energy of the incident electrons was fixed to 200 KeV while the energy loss of the first edge was put to 190, 285 and 400 eV for boron, carbon and nitrogen, respectively. The spectra relative to the inequivalent atom positions have been calculated separately and weighted to equal amounts in the following Figures.

In order to test our calculational scheme, diamond and c-BN have also been inves-

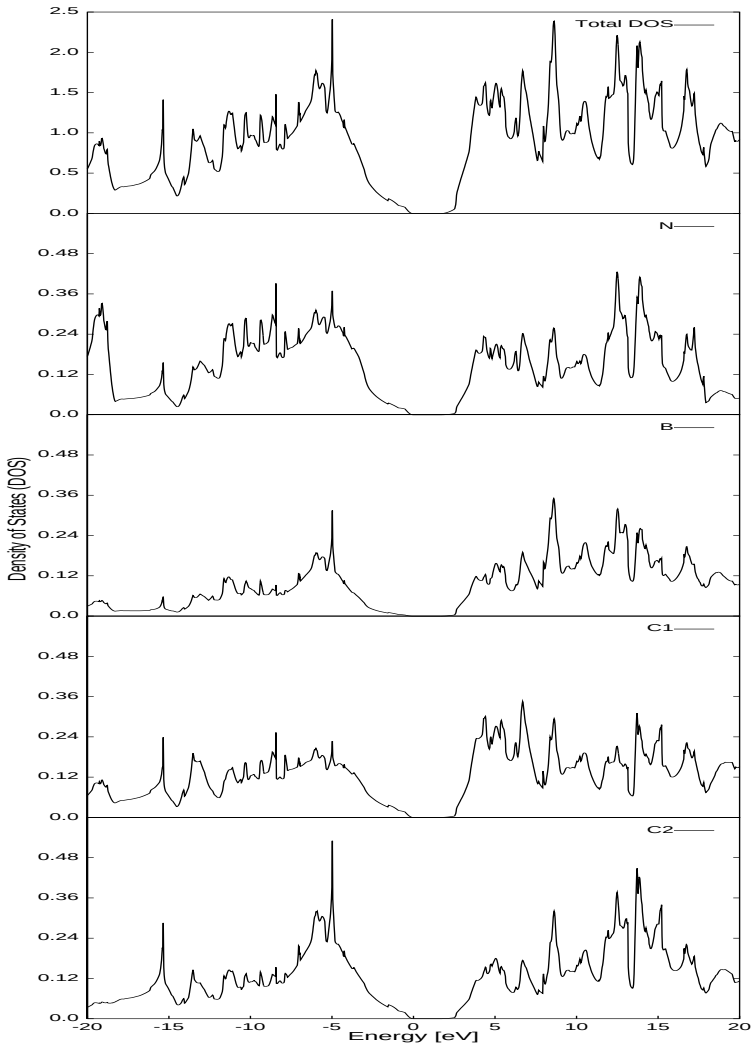

Figure 9.18: The calculated partial density of states of III-BC_2N.

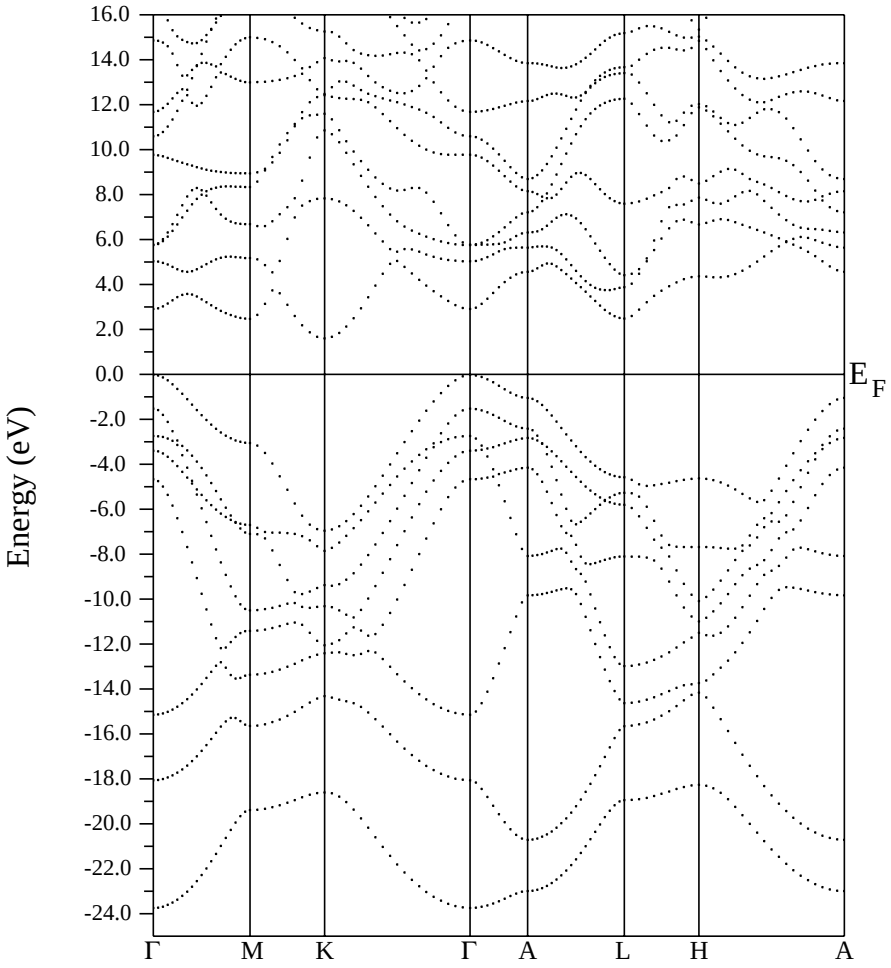

Figure 9.19: Band structure of III-BC_2N along the symmetry lines of the hexagonal Brillouin zone: Γ=(000) $\rightarrow$ M=$(0\frac{1}{2}0)$ $\rightarrow$ K=$(\frac{\overline{1}}{3}\frac{2}{3}0)$ $\rightarrow$ Γ=(000) $\rightarrow$ A=$(00\frac{1}{2})$ $\rightarrow$ L=$(0\frac{1}{2}\frac{1}{2})$ $\rightarrow$ H=$(\frac{\overline{1}}{3}\frac{2}{3}\frac{1}{2})$ $\rightarrow$ A=$(00\frac{1}{2})$.

tigated as representative of the BC_2N starting materials. Their relative C, N and B *K* ELNES spectra are presented and commented. The position of the most prominent peaks (labelled A to E) are listed in Tab. 9.14. The calculated relative peak positions

			Peak position relative to peak A					
Phase	Edge		A	B	C	C'	D	E
Diamond	C *K*	Thesis	0	5.3	13.6†;12.9‡	-	-	-
		MS[181]	0	4.4	12.0	-	-	-
		exp.[204]	0	5.5	12.9	-	-	-
c-BN	B *K*	Thesis	0	8.1	14.9	-	-	-
		MS[181]	0	5.5	14.2	-	-	-
		exp.[205]	0	6.9	16.9	-	-	-
	N *K*	Thesis	0	7.8	14.6	-	-	-
		MS[181]	0	6.1	15.2	-	-	-
		exp.[205]	0	6.4	14.8	-	-	-
I-BC_2N	C *K*	Thesis	0	6.2	11.7	15.9	-	-
	N *K*	"	0	6.1	11.4	-	16.0	-
	B *K*	"	0	4.8	10.1	-	15.0	-
II-BC_2N	C *K*	Thesis	0	5.5	11.1	15.1	-	-
	N *K*	"	0	4.8	10.8	-	15.3	-
	B *K*	"	0	4.2	10.3	-	14.3	-
III-BC_2N	C *K*	Thesis	0	3.7	9.5	-	15.3	19.2
	N *K*	"	0	8.5	11.3	-	15.3	19.3
	B *K*	"	0	3.7	7.8	-	19.2	0

†The energy position refers to the maximum of the peak.
‡The energy position refers to the averaged values of the two peaks extremes.

Table 9.14: Positions of the peaks A-E relative to the spectra shown in Figs. 9.20, 9.21 and 9.22. All the positions are scaled with respect to the main σ^* peak A and refer to the broadened spectra. Values are expressed in units of eV with an estimated error of ± 0.25 eV.

show a good match with the experimental finding and with the Multiple Scattering (MS) approach [181]. The largest error was found for the C peak in the calculation of the B *K* ELNES of *c*-BN. Both theoretical methods tend to underestimate its relative energy position by more than 2 eV with respect to the experimental curve. Peaks A to C in the C, N and B *K* edges of diamond and *c*-BN correspond to the electronic transitions 1s $\rightarrow$ σ^*. This feature usually identifies sp^3-hybridised materials. Low energy peaks related to 1s $\rightarrow$ π^* transitions are absent indicating the presence of a perfect tetrahedrally bonded

system.

The calculated plain and broadened spectra for the proposed BC_2N phases are shown in Figs. 9.20, 9.21 and 9.22 for the C, N and B K edges, respectively. The same instrumental broadening, corresponding to a Gaussian function, has been utilised in all the analysed spectra. In the C K ELNES the two orthorhombic phases show an evident splitting of the diamond C peak into C and C', indicating the possibility of identifying three-dimensional BC_2N phases in the carbon edge. Furthermore, in the N and B K ELNES the number of peaks vary with respect to the reference c-BN. In particular, in the energy range between 5 and 15 eV two σ^* peaks were found instead of one of the c-BN. Their relative peak positions are shown in details in Tab. 9.14. These different features are expected to be discovered in thin film samples for which EELS results as an important technique for bonding type characterisation.

Phase III presents plain spectra which are slightly more complicated to interpret than those of the two orthorhombic phases. Nonetheless, a characteristic feature, common to all the three edges, can be individuated in the energy region between 5-17 eV. The broadened spectra show three main σ^* peaks for the phase III of BC_2N, whereas the other phases possess only two. A very similar σ^* peak distribution should be thus exhibited in all those BC_2N samples for which the same bonding type configuration as in the phase III is expected.

9.7.1 The layered BC_2N model system

Beside the systematic study described for the three-dimensional BC_2N crystals, the band structure approach to ELNES is here used further to analyse the near-edge fine structure of a layered BC_2N system (*graphitic*-BC_2N). Owing to the absence of structurally well-characterised graphitic-like BC_2N reference samples, the results of such an investigation can serve as preliminary reference spectra for material characterisation until reliable ELNES become available. The calculated near-edge structure of the K edges are displayed in Figs. 9.23, 9.24 and 9.25. The estimated relative peak positions are shown in Tab. 9.15. All the three spectra exhibit a π^* peak between 0-7 eV and a complex σ^* feature between 9 and 16 eV. The separation between the π^* and σ^* features of *graphitic*-BC_2N are listed in Tab. 9.16 together with some of the experimental EELS results. Peak separations seem to match better with the values of Kouvetakis, though the comparison of the calculated values with those from experimental investigation is somehow aleatory. As a matter of fact, most of the published values given in Tab. 9.16 refer to hybrid boron-carbon-nitrogen phases with a stoichiometry "*approaching*" that of BC_2N.

Contrary to what has previously been found with MS calculations [181], the band structure method has shown some characteristic dissimilarities between K edges of h-BN/graphite and layered BC_2N which would likely provide an unambiguous identification of the *graphitic*-BC_2N phase. The calculated N K ELNES of BC_2N exhibits two π^*

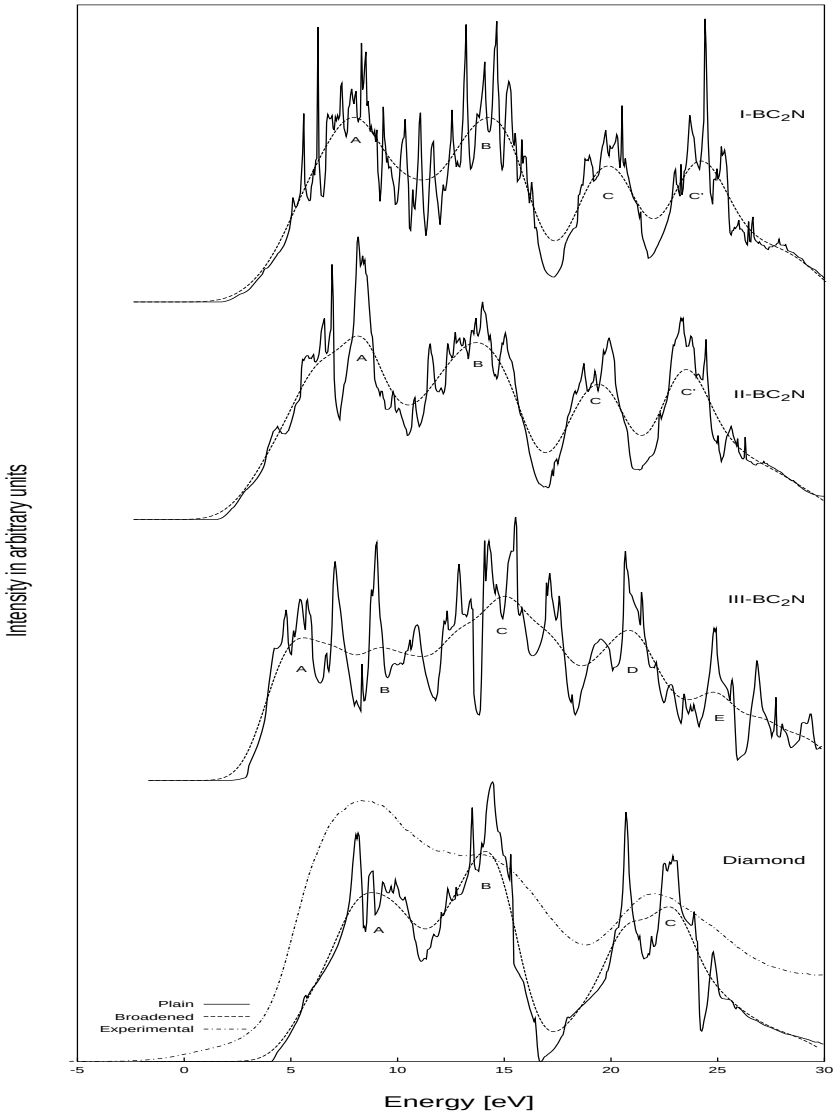

Figure 9.20: Theoretical C K ELNES of various phases (FP-LAPW). The experimental CVD diamond spectra [204] has been shifted by +1.05 eV along the energy axis in order to align its first σ^* peak with the one of the theoretical curve.

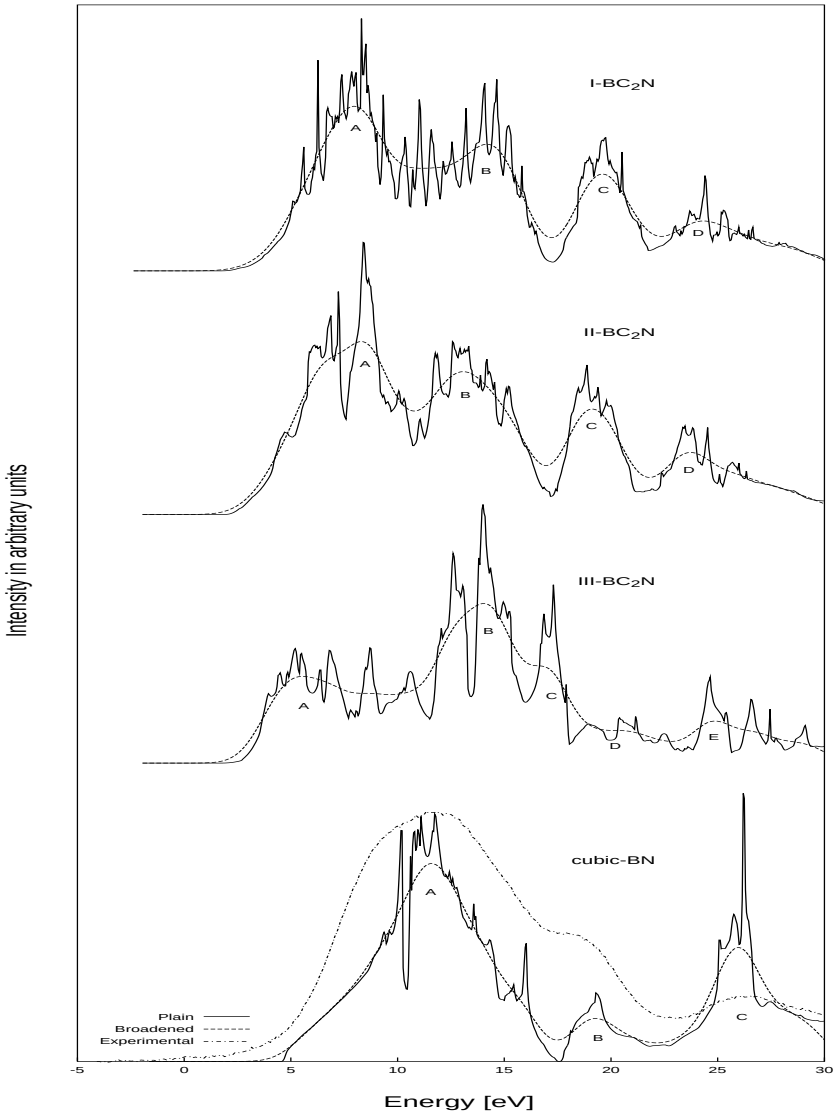

Figure 9.21: Theoretical N K ELNES of various phases (FP-LAPW). The spectra of the high pressure synthesised c-BN [205] has been moved by +2.05 eV to match the first theoretical σ^* peak.

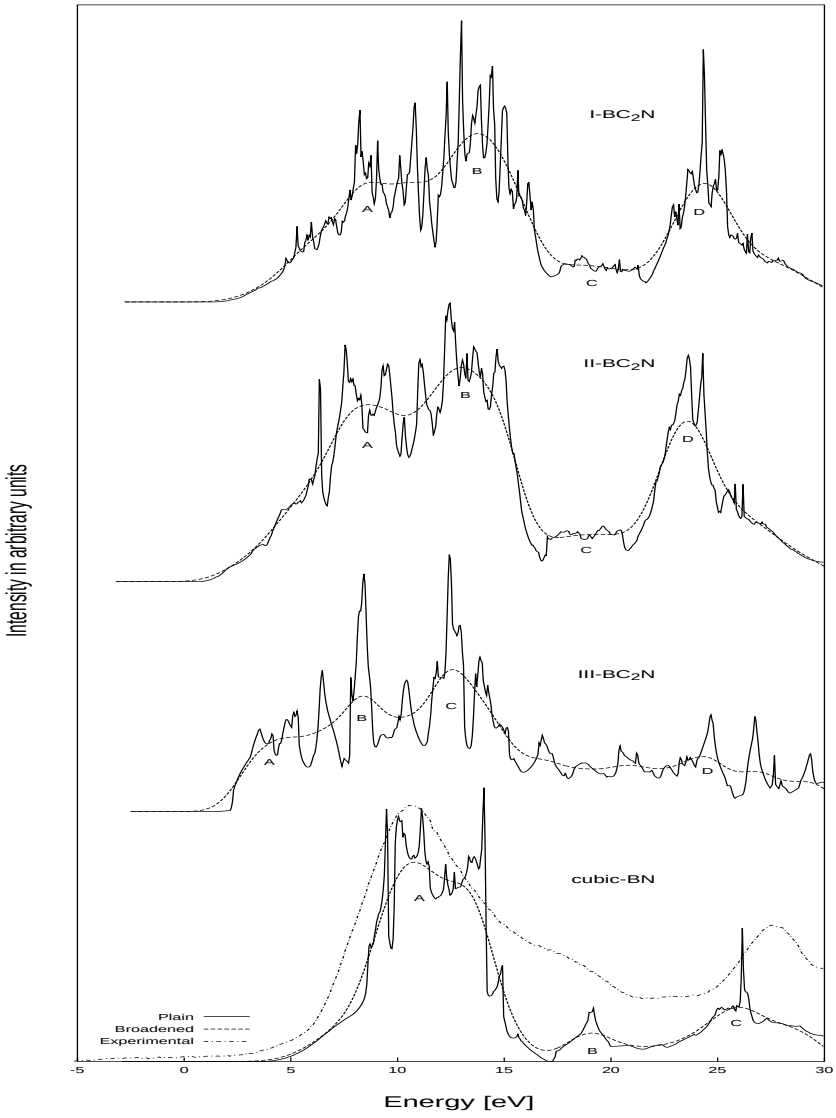

Figure 9.22: Theoretical B K ELNES of various phases (FP-LAPW). The high pressure synthesised c-BN spectra [205] has been shifted by +3.15 eV in order to align the first σ^* peak with the theoretical curve.

			Peak position relative to peak B (eV)							
Phase	Edge		A	A'	B	C	D	E	F	G
Graphite	C *K*	Thesis	-6.4	-	0	4.6	10.0	14.3	-	-
		MS[181]	-4.9	-	0	2.5	6.6	10.3	-	-
		exp.[181]	-6.8	-	0	4.4	11.2	14.7	-	-
h-BN	B *K*	Thesis	-6.3	-	0	4.3	8.5	15.5	-	-
		MS[181]	-8.4	-	0	5.7	-	12.5	-	-
		exp.[181]	-6.8	-	0	5.6	-	16.1	-	-
	N *K*	Thesis	-5.0	-	0	8.0	14.0	-	-	-
		MS[181]	-6.8	-	0	4.1	8.2	-	-	-
		exp.[181]	-6.1	-	0	7.2	17.6	-	-	-
graphitic-BC_2N	C *K*	Thesis	-6.9	-	0	2.5	4.1	6.8	13.1	15.8
	N *K*	"	-7.2	-3.8	0	1.9	4.4	6.7	12.6	15.9
	B *K*	"	-6.6	-3.9	0	2.3	4.4	11.6	16.1	-

Table 9.15: Positions of the peaks A-G relative to the spectra shown in Figs. 9.23, 9.24 and 9.25. All the energies are scaled with respect to the first σ^* peak B and refer to the broadened spectra. The estimated error is $\pm$ 0.25 eV.

features, namely π_1^* and π_2^*, separated by 3.4 eV. The same doublet of π^* peaks, but with a lower intensity, was found close to the onset of the σ^* peaks in the B *K* edge. Moreover, the marked changing found in the σ^* transition region of the C, N and B *K* ELNES might be utilised as a distinctive fingerprint in the identification of the *graphitic*-BC_2N. Therefore, in spite of the usually very large broadening found in the experimental EELS spectra (*i.e.* compared to the calculated one), the above peculiar characteristics, together with the changing in the peak positions (cfr. Tab. 9.15 and Figs. 9.23, 9.24 and 9.25), should likely guarantee the spectroscopic discrimination of a pure and crystalline layered BC_2N sample over the *K* edges of *h*-BN and graphite.

9.8 Conclusions

In the present study it has been performed the replacement of some of the carbon atoms with boron and nitrogen on the hexagonal and cubic diamond in order to design new hard and possibly stable BC_2N crystals. The substituted diamond structures have been relaxed with the US-PP method to obtain their fundamental ground states. Three novel heterodiamond phases have been presented, namely I-, II- and III-BC_2N, for which the hardness and the relative stability have been computed. Structures, such as the trigonal III-BC_2N, that contain alternate -C-C- and -B-N- rings and maximise the number of B-N

			$\pi_1^* - \sigma_1^*$ Separation in eV		
Author(s)	Method	Ref.	B *K*	C *K*	N *K*
M. Mattesini *et al.*	Band structure	Thesis	6.6	6.9	7.2
Wibbelt *et al.*	MS calculations	[181]	8.5	7.5	5.5
Kouvetakis *et al.*	exp.	[13]	7.0	6.5	6.0
Weng-Sieh *et al.*	exp.	[206]	8.0	7.0	6.0
Sasaki *et al.*	exp.	[207]	6.0	7.5	5.5

Table 9.16: Values of the separation between the first π^* and σ^* peaks ($\pm$ 0.5 eV) for the *K* edges of *graphitic*-BC_2N.

bonds are predicted to behave as some of the most stable forms of the three-dimensional BC_2N system. From the total energy calculations this phase results also in competition with the formation of the two-dimensional layered form. The standard molar enthalpy change of formation has been computed for the phase III to be exothermic and with a magnitude of -208 (LDA), -136 (PBE) or -129 (PW91) kJ/mol, depending on the type of the chosen exchange-correlation functional. This finding indicates the possibility of synthesising crystalline sp^3-bonded BC_2N samples at smoother temperature and pressure conditions with respect to the deposition of carbon nitrides.

Furthermore, two model BC_2N phases (I and II) formally derived by the carbon substituted *fcc* diamond have been presented. According to the bond counting rule these orthorhombic crystals have been found to be metastable with respect to diamond and cubic boron nitride. Total energy calculations predict for both structures a cohesive energy which is slightly lower than that of *c*-BN. This finding has been interpreted by considering the bonding configuration around each B and N sites (*i.e.* which maximises the B-N bonds) and the effect of the C-C bond polarisation. In particular, the latter upshot is also believed to have been responsible for the shifting in the DOS of the carbon states at higher and lower energies in the VB and CB, respectively. As a consequence an evident closing of the band gap has been found by going from diamond or *c*-BN to the isoelectronic BC_2N stoichiometry. The calculated $\Delta H^o_{f,0}$'s for the model systems I and II are still exothermic, however their values are at about 100 kJ/mol smaller than that of the phase III. Nonetheless, all the investigated BC_2N models have shown a thermodynamic stability significantly larger than the corresponding isoelectronic CN_x compounds.

The estimation of the hardness has been carried out by the calculation of the isotropic shear modulus. According to Gerk [30] and Teter [22], a better correlation with the hardness of solids is expected from the combination of the inequivalent elastic constants. However, I have also calculated the bulk modulus which has been considered for a long time as the best predictor of hard materials. With the use of US-PP method, calculations

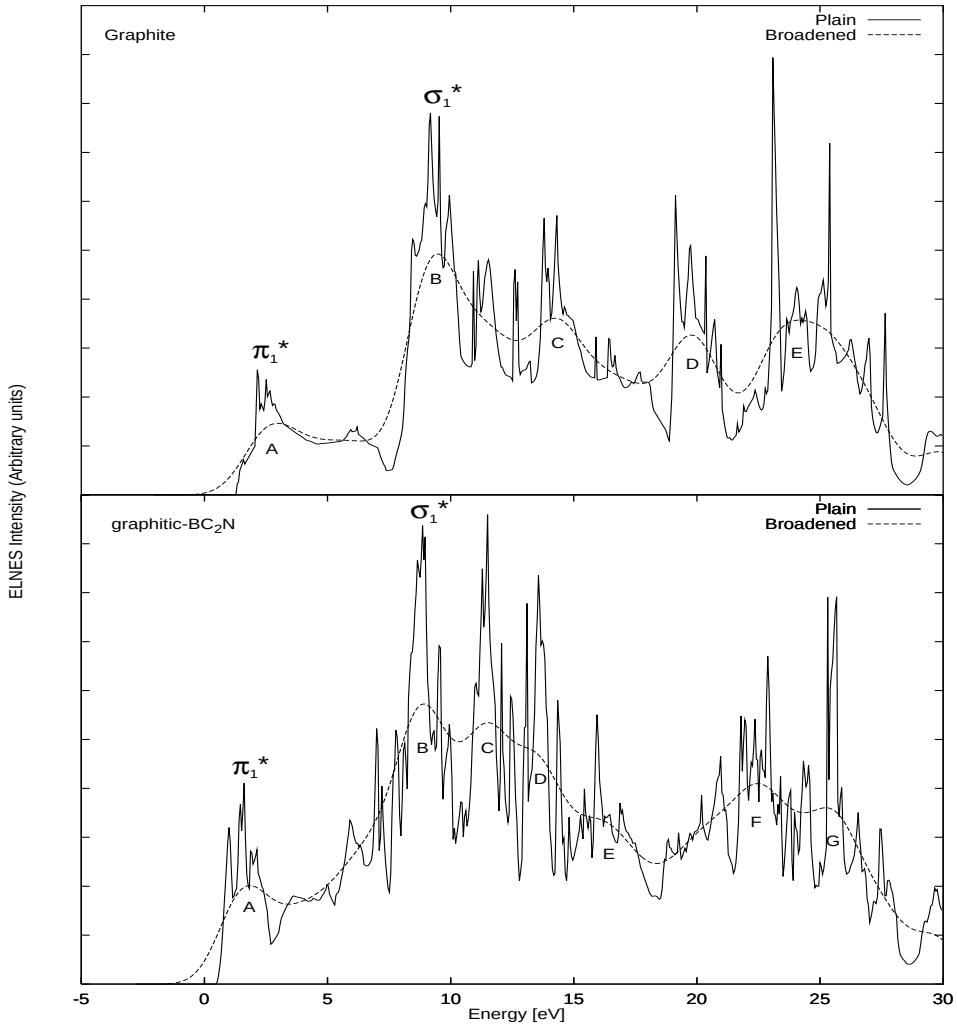

Figure 9.23: Theoretical C K ELNES of *graphitic*-BC_2N in comparison to Graphite.

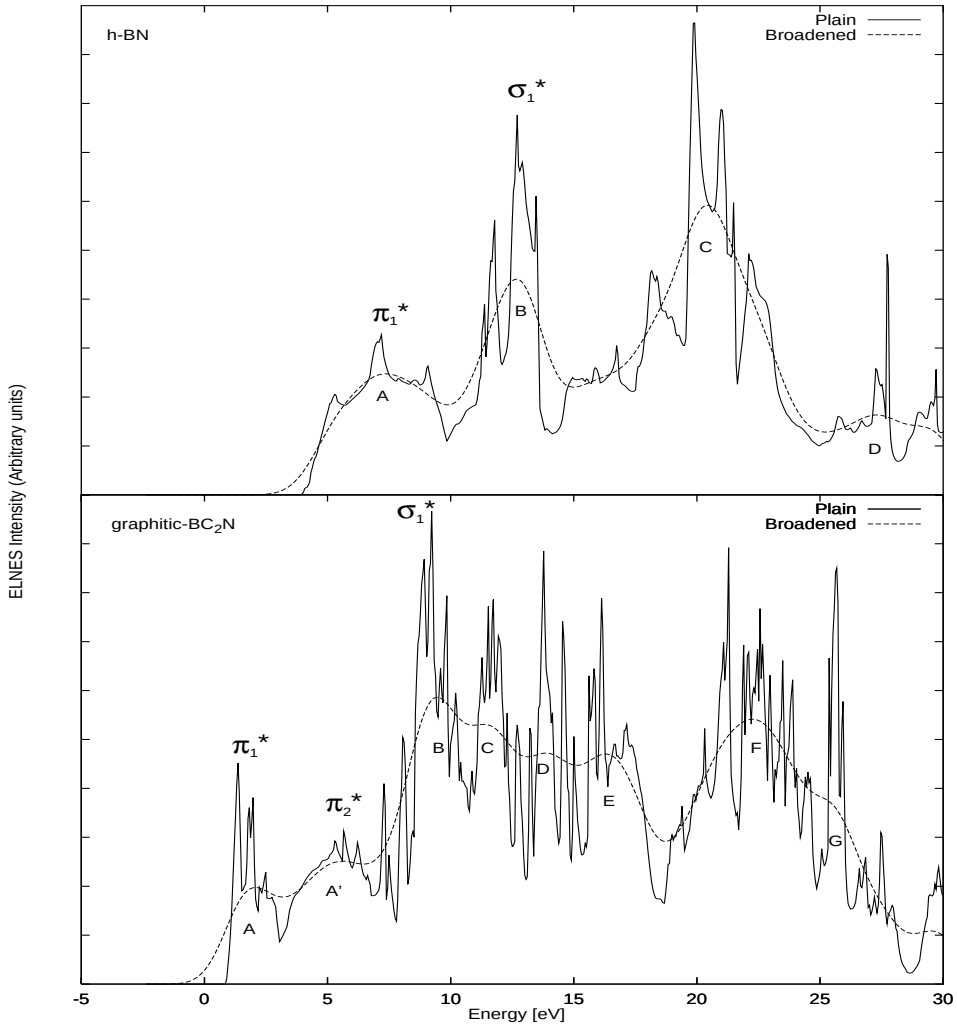

Figure 9.24: Theoretical N K ELNES of *graphitic*-BC_2N in comparison to h-BN.

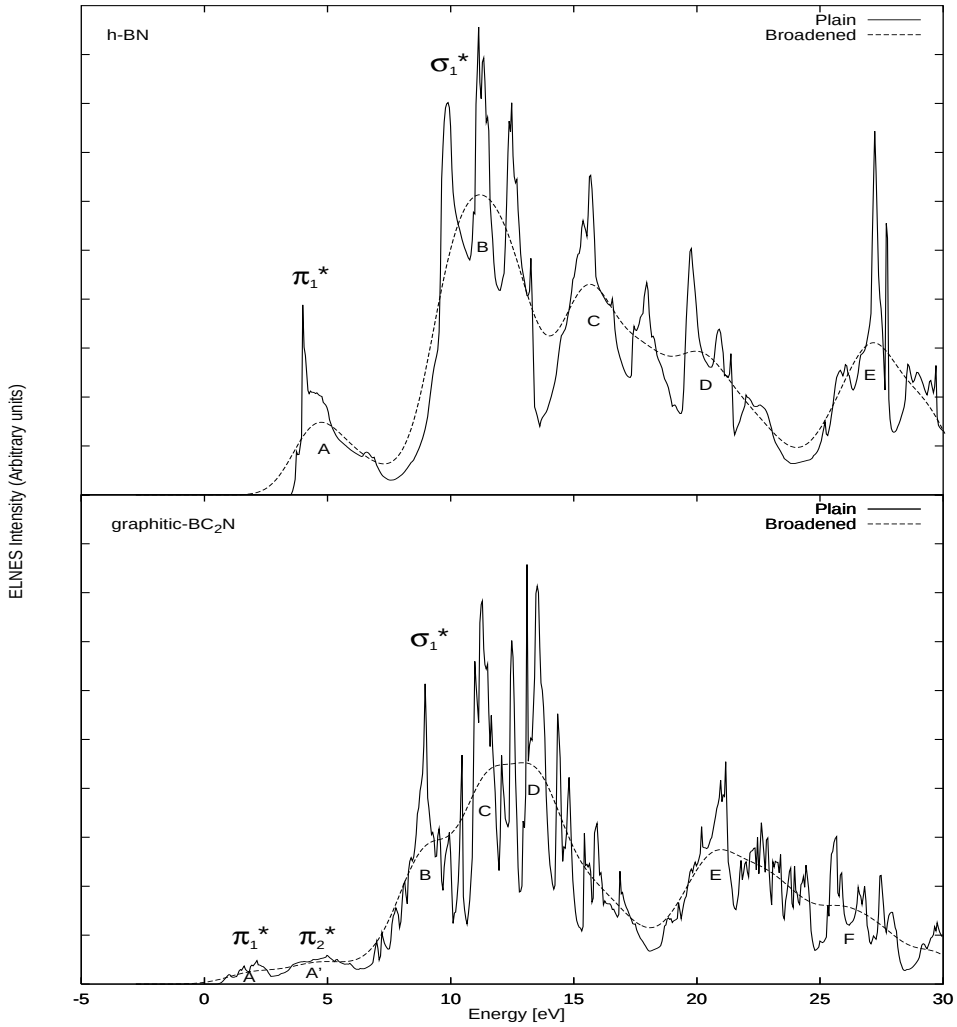

Figure 9.25: Theoretical B K ELNES of *graphitic*-BC_2N in comparison to h-BN.

suggest isotropic G values which are about 13.2 (I-BC_2N), 8.5 (II-BC_2N) and 10.7 % (III-BC_2N) higher than that of *c*-BN. That involves an obvious hardening of the system with respect to the well known cubic boron nitride. The computed bulk moduli confirm the same tendency: B values are in between those of the starting materials. According to such a theoretical finding, these ternary compounds are all predicted to be good candidates for materials harder than *c*-BN.

The density of states and band structure analysis have led to a band gap of 2.04, 1.69 and 1.79 eV for the phases I, II and III, respectively. Since it is well-known that the LDA approximation generally underestimates the experimental band gaps by as much as 30 % the phase I can be tentatively classified as insulator.

The study of the electron energy loss near edge structures of C , N and B *K* ionisation edges have also been simulated for the presented phases. An evident splitting of the σ^* peak at around 20-25 eV has been found in the C *K* ELNES of the two orthorhombic BC_2N crystals with respect to diamond. Furthermore, the changing of the number of peaks in the region between 5 and 15 eV and the variation of the fingerprints in the N and B *K* edges may be utilised as an important guide in the experimental characterisation of the sp^3-bonded BCN samples. For the trigonal system three σ^* peaks, common to all the three edges, have been individuated in the region between 5-17 eV. Since in the same energy range the orthorhombic models have shown only a doublet, this feature can be used to discriminate the phase III of BC_2N from the others. Finally, reference spectra have been calculated for the *graphitic*-BC_2N in all the three different edges. A doublet made of π^* peaks has been displayed in the N and B *K* ionisation edges just before the onset of the σ^* peak. Owing to the presence of only one π^* signal in the edges of the reference materials (graphite and *h*-BN), an evident detection of the layered BC_2N phase it is thus highly expected from the use of the EELS technique.

Chapter 10

Summary and Outlook

10.1 Carbon Nitrides

Based on the results presented in Chapter 8 it has been suggested that pure crystalline C_3N_4 systems are generally semiconductor materials with remarkable mechanical properties. However, very high temperature and high pressure reactions are likely to be required for their preparation in order to overcome the calculated positive standard enthalpy of formation. Moreover, the possibility to synthesise a pure carbon nitride sample with C_3N_4 composition should be generally hindered by the fact that different model systems have shown a very close energy stability. Comparing, for example, the two graphitic-like phases (*i.e.* hexagonal and orthorhombic) a small energy difference has been computed ($\sim$ 5-6$\cdot 10^{-4}$ eV/atom with FP-LAPW method), thus confirming the difficulty found at the experimental level in discriminating single crystalline sp^2-bonded forms. Molecular calculations suggest that polymorphic samples containing both types of layered structures should possess two main ^{13}C NMR signals spaced by approximately 15 ppm. This result seems to be in very good agreement with the latest experimental finding.

When considering the formation of substances with $C_{11}N_4$ stoichiometry (this is the subject of the second part of Chapter 8) calculations have shown that isoelectronic carbon rich model systems possess larger cohesive energies and they are usually stiffer than the analogue C_3N_4 compounds. However, in spite of this general improvement of the properties, the enthalpies for the formation reactions have been evaluated to be positive and most frequently larger than the analogue carbon poor phases. Furthermore, a very similar $\Delta H^o_{f,0}$ (4 kJ/mol of difference) has been computed for the layered $C_{11}N_4$ form and the sp^3-bonded β-C_3N_4 system. It can be thus strongly suggested that polyphasic samples will be often obtained upon trying to deposit carbon rich compounds. In particular, it is quite likely that a mixture of different forms, belonging to different stoichiometries, will always be achieved simultaneously during the synthesis of carbon nitrides. However,

such a conclusion should be weighted with an accurate kinetic investigation of the studied model phases (cfr. for example the case of diamond and graphite).

The characteristic ELNES coordination fingerprints have also been reported and analysed for the selected C_3N_4 and $C_{11}N_4$ structures. Theoretical spectra indicate the possibility to differentiate the various phases by looking at the changing in the number and position of peaks in both C and N K edges.

Despite many unsuccessful attempts to produce single phase CN_x materials it is however worth to note that amorphous samples can still find important applications in a wide range of interesting fields. The main commercial application of carbon nitrides is nowadays as protective coating on hard discs and recorder heads. However, coatings can also have a large potential application on medical area. The recovery of orthopaedic substrates has in fact already been tested for joint arthroplasty in human implants. In general, amorphous films can be used in all applications where amorphous carbon films are usually employed. Hence, despite the lack of pure crystalline samples the importance of producing homogeneous and well characterised thin-films carbon-based hard materials should not be neglected.

10.2 Boron Carbon Nitrides

In Chapter 9 it has been computed the investigation of the isoelectronic BC_2N class of compounds. Carbon atoms have been replaced with boron and nitrogen in the hexagonal and cubic diamond in order to design novel three-dimensional ultra-hard boron carbon nitrides. The structure called III-BC_2N has been predicted to be one of the most stable forms of the three-dimensional BC_2N system. In particular, its large cohesive energy has been addressed to the large number of B-N bonds and to the presence of alternate -C-C- and -B-N- rings. Furthermore, a detailed study of the unit cell response upon volume and shape changing has shown an evident hardening of the BC_2N phases with respect to the well-known cubic boron nitride. Consequently, by looking at the relative energy stability and at the computed elastic and bulk moduli, the phase III of BC_2N results, among the presented model phases, as the best candidate for replacing c-BN or diamond in various mechanical applications. The standard molar enthalpy change of the formation reaction has also been computed for this phase to be largely exothermic ($\sim$ -133 kJ/mol[1]), thus pointing to the possibility of depositing BC_2N crystalline forms at relative low temperature and pressure conditions with respect to carbon nitrides.

Finally, reference ELNES spectra have been proposed for different sp^2- and sp^3-bonded model systems, providing the possibility to identify pure crystalline phases in polymorphic samples.

[1] Averaged FP-LAPW/GGA values.

10.3 Prospective studies and "*what's left*"

In order to get a deeper insight into the subject of carbon nitrides, the general trend found in the stability, electronic and mechanical properties should also be checked for other isoelectronic compounds. Model crystals such as C_5N_4, C_3N_2, C_7N_4 (Fig. 10.1), C_9N_4 *etc...* have to be proposed and investigated to address further trends in CN_x materials. As mentioned in Section 8.3.7 the possibility to have a larger increment in the stability must also be searched in fulleren-like phases. In view of the latest experimental outcomes, nanotubes and nanofibers should also be considered as important forms for both carbon nitrides and boron carbon nitrides. However, the synthesis and study of such nanotube-like compounds should mostly concern the generation of novel classes of electron field emitters rather than novel ultra-hard systems.

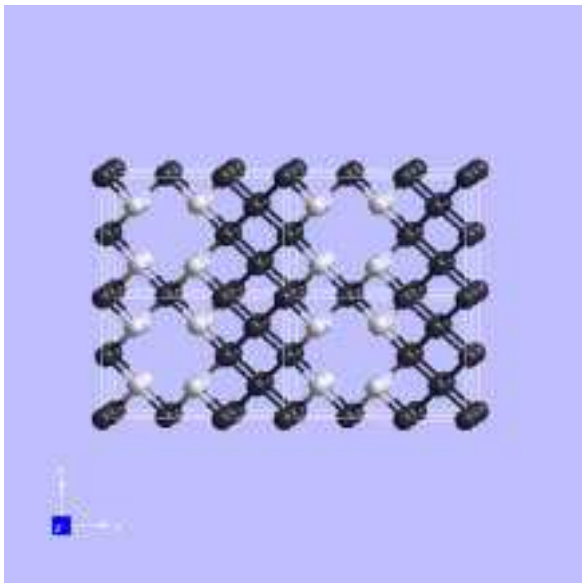

Figure 10.1: The three-dimensional C_7N_4 model system. Ongoing calculations seem to indicate the same general tendency found for the C_3N_4 and $C_{11}N_4$ compositions.

Chapter 11

Conclusions

11.1 Nitrures de Carbone

Les résultats présentés au Chapitre 8 permettent de proposer de nouveaux systèmes cristallins de formulation C_3N_4 ayant des propriétés de semi-conducteurs et susceptibles de posséder des caractéristiques mécaniques exceptionnelles. Cependant des conditions de très hautes température et de pression seraient requises pour leur préparation si l'on veut surmonter les enthalpies de formation standard positives qui les caractérisent.

De plus, la possibilité de synthétiser un échantillon pur de C_3N_4 serait difficile compte tenu des faibles différences d'énergies caractérisant la stabilité des systèmes modèles examinés. En effet, la comparaison des deux phases graphitiques (*i.e.* hexagonale et orthorhombique) montre une faible différence d'énergie de cohésion, $\sim$ 5-6$\cdot 10^{-4}$ eV/atom (calculs précis avec la méthode FP-LAPW), ce qui confirme la difficulté à l'échelle expérimentale de différencier des phases à hybridation sp^2 dominante (structures à caractère bi-dimensionnelle (2D)).

Les calculs de résonance magnétique nucléaire (RMN) du ^{13}C menées sur des clusters moléculaires permettent de suggérer que les échantillons polymorphiques contenant les deux types de structures à caractère 2D dominant possèdent deux signaux séparés d'environ 15 ppm. Ce résultat semble être appuyé par les dernières observations expérimentales.

Concernant la formation des phases de stoechiométrie plus riche en carbone, $C_{11}N_4$ (objet de la deuxième partie du Chapitre 8), les calculs ont montré que les systèmes modèles correspondants possèdent de plus fortes énergies de cohésion et se présentent comme plus durs que les analogues isoélectroniques C_3N_4. Néanmoins, malgré cette amélioration des propriétés recherchées, les bilans des enthalpies des réactions évaluées à partir des solides et molécules de référence, sont positives et souvent supérieures à celles des phases analogues moins riches en carbone.

De plus, une valeur similaire de $\Delta H^o_{f,0}$ (4 kJ/mol de différence) a été calculée pour la structure 2D de $C_{11}N_4$ et pour la structure β-C_3N_4 caractérisée par des liaisons sp^3, *i.e.*

tri-dimensionnelle (3D). Ce résultat permet de suggérer que des échantillons polyphasiques seront fréquemment obtenus lors du dépôt de composés riches en carbone. En particulier, il est vraisemblable qu'un mélange des différentes formes, appartenant à différentes stoechiométries, sera toujours présent lors de la synthèse des nitrures de carbone. Cependant cette conclusion devrait être modulée par un examen approfondi des aspects cinétiques des phases modèles étudiées (cf. par ex. les cas du diamant et du graphite).

Les signatures ELNES ont également été raportées pour les phases modèles des deux stoechiométries C_3N_4 and $C_{11}N_4$. Les spectres théoriques indiquent la possibilité de distinguer les différentes phases par l'examen du changement du nombre et positions des pics pour les seuils K de C et N.

Malgré plusieurs tentatives infructueuses de produire des matériaux CN_x monophasiques, dans l'état actuel de l'art, il reste néanmoins pour les phases amorphes formées des applications importantes dans différents domaines. L'utilisation commerciale principale des nitrures de carbone est aujourd'hui dans le domaine de l'enregistrement magnétique (protection des têtes de lecture et des disques durs pour la micro-informatique). Cependant les enrobages protecteurs sont également utiles en médecine pour les implants humains en arthroplastie. Généralement, des films amorphes peuvent être utilisés dans toutes les applications où les enrobages avec des films minces de carbone sont requis. Par conséquent, malgré le manque d'échantillons de nitrure de carbone cristallins et purs, l'importance de produire des films minces homogènes et bien caractérisés (mécaniquement et spectroscopiquement) de matériaux durs à base de carbone ne devrait pas être négligée.

11.2 Boronitrures de Carbone

Au Chapitre 9, nous avons entrepris l'étude détaillée d'un classe isoélectrique (du carbone) de matériaux dans le ternaire BCN : BC_2N. Les atomes de carbone ont été remplacés par le bore et l'azote dans les structures hexagonale (lonsdaleite) et cubique du diamant, avec comme objectif, la mise en évidence de nouveaux boronitrures de carbone tri-dimensionnels susceptibles d'être ultra-durs.

La structure tri-dimensionnelle, appelée III-BC_2N, a pu ainsi être prédite comme une des formes les plus stables des phases BC_2N. En particulier, sa grande énergie de cohésion a été attribuée au grand nombre de liaisons B-N et à la présence de cycles alternés : -C-C- et -B-N-. De plus, une étude détaillée de la réponse de la maille élémentaire aux changements de volume et de forme a montré un accroissement de la dureté des phases BC_2N par rapport au nitrure de bore cubique. Par conséquent, en examinant les stabilités relatives et les valeurs calculées des modules d'élasticité et de compressibilité, la phase III de BC_2N résulte, parmi les phases modèles étudiées, comme le meilleur candidat pour le remplacement de BN cubique ou du diamant dans différentes applications mécaniques. L'enthalpie molaire standard de la

réaction de formation a été également évaluée exothermique ($\sim$ -133 kJ/mol[1]), ce qui est en faveur du dépôt de BC_2N sous forme cristalline dans des conditions de température et pression relativement faibles par rapport aux nitrures de carbone.

Enfin, les spectres de référence ELNES ont été proposés pour différentes phases à liaisons types sp^2 et sp^3 -systèmes modèles 2D et 3D respectivement-. De tels signatures seront susceptibles d'identifier les phases cristallines pures au sein d'échantillons polymorphes.

11.3 Prospectives et "*ce qui reste à faire*"

Dans l'objectif d'approfondir davantage le sujet des nitrures de carbone, la tendance générale trouvée au niveau de la stabilité, des propriétés électroniques et mécaniques devrait également être vérifiée pour les autres composés isoélectroniques. Des structures cristallines modèles telles que les compositions C_5N_4, C_3N_2, C_7N_4 (Fig. 10.1), C_9N_4 *etc*... pourraient être proposées et étudiées pour établir une systématique des tendances dans les matériaux CN_x.

Comme il a été mentionné dans la Section 8.3.7 la possibilité d'avoir une stablité accrue des CN_x pourrait être recherchée dans les phases de type fullerène. Au vu des derniers résultats expérimentaux, des systèmes à nanotubes et nanofibres devraient également être pris en compte comme de nouvelles formes potentielles de nitrures ainsi que de boronitrures de carbone. Cependant, la synthèse et l'étude de tels composés concernerait plutôt que les ultra-durs, les nouvelles générations d'émetteurs électroniques par effet de champ.

[1] Valeur moyenne obtenue à partir de calculs FP-LAPW dans la fonctionnelle GGA.

Bibliography

[1] F.P. Bundy, H. T. Hall, H. M. Strong and R. J. Wentorf, *Nature*, *176*, 51 (1955).

[2] R. H. Wentorf, *J. Chem. Phys.*, **26**, 956 (1957).

[3] R. H. Wentorf, *J. Chem. Phys.*, **34**, 809 (1961).

[4] J. M. Leger, J. Haines, M. Schmidt, J. P. Petitet, A. S. Pereira and J. A. H. da Jornada, *Nature*, *383*, 401 (1996).

[5] A. Zerr, G. Miehe, G. Serghiou, M. Schwarz, E. Kroke, R. Riedel, H. Fueß, P. Kroll and R. Boehler, *Nature*, *400*, 340 (1999).

[6] L. Solozhenko, D. Andrault, G. Fiquet, M. Mezouar and D. C. Rubie, *Appl. Phys. Lett.*, **78**, 1385 (2001).

[7] J. C. Angus, C. C. Hayman, *Science*, **241**, 913 (1988).

[8] K. E. Spear, *J. Am. Ceram. Soc.*, **72**, 171 (1989).

[9] W. A. Yarbrough and R. Messier, *Science*, **247**, 688 (1990).

[10] P. K. Bachmann, *Adv. Mater.*, 2, 195 (1990).

[11] P. K. Bachmann, *Keramische Zeitschrift*, 2, 93 (1992).

[12] A. Y. Liu and M. L. Cohen, *Science*, **245**, 841 (1989).

[13] J. Kouvetakis, T. Sasaki, C. Shen, R. Hagiwara, M. Lerner, K. M. Krishnan and N. Bartlett, *Synth. Met.*, **34**, 1 (1990).

[14] R. B. Kaner, J. Kouvetakis, C. E. Warble, M. L. Sattler and N. Bartlett, *Mater. Res. Bull.*, **22**, 399 (1987).

[15] A. K. Butylenko, G. V. Samsonov, L.I. Timofeeva and G. N. Makarenko, *Pis'ma Zh. Tekh. Fiz.*, **3**, 186 (1977).

[16] N. N. Sirota and M. M. Zhuk, Vestsi Akad. Navuk BSSR, *ser. Fiz. -Mat. NavukI*, **3**, 122 (1979).

[17] S.Nakano, M. Akaisji, T. Sasaki and S. Yamaoka, *Chem. Mater.*, **6**, 2246 (1994).

[18] T. Sasaki, M. Ajaishi, S. Yamaoka, Y. Fujiki and T. Oikawa, *Chem. Mater.*, **5**, 695 (1993).

[19] S. Nakano, M. Akaisji, T. Sasaki and S. Yamaoka, *Mater. Sci. Eng. A*, **209**, 29 (1996).

[20] Y. Tateyama, T. Ogitsu, K. Kusakabe, S. Tsuneyuki and S. Itoh, *Phys. Rev. B*, **55**, 10161 (1997).

[21] D. M. Teter and V. Ozolins, *unpublished manuscript.*

[22] D. M. Teter, *MRS Bulletin*, **23**, 22 (1998).

[23] M. L. Cohen, *Phys. Rev. B*, **32**, 7988 (1958).

[24] J. C. Phillips, *Bonds and Bands in Semiconductors* (Academic, New York, 1973).

[25] R. Riedel, *Adv. Mater.*, **6** (7/8), 549 (1994).

[26] C. M. Sung and M. Sung, *Mater. Chem.*, **43** 1 (1996).

[27] M. L. Cohen, *Mater. Sci. Eng. A*, **105/106**, 11 (1988).

[28] M. L. Cohen, *J. Hard Mater.*, **2**, 13 (1991).

[29] D. M. Teter and R. J. Hemley, *Science*, **271**, 53 (1996).

[30] A. P. Gerk, *J. Mater. Sci.*, **12**, 735 (1977).

[31] F. Birch, *J. Geophys. Res.*, **83**, 1257 (1978).

[32] G. R. Barsch, and Z. P. Chang, *J. Appl. Phys.*, **39**, 3276 (1968).

[33] F. Birch, *J. Geophys. Res.*, **457**, 227 (1952).

[34] J. F. Nye, *Physical Properties of Crystals: Their Representation by Tensors*, Oxford University Press, New York (1985).

[35] M. Dacorogna, J. Ashkenazi and M. Peter, *Phys. Rev. B*, **26**, 1527 (1982).

[36] A. Reuss, *Z. Angew. Math. Mech*, **9**, 49 (1929).

[37] P. A. M. Dirac, *Proc. Roy. Soc. (London)*, **123**, 714 (1929).

[38] H. Hohenberg and W. Kohn, *Phys. Rev. B*, **136**, 864 (1964).

[39] J.C. Slater, *Phys. Rev.*, **81**, 385 (1951).

[40] J.C. Slater, *The Self-Consistent Field for Molecules and Solids*, (McGraw-Hill, New York, 1974).

[41] V. L. Moruzzi, J. F. Janak and A. R. Williams, *Calculated Electronic Properties of Metals*, (Pergamon, New York, 1978).

[42] A. Zunger, A. J. Freeman, *Phys. Rev. B*, **15**, 5049 (1977).

[43] A. Zunger, A. J. Freeman, *Phys. Rev. B*, **16**, 906 (1977).

[44] A. Zunger, A. J. Freeman, *Phys. Rev. B*, **16**, 2901 (1977).

[45] D. C. Langreth and M. J. Mehl, *Phys. Rev. B*, **28**, 1809 (1983).

[46] A. D. Becke, *Phys. Rev. A*, **38**, 3098 (1988).

[47] J. P. Perdew, J. A. Chevary, S. H. Vosko, K. A. Jackson, M. R. Pederson, D. J. Singh and C. Fiolhais, *Phys. Rev. B*, **46**, 6671 (1992).

[48] O. Gunnarsson, M. Jonson and B. I. Lundqvist, *Solis State Commun.*, **24**, 765 (1977).

[49] O. Gunnarsson, M. Jonson and B. I. Lundqvist, *Phys. Rev. B*, **20**, 3136 (1979).

[50] O. Gunnarsson and R. O. Jones, *Phys. Scr.*, **21**, 394 (1980).

[51] W. Kohn and L. J. Sham, *Phys. Rev. A*, **140**, 1133 (1965).

[52] P. Bendt and A. Zunger, *Phys. Rev. B*, **26**, 3114 (1982).

[53] R. Car and M. Parrinello, *Phys. Rev. Lett.*, **55**, 2471 (1985).

[54] C. G. Broyden, *Math. Comp.*, **19**, 577 (1965).

[55] M. C. Payne, M. P. Teter, D. C. Allan, T.A. Arias, J. D. Jannopoulos, *Rev. Mod. Phys.*, **64** 1045 (1992).

[56] D. M. Ceperley and B. J. Alder, *Phys. Rev. Lett*, **45**, 1196 (1980).

[57] J. P. Perdew, *Phys. Rev. B*, **33**, 8822 (1986).

[58] VASP (Vienna *ab initio* simulation program), developed at the Institut für Theoretische Physik of the Technische Universität Wien; G. Kresse and J. Hafner, *Phys. Rev. B*, **47**, 558 (1993); G. Kresse and J. Hafner, *Phys. Rev. B*, **49**, 14251 (1994); G. Kresse and J. Furthmüller, *Comput. Mat. Sci.*, **6**, 15 (1996); G. Kresse and J. Furthmüller, *Phys. Rev. B*, **55**, 11 (1996); G. Kresse and J. Furthmüller, *Phys. Rev. B*, **55**, 169 (1996).

[59] W. Kohn and L. J. Sham, *Phys. Rev. A*, **140**, 1133 (1965); P. Hohenberg and W. Kohn, *Phys. Rev. B*, **136**, 864 (1964).

[60] J. P. Perdew and A. Zunger, *Phys. Rev. B*, **23**, 5048 (1981).

[61] D. Vanderbilt, *Phys. Rev. B*, **41**, 7892 (1990).

[62] P.E. Blöchl, O. Jepsen, and O. K. Anderson, *Phys. Rev. B*, **49**, 16223 (1994).

[63] H. J. Monkhorst and J. D. Pack, *Phys. Rev. B*, **13**, 5188 (1976).

[64] W. C. Toop and J. J. Hopfield, *Phys. Rev. B*, **7**, 1295 (1974).

[65] T. Starkloff and J. D. Joannopoulos, *Phys. Rev. B*, **16**, 5212 (1977).

[66] G. Kresse and J. Hafner, *J. Phys.: Condens. Matt.*, **6**, 8245 (1994).

[67] J. Furthmüller, J. Hafner and G. Kresse, *Phys. Rev. B*, **50**, 15506 (1994).

[68] P. Blaha, K. Schwarz and J. Luitz, WIEN97, A Full Potential Linearized Augmented Plane Wave Package for Calculating Crystal Properties, (Karlheinz Schwarz, Techn. Univ. Wien, Vienna 1999). ISBN 3-9501031-0-4. Updated version of P. Blaha, K. Schwarz, P. Sorantin, and S. B. Trickey, *Comp. Phys. Commun.*, **59**, 399 (1990).

[69] J. C. Slater, *Phys. Scr.*, **51**, 846 (1937).

[70] J. C. Slater, *Advances in Quantum Chemistry*, **1**, 35 (1964).

[71] M. Weinert, E. Wimmer and A. J. Freeman, *Phys. Rev. B*, **26**, 4571 (1982).

[72] J.C. Slater, *Quantum Theory of Molecules and Solids*, Vol. 2 New-York: McGraw-Hill (1965).

[73] W. Kohn and N. Rostoker, *Phys. Rev. A*, **94**, 1111 (1954).

[74] A. R. Williams, J. Kübler and C. D. Jr. Gelatt, *Phys. Rev. B*, **19**, 6094 (1979).

[75] V. Eyert, "Basic notions and applications of the augmented spherical wave method", *Int. J. Quant. Chem.*, **77**, 1007 (2000). Special Issue: Electronic Structure of Materials, edited by M. Defranceschi.

[76] O. K. Andersen, *Phys. Rev. B*, **12**, 3060 (1975).

[77] E.P. Wigner and F. Seitz, *Solid State Physics*, Vol. 1: Seitz and Turnbull Eds. (1955).

[78] S. Y. Savrasov, D. Y. Savrasov, and O. K. Andersen, *Phys. Rev. Lett.*, **72**, 372-375 (1994).

[79] P. M. Morse and H. Feshbach, *Methods of Theoretical Physics*, Vol. II, McGraw-Hill, New York (1953).

[80] S. Iijima, *Nature*, **354**, 56 (1991).

[81] S. L. Sung, S. H. Tsai, C. H. Tseng, F. K. Chiang, X. W. Liu and H. C. Shih, *Appl. Phys. Lett.*, **74**, 197 (1999).

[82] K. Suenaga, M. P. Johansson, N. Hellgren, E. Broitman, L. R. Wallenberg, C. Colliex, J-E. Sundgren and L. Hultman, *J. Vac. Sci. Technol. B*, **300**, 695 (1999).

[83] M. Terrones, P. Redlich, N. Grobert, S. Trasobares, W-K. Hsu, H. Terrones, Y-Q. Zhu, J. P. Hare, C. L. Reeves, A. K. Cheetham, M. Rühle, H. W. Kroto and D. R. M. Walton, *Adv. Mater.*, **11**, 655 (1999).

[84] A. G. Rinzler, J.H. Hafner, P. Nikolaev, L. Lou, S. G. Kim, D. Tománek, P. Nordlander, D. T. Colbert and R. E. Smalley, *Science*, **268**, 1550 (1995).

[85] W. A. de Heer, A. Châtelain and D. Ugarte, *Science*, **270**, 1179 (1995).

[86] W. A. de Heer, J-M. Bonard, K. Fauth, A. Châtelain, L. Forró and D. Ugarte, *Adv. Mater.*, **9**, 87 (1997).

[87] Yu. V. Gulyaev, L. A. Chemozatonskii, Z. Ja. Kosakovskaja, N. I. Sinitsyn, G. V. Torgashov and Yu. F. Zakharchenko, *J. Vac. Sci. Technol. B*, **13**, 435 (1995).

[88] E. Broitman, W. Macdonald, N. Hellgren, G. Radnóczi, Zs. Czigány, A. Wennerberg, M. Jacobsson and L. Hultman, *Diamond Relat. Mater.*, **9**, 1984 (2000).

[89] S. Muhl and J. M. Mendéz, *Diamond Relat. Mater.* **8**, 1809 (1999).

[90] J. J. Cuomo, P. A. Leary, D. Yu, W. Reuter and M. Frisch, *J. Vac. Sci. Technol.*, **16**, 299 (1979).

[91] M. Iwaki, K. Takahashi and A. Sekiguchi, *J. Mater. Res.*, **5**, 2562 (1990).

[92] C. J. Torng, J. M. Siversten, J. H. Judy and C. Chang, *J. Mater. Res.*, **5**, 2490 (1990).

[93] H-X. Han and B. J. Feldman, *Solid State Commun.*, **65**, 921 (1988).

[94] J. D. F. Chubaci, T. Sakai, T. Yamamoto, K. Agata, A. Ebe and F. Fujimoto, *Phys. Rev. B*, **80/81**, 463 (1993).

[95] D. Li, Y. Chung, M. Wong and W. D. Sproul, *J. Appl. Phys.*, **74**, 219 (1993).

[96] L. Maya, D. R. Cole and E. W. Hagaman, *J. Am. Ceram. Soc.*, **74**, 1686 (1991).

[97] M. Ricci, M. Trinquecoste, F. Auguste, R. Canet, P. Delhaes, C. Guimon, G. Pfister-Guillouzo, B. Nysten and J. P. Issi, *J. Mater. Res.*, **8**, 480 (1993).

[98] F. Fujimoto and K. Ogata, *Jpn. J. Appl. Phys.*, **32**, 420 (1993).

[99] C. Niu, Y. Z. Lu and C. M. Lieber, *Science*, **261**, 334 (1993).

[100] N. Hellgren, M. P. Johansson, E. Broitman, L. Hultman and J-E. Sundgren, *Phys. Rev. B*, **59**, 5162 (1999).

[101] N. Hellgren, "*Sputtered Carbon Nitride Thin Films*", Ph.D. Thesis, Linköping University, Linköping (ISBN 91-7219-597-5), Sweden (1999).

[102] W. T. Zheng, H. Sjöström, I. Ivanov, K. Z. Xing, E. Broitman, W. R. Salaneck, J-E. Sundgren, *J. Vac. Sci. Technol A*, **14**, 2696 (1996).

[103] H. Sjöstrom, L. Hultman, J-E. Sundgren, S. V. Hainsworth, T. F. Page and G. S. A. M. Theunissen, *J. Vac. Sci. Technol. A*, **14**, 56 (1996).

[104] D. A. Zhogolev, O. P. Bugaets and I. A. Marushko, *Zh. Strukt. Khim.*, **22**, 46 (1981).

[105] T. H. Hall, *Science*, **148**, 1331 (1965).

[106] T. H. Hall and L. A. Compton, *Inorg. Chem.*, **4**, 1213 (1965).

[107] R. Merchant, D. G. McCulloch, D. R. McKenzie, Y. Yin, L. Hall and E. G. Gerstner, *J. Appl. Phys.*, **79**, 6914 (7988).

[108] M. Y. Ching, D. Li, X. Lin, V. P. Dravid, Y. Chung, M. Wong and W. D. Sproul, *J. Vac. Sci. Technol. A*, **11**, 521 (1993).

[109] D. M. Bhusari, C. K. Chen, K. H. Chen, T. J. Chuang, L. C. Chen and M. C. Lin, *J. Mater. Res.*, **12**, 322 (1997).

[110] J. Martin-Gill, F. Martin-Gill, M. Sarlkaya, M. Quian, M. Jose-Yacaman, and A. Rubio, *J. Appl. Phys.*, **81**, 2555 (1997).

[111] K. Yamamoto, Y. Koga, K. Yase, S. Fijiara and M. Kubota, *Jpn. J. Appl. Phys.*, Part 2, **36**, L230 (1997).

[112] M. L. Cohen, *Solid State Commun.*, **45**, 92 (1994).

[113] E. Knittle, R. M. Wentzcovitch, R. Jeanloz, M. L. Cohen, *Nature*, **337**, 349 (1989).

[114] Y. Liu, R. M. Wentzcovitch, *Phys. Rev. B*, **50**, 10362 (1994).

[115] J. Ortega, O. F. Sankey, *Phys. Rev. B*, **51**, 2624 (1995).

[116] M. L. Cohen, *Int. J. Quantum Chem.*, **61**, 603 (1997).

[117] M. Mattesini, S. F. Matar, A. Snis, J. Etourneau and A. Mavromaras, *J. Mater. Chem.*, **9**, 3151 (1999).

[118] M. Mattesini, S. F. Matar and J. Etourneau, *J. Mater. Chem.*, **10**, 709 (2000).

[119] S. Han and J. Ihm, *Phys. Rev. B*, **55**, 15349 (1997).

[120] V. Eyert, Electronic structure calculations for crystalline materials, in: *Density Functional Methods: Applications in Chemistry and Materials Science*, ed. M. Springborg, Wiley, Chichester, (1997), pp. 233-304; R. Hoffmann and C. Zheng, *J. Phys. Chem.*, **89**, 4175 (1985); S. F. Matar, *Int. J. of Quantum Chemistry*, **77**, 911 (2000).

[121] O. K. Andersen, O. Jepsen, *Phys. Rev. Lett.*, **53** 2571 (1984).

[122] J. van Barth and D. Hedin, *J. Phys. C.*, **5**, 1629 (1972).

[123] J. F. Janak, *Solid State Commun.*, **25**, 53 (1978).

[124] K. T. Park, K. Terakura and N. Hamada, *J. Phys. C*, **20**, 1241 (1987).

[125] I. Alves, G. Demazeau, B. Tanguy, F. Weill, *Solid State Comm.*, **109**, 697 (1999).

[126] H. Montigaud, S. Courjault, B. Tanguy, G. Demazeau, J. Peyronneau, D. Andrault, M. Jaouen and G. Hug, *High Pressure Research*, **18**, 213 (2000).

[127] O. Gunnarsson and R. O. Jones, *Phys. Rev. B*, **31**, 7588 (1985).

[128] C. Mailhiot, L. H. Yang and A. K. McMahan, *Bull. Am. Phys. Soc.*, **38**, 1496 (1993).

[129] S. Fahy, X. W. Wang and S. G. Louie, *Phys. Rev. B*, **42**, 3503 (1990).

[130] J. P. Perdew and Y. Wang, *Phys. Rev. B*, **45**, 113244 (1992).

[131] J. P. Perdew, S. Burke and M. Ernzerhof, *Phys. Rev. Lett.*, **77**, 3865 (1996).

[132] D. C. Patton, D. V. Porezag and M. R. Pederson, *Phys. Rev. B*, **55**, 7454 (1997).

[133] C. Kittel, *Introduction to Solid State Physics*, 6^{th} ed. Wiley, New York (1986).

[134] G. S. Painter and F. Averill, *Phys. Rev. B*, **26**, 1781 (1982).

[135] In-Ho Lee and R. M. Martin, *Phys. Rev. B*, **52**, 7197 (1997).

[136] A. K. McMahan, *Phys. Rev. B*, **30**, 5835 (1984).

[137] C. Mailhiot, J. B. Grant and A. K. McMahan, *Phys. Rev. B*, **42**, 9033 (1990).

[138] J. V. Badding, *Adv. Mater.*, **9**, 877 (1997).

[139] D. A. Johnson, *Some Thermodynamic Aspects of Inorganic Chemistry*, Cambridge University Press, Cambridge (1982).

[140] D. S. Kempt and F. Vellaccio, *Organic Chemistry*, Worth Publishers, New York (1980).

[141] J. E. Lowther, *Phys. Rev. B*, **59**, 11683 (1999).

[142] R. M. Wentzcovitch, K. J. Chang and M. L. Cohen, *Phys. Rev. B*, **34**, 1071 (1986).

[143] S. Matar, V. Gonnet and G. Demazeau, *J. Phys. I France*, **4**, 335 (1994).

[144] P. E. Van Camp. V. E. Van Doren and J. T. Devreese, *Phys. Status Solidi B*, **146**, 573 (1988).

[145] L. Vel, G. Demazeau and J. Etourneau, *J. Mat. Sci. Eng. B*, **10**, 149 (1991).

[146] J. Sanjurgo, E. Lopez-Cruz, P. Vogl and M. Cardona, *Phys. Rev. B*, **28**, 4579 (1983).

[147] R. W. Hertzberg, *Deformation and Fracture Mechanics of Engineering Materials*, 3rd edn, Wiley, New York (1989).

[148] A. Kelly and N. H. Macmillan, *Strong Solids*, 3rd edn, Clarendon Press, Oxford (1986).

[149] R. Riedel, *Handbook of Ceramic Hard Materials*, R. Riedel (Ed.), Vol. 1 p. L, Wiley-VCH (2000).

[150] H. B. Huntington, *Solid State Physics: Advances in Research and Applications*, F. Seitz and D. Turnbull (Eds.), Vol. 7, Academic Press, New York (1958).

[151] O. L. Anderson, *Physical Acoustics:Principles and Methods*, W. P. Mason (Ed.), Vol. III, Part B, Academic Press, New York (1965).

[152] Y. Guo and W. A. Goddard, *Chem. Phys. Lett.*, **237**, 72 (1995).

[153] M. Mattesini and S. F. Matar, *Comp. Mater. Sci.*, **20/1**, 107 (2001).

[154] Y. Miyamoto, M. L. Cohen and S. G. Louie, *Solid State Commun.*, **102**, 605 (1997).

[155] W. H. Press, B. P. Flannery, S. A. Teukolsky and W.T. Vetterling, *Numerical Recipes*, Cambridge University Press, New York (1986).

[156] M. Methfessel and A.T. Paxton, *Phys. Rev. B*, **40**, 3616 (1989).

[157] R. Hoffmann, *Solid and Surfaces: A Chemist's View of Bonding in Extended Structures*, VCH Publishers, New York (1988).

[158] Gaussian 98, Revision A.9, M. J. Frisch, G. W. Trucks, H. B. Schlegel, G. E. Scuseria, M. A. Robb, J. R. Cheeseman, V. G. Zakrzewski, J. A. Montgomery, Jr., R. E. Stratmann, J. C. Burant, S. Dapprich, J. M. Millam, A. D. Daniels, K. N. Kudin, M. C. Strain, O. Farkas, J. Tomasi, V. Barone, M. Cossi, R. Cammi, B. Mennucci, C. Pomelli, C. Adamo, S. Clifford, J. Ochterski, G. A. Petersson, P. Y. Ayala, Q. Cui, K. Morokuma, D. K. Malick, A. D. Rabuck, K. Raghavachari, J. B. Foresman, J. Cioslowski, J. V. Ortiz, A. G. Baboul, B. B. Stefanov, G. Liu, A. Liashenko, P. Piskorz, I. Komaromi, R. Gomperts, R. L. Martin, D. J. Fox, T. Keith, M. A. Al-Laham, C. Y. Peng, A. Nanayakkara, M. Challacombe, P. M. W. Gill, B. Johnson, W. Chen, M. W. Wong, J. L. Andres, C. Gonzalez, M. Head-Gordon, E. S. Replogle, and J. A. Pople, Gaussian, Inc., Pittsburgh PA, 1998.

[159] K. Wolinski, J. F. Hinton and P. Pulay, *J. Am. Chem. Soc.*, **112**, 8251 (1990).

[160] Y. Wang and J. P. Perdew, *Phys. Rev. B*, **43**, 8911 (1991).

[161] P. P. Lottici, G. Antonioli, C. Razzetti, *J. Chem. Phys. Solids*, **50**, 967 (1989).

[162] A. Snis and S. F. Matar, *Phys. Rev. B*, **60**, 10855 (1999).

[163] A. Snis, S. F. Matar, O. Plashkevych and H. Ågren, *J. Chem. Phys.*, **111**, 9678 (1999).

[164] O. Plashkevych, A. Snis, L. Yang, H. Ågren and S. F. Matar, *Physica Scripta*, **63**, 70 (2001).

[165] T. Hughbanks and Y. Tian, *Solid State Commun.*, **96**, 321 (1995).

[166] A. Y. Liu, R. M. Wentzcovitch and M. L. Cohen, *Phys. Rev. B.*, **39**, 1760 (1989).

[167] H. Nozaki and S. Itoh, *J. Phys. Chem. Solids*, **57**, 41 (1996).

[168] D. A. Johnson, *Some Thermodynamic Aspects of Inorganic Chemistry*, Cambridge University Press, Cambridge (1982).

[169] J. V. Badding and D. C. Nesting, *Chem. Mater.*, **8**, 535 (1996).

[170] S. F. Matar and M. Mattesini, *C. R. Acad. Sci. Paris*, **4**, 255 (2001).

[171] P. Ravindran, J. Wills, O. Eriksson, *J. Appl. Phys.*, **84**, 4891 (1998).

[172] M.L. Mehl, J. E. Osburn, D. A. Papaconstantopoulos and B. M. Klein, *Phys. Rev. B*, **41**, 10311 (1990).

[173] M.L. Mehl, *Phys. Rev. B*, **47**, 2493 (1993).

[174] M. Born, *Proc. Cambridge Philos. Soc.*, **36**, 160 (1940).

[175] M. Born and K. Huang, *Dynamical Theory of Crystal Lattices*, (Clarendon, Oxford, 1956).

[176] D. C. Wallace, *Thermodynamics of Crystals*, (John Wiley and Sons, New York, 1972).

[177] W. A. Harrison, *Electronic Structure and the Properties of Solids*, (W. H. Freeman, San Francisco, 1980).

[178] http://www.iaf.fhg.de/budipr/cont-e.htm

[179] S. F. Pugh, *Philos. Mag.*, **45**, 823 (1954).

[180] M. Nelhiebel, P. H. Louf, P. Schattschneider, P. Blaha, K. Schwarz and B. Jouffrey, *Phys. Rev. B*, **59**, 12807 (1999).

[181] M. Wibbelt, H. Kohl and Ph. Kohler-Redlich, *Phys. Rev. B*, **59**, 11739 (1999).

[182] É. Sandré, C. J. Pickard and C. Colliex, *Chem. Phys. Lett.*, **325**, 53 (2000).

[183] A. R. Badzian, *Mater. Res. Bull.*, **16**, 1385 (1981).

[184] E. Knittle, R. B. Kaner, R. Jeanloz and M. L. Cohen, *Phys. Rev. B*, **51**, 12149 (1995).

[185] B. P. Singh, *Mater. Res. Bull.*, **21**, 85 (1986).

[186] Y. Miyamoto, M. L. Cohen and S. G. Louie, *Phys. Rev. B*, **52**, 14971 (1995).

[187] H. Nozaki and S. Itoh, *Phys. Rev. B*, **53**, 14161 (1995).

[188] H. Nozaki and S. Itoh, *J. Phys. Chem. Solids*, **57**, 41 (1995).

[189] T. Kar, M. Cuma and S. Scheiner, *J. Phys. Chem. A*, **102**, 10134 (1998).

[190] P. Saalfrank, W. Rümler, H. -U. Hummel and J. Ladik, *Synthetic Metals*, **52**, 1 (1992).

[191] W. R. L. Lambrecht and B. Segall, *Phys. Rev. B*, **47**, 9289 (1993).

[192] W. R. L. Lambrecht and B. Segall, *Phys. Rev. B*, **40**, 9909 (1993).

[193] Y. Bando, S. Nakano and K. Karrashima, *J. Electron. Microsc.*, **45**, 135 (1996).

[194] T. Komatsu, M. Nimura, Y. Kakudate and S. Fujiwara, *J. Mater. Res.*, **6**, 1799 (1996).

[195] W. H. Bragg and W. L. Bragg, *Nature*, **91**, 557 (1913).

[196] J. Donohue, *The Structures of the Elements*, Wiley, New York, (1974).

[197] M. Grimsditch, E. S. Zouboulis and A. Polian, *J. Appl. Phys.*, **76**, 832 (1994).

[198] R. S. Pease, *Acta Crystallogr.*, **5**, 536 (1952).

[199] *Handbook of Chemistry and Physics*, 81^{st} ed., D. R. Lide Editor-in-Chief, CRC Press Inc. (2000).

[200] V. Ya. Leonidov, I. V. Timofeev, V. L. Solozhenko and I. Rodionov, *Zh. Fiz. Khim.*, **61**, 2851 (1987).

[201] R. Hultgren, P. D. Desai, D. T. Hawkins, M. Gleiser, K. K. Kelley and D. D. Wagman, *Selected Values of the Thermodynamic Properties of the Elements*, Am. Soc. Metals, Metals Park, Ohio (1973).

[202] M. W. Jr Case, C. A. Davies, J. R. Jr Downey, D. J. Frurip, R. A. McDonald and A. N. Syverud, *J. Phys. Chem. Ref. Data*, **14**, Suppl. 1 (1985).

[203] P. B. Mirkarimi, D. L. Medlin, K. F. McCarty, D. C. Dibble, W. M. Clift, J. A. Knapp and J. C. Barbour, *J. Appl. Phys.*, **82**, 1617 (1997).

[204] V. Serin, E. Beche, R. Berjoan, O. Abidate, D. Rats, J. Fontaine, L. Vandenbulcke, C. Germain and A. Catherinot, *Proc. of the V^{th} Int. Symp. on Diamond Materials*, J. L. Davidson, W. D. Brown, A. Gicquel, B. V. Spytsin and J. C. Angus Eds, The Electrochem. Soc., Pennington (New York), 126 (1998).

[205] M. Jaouen, G. Hug, V. Gonnet, G. Demazeau, G. Tourillon, *Microsc. Microanal. Microstruc.*, **6**, 127 (1995).

[206] Z. Weng-Sieh, K. Cherrey, N. G. Chopra, Y. Miyamoto, A. Rubio, M. L. Cohen, S. G. Louie, A. Zettl and R. Gronsky, *Phys. Rev. B*, **51**, 11229 (1995).

[207] T. Sasaki and N. Bartlett, (unpublished data in Ref. [166]).

Index

α_{12}-B, 109
    cohesive energy, 109
^{13}C NMR chemical shift, 66
    graphitic-like C_3N_4, 69
c-BN, 106

Al_2O_3, 2
APW, 29
ASA, 34, 43
    definition of, 34
ASW, 33, 43
    formalism, 34

B/G ratio, 88
BC_2N, 1, 100
    band structure, 120
    brittleness and ductility, 118
    bulk modulus, 117
    cohesive energies, 116
    elastic constants, 119
    electron density map, 117
    electronic density of states, 120
    ELNES, 127
        B K edge, 134
        C K edge, 132
        N K edge, 133
        peaks positions, 130
    enthalpy of formation, 108
    hardness, 114
    mechanical stability, 118
    model phases
        I, 103, 104
        II, 103, 105
        III, 104, 106
    Poisson's ratio, 120
    shear modulus, 117
    Young's modulus, 120
Blöch's theorem, 22
BN, 2
    bulk modulus, 52
    cohesive energy, 116
    cohesive properties, 106
    density of states, 126
    elastic constants, 117
    ELNES
        B K edge, 134
        N K edge, 133
        peaks positions, 130
    enthalpy of formation, 111
    hexagonal, 107
        structure, 108
    shear modulus, 54, 117
Bond enthalpies, 49
Born stability criteria, 85
    cubic, 87
    orthorhombic, 87
    tetragonal, 87
    trigonal, 118
Boron carbon nitrides, 98
Brittleness, 88
    BC_2N, 118
    $C_{11}N_4$, 89
    C_3N_4, 89
Bulk modulus, 5, 6, 9

BC_2N, 117
Birch equation, 10
$C_{11}N_4$, 86
C_3N_4, 42
diamond, 106
empirical relation, 6
frozen, 56
lonsdaleite, 106
relaxed, 56
volumetric compressibility, 5

$C_{11}N_4$, 41, 72
brittleness and ductility, 88
elastic constants, 86
electronic structure, 89
density of states, 89
ELNES, 91, 93
C K edge, 95
N K edge, 96
lattice stability, 87
model systems
alpha, 72
beta, 72
graphitic-like, 78
nitrogen hole, 89
phase transitions, 76
Poisson's ratio, 88
relative stability, 76
thermodynamic stability, 80
$\Delta H^o_{f,0}$, 81
Young's modulus, 88
C_2N_2, 41
C_3N_4, 2, 42
$\Delta H^o_{f,0}$, 50
brittleness and ductility, 88
electronic structure, 89
density of states, 68, 90
electron density map, 67
ELNES
C K edge, 93
N K edge, 96
hardness, 51
compressibility, 51
resistance against strains, 53
model systems, 43
alpha, 44
beta, 2, 43
cubic, 44
graphitic hexagonal, 44
graphitic orthorhombic, 44
graphitic rhombohedral, 44
pseudo-cubic, 44
Poisson's ratio, 88
relative stability, 44
thermodynamic stability, 48
Young's modulus, 88
$C_{\frac{3}{4}}N$ fragment, 50
Carbon hole, 80
Carbon nitrides, 40
fulleren-like, 41
giant molecules, 49
graphitic-like, 41
Ceperly-Alder, 21
COOP, 61
C_3N_4
hexagonal *vs.* orthorhombic, 63

Density functional theory, 13
GGA, 15
Kohn-Sham orbitals, 16
LDA, 13
Deposition techniques
CVD, 1
PVD, 1
DFT-LDA, 48
Diamond, 1, 2, 40, 43
Bulk modulus
empirical equation, 6
bulk modulus, 52
carbon substitution, 101

cohesive energy, 49
cohesive properties, 107
crystal structure, 100
density of states, 126
diamond-like matrix, 79
diamond-like structure, 98
elastic constants, 55, 119
frozen, 56
relaxed, 56
ELNES, 94
experimental CVD diamond spectra, 132
peaks positions, 93, 130
theoretical spectra, 132
energy *vs.* volume, 108
hardness
Mohs and Knoop, 8
hexagonal (see *Lonsdaleite*), 99
isoelectronic to, 6, 42
Poisson's ratio, 88
primitive unit cell, 102
rehybridisation and *d*-states, 88
shear modulus, 54, 87, 119
substituted, 99
the hardest known material, 1
Young's modulus, 88
Ductility, 88
BC_2N, 118
$C_{11}N_4$, 89
C_3N_4, 89

EELS, 29, 93
Elastic constants
calculation of, 11, 83
definition of, 11
frozen, 56
inequivalents
cubic, 12
orthorhombic, 83
tetragonal, 84
relaxed, 56
strains
cubic, 85
orthorhombic, 84
tetragonal, 85
Electron counting, 6
isoelectronic compounds, 7
Electronic properties
C_3N_4
graphitic forms, 65
density of states
C_3N_4, 65
site projected density of states
C_3N_4, 66
ELNES, 73, 91
BC_2N, 132–134
BN, 131
$C_{11}N_4$, 91, 93, 96
C_3N_4, 93, 96
diamond, 94
graphite, 94
Equation of state
Birch equation, 10

Fermi energy, 5, 62, 65, 91, 120
FP-LAPW, 29, 43, 73, 79

Gauge independent atomic orbital, 67
GAUSSIAN98, 67
Geometry optimisation
C_3N_4, 59
GGA
PBE, 48
PW91, 48

Hardness
and covalency, 5
definition of, 1
minerals and synthetic ceramic
Knoop scale, 8
Mohs scale, 8

Mohs scale, 9
scratch test, 9
Vickers test, 9

ICOOP, 62
C_3N_4
hexagonal *vs.* orthorhombic, 63
Isoelectronic compounds
schematic composition diagram, 7

LAPW, 30
LDA, 43
LMTO, 33, 43
LMTO-ASA, 34
Lonsdaleite, 100
bulk modulus, 107
carbon substitution, 103
cohesive properties, 107
crystal structure, 100
elastic constants, 117
shear modulus, 117

M3PEC, vi
muffin-tin
approximation, 31
radius (R_{mt}), 30
BC_2N, 106
$C_{11}N_4$, 73
C_3N_4, 43, 58

N_2, 41

Plastic deformation, 53
Poisson's ratio, 88, 120
Pseudo-potential method, 44

Quantum monte carlo, 48

Schrödinger's equation, 13
Shear modulus, 9
isotropic, 11, 12
cubic, 85
general form, 12, 84
orthorhombic, 85
tetragonal, 85
relation stress-strain, 11
Si_3N_4, 1
SiO_2
stishovite, 1
Snake-like density, 67
Stiffness, 88

TiC, 2
TiN, 2

US-PP, 24, 79

VASP, 21

WC, 2
WIEN97, 29

Young's modulus, 88, 120

Zn_2SiO_4, 44